



UNIVERSITAT DE
BARCELONA

Late Holocene Climate Variability in the North Atlantic based on biomarker reconstruction

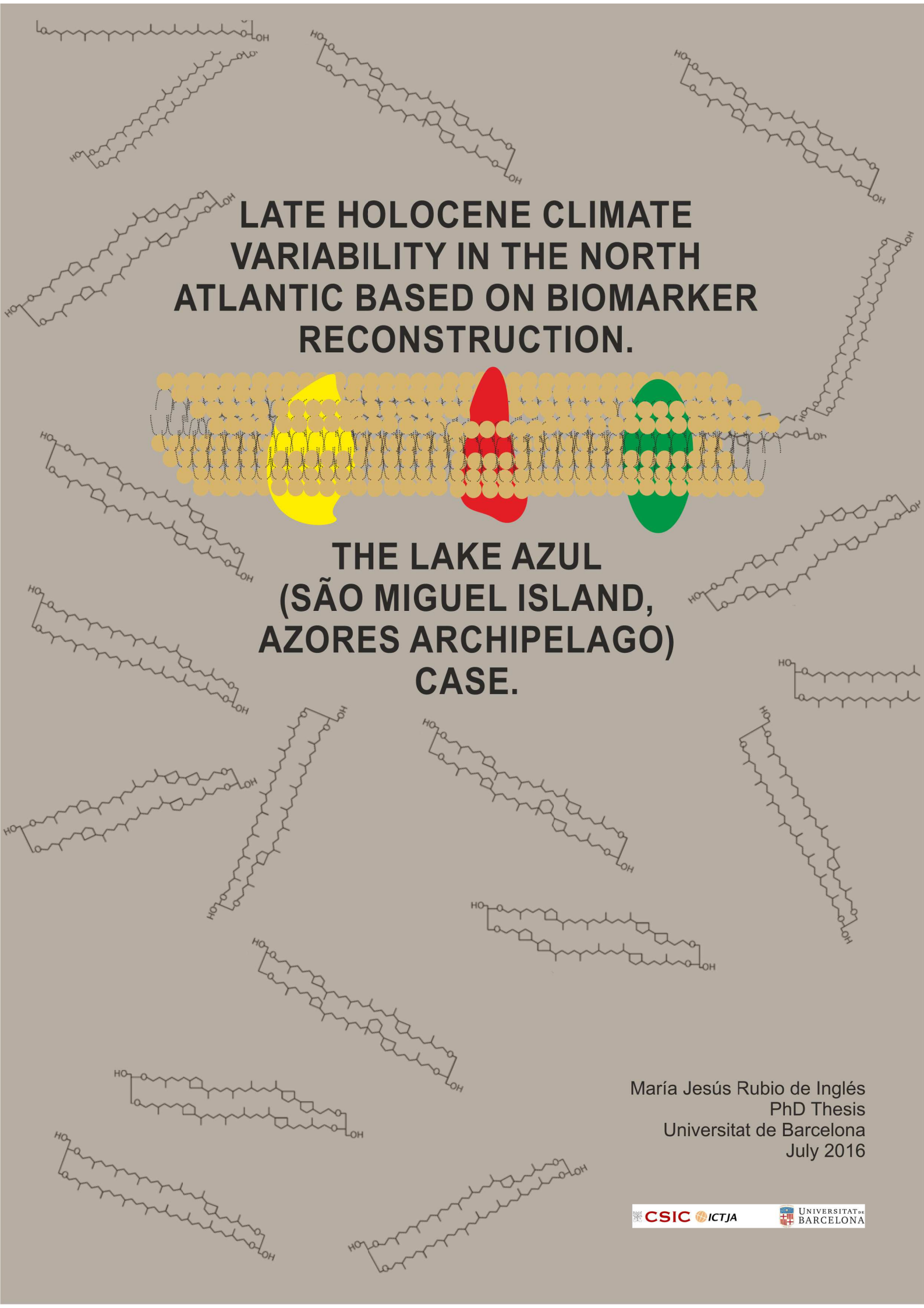
The lake Azul (São Miguel, Azores archipelago) case

María Jesús Rubio de Inglés

ADVERTIMENT. La consulta d'aquesta tesi queda condicionada a l'acceptació de les següents condicions d'ús: La difusió d'aquesta tesi per mitjà del servei TDX (www.tdx.cat) i a través del Dipòsit Digital de la UB (diposit.ub.edu) ha estat autoritzada pels titulars dels drets de propietat intel·lectual únicament per a usos privats emmarcats en activitats d'investigació i docència. No s'autoritza la seva reproducció amb finalitats de lucre ni la seva difusió i posada a disposició des d'un lloc aliè al servei TDX ni al Dipòsit Digital de la UB. No s'autoritza la presentació del seu contingut en una finestra o marc aliè a TDX o al Dipòsit Digital de la UB (framing). Aquesta reserva de drets afecta tant al resum de presentació de la tesi com als seus continguts. En la utilització o cita de parts de la tesi és obligat indicar el nom de la persona autora.

ADVERTENCIA. La consulta de esta tesis queda condicionada a la aceptación de las siguientes condiciones de uso: La difusión de esta tesis por medio del servicio TDR (www.tdx.cat) y a través del Repositorio Digital de la UB (diposit.ub.edu) ha sido autorizada por los titulares de los derechos de propiedad intelectual únicamente para usos privados enmarcados en actividades de investigación y docencia. No se autoriza su reproducción con finalidades de lucro ni su difusión y puesta a disposición desde un sitio ajeno al servicio TDR o al Repositorio Digital de la UB. No se autoriza la presentación de su contenido en una ventana o marco ajeno a TDR o al Repositorio Digital de la UB (framing). Esta reserva de derechos afecta tanto al resumen de presentación de la tesis como a sus contenidos. En la utilización o cita de partes de la tesis es obligado indicar el nombre de la persona autora.

WARNING. On having consulted this thesis you're accepting the following use conditions: Spreading this thesis by the TDX (www.tdx.cat) service and by the UB Digital Repository (diposit.ub.edu) has been authorized by the titular of the intellectual property rights only for private uses placed in investigation and teaching activities. Reproduction with lucrative aims is not authorized nor its spreading and availability from a site foreign to the TDX service or to the UB Digital Repository. Introducing its content in a window or frame foreign to the TDX service or to the UB Digital Repository is not authorized (framing). Those rights affect to the presentation summary of the thesis as well as to its contents. In the using or citation of parts of the thesis it's obliged to indicate the name of the author.



**LATE HOLOCENE CLIMATE
VARIABILITY IN THE NORTH
ATLANTIC BASED ON BIOMARKER
RECONSTRUCTION.**



**THE LAKE AZUL
(SÃO MIGUEL ISLAND,
AZORES ARCHIPELAGO)
CASE.**

María Jesús Rubio de Inglés
PhD Thesis
Universitat de Barcelona
July 2016

1. INTRODUCTION

1.1 LAKES.

Lakes are inland bodies of standing water (Encyclopedia of science, 2002). The total abundance of lakes larger than 0.002 km² obtained by remote sensing larger than 0.002 km² are 117 million occupying an area of $9.6 \cdot 10^6$ km² and constituting the 7.2 % of the non-glaciated land. Those water bodies are widespread from pole to pole but, mostly located at high latitudes of the Northern Hemisphere (Larson and Schaetzl, 2001). Only Canada accounts with the 50 % of the total lakes of the world. The largest lake depending on the area is the Lake Superior between Canada and United States with an area of 82100 km², the largest lake depending on length is the Lake Tanganyika with 676 km² and lake with largest water volume and depth is the Lake Baikal with 23600 km³ and 1637 m depth respectively (“Lakenet”, 2016). Lakes have been widely studied under a huge number of points of view, which include their importance in the trophic chain of the ecosystems (Margalef 1983) and their impact on the local and regional economy (Robins 1983).

Depending on the physical factor triggering the formation of the water body, lakes can be classified in eight types: glacial, riverine, human-made, eolian, coastal, karstic, tectonic and volcanic (Wetzel, 2001).

Glacial lakes are the most common type. Almost all of them were formed by the ice sheet and ice caps retreating from the last glacial period (Wetzel, 2001). Examples of these glacial lakes are the Great Lakes in North America (Larson and Schaetzl, 2001) as well as those found in the alpine ranges. Inside this group there is other kind of lakes formed by the action of the rocky debris gathered by the glacial movement. Those lakes are referred as moraine lakes and the kettle ponds in Siberia are an example of this (Wetzel, 2001).

The lateral migration of river courses can also form lakes. Those lakes are formed in two different ways: 1) at the waterfall foot as a consequence of an intense erosion process (plunge-pool lakes), or 2) by the dam formation owing to the accumulation of

fluvial transport of sediments (oxbow lakes) (Wetzel, 2001). An example of riverine formation lakes are the oxbow lakes of the river Borneo in Malasia (Purcell, 1941).

Tectonic lakes are formed by tectonic movements and they typically are located following fault lineations and planes. Their principal characteristic is that those lakes tend to be the largest, deepest and oldest lakes over the Earth. Famous examples are Lake Baikal and most of the African rift valley lakes.

Volcanic lakes are formed by the water accumulation in a crater fissure or by the crater itself. The main characteristic is the little productivity that they show at their beginning (Wetzel, 2001). Sometimes lakes that form inside caldera without volcanic activity are considered caldera lakes. Those lakes have some intrinsic characteristics such as they are hidrological close systems (endorheic basin) and their area depends on the morphology of the occupying crater (Wetzel, 2001). An example of volcanic lakes is the Lake Azul in Azores (Constancia et al., 2000).

The humans also make inland water accumulation areas, which most of them might end as lakes. These artificial lakes are commonly used as drink water reservoirs during dry months or droughts, for power generation and/or recreational issues. Many countries such as Canada, Russia, Spain, Egypt, Venezuela and many others have examples of this lake type (Wetzel, 2001).

The lake level depends on the hydrological conditions in the area that, in turn, affect the hydrological cycle. The inputs of water to the lake are the direct precipitation; the surface inflow and the ground water discharge whereas the water outputs in a lake are the evaporation, the evapotranspiration, the groundwater recharge and the surface discharge (Fig. 1.1). If the water supplied by the inputs is equal to the losses by the outputs, the water level remains constant. If inputs (outputs) are greater, the water level increases (decrease) (Cohen, 2003). The lake level changes produces fluctuations in the physico-chemical parameters of the lake water column which, in turn, affect the biogeochemical cycles of the main chemical elements, such as carbon and nitrogen.

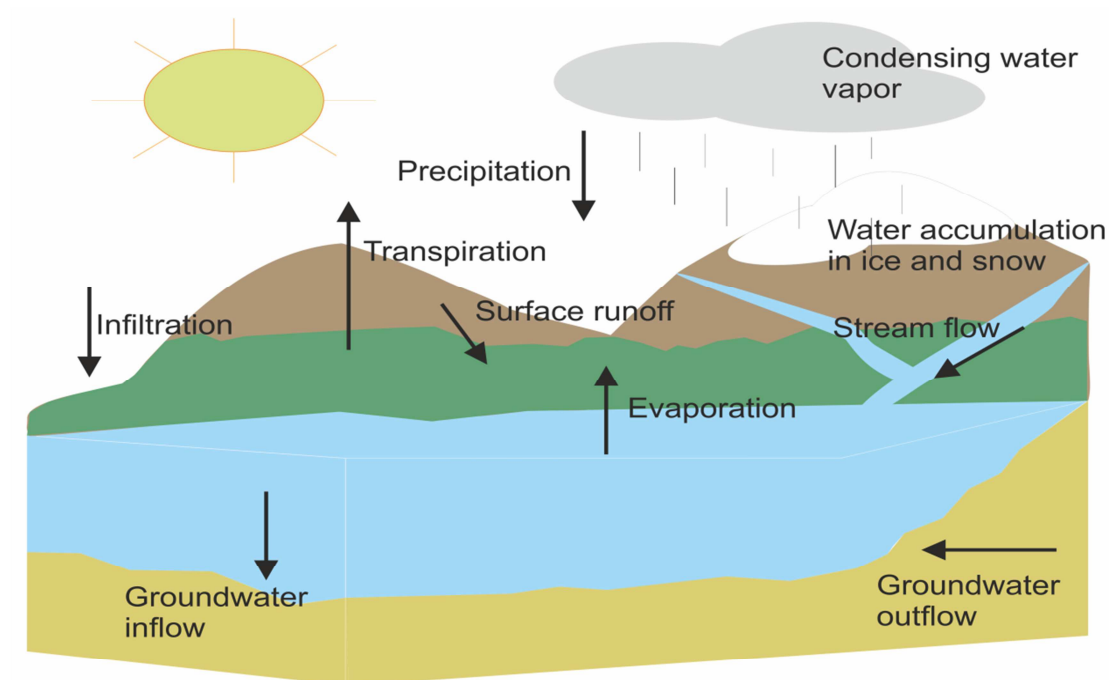


Figure 1.1: Scheme showing the water cycle on the Earth surface involving the role of lakes. The water fall on the ground after condensation via precipitation and it is transferred to the lakes via surface runoff, stream flow and/or groundwater outflow. The water that reaches the ground can be also obtained from the ice melting. The lakes and ground lose water via evaporation and transpiration, respectively. The lake can also lose water via groundwater inflow.

The carbon cycle is one of the most complex biogeochemical cycles since it involves organic and inorganic chemical reactions. A general diagram flow of the carbon cycle can be observed in figure 1.2. The carbon content in lakes can be present in organic (organic matter) and inorganic (carbonates) forms as particulate and/or dissolved material (Leng et al., 2006). CO_2 comprises the 0.0035% of the atmosphere composition but, owing to the combustion of fossil fuels the net CO_2 accumulation in the atmosphere increase in a rate of 0.4% per year (Siegenthaler and Sarmiento, 1993). Therefore, the scientific community has an increasing interest in lakes as a carbon sinks because the elevated solubility of the CO_2 in the water (Dean and Gorham, 1998; Cohen, 2003).

Mechanisms such as photosynthesis or CO_2 degassing can modify the CO_2 content in the lake water column. Much of the carbon content in lakes is in the organic carbon form contained in molecules such as carbohydrates, lipids, proteins and humic substances (Meyers and Ishiwotari, 1993). The dissolved organic carbon (DOC) inputs

are produced by the breakdown of autotrophic organisms, the allochthonous plant organic matter and the excretion of zooplankton (Søndergaard et al., 1995; Wetzel, 2001; Cohen, 2003). The lake autochthonous DOC depends on the productivity and usually displays seasonal variation. Changes on the DOC imply physical variation on the water column because a decrease in DOC content results in a water transparency and, consequently, an expansion of the photic zone (Wetzel, 2001). On the other hand, the Particulate Organic Carbon (POC) fraction corresponds uniquely to the 10% of the total organic carbon. This POC can reach the sediment in shallow lakes but, it is dissolved in deep lakes (Meyers and Ishiwotari, 1993).

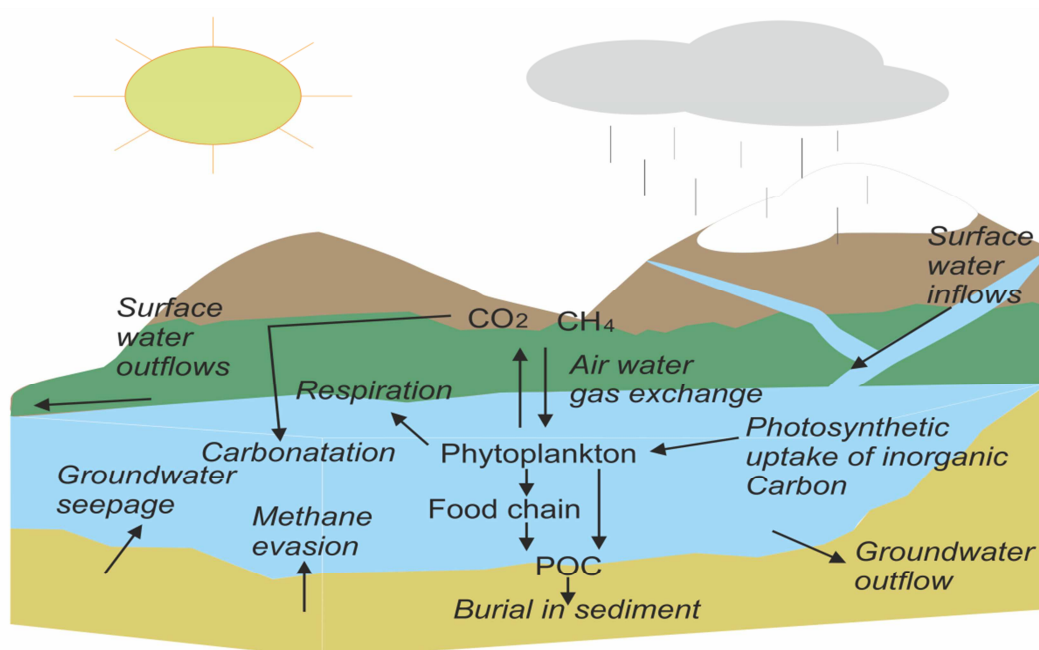


Figure 1.2: Scheme showing the carbon cycle in lakes. The carbon is present in the atmosphere and transferred to the lakes via dilution (carbonatation) or air water gas exchange (in equilibrium reaction). Inside the lake, the carbon is used by photosynthetic organisms and incorporated to the food chain or sedimented as Particulate Organic Matter (POM). Those organisms also lose part of this carbon via respiration. Once in sediment, the organism degradation produces carbon release to the water column via methanogenesis. The carbon is also in equilibrium with the ground water composition and it is incorporated or released via groundwater outflow or inflow.

The Nitrogen represents a very complex biogeochemical cycle (Figure 1.3). It is the most abundant component of the atmosphere (78%) and it is basically found in the N_2 form. The atmospheric N_2 molecules show a strong covalent bonding that, uniquely, can be reduced by biological processes. The reduction processes are conducted by

bacteria and blue-green algae (cyanobacteria). This procedure is called nitrogen fixation and it can occur in soils and water (Wetzel, 2001).

The N_2 fixed by bacteria or algae is introduced to the food chain via phytoplankton towards higher levels (Figure 1.3). At each trophic level, waste containing N is created. This waste can be either dissolved or sedimented on the lake floor. Fixed nitrogen can also be added to the system from rivers, precipitation water and aerosols (Cohen, 2003). The bacteria breakdown generates ammonia (NH_4^+) that can be oxidized to nitrate (NO_3^-) in a process called nitrification, and vice versa, Nitrates can be reduced to ammonia and assimilated by plants and algae. The NO_3^- can also be reduced to N_2 or NO_2 in a process called denitrification that results in the loss of useable nitrogen (Seitzinger, 1988). Plants can also add nitrogen to the system but unequally depending on their environment. Terrestrial plants with woody tissue and cellulose has low N concentration compared to aquatic plants (Cohen, 2003).

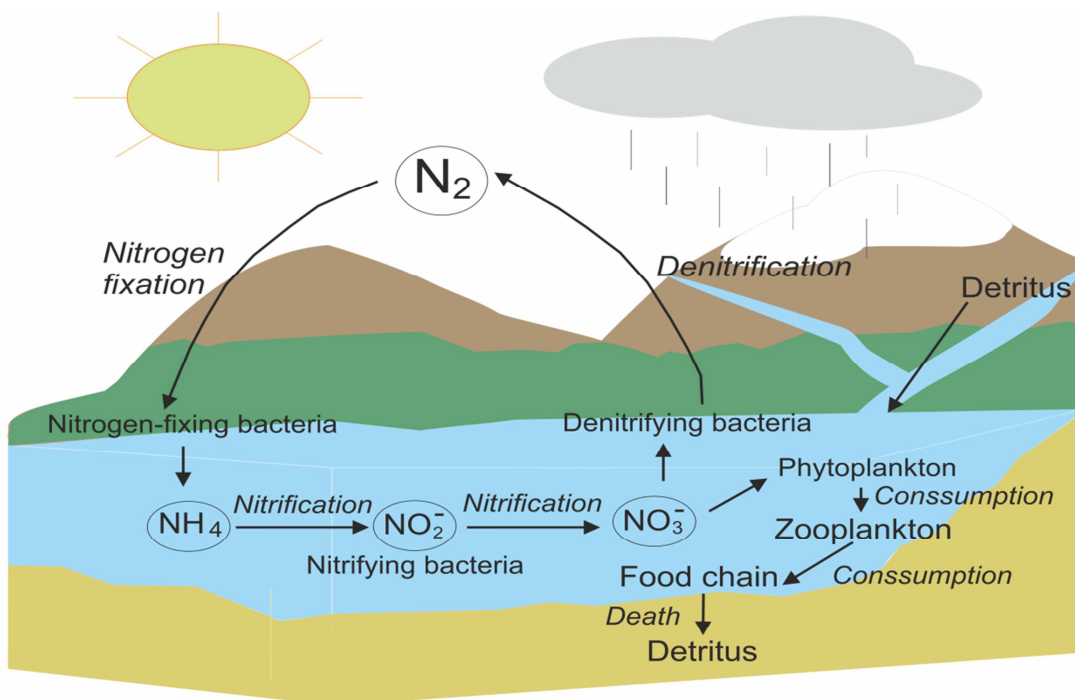


Figure 1.3: Scheme showing the nitrogen cycle in lakes. The atmospheric nitrogen (N_2) is fixed by bacteria or cyanobacteria that transform it via nitrification to NO_3^- . This NO_3^- is consumed by phytoplankton and incorporated to the food chain or released to the atmosphere via denitrifying bacteria. The N is incorporated via food trophic chain is deposited on the lake bottom after the organism death and accumulated in the sediments.

The trophic state is based on lake fertility, which in turn, is based on nutrients availability. The nutrients determining the lake primary production are mainly nitrogen (N) and phosphorous (P) because they are limitant in the ecosystem. The primary production affects the entire food chain affecting the lake biology (Cohen, 2003).

Depending on the trophic state, the lakes can be classified in oligotrophic, mesotrophic and eutrophic (Carlston and Simpson, 1996). One ecosystem is considered oligotrophic when the low production is associated with the scarcity of nutrients (N and P). Lakes are eutrophic when the amount of nutrients is high and, therefore, there is an enhancement in production. The mesotrophic state is in between of the two previous statuses.

Another way to classify lakes is, according to Hutchinson-Löffler that can be ordered in six categories with respect to the lake water column mixing: 1) amictic, 2) cold monomictic, 3) Dimictic, 4) warm monomictic, 5) oligomictic, and 6) polymictic (Wetzel, 2001).

1.2 LAKE SEDIMENTS AS PALEOCLIMATIC AND PALEOENVIRONMENTAL ARCHIVES.

Lake sedimentary records are widely employed to carry out multi-proxy environmental and climate reconstructions (Cohen, 2003; Bradley, 2015). The robustness and accuracy of these reconstructions primarily depends on both the quality of the proxies (Birks et al., 2010) employed in these reconstructions as well as on the quality of the chronological models (Telford et al., 2004).

Age modelling and datation.

The acquisition of an accurate dating is essential for paleoclimatic studies. Strenuous efforts have been done to improve the dating methods and nowadays it is possible to date a large variety of materials and tiny amounts of them (Bradley, 2015). Dating methods are divided in four categories: radioisotopic methods, paleomagnetic correlations, chemical methods and biological methods (Bradley, 2015). Not all the dating methods can provide a confident numerical age but, they can give methods of stratigraphic correlation (in instance, paleomagnetic methods).

The most widely used are the radioisotopic methods which consist on measurement of cosmogenic nuclides, direct measurements of radioisotope decay products (^{14}C , ^{210}Pb), and integrated effects (TL, fission track). For those, the most commonly used to constrain the age of the sedimentary sequences is the radiocarbon dating (^{14}C) (Bradley et al., 2015).

Since the dating methods have improved through time, also the construction of the age-depth models has been revised (Blaauw, 2010, Telford et al., 2004). Age-depth models have progressively moved towards a more realistic concept of sedimentation, trying to represent and assess natural processes by means of many mathematical and statistical approaches. These approaches go from simple linear regressions to sophisticated Bayesian estimations (e.g. Parnell et al., 2011).

Pioneering works like Grimm (1990) proposed new software to calculate the age between dated points using linear interpolation, cubic spline interpolation and polynomial fitting. The dating uncertainties were not accounted in these first models; however this issue was solved using the mixed-effect regression presented by Heegard

et al. (2005). A new generation of approaches to construct age-depth models began using Bayesian methods (Bucks et al., 1991) being Bpeat one of the first Bayesian model software proposed (Blaauw and Christen, 2005). This model employed a non-linear relationship between ^{14}C and calendar years (wigggle-matching) but, a linear accumulation between dated points. Oxcal is based on the same premise that Bpeat but, generates all the possible age models for the profile using a Bayesian approximation. Hasslet and Parnell (2008) presented a continuous monotone stochastic process (Bchron). This could be explained as an integrated method with a positive and constant piecewise process. Other existing software, such as Clam (Blaauw, 2010) and Bacon (Blaauw and Christen, 2011) were designed to provide a more user-friendly interface of the Bayesian age-depth models and a modeling of the accumulation rate to establish a coherent age for each depth, respectively. These software enabled to add to the model previous information (prior probabilities) which is evaluated by the model accordingly (posterior predictive distribution) to some parameters established by the user. This additional information enriches the chronological model construction, obtaining more realistic results.

A common feature of all these approaches is that they only model the fluctuations of the sedimentation rate (SR) following a more or less holistic approach. This approach works well with sedimentary records that present a roughly constant SR, but it hardly works when sudden and abrupt SR changes occur. Changes in the SR of many sedimentary environments, such as lakes, are mainly triggered by fluctuations in the input of terrigenous material and variations in the type of processes transporting and depositing particulate material. These abrupt and sudden changes in the SR can be clearly identified in a large number of lacustrine sediment sequences where two or more distinctive depositional facies have been identified (e.g. Valero-Garcés et al., 2014). The extensive literature based on sedimentary processes shows that each of these distinctive facies can be accumulated at very different velocities (Einsele, 2000 and references therein). The extreme case of this would be the deposition of coarse material because of flooding flashy processes (almost an instantaneous deposit or deposited within few days) in opposition with the hemipelagic sedimentation of clayey fine material (which, in some cases, 10 mm might represent years or even decades of

deposition). Therefore, the construction of the chronological models for these sedimentary sequences using the available software most probably overrun these marked lithological changes and overestimate (e.g. coarse siliciclastic material) and underestimate (e.g. hemipelagic clays) the time that these lithofacies might represent. These errors in the time distribution might not be significant when working with sedimentary successions that record thousands of years since these errors might be smaller than the uncertainties associated to the chronological model (Ramsey, 2008). However, they might be of paramount importance when working with historical sedimentary records. In this case, the errors of time distribution would be larger than the uncertainties of the radiometric dates, hampering the correct attribution of the identified environmental/climatic/anthropogenic events in the sediments to the instrumental/written sources, and hindering their correct interpretation as well as their regional and global correlation. Therefore, an additional effort must be carried out in order to improve the correct distribution of time in historical sedimentary sequences.

The parameter that determines the distribution of time along lacustrine deposits is the SR. This SR is predominantly affected by two factors: 1) the production of in-lake material and 2) the inputs of terrigenous particles (Cohen, 2003). The in-lake production is usually related to several organisms and it can fluctuate seasonally, whereas the terrigenous material is delivered to the lake by different processes such as superficial drainage (runoff and streams) and eolian activity (Bradley, 2015) at variable time scales (i.e. instantaneous vs multiannual). In most lakes, the allochthonous material is mainly composed of siliciclastic material, with a broad range of chemical composition and particle size (Smith and Carroll, 2015). The siliciclastic particulate material represents the main volume of sediments in non-carbonatic and non-evaporitic lakes. Thus, the accurate determination of the total amount of siliciclastic material would correctly assess the long- and short-term variations of the SR. This precise assessment would permit a better time distribution thorough the sediments, largely improving the age-depth models of historical sedimentary sequences.

Inorganic proxies

A large and continuously increasing set of proxies can be employed to perform accurated and robust paleoclimate and paleoenvironmental reconstructions. Amongst other, XRF, bulk organic matter and biomarkers.

The X-Ray Fluorescence (XRF) core scanning is an essential tool for high-resolution geochemical characterization of sedimentary records (e.g. Rothwell, 2006; Hennekam and de Lange, 2012). The XRF has been successfully applied to a large amount of lacustrine records to qualitatively reconstruct a large variety of geologic (Rothwell et al, 2006), environmental (Ziegler et al., 2008) and climate processes (Peng et al., 2005). Since this technique allows the user to continuously determine the chemical composition of the sediments up to every 100 μm , it permits to track with a high degree of detail and accuracy physical and chemical processes. Furthermore, the abundant scientific literature available largely proves that this is a low-cost technique with robust and reliable results (Rothwell, 2006; Hennekam and de Lange, 2012). One of the most frequent processes reconstructed by the XRF data are those associated with the volume of the siliciclastic particulate material inputs to the lakes (e.g. Moreno et al. 2008; Kylander et al. 2011), allowing a precise assessment of the fluctuations in the SR. Therefore, the XRF data can also be a useful tool to improve the chronological models of historical sedimentary sequences by correctly distributing the time when more or less contrasting lithofacies are present.

Bulk organic matter proxies and their isotopic composition.

The total amount of organic matter is represented by the percentage of Total Organic Carbon (% TOC) in lake sediments. TOC values depend on both the initial production and the degree of degradation of the organic matter (Meyers and Teranes, 2001; Leng et al., 2006). The primary source of organic matter to lake sediments is from plants in and around the lake (Meyers and Teranes, 2001). The photosynthetic organisms responsible of this organic matter can be divided in two groups: i) non-vascular plants with little or no cellulose and lignin having large amounts of nitrogen-rich proteinaceous material (for ex., phytoplankton), ii) vascular plants with large proportions of woody tissues rich in waxy hydrocarbons such as grasses, shrub and

trees (Meyers, 2003). The organic nitrogen is preferentially produced by proteins and nucleic acids that are more abundant on lower plants (Talbot and Johannessen, 1992; Leng et al., 2006) while organic carbon is preferentially produced by terrestrial plants with great amount of cellulose (Meyers and Teranes, 2001; Leng et al., 2006). Another important source of organic matter is the bacterial biosynthesis in strongly stratified lakes and the effect of wind transporting material (Meyers and Ishiwatari, 1993).

This organic matter that reaches the lake suffers substantial changes before being deposited on sediment (Meyers and Ishiwatari, 1993). In one hand, the organic matter in the water column suffers different transformations such as the oxidative alteration and destruction. On the other, the organic matter already deposited on sediments can be re-suspended and exposed again to the water column, affected by the bioturbation, oxidation and, finally, altered by the methanogenic bacteria (Meyers and Ishiwatari, 1993).

Changes on the $\delta^{13}\text{C}$ composition of the lacustrine organic matter can be related to productivity, nutrient supply (Leng et al., 2006), atmospheric CO_2 , climate (Meyers and Teranes, 2001) and changes on vegetation or landscape management (Leng et al., 2006). Many authors have used the $\delta^{13}\text{C}$ signal as a proxy to evaluate changes on the vegetation cover. Increases in the $\delta^{13}\text{C}$ ratio have been widely used as indicator of aquatic productivity in lakes (Hollander and Mckenzie, 1991; Hollander et al., 1992; Hodell and Schelske, 1998; Brenner et al., 1999; Meyers, 2003). For terrestrial plants, the $\delta^{13}\text{C}$ composition depends on the photosynthetic pathway. The major part of the photosynthetic plants use the C_3 Calvin-Benson pathway to incorporate the carbon to the organic matter producing a shift of -20‰ on the $\delta^{13}\text{C}$ signal, but some other plants use C_4 Hatch-Slack or CAM (Crassulacean acid metabolic) pathway. In this second case, the carbon isotope composition is between -8 and -12‰ for C_4 plants and -10 to -20‰ for CAM plants. This different signature offers a possibility to reveal the source of the organic matter and/or changes on vegetation (Meyers and Ishiwatari, 1993).

Another common use of the $\delta^{13}\text{C}$ composition of the lake organic matter is as a proxy of hydrological changes. Periods of desiccation and/or dry periods can alter the

composition of $\delta^{13}\text{C}$ (Meyers and Ishitawari, 1993). Some authors suggested that evaporation processes have a preference on light carbon than on heavy carbon producing this type of fractionation (Talbot and Johannessen, 1992; Meyers and Ishitawari, 1993)

Nitrogen isotopes ($\delta^{15}\text{N}$) also provide paleoenvironmental information but, it is not as widely used as $\delta^{13}\text{C}$ because of its complexity (Leng et al., 2006). Atmospheric nitrogen can be deposited in the form of dissolved inorganic nitrogen (nitrate and ammonium) and dissolved organic nitrogen. This atmospheric nitrogen has an isotopic value of 0‰. The N directly fixed from the atmosphere by bacteria or cyanobacteria suffers a very little fractionation showing values around 0‰ as well (Fogel and Cifuentes, 1993; Leng et al., 2006). Plants $\delta^{15}\text{N}$ have values in the range of -5‰ and 8‰; soil values range between 0 and +8‰, fertilizers contain values between -4 to +4 ‰, and human and animal sewage waste display values between +8 to +18‰. But, the $\delta^{15}\text{N}$ signal is more complex than that and it shows important changes on fractionation depending on the studied area (Leng et al., 2006).

Biomarkers: Compound specific organic matter proxies.

The last two decades have been witnesses of the improvement on analytical techniques that allowed scientists to use biomarkers as paleoclimate proxies (Tierney, 2012; Sachs et al. 2013). Lipids showed to be a promising tool in this respect because they are widely present in membranes of bacteria, algae and higher plants; and, persist in the sedimentary record over geological timescales (Eglinton and Eglinton, 2008).

Biomarkers are defined as organic compounds produced by specific organisms. After the organism decease, those biomarkers get preserved on sediment recording the life conditions of the carrying organisms (Eglinton and Eglinton, 2008; Bradley et al., 2015). This organic matter is formed by a complex mixture of lipids, carbohydrates, proteins and other chemical components (Meyers, 2003). Changes on biota community structure affect the amount and type of these organic compounds (Meyers and Eadil, 1993). The biota structure and composition is not the uniquely factor affecting the organic composition. During deposition, the organic matter is subjected to microbial reworking (Meyers and Ishiwatari, 1993), remineralization and early diagenetic

processes (Meyers, 2003). Therefore, the quantity and type of organic matter permits to identify their origin and the processes suffered after sedimentation (Meyers et al., 2003).

Lipids are defined as grease or oily organic substances occurring naturally as hydrophobic molecules soluble in non-polar solvents. Those compounds include fats, oils, waxes and phospholipids. There is no common single structure that defines lipids but, the most common structures are triglycerids and phospholipids. The triglycerids have three fatty acids linked to a glycerol backbone and the phospholipids are components of the cell membrane that contains glycerol, fatty acids, phosphoric acids and low molecular weight alcohol. The functions of lipids are: 1) energy storages, 2) cell membrane structures, 3) membrane permeability regulators, 4) source of fat soluble vitamins, 5) act as electrical insulators as for the myelin sheath, 6) components of enzyme systems, 7) cellular metabolic regulators, 8) signaling molecules, 9) protection from cold, 10) transport, 11) fluidity maintaince, and 12) play an important role in pain or fever ("Lipids", 2016). Lipids are chemically knows as the fraction of the organic matter that can be extracted by organic solvents (Meyers and Ishiwatari, 1993). Those lipids also suffer a degradative alteration during sinking. For example, short-chain acids (n-C₁₆ and n-C₁₈) are 10 times faster degraded than long-chain acids (Meyers and Eadie, 1993). The alteration of lipid composition continues in sediments were solvent extractable lipids concentration became smaller while bound lipids concentration increase. But, the lipids associated to waxes or carbonate skeletons are less prone to suffer microbial degradation and are rapidly buried on sediments preserving its degradation (Meyers and Ishitawari, 1993).

Alkenones

The Alkenones are long chain unsaturated methyl and ethyl ketones with 37 to 40 carbon atoms and 2 to 4 double bounds and/or unsaturations with spacing for methylene groups. The function of alkenones remains unknown but, those seem to be used as storage lipids. They are ubiquitous in ocean and at some other environments such as lakes or soils (Rueda, 2013)

The main advantage of the alkenines is that they are not affected by precipitation, easy to understand and relatively simple to analyze at the laboratory. Based on that, many analyses regarding to the molecular structure and ratios of alkenones have been developed (Sachs et al., 2013). Alkenones environmental controls are relatively uncomplicated, showed well preservation and are ubiquitous (Tierney et al., 2012). Moreover, it was observed that alkenones were capable to record changes on temperature. Therefore, paleotemperature proxies based on molecular biomarkers showed to be a promising tool (Tierney et al., 2010).

The biomarker-based paleothermometers are based upon the principle that microorganisms adjust the rigidity of their cell membrane by altering the number of double bonds, rings or branches in response to environmental conditions such as temperature or pH (Ray et al., 1971; Kita et al., 1973; Nozawa et al., 1974; Tierney, 2012). The growth temperature or pH changes alter the alkyl or isoprenoid chain, apparently, to maintain the proton permeability through the cytoplasmic membrane (Van de Vossenbergh et al., 1999). The cytoplasmic membrane becomes more permeable by the addition of branches and/or rings; and, it can be observed analytically by the loss of molecular weight (Weijers et al., 2007). The permeability is only optimized for small species, such as H^+ or dissolved gasses. Large molecules such as nutrients are not related to the membrane permeability because, they pass through membrane channels. Therefore, no significant relation between the cell membrane permeability and trophic conditions of the environment are expected (Loomis et al., 2012). Despite all the information about the biological principle of alkenones, their metabolic role remains unknown (Tierney, 2012).

Alkenones have been used as paleothermometers in numerous environments: marine (Prah and Wakeham, 1987; Bard et al., 1997; Sachs and Lehman, 1999; Huguet et al., 2006; Castañeda et al., 2010), loess (Peterse et al., 2011), soils (Weijers et al., 2006) and lakes (Shanahan et al., 2012; Tierney and Russel, 2009; Sinninghe-Damsté et al., 2009; Blaga et al., 2010; Tierney et al., 2010); and in modern and ancient sedimentary deposits (Chappe et al., 1980; Brasell et al., 1981).

The most widely studied paleothermometers indexes based on alkenones are U_{37}^k , TEX_{86} and Cyclization Ratio of Branched Tetraethers/Methylation ratio of Branched Tetraethers (CBT/MBT).

The first alkenone used as paleothermometer was based on the relative distribution of the unique long-chain (C_{37}) ketones di- and tri-unsaturated. This biomarker is produced by marine haptophyte algae such as the ubiquitous coccolithophore *Emiliana Huxleyi* (Volkman et al., 1980; Marlowe et al., 1984 and Tierney, 2012). The U_{37}^k ratio preserved on sediments mainly reflects the mean annual temperature (Müller and Fischer, 2001; Prah et al., 1993) but, at high latitudes there is an strong summer to fall bias (Prah et al., 2010; Sikes and Volkman, 1993; Sikes et al., 2005; Ternois et al., 1998). The U_{37}^k has been widely used in the ocean until the mid-Cretaceous (Brassel et al., 2004) or even mid-Jurassic (Herbert, 2003; Tierney et al., 2012). Temperature reconstructions limitations to this technique are the upper temperature threshold, which is limited to 28 °C (not suitable for tropics or hothouse climates, Tierney, 2012), and the assumption that an ancient relative of *E. Huxley* had similar temperature sensitivity than the actual *E. Huxley* (Tierney, 2012).

In order to complete and extent the biomarker U_{37}^k , a proxy based on the relative abundance of Glycerol Dyalkyl Glycerol Tetraethers (GDGT) was setup. The GDGTs are core membrane-spanning lipids produced by archaea and bacteria (Blaga, 2010). GDGTs production can vary drastically depending on seasonality. At low latitudes, the GDGTs production occurs the entire year but at higher latitudes the production peak is reduced to only the summer period (Shanahan et al., 2013). This summer bias can also be affected by other parameters. For example, it has been observed that the moment of greatest flux of GDGTs from the water surface towards bottom of the lake coincide with the thermocline breakdown (Loomis et al., 2014). This could be a problem in temperate lakes since it might introduce a bias in the temperature reconstruction. Therefore, these lakes require a prior and careful study of the production and flux of GDGTs through the year before conducting any temperature reconstruction using this proxy (Loomis et al., 2014). The most important feature of the GDGTs relies on the core structure because their polar groups are lost during

diagenetic processes (Sturt et al., 2004; Schouten et al., 2008; Pitcher et al., 2010; Tierney, 2012). Depending on their core structure, there are two types of GDGTs: Isoprenoidal GDGTs (Iso-GDGTs) that have their origin in the Archaea phylum and branched GDGTs (BrGDGTs) that are from bacterial origin (Tierney, 2012) (Fig 1.4).

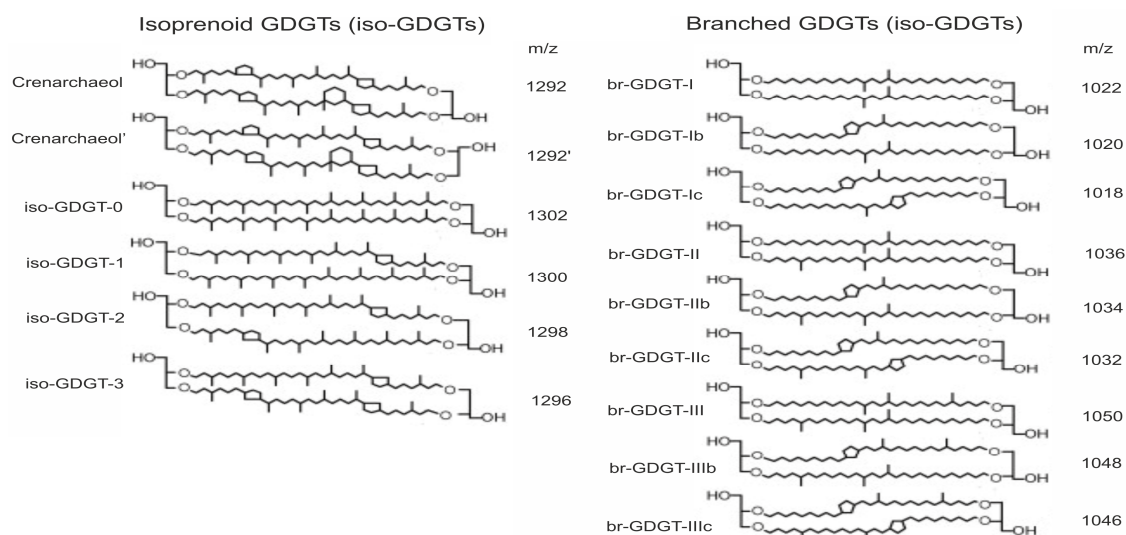


Figure 1.4: Isoprenoid and bacterial GDGTs chemical structure and molecular weight (m/z). On the left the isoprenoid GDGTs produced by the Archaea of the gender Thaumarchaeota. Those GDGTs are Crenarchaeol and its isomer, iso-GDGT-0, iso-GDGT-1, iso-GDGT-2 and iso-GDGT-3. On the right, bacterial GDGTs divided in three triplets depending on the number of methyl branches and differentiated within each triplet by the number of cyclopentane moieties. The first triplet is composed by br-GDGT-I, br-GDGT-Ib and br-GDGT-Ic and their respective chemical structure and m/z. The second triplet is composed by br-GDGT-II, br-GDGT-IIb and br-GDGT-IIc. And, the third triplet is composed by br-GDGT-III, br-GDGT-IIIb and br-GDGT-IIIc.

Archaeal GDGTs have an isoprenoid skeleton that consists of two head-to-head C₄₀ isoprenoid chains that connect ether bounds pentane or hexane rings (Weijers et al., 2006) (Fig 1.5). Iso-GDGTs can be produced by methanogenic, hyperthermophylic and mesophilic archaea. However, their paleothermometer condition is based on the phylum Thaumarchaeota (former Crenarchaeota, Brochier-Armanet et al., 2008; Spang et al., 2010) that is not restricted to extreme environments (Tierney et al., 2013). Thaumarchaeota is the only known Archaea that can produce crenarchaeol, which is the unique GDGT with cyclohexane rings. Crenarchaeol and its regioisomer are commonly produced at moderate and relatively high temperatures (Tierney, 2012).

Thaumarchaeota biosynthesize four types of GDGTs depending on the number of

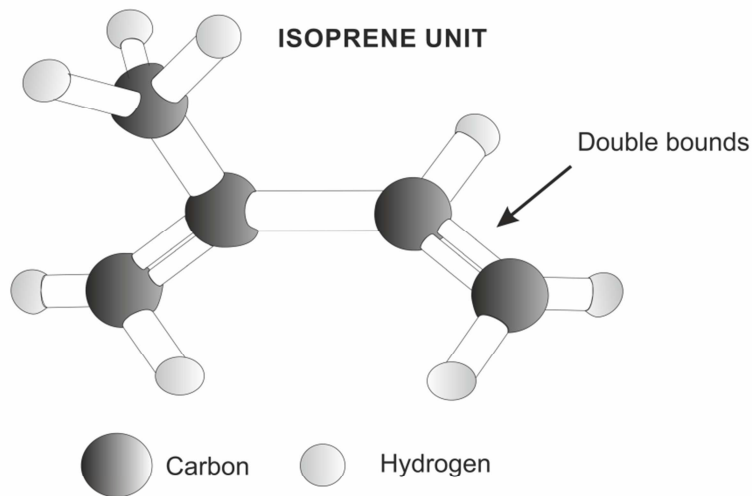


Figure 1.5: Chemical 3D structure of an isoprenoid chain unit. The dark circles represent carbon units and the light circles represent hydrogen units. The bonds are represented by cylinders.

cyclopentane and of moieties (Schouten et al., 2002; Sinningh-Damsté et al., 2002; Pitcher et al., 2005) (Fig 1.4). Based on the relative amount of cyclopentane and cyclohexane rings, the TEX₈₆ index appears as a new paleothermometer.

TEX₈₆ are the initials of TetraEther index of 86 carbons and represents the degree of cyclization of the GDGTs produced by the phylum Thaumarchaeota (Schouten et al., 2002). However, the application of this paleotemperatures is limited to large lakes owing to Thaumarchaeota soil production is very low (Weijers et al., 2006; Tierney et al., 2010; Tierney J.E., 2012). Small lakes do not have chemical or limnological conditions to support large populations of Thaumarchaeota and their validity (in case they are present) can be compromise by contamination from the methanogenic Euryarchaeota production (Blaga et al., 2009; Power et al., 2010).

In order to diminish the uncertainties contemplated by the TEX₈₆ temperature reconstructions, the alkenones as paleothermometers were further investigated. These investigations leaded to the use of br-GDGTs that showed valid temperature reconstructions in medium and small lakes (Shanahan et al., 2013). Br-GDGTs are from bacterial production. The stereochemistry of br-GDGT is similar to the previously explained isoprenoid GDGTs but, instead of the C₄₀ isoprenoid chain, they have C₃₀ alkyl chains that contain 4-6 methyl groups (Fig 1.6).

Br-GDGTs have an spanning membrane nature and double bounds like the archaeas but, they have a straight alkyl chain and stereo configuration at the C₂ position. Presumably, they are produced by anaerobic bacteria (Weijers et al., 2006) but, the origin of the bacterial production of GDGTs is not fully known. Sinninghe Damsté et al (2011) observed that GDGT-I

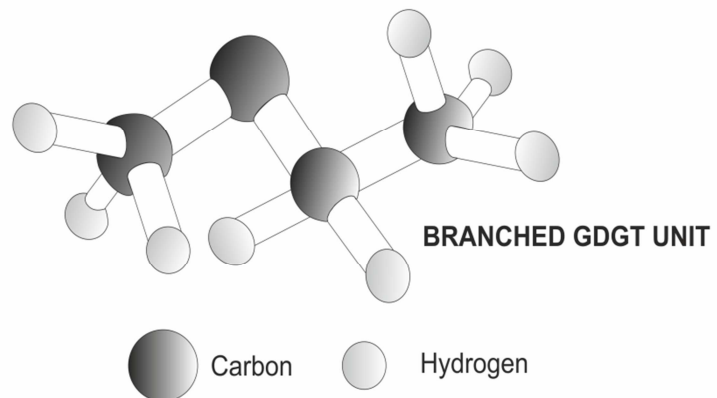


Figure 1.6: Chemical 3D structure of an alkyl chain unit. The dark circles represent carbon units and the light circles represent hydrogen units. The bounds are represented by cylinders.

was produced by an Acidobacteria strain (Fig 1.4). Originally, br-GDGTs were meant to be from soil origin (Hopmans et al., 2004; Sinninghe-Damsté et al., 2000; Weijers et al., 2006) but recently, they have also been found in peats (Huguet et al., 2010), marginal/deltaic environments (Tierney, 2013), shallow marine sediments (Weijers et al., 2007, Donders et al., 2009) and lakes (Sinninghe-Damsté et al., 2009; Tierney and Russell, 2009). Surprisingly, they are not found in pelagic marine environments (Hopmans et al., 2004).

There are nine types of br-GDGTs divided in three triplets depending on the number of methyl branches and the triplets are divided depending on the number of cyclopentane moieties (Weijers et al., 2007; Tierney and Russell, 2009) (Fig 1.4).

The Branched and Isoprenoid Tetraether index (BIT, 1) was originally created to distinguish between the in situ production in lakes and coastal environments and, the soil contribution (Hopmans et al., 2004). This was based in the belief that bacterial GDGTs were uniquely produced in soils (Hopmans et al., 2004; Weijers et al., 2007). Nevertheless, the BIT index has been more commonly used to calculate the proportion of archaeal versus bacterial production in a certain sites because br-GDGTs are not uniquely produced in soils (Tierney and Russell, 2009).

$$BIT = \frac{I+II+III}{I+II+III+IV} \quad (1)$$

There are two more indices that present the base of the MBT/CBT paleothermometers. Those indices are: Cyclization of Branched Tetraethers (CBT, 2) index and Methylation of Branched Tetraethers (MBT, 3).

$$CBT = -\log\left(\frac{Ib+IIb}{I+II}\right) \quad (2)$$

$$MBT = \frac{I+Ib+Ic}{(I+Ib+Ic)+(II+IIb+IIc)+(III+IIIb+IIIc)} \quad (3)$$

The CBT index is defined as the number of cyclopentane moieties contained in the brGDGT structure. High CBT values indicate a major number of rings and viceversa (Weijers et al., 2007). In the CBT ratio formula some brGDGTs are excluded (IIIb, IIc, IIIc, Ic and III). The CBT index and the pH seem to have a causal relation (Weijers et al., 2007). This is because the permeability of the cell membrane depends on the quantity of water molecules trapped in its structure since the water molecules can favor protons to move through them (Nagle and Morowitz, 1978). The addition of rings increases the permeability through the alkyl chain because it favors water molecules to get trapped. Modifications on permeability are made to maintain the pH in the inner cell. Therefore, a decrease on permeability is observed under low pH conditions. Despite that, the relation between pH and the degree of cyclization is lower than expected ($r=0.70$, $p<0.01$). This is because the cell membrane also pumps out H^+ to help maintain the pH gradient (Weijers et al., 2007).

The MBT index is defined as the degree of methylation at a position C-5 and C-5' of brGDGTs. The high MBT index values represent a low degree of methylation and vice versa (Weijers et al., 2007). The MBT index formula use the nine types of br-GDGTs. Weijers et al. (2007) found that GDGTs acquired between tropics and Equator

have a great number of GDGT-I triplet while samples in the Arctic were found to have a predominance of GDGT-II and GDGT-III. Apparently, bacteria biosynthesize GDGTs with more methyl groups at low temperatures. This is because the number of methyl branches results into a loose of packing that allows the membrane to remain in a liquid crystal state at low temperatures. Moreover, it seems that the energy producing methyl groups is more favorable for the cell metabolism than other remedies to fight the cold such as increase the length of the alkyl chain or make double bounds (Weijers et al., 2007). Same authors (Weijers et al., 2007) found a general relationship between MBT and Mean Air Temperature (MAT) ($r=0.47$, $p<0.01$). However, this relationship is not completely straightforward owing to other parameters that are probably affecting it. The most probable environmental variable affecting the MBT is the pH since, as mentioned before, the cell membrane also needs to adapt its permeability in front of pH changes (Weijers et al., 2007). Since the br-GDGTs producers are not known, the physiological relationship between br-GDGTs cyclization and methylation is not fully understood (Tierney, 2012).

Using the MBT-MAT relationship Weijers et al. (2007) proposed an air temperature calibration applied for soils based on the MBT/CBT indexes. This calibration was applied to lakes by different authors (Tierney and Russell, 2009; Zink et al., 2010; Tyler et al., 2010) that observed an underestimation of the air temperature by 10 °C. This underestimation revealed that GDGTs could probably be differenced in two populations: one from soils and the other from lakes (Tierney and Russell, 2009). The main differences on temperature estimation between these two GDGT communities were probably caused by i) the different mechanism used to adapt the membrane permeability and ii) the water availability that can alter membrane fluidity and permeability (Loomis et al., 2012). The observation of intact polar br-GDGTs in the lake water column confirmed the previous theory of the in situ lake production of GDGTs (Tierney et al., 2010). Tierney and Russell (2009) proposed a new MBT/CBT index based on East African lakes. Since then, other authors have tried to improve or make their own calibration. Pearson et al., (2011) formulated a new calibration containing lake top sediment cores from the Arctic to the Antarctica. Sun et al., (2011) compiled data from different parts of Asia at different altitudes. Loomis et

al. (2012) tried to improve Tierney's calibration by adding more east African lakes to the previous dataset. Pearson et al. (2011) observed that the relations found in the African East Lakes (Tierney et al., 2010) were robust and can be applied for a wide range of lakes and regions.

Despite of the great efforts on MBT/CBT paleothermometers construction, they seemed to be less accurated in reconstructing the temperature than the TEX₈₆ index. The relatively low accuracy of the MBT/CBT paleothermometer could be related to this ratio is highly affected by the pH (Tierney, 2012). For that reason, some authors have proposed alternative calibrations that better performs the temperature reconstruction (Loomis et al., 2012; Pearson et al., 2011; Tierney et al., 2010).

Previous studies have shown that the best correlated br-GDGT with the mean air temperature (MAT) was GDGT-III ($r=0.96$, $p < 0.01$; Tierney et al., 2010) and that the GDGTs with cyclopentane moities were affected by the pH. Therefore, those paleothermometers, called MbrGDGTs, were only based on GDGT-I, GDGT-II and GDGT-III (Tierney et al., 2010; Pearson et al., 2011; Loomis et al., 2012). Other versions of this calibration have been performed using the best subset regression, which included the GDGT-IIIb (Pearson et al., 2011) and the stepwise forward selection that included GDGT-IIc and GDGT-IIIb (Loomis et al., 2012). The last approximation has not been proved worldwide.

Compound specific δD composition: the use of δD composition from leaf waxes.

Most of the organic matter found on lacustrine and oceanic sedimentary records belongs to photosynthesizing organisms. Those organisms take up water from the environment as the principal source of hydrogen and the relative isotopic composition of this hydrogen depends on the isotopic composition of the precipitation and on the amount of evaporation that enrichs the δD , which in turn is related to the fluxes of water in the hydrological cycle (Craig, 1961; Dansgard, 1964; Gat, 1996). The hydrogen isotopic composition of precipitation can substantially vary in space and time and this variability can be explained by Rayleigh-type processes. This water becomes part of the

intracellular water and its hydrogen is used to create the photosynthesizing products that suffer a fractionation respect to the intracellular water (Sachse et al., 2012).

The terrestrial plants take up the water mainly from the soil moisture but also from groundwater, fog and/or dew (Dawson 1998). The water intake from the soil moisture does not typically show isotopic fractionation (Sachse et al., 2012). However, the isotopic composition of the leave water varies substantially from the source (Barbour et al., 2004; Farquar et al., 2007). One of the most important factors affecting the leaf water isotopes is the transpiration, which is influenced by humidity, temperature and the vapor surrounding the leaf (Sachse et al., 2012). Moreover, it has been observed that the isotopic composition of the photosynthesizing organisms products differ from the leaf water isotopy despite that, the leaf water is the source of hydrogen for these products. These variations observed large isotopic fractionation with values between -400 ‰ and +200 ‰ (Sachse et al., 2012).

The isotopic differences between intracellular water (aquatic organisms) or leaf water (terrestrial organisms) and photosynthesizing products can be explained by: a) isotopic fractionation derived from the biosynthetic pathways, b) hydrogen exchange reactions (hydrogenation and dehydrogenation), c) influence of extrinsic secondary fractionations and, d) influence on secondary Hydrogen exchange reactions.

Biosynthetic pathways. The precursor of all the biosynthetic pathways is the Calvin cycle or secondary carbohydrate metabolism. Hereafter, the main lipid biosynthetic pathways are: i) the acetogenic pathway for n-alkyl lipid, ii) the mevalonic acid (MAV) pathway for steroid, terpenoid, and hopanoids and iii) the 1-deoxy-D-xylulose-5-phosphate (DOXP)/2-methyl-erythroyl-4-phosphate (MEP) for isoprenoid lipids such as phytol and hopanoids. The acetogenic and DOXP/MEP pathways are produced in the cell plastids of photosynthesis organisms and the MAV pathway is produced on the heterotrophic bacteria cytosol. The smallest depletion is observed for n-alkyl lipids and the highest for phytol and related compounds (Sachse et al., 2012).

Hydrogen exchange reaction. The secondary hydrogen exchange reactions such as the hydrogenation and dehydrogenations also produce changes on the isotopic composition. Those changes are produced while the large enzymatic processes

produced both hydrogenation (saturation) and Dehydrogenation (desaturation). The decarboxylation of n-alkanoic acids to derive in n-alkanes produces a depletion of $25\text{‰} \pm 16\text{‰}$ (Chikaraishi and Naraoka, 2007).

Extrinsic secondary fractionations. These fractionations are caused by environmental factors such as salinity, temperature, growth rate and sunlight that can affect the hydrogen-isotopic composition of lipids (Sachse et al., 2012). The life form (shrubs, trees, forbs and graminoids) can also affect the δD composition but, those changes are usually linked to different habitats. All of these factors are poorly understood nowadays (Sachse et al., 2012). The interspecific variability is usually linked to photosynthetic pathway or life-form but, sometimes it can be linked to differences on sampling protocol (i.e. shadow or sun leaves) and/or the timing of leaves-wax synthesis (Sachse et al., 2012). The leave-wax synthesis time depend on the different leaf-wax generation or the growing season. This variability has only be found on greenhouse experiments (Kahmen et al., 2011) because, field-grown leaves continuously produces wax due to the abrasion derived from rain and/or wind (Sachse et al., 2010). The δD values are also influenced by the soil-water evaporation and leaf-water transpiration. The soil-water evaporation and the leaf-water evaporation are poorly understood, however, it is observed that in dry sites the δD on the leaf wax is enriched respect to the wet sites. This enrichment variates among species depending on the rooting depth (Sachse et al., 2012).

Secondary hydrogen exchange reactions. The hydrogen added to the carbon skeletons that comes from the reduced Nicotinamida-Adenina-Dinucleótido-Fosfato NADPH is strongly depleted and the degree of this depletion depends on the metabolic pathway and the organism type (Sachse et al., 2012). For example, the heterotrophic bacteria produces higher depletion on the NADPH produced by photosynthesis than the produced whilst sugar metabolism that includes the oxidative pentose phosphate pathway (PPP). In the other hand, photosynthesizing organisms use the photosynthesis as the main source of NADPH. Therefore, the relationships between the water source and the lipid δD are higher in photosynthesizing organisms than for heterotrophic bacteria because of its metabolic pathway preference (Sachse et al., 2012). The isotopically differences (around $\approx -200\text{‰}$) for photosynthesizing organisms are derived

from the photosynthetic pathway (C_3 , C_4 and CAM). For hydrological reconstructions the offset amongst photosynthetic pathways can be corrected by the carbon isotope (Collins et al., 2013) or pollen data (Pollissar and Freeman, 2010).

The aforementioned discussion on the δD fractionation are based on single samples but, studies on sediments showed a spatial and temporal integration that exhibit strongly reduced variability compared to data sets from individual organisms (Sachse et al., 2012). For that reason, the study of δD values on lake surface sediments along climatic gradients has showed strong correlation with lake-water δD and lipid δD values for aquatic and terrestrial photosynthesizing organisms, respectively (Garcin et al., 2012; Hou et al., 2008; Huang et al., 2004; Polissar and Freeman, 2010; Sachse et al., 2004).

Therefore, stable isotope ratios of hydrogen (and also oxygen) in water have been considered powerful tools in paleoclimatology because the isotope composition of the organic matter preserved in lakes contains the isotopic signature of the water from which it was formed (Leng et al., 2006). The isotopic fractionation due to climatic factors can occur in many ways and those are of great attractiveness because of their links to climatic parameters (Araguas-Araguas et al., 2000).

Dansgaard et al., (1964) stated some relationships between the observed isotopic composition of precipitation and environmental parameters. These relationships, usually called effects, have been confirmed by other authors (Yurtsever and Gat, 1981; Gonfiantini, 1985; Rozanski et al., 1993; Araguas-Araguas et al., 2000). The isotopic precipitation values on tropical coastal areas represent the first step condensation of the marine moisture. Travelling towards higher latitudes, the water isotopes suffer depletion because of the progressive removal of the isotopically heavy moist air transported from the equator towards to poles (Araguas-Araguas et al., 2000). The increase on elevation (and the consequent decrease on temperature) leads to a depletion of the isotopic signature in mountainous regions. This process is widely known as the altitude effect. The regions with minimal seasonal or altitudinal variations, the isotopic composition of water are related to the amount of rainfall. This procedure is called the amount effect (Dansgaard et al., 1964; Araguas-Araguas et al.,

2000). At mid latitudes there is a progressive isotopic depletion with the distance from the coast. For example, in Europe this depletion is of -1‰ per 1000 km (Rozanski et al., 1982; Araguas-Araguas, 2000). Seasonal variability on the isotopic composition can be found due to changes on temperature, on evapotranspiration flux and/or changes on the moisture origin. The vapor generated under low relative humidity contains high isotopic values. An example of this isotopic signal enhancement is the Mediterranean Sea (Araguas-Araguas et al., 2000).

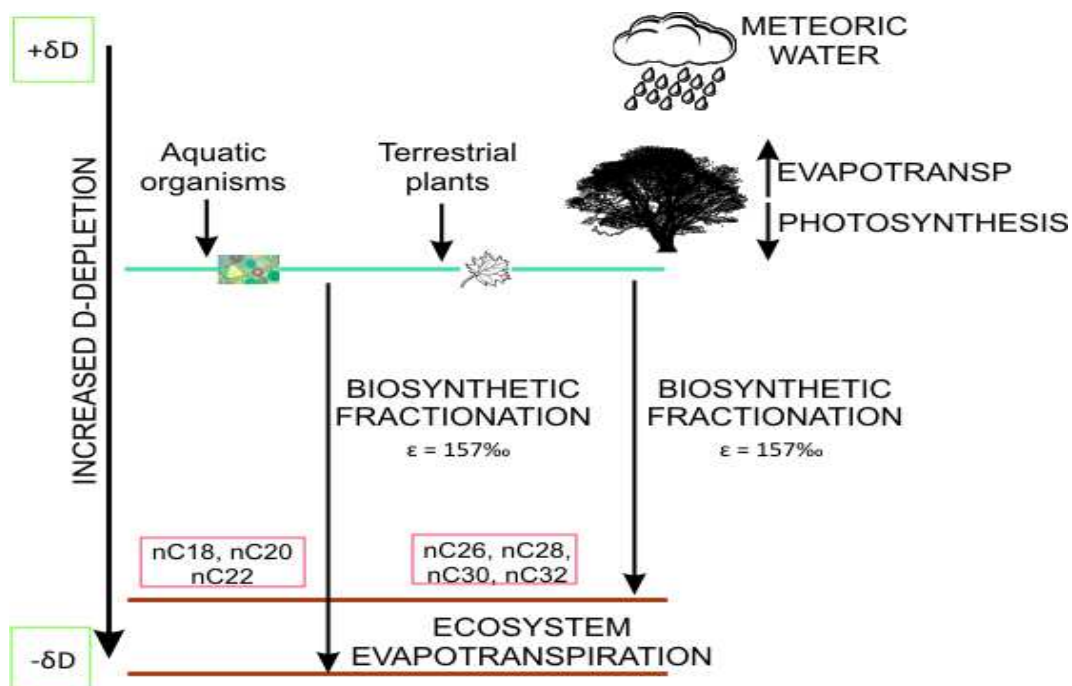


Figure 1.7: Diagram showing the main isotopic fractionation processes from the water acquisition by the aquatic and/or terrestrial organism, the incorporation to the tissues, the entrance to the lake and the sedimentation. In pink squares the most common carbon chain lengths for aquatic organisms (box on the left) and terrestrial organisms (box on the right).

The use of lipid δD in paleohydrology assumes that the intracellular water used on biosynthetic reactions has similar or prone to correct isotopic fractionation and that the isotopic composition reflects the isotopic signature of the surrounding water plus a known offset (Kreuzer-Martin et al., 2006). The use of the isotopic composition of cuticular wax of higher terrestrial plants that contains n-alkanes, n-alcohols, n-alkanoic acids and triterpenoids is a new technique based on the same premise (Fig 1.7).

1.3 NORTH ATLANTIC CLIMATE

Climate in the North Atlantic is triggered by the conjunction of few atmospheric patterns and oceanic currents. The most prominent and recurrent pattern of atmospheric circulation in this area is the North Atlantic Oscillation (NAO). The NAO was firstly described by the Scandinavian sailors that found an opposite phase between Scandinavia and Greenland temperatures (Wanner et al., 2001; Pinto et al., 2012). Therefore, the first published works about the NAO were based on this temperature seesaw (Egede, 1745 information; Crantz, 1765 information). The development of statistical correlation techniques and the availability of instrumental pressure data permitted to observe that the NAO covered a wider area than previously defined and was not only been defined by temperature. Nowadays, the NAO is defined as the redistribution of the atmospheric masses between the Arctic and subtropical latitudes forming two dipoles of action: one over Azores and the other over Iceland (Pinto et al., 2012). Depending on this redistribution, it can swing from positive to negative phase (Hurrell et al., 2003). The positive phase of NAO is characterized by an intensification of the Azores high with the consequent detriment of the Icelandic low while the negative phase of NAO is characterized by the reduction of the Azores high making shallower the Icelandic low (Pinto et al., 2012). Since the most part of the NAO reconstructions are based on temperature and precipitation fluctuations they are not actually reconstructing the NAO itself but the effects and impacts of the NAO on a given point.

The consequences of the NAO affect surface temperature, precipitation, ice formation, ocean currents and ecosystems ecology amongst other variables (Hurrell et al., 2003). During positive (negative) phase of NAO the North Atlantic Sea Surface Temperature (SST) colds down (warms up) in the Northwest Atlantic and off to the African coast due to upwelling (downwelling) phenomenon while it increases (decreases) in the central-southwestern region of the Atlantic Ocean (Hurrell et al., 2003; Pinto et al., 2012). This positive (negative) phase enhance (weaken) westerlies across the North Atlantic transporting warm and moist air toward north (south) of Europe affecting temperature and rainfall (Hurrell et al., 2003). The phase of NAO is also reflected in the ice phenology (freezing, thawing onset and ice cover duration) in lakes. In Northern Europe, the ice phenology depends exclusively on temperature (Yoo and D'Odorico,

2002). Visually, in the negative NAO phase the freezing onset will start earlier and the ice cover duration will last longer. On the contrary, the ice phenology on the south of Europe is affected by both, temperature and precipitation (Sánchez-López et al., 2015). Moreover, it has been observed that the extratropical cyclones path changes depends on the NAO phase. Kossin et al. (2010) observed that negative May-June NAO phase is related to a weakness over the western end of the subtropical high during most of the hurricane season. This weakness is used by tropical storms that take this path increasing the possibilities of landfall in North American Coast and Azores islands (Kossin et al., 2010).

Although the NAO is an internal atmospheric process, there are some evidences that external factors such as volcanic activity (Marshall et al., 2001; Fisher et al., 2007), and variations in the solar activity (Spang et al., 2010; Shindell et al., 2001) can affect the NAO. Moreover, recent works have highlighted that the NAO seems to be modulated by other atmospheric patterns that also determine climate in the North Atlantic. Those patterns are the East Atlantic, the Scandinavian, the Atlantic Meridional Mode and the British Isles blocking events (Comas-Bru and McDermott, 2014; Moore et al., 2013).

The Eastern Atlantic (EA) is defined by two centers of action based on pressure. The southern center of action is located in the north of Africa while the northern center of action is located between Newfoundland and England (Comas-Bru and McDermott, 2014). Among others, the EA is an atmospheric pattern closely linked to NAO because it has been proposed to modulate the strength and variability of the NAO dipole at several temporal scales (Bastos et al., 2016; Moore et al., 2013). The influence of the EA on the NAO seems not to be widely observed. For example, Hernández et al. (2016) did not found a significant relationship between the precipitation in Azores and the EA climate mode for the 1873-2012 AD periods.

The Scandinavian pattern (SCAND) is characterized by pressure centers of action of opposite sign over Western Europe and eastern Russia-western Mongolia (Bueh and Nakamura, 2007). This pattern increase temperature and precipitation in the Iberian Peninsula masking the effects of NAO at those latitudes (Hernández et al., 2015).

Another climatic mode affecting North Atlantic conditions is the Atlantic Meridional Oscillation (AMO). The AMO is defined as the time series of low-pass filtered average Sea Surface Temperature (SST) in the North Atlantic after remove the effect of the Global Warming (Marini and Frankignoul, 2014). This pattern is reflected in a long duration SST conditions that are associated to the Thermohaline Circulation (THC) and, in turn, to the Atlantic Meridional Overturning Circulation (AMOC). THC and AMOC are keys on the climate system because of the heat transport from the tropics towards the poles (Kushnir 1994). A positive (negative) phase of AMO warm up (colds down) tropical areas and display an anomalous cold (warm) SST off USA East Coast (Grossman and Klotzbach, 2009). AMO also affects temperature and precipitation in America, Europe and North Africa – Sahel region (Threnberth and Shea, 2006); and, it is the dominant precipitation pattern at some areas (Azores archipelago) during the negative NAO phase (Hernández et al., 2016). The intensity and frequency of tropical storms has been also related to AMO (Endfield et al., 2001; Sutton and Hodson, 2005). Mestas-Núñez et al. (1999) suggested that a link exists between the AMO in the north Atlantic and SST in the Pacific through fluctuations in the tropospheric polar vortex. The AMO shows dominant periodicities from 60 – 80 years (Schlesinger and Ramankutty, 1994) although those cycles might range from 30 up to 130 years according to some proxy records (Delworth and Mann, 2000; Gray et al., 2004) and climate models (Knight et al., 2005). These AMO cycles have been found to be similar to the NAO variance. For the instrumental period, the warm AMO phases were observed between 1860-1880 and 1940-1960 AD and the cold phases were observed between 1905-1925 and 1970-1990 AD (Endfield et al., 2001).

The Atlantic Warm Pool (AWP) is the region that encloses the Gulf of Mexico, the Caribbean area and the western tropical north Atlantic (Wang et al., 2007). This region is characterized by warm temperatures and is responsible of the amount of heat transported from the equatorial regions towards poles (Wang et al., 2007).

The Intertropical Convergence Zone (ITCZ) is the area in the tropics where the convergence between north and south hemispheres occurs. Shifts of the ITCZ towards North produce warmer conditions in the north Hemisphere and an increase on precipitation in the Caribbean. Shifts towards south increases precipitation in the

tropical area of the southern hemisphere and increase temperatures at those latitudes (Haug et al., 2001).

Oceanic circulation

The most important north Atlantic currents are the Gulf Stream (GS) and its continuation the North Atlantic Current (NAC). The GS is originated in the Florida Strait as a continuation of the Florida Current whilst the NAC is originated between the Great Banks and the Mid Atlantic Ridge as a continuation of the GS (Mann, 1972). GS and NAC transport heat from lower to upper latitudes but, those currents suffer bifurcations on their way towards north. The principal bifurcations of the GS are the the Canary Current (CC) and the Azores Current (AzC). The CC is part of the North Atlantic Gyre and flows along the African coast (Fedoseev, 1970) and the AzC is also part of the North Atlantic Gyre and is also originated near the Great Banks and the Mid Atlantic Ridge (Volkov and Fu, 2010). The AzC formation occurs because of the existence of the Gibraltar Strait that allows the Mediterranean Overflow Water (MOW) to cross through this strait but, the location of the GS bifurcation depends on the Gulf Stream North Wall (GSNW) (Volkov and Fu, 2010). The NAC main bifurcations are the Irminger Current (IC) and the Norwegian Current (NC). The IC is located on the western slope of the Reykjanes ridge and the NC is the NAC bifurcation towards the Norwegian coast (Saetre, 2007) (Fig 1.8).

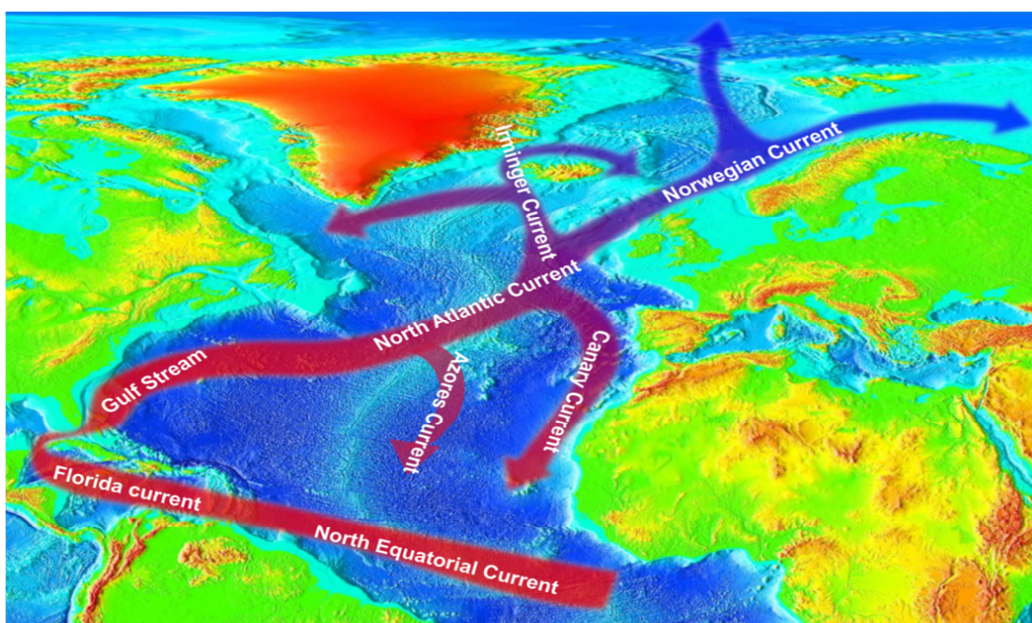


Figure 1.8: Main surface oceanic currents travelling from the equator towards northern latitudes. Red colors represent warm temperatures while blue colors represent cold temperatures.

In the North Atlantic, the position and strength of the currents depends on the Eddy Kinetic Energy (EKE) and the Gulf Stream North Wall (GSNW). Eddies are formed by two factors: the wind on the sea surface and the friction on the sea floor. For a certain site with a given depth, the EKE increases with the enhancement of wind and this factor is related to the current velocity (Barnes and Garfinkel, 2012). The increase in EKE is produced by an increase on the oceanic currents velocity but the EKE also helps to increase and maintain this velocity (Borkman and Smayda, 2009). The position of the GSNW determines the GS pathway and the bifurcation location of the other currents (Taylor and Stephens, 1998; Volkov and Fu, 2010). An increase on EKE means an enhancement of the current velocity. This enhancement drives towards northern latitudes de GSNW and this movement towards north produces the choose of a northern pathway for the GS (Taylor and Stephens, 1998; Hameed and Piontkovski, 2004; Curry and McCartney, 2001). This shift towards north produces a bifurcation at northern latitudes of the AzC, CC and NAC (Volkov and Fu, 2010). Therefore, depending on the strength and position the heat transport towards the north affect in a great or lesser extent the northern latitudes. This is because increased water current velocities might imply that larger volumes of warmer water might arrive to further northwards places in the ocean without completely losing their heat content (Bindoff et al., 2007).

A decrease on the Northern Hemisphere insolation is known to have been companied by southwards migration of the ITCZ. This affects the atmospheric circulation by moving southwards the Jet Stream and the Icelandic low (Knudsen et al., 2011). Those atmospheric variations produce a decrease on temperature in the northern hemisphere. This decrease on temperatures is reflected on the sea via both a decrease of the SST temperatures and an increase on the sea surface densities (Bindoff et al., 2007). Those variations produced a decrease on the strength towards north of the AMOC, which in turn reduces the heat transport towards northern latitudes that impede the ice cap melting (Knudsen et al., 2011). For instrumental data, an AMOC reducing is observed on the GS and NAC slowdown and the EKE decrease (Taylor and Stephens, 2002). In addition, the phase of NAO has also been related to the velocity and position of those currents. A positive NAO phase enhances westerlies towards northern latitudes. The increase on wind velocities affects the velocity of the sea

surface currents that maintain their strength by eddies formation (Borkman and Smayda, 2009). This increase on the EKE, usually around Bermuda, displaced towards northern latitudes the GSNW that allows a northern pathway of the GS (Taylor and Stephens, 1998; Hamned and Piontkovski, 2004; Curry and McCartney, 2001) and, consequently, a northern bifurcation of the NAC. Changes on the GS direction (Taylor and Stephens, 1998) and velocity (Olsen et al., 2012; Trouet et al., 2009) have provoked variations on temperature in the North Atlantic deep water production dynamics (Olsen et al., 2012), different precipitation patterns (Kushnir 1994), and even, ocean productivity changes (Borkman and Smayda, 2009). Therefore, the role of the oceanic currents on the North Atlantic climate should not be separated from the atmospheric pattern. An example of this is observed in the global warming scenarios that suggest an increase on the ocean currents in the north Atlantic helped by a positive NAO phase that would increase the deep water formation at Labrador Sea (Gillett et al., 2003).

1.4. LATE HOLOCENE VARIATIONS. LINKS BETWEEN OCEANIC AND ATMOSPHERIC CIRCULATION.

The last 1000 years of climate history can be roughly subdivided in three climatic periods: the Medieval Climate Anomaly (MCA), the Little Ice Age (LIA) and the recent Global Warming (GC). Teleconnections between the atmospheric patterns that trigger climatic conditions in the North Atlantic, their coupling with ocean water currents and the solar forcing have promoted the conditions to develop these climate periods.

The Medieval Climate Anomaly.

The MCA was a period of warmer temperatures over the north Atlantic that goes from 950 to 1250 AD (Stansell et al., 2013; Cronin et al., 2010) although the starting and ending dates could change depending on the author. This climatic period was characterized by a movement towards North of the ITCZ that produced wetter conditions on the Caribbean and North Africa and drier conditions in United States (Fig 1.9; Lund et al., 2006; Trouet et al., 2009). The wet conditions in the Caribbean increased the input of fresh water to the sea making the Florida Current warmer and fresher during this period (Lund and Curry, 2004). The Atlantic Warm pool (AWP) became bigger under this conditions (Lund et al., 2006) transporting easily heat towards northern latitudes via the NAC (Gray et al., 2004; Lund et al., 2006; Moffa-Sánchez et al., 2014). The NAC, in turn, increased its velocity helped by an increment of westerlies (Moffa-Sánchez et al., 2014). Other branches of NAC such as the IC, the AzC and the CC also increased their velocity (Lund et al., 2006; Moffa-Sánchez et al., 2012). The heat transport towards north enhanced the thawing of ice caps and this melting produced the cooling of the Labrador Sea (Olsen et al., 2012). The Labrador Sea cooling increased the depth water formation rate that accelerated the Thermohaline Circulation, which in turn modified the AMOC (Wannamaker et al., 2012; Nieto-Moreno et al., 2014). The velocity on currents and thermohaline circulation was enhanced by the predominant positive phase of the NAO that also drove northwards the NAC because of the increment of the potential vorticity on Bermudas (Borkman and Smayda, 2009). This driving affected the divergence point of the branched currents AzC and IC because the increase of westerlies move those branches towards north

Atlantic east coasts and the exact point of divergence move towards north due to the northern position of the GS (Volkov and Fu, 2010). This positive phase of NAO also produced wetter and mild conditions on Northern Europe and opposite conditions on Iberian Peninsula and Mediterranean (Trouet et al., 2009; Nieto-Moreno, 2014). Vaquero and Trigo (2012) stated that the solar activity during the MCA was not anomalously high. Therefore, they attributed the warmth of the MCA to the lack of volcanic activity and enhanced AMOC that, in turn, generated a cross equatorial salinity that pushed the ITCZ northwards (Trouet et al., 2009; Moffa-Sánchez et al., 2012).

The Little Ice Age.

The LIA was the period enclosed between 1450 and 1850 AD but, those dates slightly vary between authors (Stansell et al., 2012; Cronin et al., 2010) (Fig 1.10). This period is generally considered cold owing to the temperature decline of about 1.5-2 °C (Nieto-Moreno et al., 2014). During the LIA, the ITCZ described a southwards movement (Trouet et al., 2009; Moffa-Sánchez et al., 2012) that produced drier and cooler conditions in the Caribbean Sea reducing the AWP area (Lund et al., 2006; Richey et al., 2009). The reduction of the NAC was accompanied by the slowdown of the NAC branches. An established negative phase of NAO produced a movement southeast of the NAC that affected the relative branches (Wannamaker et al., 2012). The hydrological conditions in Europe reversed producing cold weather in North Europe and humid conditions in South Europe (Trouet et al., 2009; Nieto-Moreno et al., 2014). Those conditions were exacerbated by the persistent blocking formation over the British islands (Shabbar et al., 2001).

The Global Warming

The AMOC weakness for the last 20 years was unprecedented showing the strongest weakening at 1970 AD (Rahmstorf et al., 2015). Solanski et al. (2000) pointed out that solar variability is unlikely to have been the dominant cause of the strong warming during the past three decades. The Global Warming scenarios suggest a persistence of the positive NAO phase (Gillett et al., 2003). This positive NAO will lead towards north the NAC and increase its velocity affecting the associated branches velocity and divergence position (Wannamaker et al., 2012). The heat transport towards north will

produce melting of the ice caps with the consequent cooling of Labrador Sea (Olsen et al., 2012). This cooling will produce in some models a final reduction of the Thermohaline Circulation (THC) but, it would depend on the degree of cooling (Delworth and Dixon, 2000; Hurrell et al., 2003).

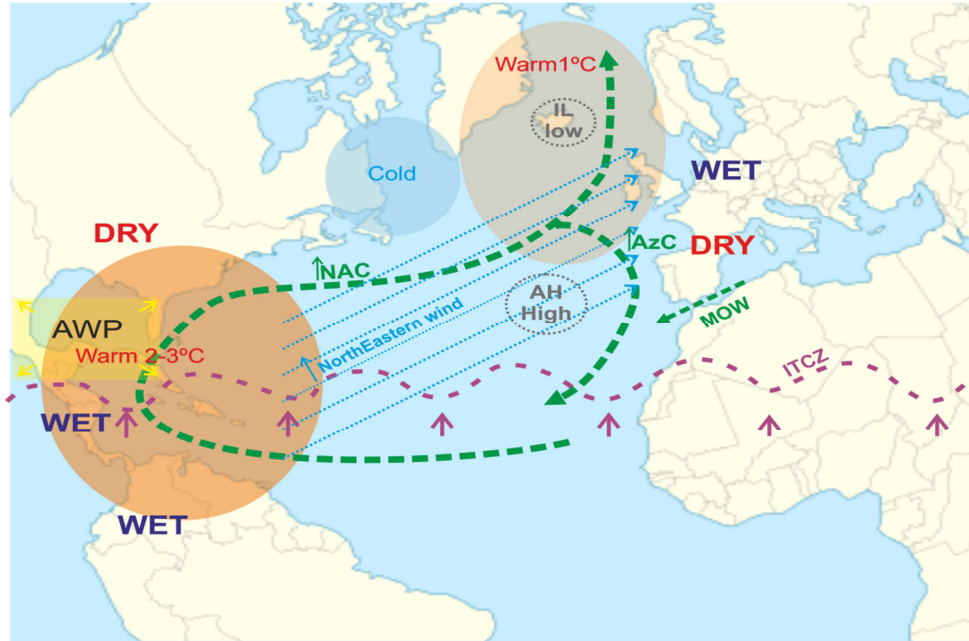


Figure 1.9: Map showing atmospheric and oceanic conditions during Medieval Climate Anomaly (MCA). Orange circles define areas of warm temperatures; blue circles are sites of cold temperatures. North Eastern winds are represented by blue arrows. The intertropical convergence zone is plotted as a purple dashed line. The main oceanic currents are plotted as green dashed lines. And, the Atlantic Warm Pool is defined by a yellow area. Note that the oceanic currents are enhanced and the NAO is mainly positive.

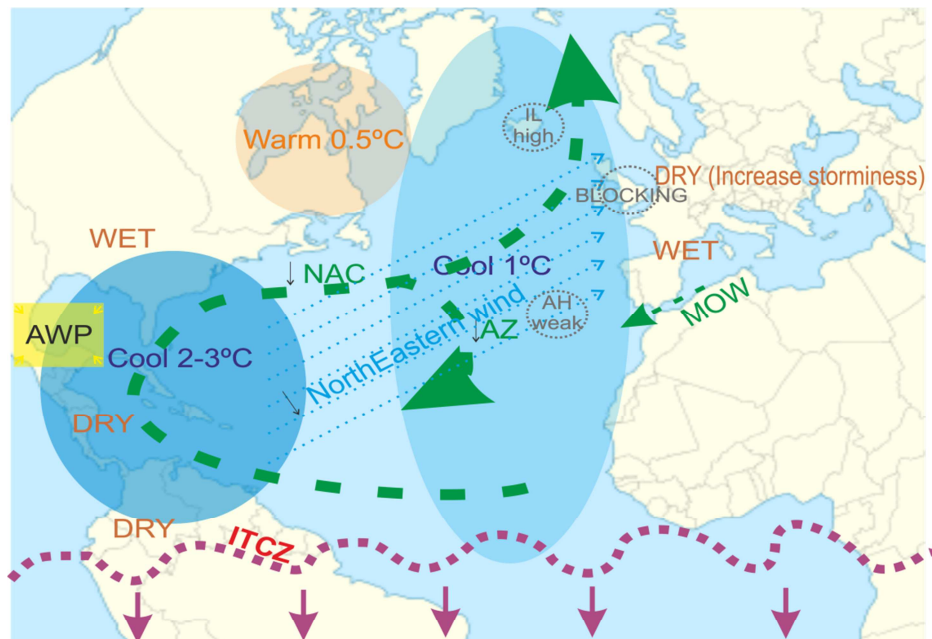


Figure 1.10: Map showing atmospheric and oceanic conditions during Little Ice Age (LIA). Orange circles define areas of warm temperatures; blue circles are sites of cold temperatures. North Eastern winds are represented by blue arrows. The intertropical convergence zone is plotted as a purple dashed line. The main oceanic currents are plotted as green dashed lines. And, the Atlantic Warm Pool is defined by a yellow area. Compare with scenario during MCA (fig. 1.9) note that the oceanic currents are slow and that the NAO is mainly negative.

1.5. AIMS

The aims of the present PhD Thesis is to characterize the Late Holocene climate variability in the southern center of action of the North Atlantic Oscillation (NAO) climate mode. In order to fully achieve this objective the following steps have been followed: 1) to characterize the Azul lake and its catchment area to understand the main sedimentary processes affecting the sedimentary record and its composition, 2) to setup an enhanced chronological model to assess both the long-term and the abrupt nature of the sedimentary record, 3) to test the relatively new biomarker based on Glycerol Dyalkyl Glycerol Tetraethers (GDGTs) to quantitatively reconstruct the Late Holocene temperature evolution, 4) to assess the climatic factors triggering the δD leaf waxes fractionation and use this signal as a precipitation proxy for paleoclimatic purposes, and 5) to characterize the climate variability of the North Atlantic for the last 730 years in terms of precipitation and temperature with special emphasis in the North Atlantic Oscillation (NAO) and Atlantic Multidecadal Oscillation (AMO).

To fulfill these purposes a coring and seismic campaign was realized in Azul lake (Sao Miguel island, Azores archipelago). The multiproxy study of the selected sediment core employed facies analysis, X-Ray Fluorescence (XRF), X-Ray Diffraction (XRD), Total Organic Carbon (TOC), Total Nitrogen (TN) and their stable isotopes ($\delta^{13}C$ and $\delta^{15}N$), alkenones (GDGTs) and hydrogen isotopes (δD) from leaf waxes. The quantitative temperature reconstruction was performed using the GDGTs while the past precipitation fluctuations were determined employing the δD leaf waxes. Both the temperature and precipitation reconstructions were validated using instrumental meteorological records from the island. The dating methods used for the present work were ^{210}Pb and AMS ^{14}C and the chronological model of the studied records were built using a new methodology that permit to accurately assess both the long- and short-term sedimentary rate fluctuations. The assessment of the climate factor triggering precipitation fractionation has been performed by the weekly collection of the rain water at the University of Azores. Furthermore, data acquired by other authors such as pollen, diatoms and chironomids were added to the previous dataset in order to

provide a wider understanding of the Late Holocene climate and environmental evolution of this sedimentary archive.

Antes morrer libres que em paz sujeitos.

(Brasão de armas dos Açores)

2. STUDY SITE

2.1 AZORES ARCHIPELAGO

2.1.1 Location

Azores archipelago (AA) is located in the middle of the North Atlantic Ocean between $36.92^{\circ} - 39.75^{\circ} \text{ N}$ and $25.00^{\circ} - 31.25^{\circ} \text{ W}$ (Fig. 2.1). This archipelago is located approximately 1500 km East from the European continent (Andrade et al., 2008) and it is composed of 9 islands and few islets, distributed along an E – W transect 620 km long. Due to the large distance between islands, the archipelago is divided in three island groups: the Eastern (made up of São Miguel and Santa Maria islands), the Central (Terceira, Graciosa, São Jorge, Pico and Faial) and the Western (Flores and Corvo). In 2000 AD, the total population of the archipelago was around 246000 inhabitants, mainly settled in the São Miguel island coast line and more specifically in Ponta Delgada (Constancia et al., 2000).

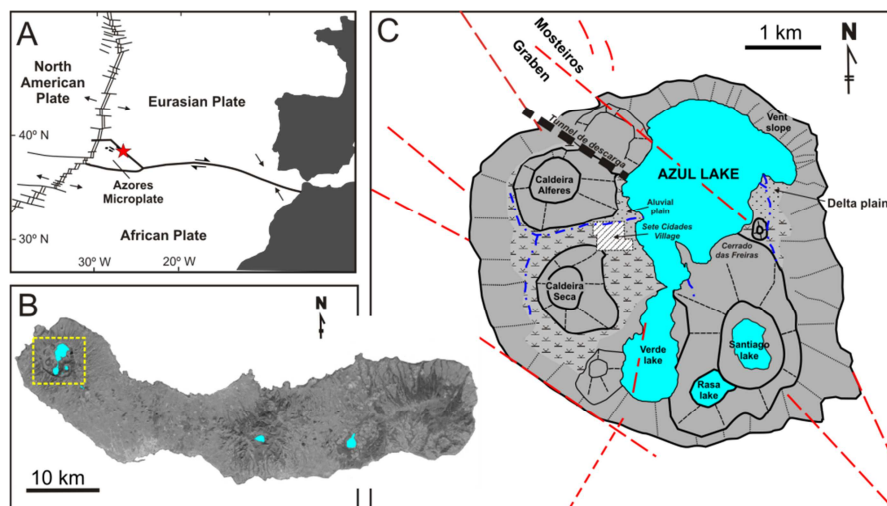


Figure 2.1: A. Map of tectonic plates in the north Atlantic showing the location of the Azores Archipelago between Eurasian Plate and Azores Microplate. B. Satellite image of São Miguel Island and the location of largest lakes in the island. Yellow square indicates Sete Cidades Caldera lake district. C. Volcanic complex of Sete Cidades Caldera composed by nine craters four of them occupied by lakes. The red lines that usually follows a NW-SE orientation corresponds to the Mosteiros Graben faults (Queiroz, 1997). Main alluvial and delta zones around the lakes are distinguished.

The name of the archipelago has been related to the presence of goshawks (*Accipiter gentilis sp*, Azor in portugues) but, recent studies have proved that the goshawks never existed in those islands (Kenward R., 2010). In any case, this prey bird is present in the AA flag. Other popular belief is that the name represents the blue color (Azul in Portugues) of the vegetation when the first settlers arrived due to the presence of the lichen *Roncella Tinctoria* that produces this dye (Kenward R., 2010).

2.1.2 Climate in Azores.

The climate in Azores is oceanic temperate. This climate is characterized by mild temperatures all year long and rather wet climate. The amount of rain is mainly controlled by the dynamics of the Anticyclone over the AA and the distribution is controlled by topography. It implies that coastal areas are drier than high ground (Santos et al., 2004).

Both precipitation and temperature in AA are ruled by few climate modes, being the North Atlantic Oscillation (NAO) the most important one since the southern center of action of this dipole is located over the islands. The low precipitation values in late spring and summer are (from June to September) favored by the dominance of the Azores anticyclone over the islands. The dissipation or displacement of this high pressure cell in autumn and winter (from October to May) allows the Atlantic storm tracks to cross over the Azores area, ruling almost 50% of the winter precipitation variability in the AA (Trigo et al., 2004; Hernández et al., 2015). The intensity and duration of these precipitation events could be more accentuated at a particular group of islands, depending on the position of the atmospheric depression, mainly during the negative NAO phase (Andrade et al., 2008). The persistence of the negative phase of this climate mode allows other climatic patterns, such as the Atlantic Meridional Oscillation (AMO), the Pacific Decadal Oscillation (PDO), and/or El Niño Southern Oscillation (ENSO), play a more relevant role intensifying them (Hernández et al., 2015). Moreover, this region is characterized by the confluence of warm air masses

from the tropics and cold masses from the North Pole generating fronts (Constancia et al., 2000). These fronts result in a storm formation that changes drastically temperature and wind intensity (Andrade et al., 2008). Another factor triggering precipitation in the AA is the abrupt topography of the islands which is mainly responsible of usually intense and short sea breeze rainfall episodes. The topography is important in the cloud formation and vegetation which is decisive in atmospheric humidity acquisition (Constancia et al., 2000). Owing to the abrupt topography of the islands, the relative humidity in the archipelago is around 77% at sea level, increasing with the altitude up to 87.5 % above 300 m a.s.l. (Constancia et al., 2000).

The AA is sometimes hit by hurricanes usually degraded to tropical storms typically from April to December (Andrade et al., 2008; Hernández et al., 2015). Elsner (2003) studied the variability of the North Atlantic Hurricanes and found that ENSO controlled factors related to the hurricanes development while NAO controls the track. Based on that, Kossin et al. (2010) observed that a negative May-June NAO phase favored the hurricanes formation at north-eastern latitudes (mainly around Florida coast). These hurricanes have northwards, through the US east coast, trajectory preference and make landfall in the eastern coast of North America, Bermuda and Azores. The track selected by these hurricanes was because the persistence of the negative phase of NAO during May - June period that creates a weakness in the western end (eastern coast of USA) of the subtropical high that remains until September. The tropical storms tracks tend to move through the weakness in the western end. Those storms are characterized as infrequent, short and intense (Kossin et al., 2010).

2.1.3 Oceanic circulation

As previously explained in the section 1.2, the AA climate is also linked to the oceanic currents, especially Gulf Stream (GS) (Constância et al., 2000; Volkov and Fu, 2010). The GS position and strength is dependent of large-scale climatic patterns such as the NAO. This is because the positive (negative) phase of NAO increases (decreases) the velocity of the oceanic currents, which produces an enhancement (detriment) of the

Eddy Kinetic Energy (EKE) that move towards northern (middle) latitudes the Gulf Stream North Wall (GSNW). The relative position of the GSNW allows the GS to move directly towards high (middle) latitudes (Allen et al., 2006; Taylor and Stephens, 2002; Borkman and Smayda, 2009). See introduction to obtain further information about this mechanism.

2.1.4 Geological setting.

The Azores islands are settled in the Mid-Atlantic Ridge (Fig. 2.1 A), rising from a 2000 m depth plateau called the Azores microplate. The Azores plateau is a triangular-shaped zone of anomalous an irregular shallow topography (Cruz et al., 2003). Its formation started around 36 Ma years ago (Campan et al., 1995) and extends west of the Mid-Atlantic Ridge (MAR) that separates American from Eurasian and African plates. This plateau is limited to the east by the East Azores fracture Zone (EAFZ), to the south by the Gloria Fault (Jimenez-Munt et al., 2000) and, to the north-east by the Terceira rift (Machado, 1959). The central (Terceira, Graciosa, São Jorge, Pico and Faial) and eastern (São Miguel and Santa Maria islands) island groups are straddle on the Azores plateau following an irregular WNW-ESE trend (Argus et al., 1989; Quartau et al., 2010) and the western (Flores and Corvo) islands group is located above the American plate. The volcanic Azores plateau was formed during an anomalous high melt production due to a change in the temperature, composition or dynamics of the mantle supplied to the Mid-Atlantic Ridge by the Azores hotspot (Cannat et al., 1999).

The islands were formed by volcanic activity around the triple junction of the American, Eurasian and African lithospheric plates (Quartau et al., 2010) that started during the Miocene (Nunes, 1999). The Azores island formation occurred from East to West along 8 million years (Constancia et al., 2000). The sequence of the island formation has been: Santa Maria (8.12 Ma), São Miguel (4.1 Ma), Terceira (3.52 Ma), Graciosa (2.5 Ma), Flores (2.16 Ma), Faial (0.7 Ma), São Jorge (0.55 Ma), Corvo (0.7 Ma) and the youngest, Pico (0.27 Ma) (Borges and Brown, 1999; Nunes, 1999). Eruptions in

AA varied from effusive, related to basaltic lava flows to explosives, connected to pumice deposits and pyroclastic flows (Cruz et al., 2010).

2.1.5 Geological hazards.

A large array of geological hazards might affect the AA. These range from earthquakes, volcanic eruptions and tsunamis. The tectonic position of Azores archipelago, close to an extensive plate tectonics border, enhances the possibilities of seismic crises. In the latest 570 years, 1200 seismic events have occurred. Their intensity has ranged from 1.5 to 10 in the Mercalli scale (Nunes, 1999). The most recurrent damages are ground mass movements, engineering structures collapse or residential buildings structure (Malheiro, 2006). One of the most important earthquakes documented in the archipelago were on São Jorge in 1757 AD with 1053 deaths, on Terceira in 1980 AD with 69 deaths and on Faial in 1998 AD with 10 deaths. In spite of their volcanic origin the AA islands have not suffered major historical volcanic eruptions. The most volcanically active area for the last 5000 years is Sete Cidades (San Miguel Island). Despite that, the last two centuries only recorded underwater eruptions with no significant damages (Malheiro, 2006).

Azores islands have high tsunamigenic potential due to their location and the highly potential earthquakes area beneath. Andrade et al (2006) suggested that submarine earthquakes were the main cause of tsunamis in Azorean coasts. Since the littoral fringe accounts with most of the economy and population, risk of tsunamis cannot be underestimated. These authors have indicated that since the archipelago was occupied in the 15th century at least 23 tsunamis have struck these islands. The worst tsunami occurred in November of 1755 AD at Terceira island which provoked heavy damaging in the coastal infrastructure (Andrade et al., 2006).

Landslides can be created by earthquakes, volcanic activity and intense precipitation. Earthquakes and the volcanic activity can generate landslides in a presence of high slopes, in areas of thick soil layers and/or superficial instability of the soil (Malheiro,

2006). In Azores, the extreme precipitation events that exceed 200 l/m^2 are expected to form landslides in areas devoid of vegetation and/or ground instability. Moreover, this author stated that rainfalls characterized by squalls or winds can produce landslides in areas with superficial roots trees such as *Cryptomeria Japonica*. In these conditions, those trees can be uprooted producing large failures of sediment. This ground movements are more often in volcano flanks, interior walls of caldera, rivers or coastal talus (Malheiro A., 2006).

2.1.6 Azorean Flora.

Azores archipelago belongs to the biogeographical region Macaronesia (Connor et al., 2012). The botanist Philip Baker attributed this name to Madeira, Selvagen and Canary islands; later, Engler (1879) added Azores to the list. The main botanical characteristic of the Macaronesian region is the Laurel Forest. The number of species endemism in Azores is relatively poor compared to the other Macronesian islands. The main endemisms of the island are *Azorina vidalli*, *Daboecia azorica*, *Erica azorica*, *Euphorbia azorica*, *Festuca petraea*, *Frangula azorica*, *Ilex azorica*, *Juniperus brevifolia*, *Lactuca watsoniana*, *Laurus azorica*, *Picconia azorica*, *Prunus azorica*, *Sanicula azorica*, *Vaccinium cylindraceum*, *Viburnum treleasei* (Lara, 2014). Nowadays, much of these species are extinguished or reduced to small bastions at the Eastern side of the island (Fig. 2.2).



Figure 2.2: Picture of Laurisilva forest located in NE of the São Miguel Island. Image is captured with a Sony Cibershoot 10.1 megapixels camera on September 2011 by M. J. Rubio-Inglés. The Laurisilva forest in Azores is dominated by *Laurus Azorica*, *Picconia azorica*, *Myrica Faya* and *Juniperus brevifolia* amongst others (see text for more information).

2.1.7 Lake water chemical characteristics.

The AA has 88 lakes that occupy the 0.4 % of the archipelago area (Porteiro, 2000). The total water volume is $9 \times 10^7 \text{ m}^3$ and, uniquely, the lakes of São Miguel contain the 93 % of this water. The 66.7 % of the Azorean Lakes are located inside volcanic craters and subsidence calderas while others are located in topographic depressions not associated with volcanic centers (Cruz et al., 2006). The mean altitude of the AA lakes is 613 m and the mean surface area is 0.02 km^2 showing a clear preference of small lakes. The mean depth of AA lakes is relatively shallow (8.7 m). The chemical composition of the lakes water reveal that the most concentrated cation in Azorean lakes is the Na^{2+} and the most concentrated ion is the Cl^- owing to the sea proximity. The mean pH value of the AA lakes is 6.83 and usually the highest pH values are found in lakes where large eutrophication processes are currently taken place (Cruz et al., 2006). The AA lakes mean surface water temperature is $18.3 \text{ }^\circ\text{C}$ but it oscillates between 11.9 and $24.6 \text{ }^\circ\text{C}$ while the electrical conductivity ranges from 26 to $623 \text{ }\mu\text{S/cm}$ (Cruz et al., 2006). The AA lakes are very poor in species (Green, 1992). The nutrients input due to human activities in the last decades have altered the nutrient cycles, promoting the cyanobacterial blooms at some lakes (Buchaca et al., 2011). The AA lakes have been mainly used for recreational purposes but, some of them have been used as sources of potable water (Cruz et al., 2006). Lake Azul is one of the biggest lakes in AA, with relatively low eutrophication and inexistent volcanic activity. Therefore, it is a great point to retrieve cores for climate reconstructions.

2.1.8 Human arrival to the Azores Archipelago. Plant and fish introductions.

The islands were officially discovered by Diogo Silves in 1427 AD but, the first documented existence is dated back to around 1330 AD in an anonymous map (Fig. 2.3). The exact date of settlement is not known (Constância et al., 2000) but, in 1439 AD Alfonso V appeal to the importance to settle this archipelago to take advantage of their productive soils and use its natural sources. Then, even more important than sovereignty was the crop of the productive island soil to supply the mainland deficiency (Moreira J.M., 1987).



Figure 2.3: Map dated around 1330 AD showing an small archipelago in the middle of the North Atlantic that could correspond with the Azorean Archipelago. The map was created by Angelino Dulcert and acquired from Moreira J.M., (1987).

The natural sources and productivity of the archipelago were described by Gaspar Frutuoso (1589) in his book entitled "Saudades da Terra". He commented that the Azores islands were impregnable due to the vegetation. The main species were typical of the Macaronesia forest such as *Laurus Azorica*, *Prunus Lusitanica spp Azorica*, *Frangula Azorica*, *Moreia faya*, *Picconia azorica* and *Taxus Baccata*. Rapidly, these ecologic features were adapted to first settler requirements. The greatest landscape modifications arrived with the orange plantation around 1524 AD (Fig. 2.4). The orange industry motivates the woody boxes manufacture in order to export the orange production. For that purpose the local vegetation was replaced by species like *Pinus*, *Cryptomeria japonica*, *Eucalyptus spp.* and *Acacia melanoxylan*. Futhermore, *Pittosporum undulatum* was used to enclose the area employed to this crop. This industry collapsed after the emergence of the *Oomycetes Phytophthora* in 1830 AD but, possible alternatives such as the potato, tea, pineapples and/or tobacco were rapidly introduces (Moreira, 1987). Ornamental plants for garnering or study their adaptation to new climates were largely introduced in the islands during the 19th century (Moreira et al., 1987).

Moreover, the large and spread damage due to the earthquake of 1563 AD highlighted the need of better communications net and, consequently, more accessible roads and

streets were constructed before the second half of the 19th century (Moreira et al., 1987). By that time, the Laurisilva regeneration was fairly impossible because the island landscape was totally modified. At present, environmental-friendly policies are taking place in order to preserve the autochthonous flora.



Figure 2.4: Orange plantation of XIX century in São Miguel Island. This photo was taken during an expeditionary voyage of the H.M.S. Challenger (1872-1876), sponsored by the British Government for scientific purposes. Natural History Museum.

The fishes were introduced in a number of lakes of the archipelago at the same time. The most introduced species were Goldfish (*Caraussius auratus*, Valois e Silva, 1886), frog (*Pelophylax Perezzi*, Drouet 1861), Carps (several species, Vicente, 1956) and Pikes (*Exos Lucius*, Flor de Lima, 1993). These introductions disrupt the trophic status of the lakes breaking the food chain (Buchaca et al., 2011; Raposeiro et al in prep).

2.2 SÃO MIGUEL ISLAND

2.2.1 Climate

Mean monthly air temperature in São Miguel island does not have high amplitudes between seasons (Fig. 2.5). For the period between 1872 and 2011 AD, the warmest temperatures usually occur in August (mean values around $\approx 19^\circ\text{C}$); whereas, the coolest ones are commonly found in February ($\approx 16.5^\circ\text{C}$). The mean annual air temperature for the same period is around 17.5°C with a standard deviation of 3.2°C . The temperature has a decreasing gradient with altitude of $0.6^\circ\text{C}/100\text{m}$ (Santos et al., 2004; Constancia et al., 2000).

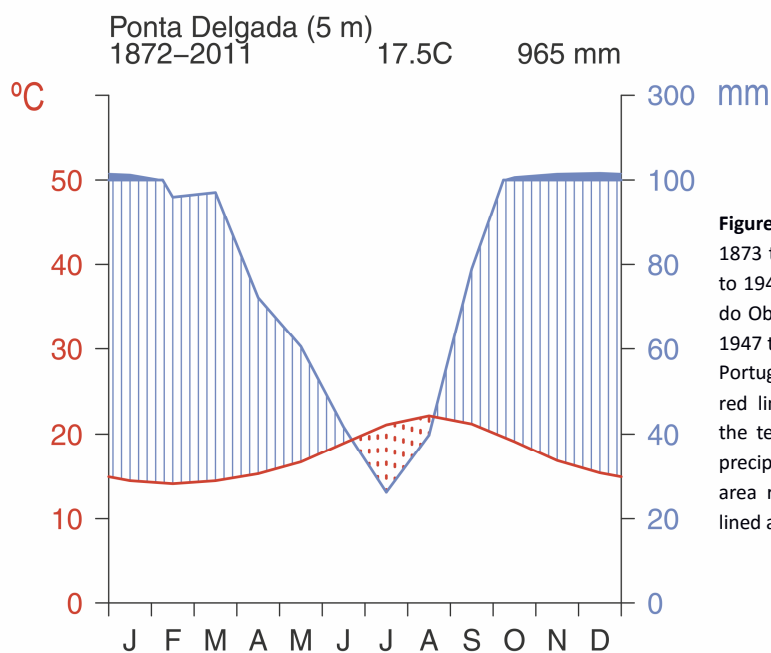


Figure 2.5: Climatic diagram obtained from 1873 to 2011 AD for Ponta Delgada from 1873 to 1946 AD were extracted from the “Annaes do Observatório Infante D. Luiz” whereas from 1947 to 2012 AD were supplied by the Instituto Portugues do Mar e da Atmosfera (IPMA). The red line shows the intra-annual variability of the temperature and the blue line shows the precipitation annual variations. The red dotted area represents the dry period and the blue lined area shows the wet period.

In terms of hydrology, the precipitation in Ponta Delgada village is defined by two seasons: one humid and one dry. The dry season spans from June to September and it has values around 30 mm while the humid season, from October to May, reaches values near 100 mm. Mean annual rainfall in Ponta Delgada for the period 1872 – 2011 AD is 958 mm, ranging from 786 mm to 1130 mm, which increases with the altitude, up to 2500 mm above 600 m a.s.l. (Constancia et al., 2000). The inter-annual variation of the precipitation in Ponta Delgada was divided in two periods (Fig. 2.6): 1) the drier

early period called SP1 from 1873 to 1942 AD; and, 2) the recent more humid period called SP2 from 1942 to 2011 AD (Hernández et al., 2016). SP1 has a mean annual precipitation of 893.3 mm that decrease to 644 the very dry years whereas SP2 shows a mean value of 1001 mm that increase to 1302 the very humid years. The average annual evapotranspiration is estimated to be about 580 mm/yr (Cruz et al., 2010).

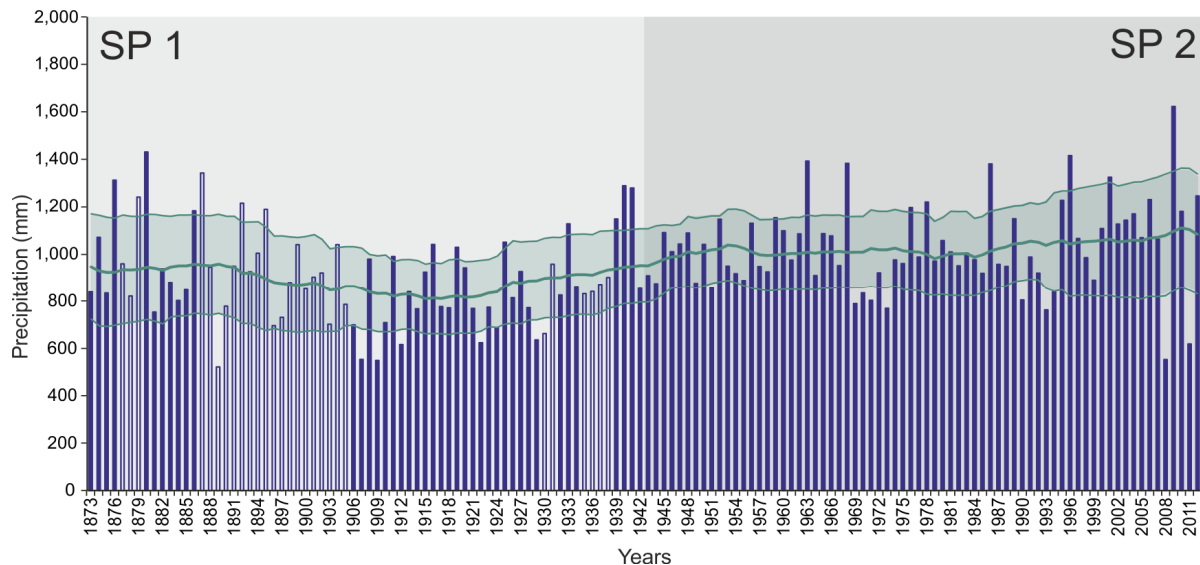


Figure 2.6: Annual series of precipitation in Ponta Delgada village for the period comprised between 1873 and 2012 AD. Solid bars indicate values calculated by summing daily values if no more than two values per month were missing. Open bars corresponds to monthly data sets from previously digitized monthly series already used by other authors (e.g. Cropper and Hanna, 2014). Green thick line represents a 31-point moving mean, which emphasizes the low-frequency variability of the annual precipitation series and green shadow band indicates the corresponding 31-point moving standard deviation. SP1 is a period comprised between 1873 and 1942 AD characterized by lower precipitation than SP2. SP2 is a period comprised between 1942 and 2012 AD characterized by higher precipitation than SP1. Note that the values obtained for both ends were calculated using as many years as possible in the moving average when the number of years was less than 31. The figure was extracted from Hernández et al. (2016).

2.2.2 Volcanic setting of the island

São Miguel Island is located near the eastern end of the Azores platform. It has six differentiated volcanic zones, all of them produced in the Quaternary except for the oldest (NE) that was partly Pliocene. The zones defined from west to east are: i) the stratovolcano of Sete Cidades, which is trachytic in composition, b) a field of alkali-basalt cinder cones and lava flows with no much trachyte, c) the stratovolcano of Água de Pau also trachytic, d) another field of cinder alkali-basalt cones, d) the Furnas stratovolcano also trachytic and, e) the Povoação caldera located in NE consisting of alkali basalt, tristanite and trachyte (Moore, 1991; Snyder et al., 2007). Despite the

small island size, Sete Cidades lavas have distinct composition compared to the other stratovolcanos (Beier et al., 2006). This suggests that a small magma reservoir can be feeding this volcano (Moore R.B., 1991).

Sete Cidades caldera, where Lake Azul is located, is settled in the western part of São Miguel Island at the eastern side of the Terceira rift axis. This rift is characterized by a very slow spread that promotes repeated volcanic episodes about large periods of time (Beier et al., 2006). The caldera formation was prone by a basaltic injection into a trachytic magma chamber about 22 ka yr BP (Beier et al., 2006; Moore, 1991). The posterior development showed three phases of major volcanic activity: a) pre-caldera, dominated by alkali basaltic phase; b) caldera consolidation, trachytic phase; c) post-caldera, small basaltic phase. The last period (post-caldera) comprises a sequence of explosives eruptions producing trachytic volcanoclastic deposits and pyroclastic flows leading to the caldera collapse (Beier et al., 2006). The oldest dated eruption, 210 ± 8 Ka yr BP is a trachyte flow of the northern caldera wall (Moore R.B., 1991). The youngest eruption from Caldeira Seca is called P17 (Booth et al., 1978) and dated 667 ± 105 yr BP by Shaton and Williams (1971). P17 is composed of grey ash and lapilli deposits. This last eruption was mainly hydromagmatic suggesting the existence of lakes or a well-developed hydrologic system (Queiroz et al., 2008). This volcano is bounded by the Atlantic Ocean most of its perimeter except for south-east part that coalesces with the Pico inland zone formed from monogenetic scoria cones and lava flows. This crater occupies about 110 km^2 with a subaerial volume of about 70 km^3 and it is occupied by nine craters, four of them occupied by lakes (Fig. 2.7). The largest water body is Lake Azul. The recent eruptive history of Sete Cidades which relates 17 intracaldera eruptions and 15 basaltic subaerial and submarine eruptions in the last 5000 years make the most active volcanic complex in Azores.



Figure 2.7: Ortophoto obtained from the Geoportail IDEE. This picture shows the environment of lake Azul in Sete Cidades Caldera. Nine volcanic craters can be observed, four of them occupied by lakes. The greatest lake is Lake Azul at the north side of the caldera. The alluvial plain is the west side of the crater and settles Sete Cidades villages. The north-eastern side of lake Azul is characterized by a steep caldera wall.

2.2.3 Human activities in the Island

As stated before, the landscape modifications and species introductions were made in the entire archipelago but, São Miguel Island was the most affected due to the greatest number of inhabitants (Constância et al., 2000). The most affected areas were under 350 m of altitude (Constância et al., 2000).

The last decades have been characterized by a general and marked water degradation of all lakes present in the island due to an increase of the human activities and a growing tourism industry. This degradation required an implantation of mitigating measures and impact assessments of the catchment basins (Martins et al., 2008). Most of this work was carried out in the framework of the Water Framework Directive (2009-2015) and, at present, friendly environmental measures are being applied in order to preserve the trophic and ecological status of the water masses.

2.2.4 Lake Azul

At the western end of the São Miguel Island lies the Sete Cidades volcanic caldera which is occupied by eight craters, four of them partially filled by lakes. Greatest lakes inside the caldera are Lake Azul and Lake Verde, which are hidrologically connected but separated as sedimentary basins by a shallow and narrow substratum threshold. Lake Azul is the largest lake in Sao Miguel island and the largest in volume of the Azores Archipelago (DROTRH INAG, 2001). The catchment has a surface of 19.3 km² and the Sete Cidades village, with 790 inhabitants, is present at the NW of Lake Azul. This catchment presents abrupt slopes at the northeastern side of the lake whereas they are much more gentle at the at the south of northwestern side where the village is located. At present, almost all catchment is forested, being *Cryptomeria japonica*, *Pittosporum undulatum* and *Hedychium gardnerarum* the main tree species present all from anthropic origin (Constancia et al., 2000).

Lake Azul has a surface of 4.35 km², 28 m of maximum depth and is located at 259 meters a.s.l. Bottom lake surface shows two main morphological areas separated by a rise zone: (1) a shallow platform (from 0 to 12 meters depth) occupying the southwestern half part of the lake, and (2) a deep plain, 25 - 28 m deep, in the northeastern third part of the lake's area. Lake Azul limnological data are scatter and only cover short time periods within the last 30 years. During these short time periods, Lake Azul has presented a mesotrophic state (Gonçalves, 2008). The recent phytoplankton community is dominated by green algae (Chlorophyceae and Zygnematophyceae) and diatoms (Bacillariophyceae). The most dominant planktonic diatoms are *Aulacoseira ambigua* and *Asterionella formosa*. A diverse benthic diatoms community is present in epilithic and epiphytic littoral habitats. *Achnantheidium minutissimum*, *Encyopsis cesatii*, *Navicula notha* are the most abundant benthic diatoms (Gonçalves, 2008).

As all Azores lakes, Lake Azul was under heavy human pressure owing to the different economic activities mainly related to cattle and crops. The last 30 years Azul and Verde

Lake has been monitored to know the ecological state. Lake Verde reaches the eutrophic state and Azul the mesotrophic state (DROTRH INAG, 2001).

The historical record shows that the lake has suffered significant lake level changes (Fig. 2.8) with catastrophic consequences for the nearby village with frequent floodings. In order to diminish these negative impacts, in 1937 AD was constructed a tunnel in the NW part of the lake which controls the lake level oscillations, not allowing it to increase more than 1 m (Constancia et al., 2000).

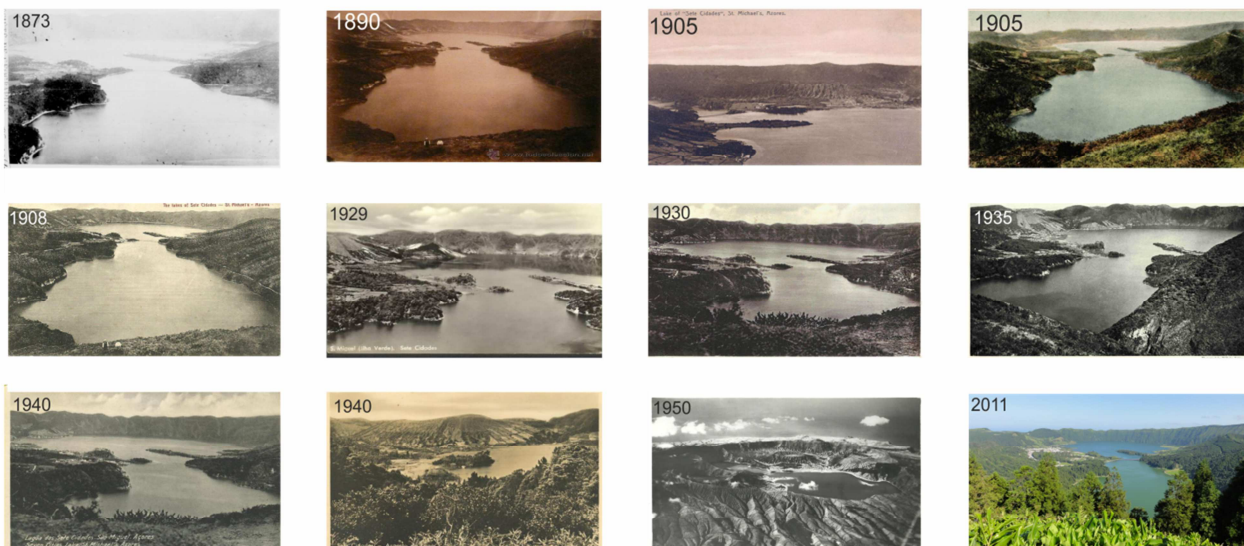


Figure 2.8: Photograph series of Sete Ciudades trough time since 1873 to 2011 AD. Evolution of landscape and lake level can be observed. Note that between 1929 and 1935 AD the lake reaches its maximum level.

*Las ciencias tienen las raíces amargas,
pero muy dulces los frutos.*

Aristoteles.

3. MATERIAL AND METHODS.

3.1 FIELD CAMPAIGN.

In September 2011, fifteen sediment cores, up to 1.5 meters long, were retrieved from Lake Azul. For this purpose, two coring extraction systems were employed: the Uwitec® piston coring system installed on a floating raft (3 cores) and Uwitec® gravity coring system (12 cores) used to minimize the water-sediment interphase disturbance. Two coring transects (NW-SE and NE-SW) were followed in order to cover all the sediment environments present in Lake Azul (Fig. 3.1). Immediately after their retrieval, the cores were sealed, transported and stored horizontally in the cold room of the ICTJA-CSIC at +4 °C until their subsampling.

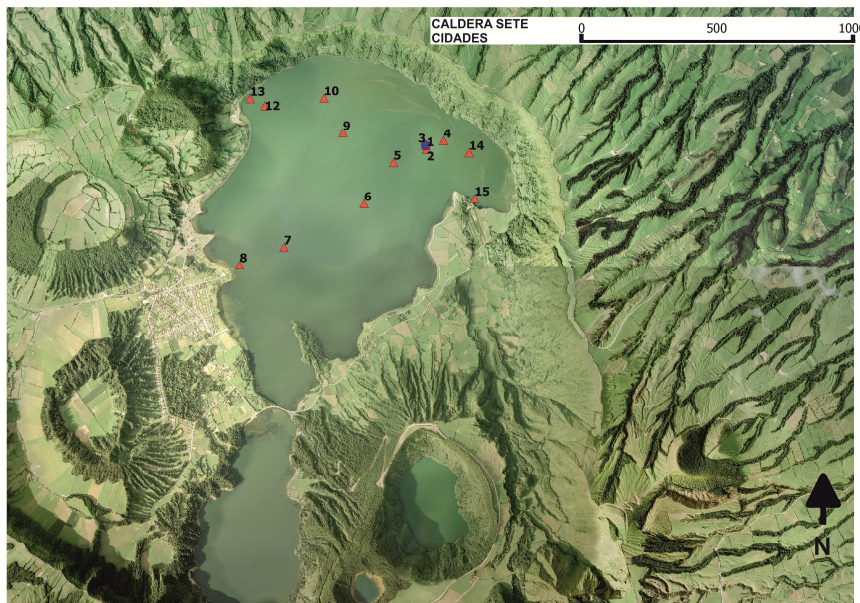


Figure 3.1: Satellite image of lake Azul showing location of the 15 retrieved cores and the water samples site during the field campaign on September 2011. Red triangles are the sediment core locations and blue circles the water sampling site. The sediment cores were obtained from Uwitec® gravity core and Uwitec® piston coring system coupled on a floating raft.

In the meanwhile, seventeen seismic profiles were performed using EdgeTech 3100 SB-424 equipment (Fig. 3.2). The profiles 1, 4, 6, 9 and 10 followed a southwest trajectory whereas the profiles 3, 5 and 7 had a northeast direction. The profile 11 went from east to west. The longest profiles that were 2 and 8 went from north to west. The EdgeTech 3100-P Portable Sub-Bottom Profiling System is a high-resolution wideband profiler. The system transmits a FM pulse that linearly swept over a full spectrum

frequency range. The acoustic return is received by hydrophones and passed through a pulse compression filter. It generates high-resolution images of the sub-bottom stratigraphy. The profiles 4, 5 and 7 were acquired at 2-15 kHz for 20 ms, the profile 6 was obtained at 2-10 kHz for 20 ms, and the profiles 1, 2, 3, 8, 10, 11, 12, 13, 14, 15, 16 and 17 were acquired at 2-12 kHz for 20 milliseconds. Simultaneously, spatial data were acquired with the attached Garmin GPSMAP 60Cx.

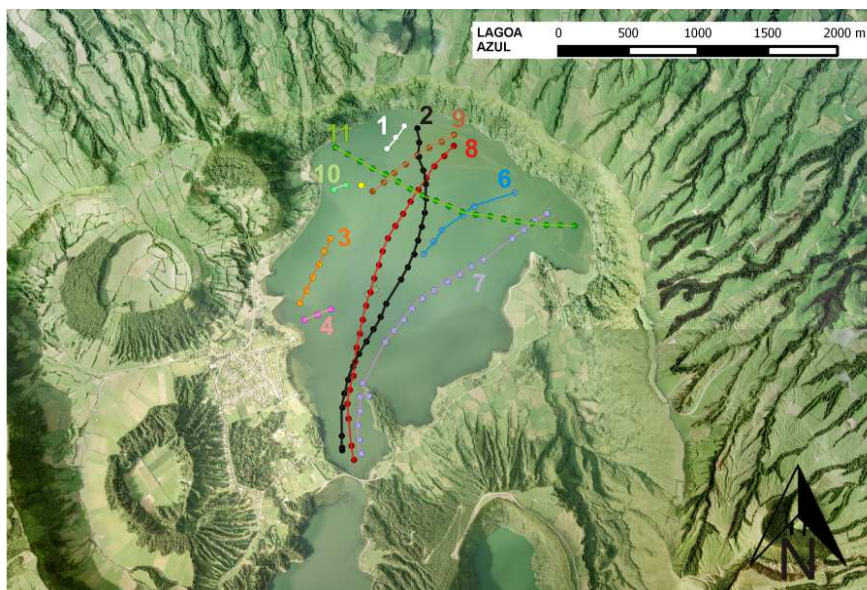


Figure 3.2: Satellite image of lake Azul showing location of seismic profiles acquired on September 2011 using the EdgeTech 3100 SB-424 equipment. The profiles 1, 4, 6, 9 and 10 followed a southwest trajectory. The profiles 3, 5 and 7 had a northeast direction. The profile 11 went from East to West. And the profiles 2 and 8 went from north to west.

Echo sounding data were obtained from Cruz et al. (2007) in the Azorean Atlas of water bodies

(<http://www.azores.gov.pt/Gra/srnrndrotrh/conteudos/publicacoes/Atlas+da+%C3%81gua.htm?lang=pt&area=ct>).

Water sampling

Water samples were collected near the AZ11_02 coring point at the lake surface, 9 m, 13 m, 18 m and 24 m of the lake water depth. Samples were collected for δD , $\delta^{18}O$, $\delta^{13}C$, $\delta^{34}S$ and major ions analyses (Ca, Na, K, Mg, S, B and Li). Each sample was filtered using a 0.45 μm Millipore© cellulose acetate filters. $\delta D - \delta^{18}O$ samples were kept in

two 50 ml polyethylene tubes whereas $\delta^{34}\text{S}$ samples were kept in 100 ml polyethylene bottles. $\delta^{13}\text{C}$ samples were poisoned with HgCl to avoid the water carbon fractionation by microorganisms.

The isotopic analyses were conducted using the gas chromatograph Finningan MAT Delta S TC/EA-CF-IRMS. The reference standards were Vienna Standard Mean Ocean Water (VSMOW) for δD and $\delta^{18}\text{O}$, Pee Dee Belemnite (PDB) for $\delta^{13}\text{C}$ and Vienna Cañon Diablo Troilite (VCDT) for $\delta^{34}\text{S}$. The analysis replications indicates a precision of $\pm <0.1$ ‰ (1σ) for $\delta^{18}\text{O}$, 1.5‰ (1σ) for δD and $\pm <0.2$ ‰ (1σ) for $\delta^{13}\text{C}$ and $\delta^{34}\text{S}$. The major ions composition was analyzed by means of ion-exchange chromatography, volumetric analysis and Inductively Coupled Plasma (ICP-OES) at the Centres Científics i Tecnològics of the University of Barcelona (CCiTUB).

The variables measured in situ were conductivity ($\mu\text{S}/\text{cm}$), oxygen concentration (mg/l), pH, temperature ($^{\circ}\text{C}$) and salinity (psu) at 0.5 meters depth resolution. These analyses were performed using the multiparametric model TURO T-613.

3.2 IMAGE ACQUISITION AND FACIES DESCRIPTION.

The fifteen sediment cores were split longitudinally in two halves and were prepared for the high resolution images capture. The camera is a CCD color line scan with RGB channels at 630, 535 and 450 nm mounted on an Avaatech XRF core scanner. The resolution is 3 x 2048 pixels and the calibration is performed on a gray ceramic reference till (Fig. 3.3). The core party and imaging was done at University of Barcelona.



Figure 3.3: The high resolution photographs of studied Azul cores. (a) core AZ11_02; (b) core AZ11_14). Images were obtained from CCD color line scan camera with RGB channels at 630, 535 and 450 nm mounted on an Avaatech. The iris aperture was 5.6 for picture (a) and 5.6+ for picture (b). The top of the sequence is on the left.

Smear slides were prepared every 10 mm. The sediment composition and semi-quantitative estimates of biogenic, clastic, endogenic material and main diatoms composition characteristics was done with the microscopy ZEISS Axioplan 2 imaging at the University of Barcelona (UB). The classification of the organic composition was based on Martin-Closas et al. (2005) and Sebag et al. (2006).

Two lithological correlation panels were employed to characterize the architecture of the sedimentary infill and select the most representative record of Lake Azul sedimentary architecture and offshore facies. In order to construct the correlation panels, the visual comparison of the cores and the smear slides were employed. The visual recognition was used to disentangle the main sedimentary processes and the smear slides were used for the transitions not completely resolved by visual approach. The core AZ11_02 was the sedimentary record that best represents the offshore lacustrine deposition but, the AZ11_02 resolution from top to the 675 mm was relatively low. In order to increase the resolution for this section, the core AZ11_14 was used for some of the analyzed proxies.

3.3 DATING METHODS.

The present-day radiocarbon effect of Lake Azul was determined by radiocarbon dating of the dissolved inorganic carbon (DIC) at the thermocline (13 m). For that, one liter of water was filtered using a 0.45 μm polycarbonate filter. The filtration process preserves the dissolved carbon content water from the alteration by any bacterial activity. Moreover, KOH was added in order to keep a basic pH favoring the precipitation of the dissolved carbon into carbonate. The water sample was radiocarbon dated in to Beta Analytic Inc. (USA) to analyze the present-day radiocarbon effect.

The chronology of the sedimentary sequence was performed using a new method presented in Chapter 5.1. This method is called the Dynamic Age Model (DAM) and it has been designed to calculate the age of samples from historical sequences. The main rationale of DAM is to incorporate to the age-depth models short-term and abrupt sedimentation changes that the available methods usually do not contemplate. These abrupt sedimentation changes may affect significantly historical sedimentary sequences hampering the correct age attribution of a given climate/environmental event and, hence, making difficult its assessment of the spatial-temporal evolution (see Chapter 5.1 for further details).

The chronological model is based on both a ^{210}Pb profile and five radiocarbon AMS dates for both, AZ11_02 and AZ11_14. The concentration profile of ^{210}Pb was determined every centimeter for uppermost 210 mm in AZ11_02 and every 25 mm for the uppermost 685 mm in AZ11_14 (Table 3.1 and Table 3.2, respectively). The concentration determination was performed through the quantification of ^{210}Po by alpha-spectroscopy following Sánchez-Cabeza et al. (1998) at the Department of Physics – Institute of Science and Environmental Technology (Autonomous University of Barcelona). A total of 22 samples for AZ11_02 and 26 samples for AZ11_14 were analyzed for ^{226}Ra (via ^{214}Pb) by gamma spectrometry using a high purity intrinsic germanium detector, and the excess ^{210}Pb concentrations were calculated by subtracting ^{226}Ra from total ^{210}Pb concentrations. ^{210}Pb -derived SRs were calculated applying the CRS model (Appleby and Oldfield, 1978).

Depth (mm)	Age CRS model (yr)	CRS Sedimentation rate (mm/yr)
0	2011 ± 1.8	5.38 ± 1.12
10	2009.1 ± 1.8	10.41 ± 3.85
20	2008.1 ± 1.8	2.28 ± 0.29
30	2003.4 ± 1.9	1.73 ± 0.16
40	1997.0 ± 2.0	1.51 ± 0.17
50	1989.6 ± 2.2	1.99 ± 0.21
60	1984.2 ± 2.4	2.89 ± 0.47
70	1980.5 ± 2.6	2.21 ± 0.38
80	1975.6 ± 2.8	4.38 ± 1.03
90	1973.3 ± 2.9	5.58 ± 2.20
100	1971.4 ± 2.9	1.75 ± 0.35
110	1965.1 ± 3.2	2.89 ± 0.69
120	1961.5 ± 3.4	1.96 ± 0.43
130	1955.9 ± 3.8	1.10 ± 0.23
140	1945.2 ± 4.6	2.31 ± 0.66
150	1940.6 ± 5.1	3.30 ± 1.95
160	1937.4 ± 5.3	2.22 ± 0.89
170	1932.5 ± 5.8	0.86 ± 0.21
180	1918.0 ± 8.4	0.88 ± 0.40
190	1903.9 ± 11.1	0.90 ± 0.53
200	1890.3 ± 14.8	0.63 ± 0.43
210	1868.4 ± 24.6	0.32 ± 0.30

Table 3.1: Chronological model base on a CRS model from ^{210}Pb datations from the top to the 210mm for the core AZ11_02. The first column is the depth, the second is the age plus uncertainties and the third is the sedimentation rate based on this model plus uncertainties.

Plant remains were isolated from sediment, rinsed with distilled water and kept for datation or microscopy purposes.

Depth (mm)	Age CRS model (yr)	CRS Sedimentation rate (mm/yr)
12.5	2011 ± 1.0	2.35 ± 0.15
37.5	2007.7 ± 1.1	2.31 ± 0.17
62.5	2004.6 ± 1.1	2.52 ± 0.21
87.5	2001.5 ± 1.1	2.96 ± 0.28
112.5	1998.1 ± 1.2	2.28 ± 0.16
137.5	1993.1 ± 1.2	2.87 ± 0.27
162.5	1989 ± 13	2.25 ± 0.20
187.5	1985.3 ± 1.3	2.12 ± 0.21
212.5	1981.3 ± 1.4	4.30 ± 0.59
250	1979.1 ± 1.5	5.27 ± 0.64
300	1975.2 ± 1.5	4.52 ± 0.64
337.5	1971.0 ± 1.5	1.48 ± 0.14
362.5	1964.1 ± 1.7	1.64 ± 0.20
387.5	1957.5 ± 1.9	2.49 ± 0.41
405	1952.5 ± 2.0	4.48 ± 1.21
427.5	1951.7 ± 2.0	2.27 ± 0.32
457.5	1944.3 ± 2.2	1.60 ± 0.20
485	1938.4 ± 2.5	1.70 ± 0.26
505	1929.9 ± 3.0	1.54 ± 0.31
522.5	1927.4 ± 3.2	1.18 ± 0.22
547.5	1918.4 ± 3.8	1.57 ± 0.42
572.5	1912.4 ± 4.3	1.33 ± 0.40
597.5	1905 ± 4.8	0.76 ± 0.17
622.5	1886.5 ± 7.6	0.54 ± 0.19
547.5	1856.1 ± 14.8	0.50 ± 0.37
572.5	1822.5 ± 23.6	0.35 ± 0.36

Table 3.2: Chronological model base on ²¹⁰Pb datations from the top to the 210mm for the core AZ11_14. And, the sedimentation rate based on this model.

The chronological model is based on both a ^{210}Pb profile and five radiocarbon AMS dates for both, AZ11_02 and AZ11_14. The concentration profile of ^{210}Pb was determined every centimeter for uppermost 210 mm in AZ11_02 and every 25 mm for the uppermost 685 mm in AZ11_14. The concentration determination was performed through the quantification of ^{210}Po by alpha-spectroscopy following Sánchez-Cabeza et al. (1998) at the Department of Physics – Institute of Science and Environmental Technology (Autonomous University of Barcelona). A total of 22 samples for AZ11_02 and 26 samples for AZ11_14 were analyzed for ^{226}Ra (via ^{214}Pb) by gamma spectrometry using a high purity intrinsic germanium detector, and the excess ^{210}Pb concentrations were calculated by subtracting ^{226}Ra from total ^{210}Pb concentrations. ^{210}Pb -derived SRs were calculated applying the CRS model (Table 3.1 and table 3.2; Appleby and Oldfield, 1978). Radiocarbon AMS dates were obtained from one pollen enrichment extract prepared by acid digestion (Rull et al., 2010) and six plant macroremains (Table 3.3) and analyzed at Beta Analytic Lab (USA). The AMS radiocarbon dates samples at 55 mm and 1140 mm for core AZ11_02 were not used for the age model owing to the first was contradictory with the ages obtained by ^{210}Pb and the second showed no coherence with the other three AMS dates. And, the radiocarbon date at 330 mm was avoided because ages were incoherent with ^{210}Pb . The AMS radiocarbon dates were calibrated using the software Calib 7.1 (Stuiver, 2005) and Intcal13 curve (Reimer et al., 2013) and taking the midpoint of the 2 standard deviations (Table 3.3). The core AZ11_14 dating was only performed for the uppermost 810 mm because at this depth was the oldest datation of the core there were not older datations and this core was not retrieved with the lower pumice layer. Then, from the top to the 810 mm the core AZ11_14 retrieved the last 470 yr BP of history. According to the ^{210}Pb profile and the three selected AMS radiocarbon dates in the core AZ11_02 the recovered lacustrine sedimentary infill (1330 mm thick) records the last 730 cal. yrs BP of history.

Core	Sample Depth (mm)	Conventional Rad.C.Age	Calibrated Rad.C.Age	C13/C12 (‰)	Material dated
AZ11_02	55	154.4 ± 0.4 pMC	1989.2 – 1990.9 yr AD	-32.7	Plant remain
	460	200 ± 20 BP	180 ± 40 yr BP	-28.6	Plant remain
	610	410 ± 30 BP	475 ± 45 yr AD	-25.8	Pollen concentrate
	860	690 ± 30 BP	660 ± 20 yr BP	-25.3	Plant remain
	1140	380 ± 30 BP	340 ± 30 yr AD	-28.6	Plant remain
AZ11_14	330	125.1 ± 0.5 pMC	1992.73 – 1993.82 yr AD	-27	Plant remain
	810	390 ± 30 BP	470 ± 40 yr BP	-25.1	Plant remain

Table 3.3: Radiocarbon datations for the core AZ11_02 and AZ11_14 performed from plant remains and one pollen concentrate. The light brown datations were not used to construct the Age-depth model

3.4 GEOCHEMICAL ANALYSES ON SEDIMENTS

X-ray fluorescence (XRF) measurements were conducted using the XRF Avaatech core scanner from University de Barcelona (Barcelona, Spain) and the XRF Itrax core scanner from the Institute National de la Recherche Scientifique (INRS, Québec-Canada). The XRF Avaatech measurements were performed every 2 mm under the following working conditions for light elements 10 kV, 2000 μ A and 20 s; and, for heavy elements 30 kV, 2000 μ A and 40 s. The measurements with and the XRF Itrax core scanner were also carried out at 2 mm under the working conditions at 30kV: 30mA, Mo tube, 60 seconds. The XRF measurements results were expressed in counts per second (cps). The XRF data were statistically analyzed to avoid the use of non-significant elements. The elements with mean values larger than 1000 cps and mean χ^2 value lower than 2 were kept. The statistically significant elements for the Avaatech XRF core scanner equipment were 11 (Sr, Rb, Zr, Nd, Al, Si, K, Mn, Fe, Ca, and Ti) while for the Itrax nine elements were significant (Si, K, Mn, Ti, Cu, Zr, Ca, Fe, and Sr). From those selected elements, the data suspected to be on a sediment hole were erased from the dataset.

X-Ray Diffractions were performed at the Institute of Earth Science Jaume Almera-CSIC (Barcelona) using an automatic Siemens D-500 X-Ray diffractometer under the following working conditions: Cu α , 40kV, 30 mA and graphite monochromator. The samples were dried at 60 °C for 48 hours and ground manually using an agate mortar. The identification and quantification of the mineralogical species was carried out following the standard procedure presented by Chung, (1974).

Some representative samples located at 108, 110, 112 and 120 mm on core AZ11_02 were characterized by Scanning Electron Microscopy coupled to an Energy Dispersive X-Ray Spectrometer (SEM-EDS) at the CCIUB. The grains selected were dried and attached to stubs using a conductive bio-adhesive tape. In the low vacuum mode (0.5 torr) was performed the morphological description and in the high vacuum mode (< 10⁻⁴) was used to recognize small grains.

3.5 ORGANIC ANALYSES

Bulk analyses

For the bulk organic analyzes, the core AZ11_02 was subsampled every 100 mm from top to the 1080 mm while the core AZ11_14 was subsampled every 50 mm from the top to the 775 mm. A total of 258 samples (109 for AZ11_02 and 149 for AZ11_14) were dried during 48 hours at 60 °C and manually ground with an agate mortar. Approximately 5 mg of sample were weighted and packed in a tin (Sn) capsule adding vanadium pentoxide (VO₅) to accelerate the combustion.

The total organic carbon (TOC), total nitrogen (TN) and their respective stable isotopes ($\delta^{13}\text{C}$ and $\delta^{15}\text{N}$) were analyzed using a Finningan delta Plus® constant Flow Elemental Analyzer – Isotope Ratio Mass Spectrometry (EA-IRMS) in the CCiTUB laboratories. The precision for $\delta^{13}\text{C}$ and $\delta^{15}\text{N}$ were 0.2‰ and 0.3‰, respectively.

Lipidic fraction

The lipid analyses were performed in the core AZ11_02 and AZ11_14 at 50 mm resolution. The core AZ11_02 was analyzed from top to the 1050 mm whereas the core AZ11_14 was analyzed from top to the 775 mm.

A total of 350 samples, 201 from AZ11_02 and 149 from the core AZ11_14 were used for the lipid extraction. The samples were wrapped with aluminum foil, to avoid contamination by plastic, and kept into the freezer at -20 °C until their analysis. The samples were transported to the University of Texas at Austin (UT, USA) where the analytic procedure was performed. The laboratory material used in this process was either combusted at 450 °C or solvent washed to avoid contamination by organic compounds. The first step was to freeze-dry the samples. After free-drying, they were homogenized and grounded by hand using a mortar. Later, the samples were weighted and filled up to 50 mg with a non-organic sand previously combusted. This sample-sand mixture was transferred to a microwave vessel and filled up with 15 ml of a dichloromethane (DCM): methanol (9:1 vol/vol) mixture. Lipids were extracted using the Accelerated Solvent Extractor MARSX microwave flushed at a temperature of 100 °C for 10 min with a ramp temperature of 15 min. After the lipid extraction, the

supernatant solution was filtered three times over a Na_2SO_4 column, to clean up from pellets or sediment remainders. The eluent used was the DCM. The samples obtained after filtration were condensed by evaporation under a constant flux of liquid N_2 and transferred to a 4 ml vial with DCM as eluent. The samples were blown down again under N_2 stream and brought up with 0.5 ml of hexane. At this point, the sample was ready to be separated by column chromatography using the rapid trace.

Before chromatographic separation, the samples were filtered again with fiber glass to avoid pellets and/or impurities and fillet up again with 0.5 ml of hexane. The liquid chromatography separation was performed in the Rapid Trace workstation through a column of 5 mg of Aminopropyl Bond Elute® (Fig. 3.4). This chromatographic separation split the samples in three fractions depending on polarity:

- 1) Aliphatic hydrocarbon fraction using 4 ml of hexane as eluent.
- 2) Ketones fraction using 4 ml of DCM: methanol (9:1 vol/vol).
- 3) Fatty acids fraction by using 8 ml of 2% formic in DCM.

The fractions were kept separately at $-20\text{ }^\circ\text{C}$.



Figure 3.4: Specialized vented cabinet used for a total of 7 Zymark Rapid Traces at the Dr Timothy Shanahan laboratory at the University of Texas at Austin. This rapid trace can separate chromatographically lipid fractions from the extracted lipids.

Aliphatic hydrocarbon fraction

This fraction was not used in the present work because the hydrocarbon amount was under the limit detection of the Isotope Ratio Mass Spectrometer analyses presented later on this section.

Ketones

The samples were filtered again with fiber glass with DCM as an eluent to avoid pellets and/or impurities. Later, the samples were blown down with N₂ and brought up again with 200 µl of 1 % isopropanol (IPA) in hexane. The resulting sample was split in two fractions. One fraction was used to analyze the Glycerol Dialkyl Glycerol Tetraethers (GDGTs) whereas the other fraction was employed to determine the fecal sterols.

The GDGTs fraction was analyzed by high performance liquid chromatography–atmospheric pressure chemical ionization–mass spectrometry (HPLC–APCI–MS) at the University of Texas at Austin (USA). The chromatograph used was an Agilent 1200 liquid chromatograph interfaced to an Agilent 6130 single quadrupole mass spectrometer operated in single ion monitoring (SIM) mode. The HPLC was equipped with a Prevail Cyano HPLC column (3 µm, 150 × 2.1 mm i.d.), a guard column and operated at 30 °C at a flow rate of 200 µl/min. The volume of the injection was 5 µl. GDGTs analyses were followed by a linear gradient to 1.8 % IPA in 45 minutes. After each analysis, the column was back-flushed for 10 min using 10% IPA at 200 µl/min. APCI source conditions followed previously published methods such as nebulizer pressure: 60 psi, vaporizer temperature: 400 °C, drying gas flow: 6 l/min at 200 °C, capillary voltage: –3 kV, corona: 5 µA (Schouten et al., 2008). Peak integration followed the methods described in Schouten et al. (2007) and Shanahan et al. (2013). Half of the samples (160 samples) were analyzed in duplicate with an average error in the fractional abundance of 0.05 % (Fig. 3.5).

Figure 3.5: Agilent gas Chromatograph flame ionizator detector coupled to an Agilent gas chromatograph with a single quadrupole mass spectrometer from the Dr. Timothy Shanahan laboratory at the University of Texas at Austin. This instrument is used for the lipid identification and quantification.



Fatty acids

The acidic fraction was blown down under N₂ continuous stream before applying the transesterification to reduce the Unresolved Complex Mixture (UCM). The transesterification procedure has several steps. The first step was to add 0.5 ml of toluene to each sample vial. After that, a solution 9:1 vol/vol of acetyl chloride and anhydrous methanol was prepared. Since this reaction is highly exothermic, the anhydrous methanol needs to be refrigerated for 30 minutes and the acetyl chloride must to be added carefully. One milliliter of the prepared mixture was added to the set of samples. After the mixture addition the samples were warmed up to 100 °C for 1 hour. After that, the samples were cooled down at room temperature. Once the samples were cold, 5 ml of water and 2 ml of hexane were added and the samples were vortex for 30 seconds. The hexane fraction, which contained the Fatty Acids Methyl Steres (FAMES), was separated by liquid-liquid extraction. The FAMES were further purified on a second LC-NH₂ column using DCM as eluent but, conditioning the column with hexane.

The same procedure was applied to the external FAMES standard. Those standards were the phthalic acid and C₂₄ fatty acid mixture, both of them of known isotopic composition (Schutter and Dick, 2000 modified).

FAMES were identified by comparison of the GC/FID, Agilent 6850 gas chromatograph/flame ionization detector retention times with respect to those of authenticated external FAMES standards. Moreover, the signal was quantified to prove its validity for the isotope ratio mass spectrometer (IRMS) explained in the following step.

The samples were separated in three groups according to their concentration before analyzing their isotopic composition: the group of samples with too low concentration to be analyzed by IRMS (38 samples), samples with low concentration (90 samples) and, samples with high concentration (202 samples). The samples that had not enough concentration were discarded and not used for the next steps. The low concentration group was analyzed only one time whereas the high concentration group was analyzed by duplicate to calculate the standard deviation.

The δD values of individual FAMES were measured on a Thermo Scientific Delta V Plus isotope ratio mass spectrometer (IRMS) coupled to an Agilent 6980 GC via a pyrolysis interface (GC-TC) operated at 1440 °C (Figure 3.6). Data were processed using Isodat 3.0 software (Thermo Scientific). The H^+ factor (Sessions et al., 2001) was measured daily and ranged from 5.6–6.2 ppm/mV over the course of the measurement period. Peaks of a propane reference gas were inserted before and after each sample during each run and used as internal calibration standard. Instrument variability was accounted by the routinely injection of an external standard mix that contained 8 fatty acid methyl and ethyl esters of known δD (F8 mixture) and adjusting the reference propane δD value to minimize the average offset between the known and measured δD values of the F8 compounds. Estimated average accuracy is ± 8.1 ‰ based on daily measurements of the F8 mixture. In order to perform the correction for the fractionation occurred during transesterification, a phthalic acid standard and C_{24} mixture of known isotopic composition was methylated in parallel to samples using the same batch of anhydrous methanol. The δD of the resulting dimethyl phthalate was measured and used to calculate the δD of the methyl hydrogen by mass balance. Values were reported using standard delta notation (δD) as per mil (‰) deviations from Vienna standard mean ocean water (V-SMOW).



Figure 3.6: Delta V stable isotope mass spectrometer from the Dr Shanahan laboratory at the University of Texas at Austin. This IRMS is equipped with a combustion furnaces for hydrogen, carbon and nitrogen isotope analyses from molecular organics.

3.6 GEOCHEMICAL ANALYSES APPLIED TO THE RAIN WATER.

The precipitation in Ponta Delgada village has been collected weekly for the period comprised between September 2011 and March 2015. The mentioned period has a total of 180 weeks but, the number of weeks with isotopic data was 147 (82%). The longest period without data was during July and August of 2014 owing to the low or scarce precipitation containing only one week of isotopic information. The collector was a plastic container covered with a plastic lid but with a hole in the middle (Fig. 3.7). This system allows the water to get in and avoids evaporation. The water collector was placed in the upper terrace of the University of Azores in Ponta Delgada avoiding any shadow effect. Every Monday (6 times on Tuesday), the rain water collected was kept in a jug and sealed to avoid any evaporation that fractionates the isotopes. Those samples were sent to the University of Barcelona where they were isotopically analyzed for oxygen ($\delta^{18}\text{O}$) and hydrogen (δD) in the CCTiUB. The method employed was a GC coupled to an IRMS.



Figure 3.7: Rain water collector located at the University dos Açores. The upper figure shows the internal structure of the water collector. The lower pictures showed the collector cover made of porexpan® to avoid evaporation and the location without any shadow effect of the collector.

The air masses tracks that promoted precipitation in the island since September 2011 were studied using a Hybrid Lagrangian Integrated Trajectory Model (Hysplit). Those tracks were defined from the location of the air mass track 72 hours and the landfall in São Miguel Island. The first time selection was 10 days as proposed by other authors in South-West Africa (Song and Gao, 2009) but, the tracks were too long to define an origin. Therefore, we re-adapted this for the North Atlantic conditions to 72 hours. The weekly air masses were plotted for the weeks that we had collected water. The parameters established were: 1) a new trajectory started every 24 hours; 2) each new trajectory contains 72 hours of air mass track; and, 3) the week started the day of the previous water collection and finished the date before the next rain water collection.

3.7 INSTRUMENTAL DATA

Daily precipitation data were digitized for the period between 1873 and 2012 AD at Ponta Delgada station (37° 44' N - 25° 40' W, 77 m a.s.l) and controlled in terms of quality according to Stickler et al. (2014). For the period comprised between 1873 and 1946 AD the precipitation data were extracted from the “Annaes do Observatório Infante D. Luiz” whereas from 1947 to 2012 AD were supplied by the Instituto Portugues do Mar e da Atmosfera (IPMA). In addition, annual and monthly series of precipitation were calculated by summing daily values if no more than two values per month were missing. When this happened, monthly and annual series were completed using the monthly datasets from previously digitized monthly series (IDL-IPMA) covering this time period (Cropper and Hanna, 2014). The precipitation data was the same than the used by Hernández et al. (2015).

Daily temperature data for the period 1873 - 1946 AD were obtained from the ‘Annaes do Observatório Infante D. Luiz’ (see Valente et al., 2008 and Stickler et al., 2014) and for 1947 to 2012 AD were supplied by (IPMA). Monthly and annual values were obtained by applying the mean to the daily data.

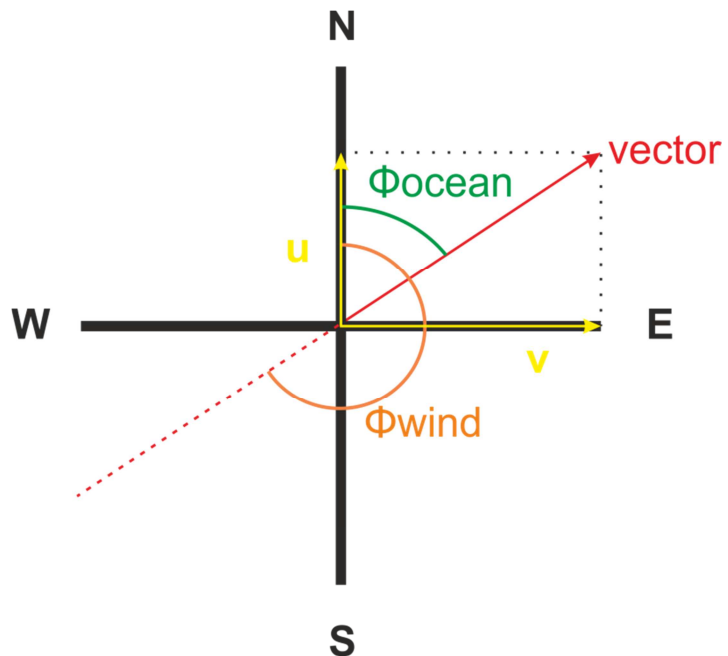
The oceanic currents for the period 1992 - 2015 AD were downloaded from the Ocean Surface Current Data Set Analyses – Real Time – NOAA (<http://www.oscar.noaa.gov/datadisply/>). Data were filtered for 1 degree of latitude and 1 of longitude for the area comprised between 80° to 20° W and from 23° to 45° N. These dataset contained 3 components: a) zonal flow velocity (u), b) meridional flow velocity (v) and, c) angle formed by the resulting vector in reference to the north (ϕ ocean). From those components, the magnitude of the vector could be calculated for each point of the selected mesh. These magnitudes of the vectors have an implicit direction and velocity (Fig. 3.8).

Sea surface temperature (SST) data from the North Atlantic were downloaded from the Earth System Research Laboratory – NOAA (<http://www.esrl.noaa.gov/psd/repository/entry/show>). These data were obtained

monthly from January 1891 to the present and subset to the same area as for the oceanic currents. The horizontal stride was 1.

The North Atlantic oscillation (NAO) index was downloaded from the Climate Prediction Center – NOAA (<ftp://ftp.cpc.ncep.noaa.gov/cwlinks/>). NAO data were obtained daily since January 1950 until present. Those data were standardized by the mean value of the monthly NAO index from 1950 to 2000. From 1821 to 1950 the NAO data were acquired from Climate Research Unit (<https://crudata.uea.ac.uk/cru/data/nao/>).

Figure 3.8: Theoretical diagram of the vectors and angles derived from the oceanic currents. The vector u (meridional) and v (zonal) appears in yellow color. The angle derived from the wind is named as ϕ_{wind} and is colored in orange. The angle derived from the ocean currents direction is colored in green and determined as ϕ_{ocean} . The resultant vector (red) is the result of apply root squared to the sum of the squared u and v .



3.8 STATISTICAL ANALYSES.

Correlation analyses were performed using the R package 'Hmisc'. The correlations were computed by calculating the Pearson product-moment correlation coefficients and their correspondent p-values. P-values were corrected using the Bonferroni in order to avoid the size-effect.

*Ara faria això, trencaria papers,
trencaria paraules fent els trossos més menuts*

Vicent Andres Estelles

4. RESULTS

4.1 PHYSICAL AND CHEMICAL WATER COLUMN CHARACTERISTICS

The continuous physical (temperature, dissolved oxygen, turbidity) analyses in the water column performed on September 2011 showed that an established thermocline was observed around 10 - 12 m depth (Fig. 4.1). This thermocline defined the epilimnion from 0 to 10 m depth, the metalimnion from 10 to 12.5 m depth and the hypolimnion from 12.5 to 22 m. The discrete analyzes of the major chemical compounds of the lake Azul showed that the Ca composition was 1.64 ppm on the top and increased towards 2.5 ppm at the bottom. The Na was around 17.0 mg/l at the top and at the bottom. The mean K was 2.91 mg/l with the highest concentration at the bottom (3.4 ppm). The Mg was 1.4 ppm but reached 1.7 ppm at the bottom, the SO_4 concentration was higher at the top (4 ppm) than at the bottom (1.7 ppm). The NO_2 oscillated from 1 ppm at the top to 0.3 ppm at the bottom. The NO_3 had a decreasing trend from top to bottom that went from 0.5 to 0.4 ppm. The isotopic values were also measured in lake Azul. The δD values were between 0 and 3‰ with a clear depletion from top to bottom. The values of $\delta^{18}\text{O}$ oscillated between 0.1 and 0.7 ‰ with a depletion from top to bottom. The $\delta^{13}\text{C}_{\text{DIC}}$ showed enrichment from top to bottom that went from -13.8 to -9.5 ‰.

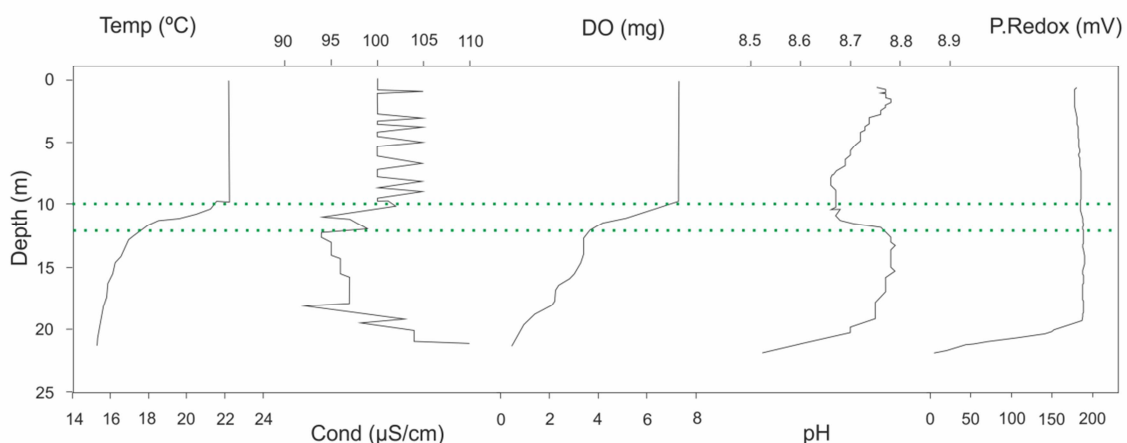


Figure 4.1: Multiparametric continuous analyzes from top (0 m) to almost bottom (22 m) of Lake Azul water column. From left to right: temperature (°C), conductivity ($\mu\text{S}/\text{cm}$), Dissolved Oxygen (mg), pH and potential redox (mV). Green dotted lines indicate depth of thermocline zone (between 10 and 12 m).

Epilimnion

The epilimnion was characterized by a constant temperature of 22.5 °C, the conductivity oscillated between 100 and 105 $\mu\text{S}/\text{cm}$, the dissolved oxygen (DO) has a constant value of 7.9 mg, the pH was basic and moved from 8.8 to 8.65 and the potential redox was around 190 mV.

Metalimnion

The range of temperature in the metalimnion moved from 22.5 to 17.5 °C. The conductivity decreased from 102 to 95 $\mu\text{S}/\text{cm}$. The DO went from 7.9 to 3 mg. The pH became more basic than in the epilimnion and moved from 8.65 to 8.8. And, the potential redox had equal values than in the epilimnion (190 mV).

Hypolimnion

The temperature decreased to the bottom from 17.5 to 15 °C. The conductivity followed more or less an increasing downward trend that went from 94 to 110 $\mu\text{S}/\text{cm}$. The DO observed a decreasing downward trend that went from 3 to 0 mg. The pH remains constant around 8.8 from 12 to 19 m depth and observed a decreasing trend from 8.8 to 8.5 from 19 m to 22 m. The potential redox remains constant from 12 to 18 m depth around 190 mV and decreased drastically from 18 to 22 m depth with values that oscillated from 190 mV to 0 mV.

4.2 GEOCHEMICAL AND BIOLOGICAL ANALYSES.

X-Ray Diffraction.

The X-Ray Diffraction (XRD) analyses showed that the sediments of Lake Azul were composed of amorphous and of crystalline fractions. The amorphous fraction constituted the major part of the sediments. For that reason, the absolute amount of the mineral species contained in the crystalline fraction could not be quantified. The mineral species identified in the crystalline fraction were smectite, chlorite, illite, zeolite, sanidine, plagioclases and amphiboles, being sanidine the dominant mineral component followed by zeolite, illite and chlorite, in this order. Plagioclases and amphiboles were scarce and only present in some samples. The volcanic deposits had little amount of sanidine (Fig. 4.2).

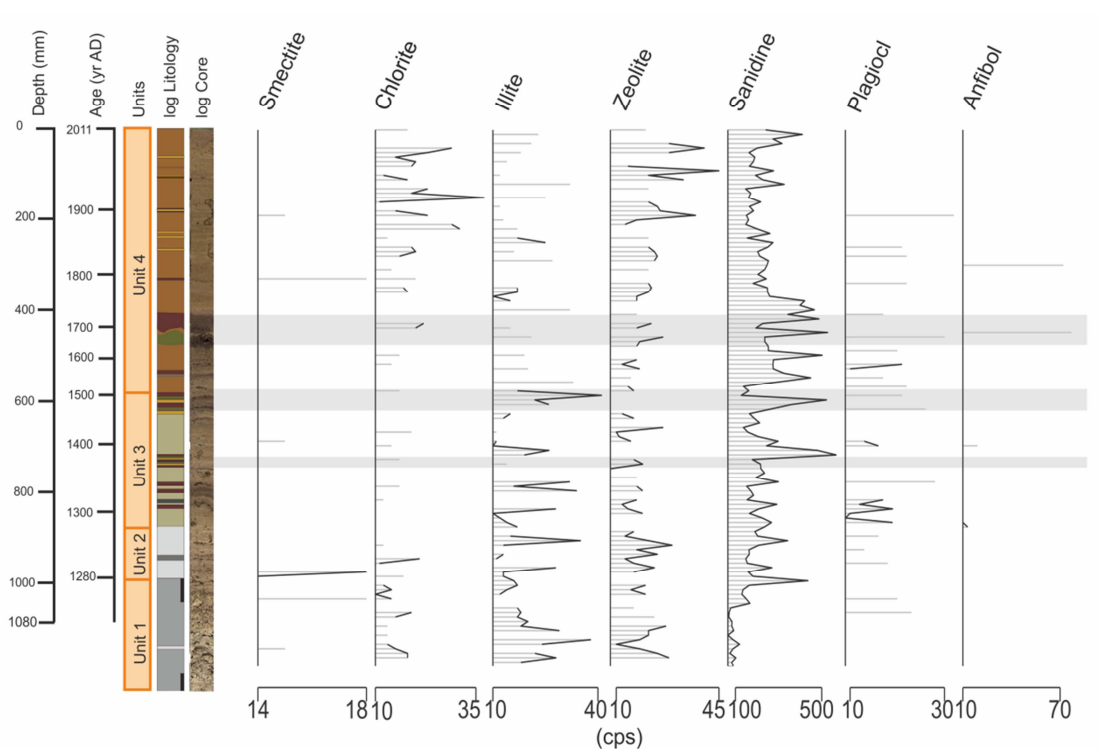


Figure 4.2: Main mineral components of Azul Lake sequence (core AZ11-02) expressed in counts per second (cps). Age, lithological units, facies and a high resolution picture of the core are included. The grey horizontal bars refer to flood events deposits (facies D) that range from brown silt to very fine sand with large amount of plant remains and high porosity. Note that sanidine is the most abundant and continuously mineral.

The sanidine fraction oscillated between 65 and 568 cps. The sanidine relative abundance remained low from the bottom to the 1000 mm with values between 65 and 160 cps. From this point to the 400 mm, the relative amount was greater than in

the previous part recording values between 130 and 530 cps. From the 400 to 180 mm, the sanidine decreased as the amplitude of fluctuation did. This section displayed values between 260 and 400 cps. From this point upwards, the sanidine concentration followed an increasing trend that went from 200 to 400 cps.

The percentage of zeolite from the total crystalline fraction oscillated between 8 and 45 cps. These relative counts were 10 times lower than sanidine. Zeolite had a decreasing trend from the bottom to the 1000 mm that went from 30 to 20 cps. From this point to the 200 mm, the concentration remained relatively low despite some peaks with mean values around 17 cps. Finally, the uppermost 200 mm showed an increasing upwards trend that went from 17 to 40 cps.

The illite cps went from 10 to 41 but, more than the 40% of the samples did not contain illite. The illite relative amount was greatest from the bottom to the 500 mm with a mean value around 20 cps. From the 500 mm upwards, the illite had less presence and the percentage decreased to a mean value ca. 20 cps.

The chlorite amount was between 10 and 37 cps but, more than the 50% of the samples did not have this mineral compound. The chlorite was more abundant from the 500 mm to the top with a mean value around 20 cps. This mineral appeared as a substitute for the illite at the upper part of the core AZ11_02.

The plagioclases content oscillated between 9 and 32 cps. Plagioclases were scarce but distributed from top to bottom. The presence of this mineral was more prominent from 800 to 400 mm, but the mean value (90 cps) remained constant for the entire profile.

The smectite relative abundance oscillated between 14 and 18 cps but, there were only seven samples containing this mineral in the AZ11_02 profile. From these seven samples, 4 were located below 980 mm and the other 3 were dispersed between 900 mm to the top. The mean value (15 cps) remained stable for the entire profile.

The amphibole relative cps went from 10 to 77 but, this mineral appeared only in four samples. From those samples, the 50% (which means 2 samples) were located from 900 to 580 mm.

X-Ray Fluorescence (XRF)

The XRF data were analyzed for the core AZ11_02 from top to the 1086 mm and AZ11_14 from top to the 1478 mm.

AZ11_02

For the core AZ11_02, the highest values were observed for the K with a mean value of ca. 68600 cps and the minimum values were observed for the Sr with a mean value of ca. 3270 cps (Fig. 4.3).

The Al displayed values between 60 and 9890 cps with a mean value of 3820 cps. From bottom to the 800 mm, the profile showed the highest values with a mean of 6450 cps. The sections with XRF lowest values (near 0 cps) were associated to deposits that range from brown silt to very fine sand grain size with large amount of plant remains and high porosity. From 800 to 400 mm, the XRF data displayed high fluctuations between 60 and 7310 cps. From 400 mm to the top, the XRF values were more stable displaying a mean of around 3190 cps.

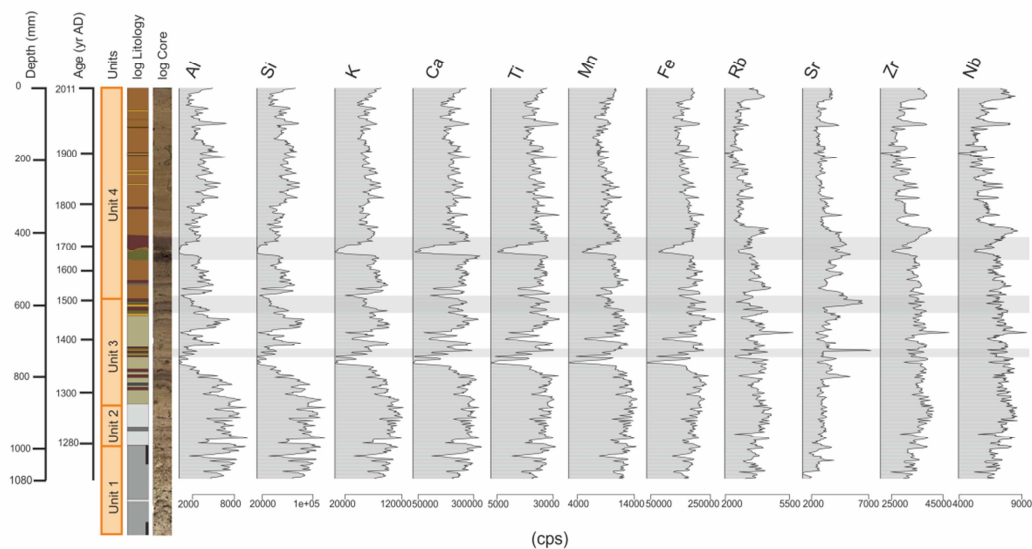


Figure 4.3: XRF geochemical elements analyzed in Azul Lake sequence AZ11-02 expressed in counts per second (cps). The grey horizontal bars refer to flood events deposits (facies D) that range from brown silt to very fine sand with large amount of plant remains and high porosity. Note that the most abundant elements are Si, K, Ca, Ti, Fe, and Zr. Also note that the coarse material and the high porosity in flood events deposits diminish greatly the counts values of all elements except for the Sr.

Si profile showed values between ca. 11600 and ca. 120000 cps and similar characteristics than Al. The highest values were also found from bottom to 800 mm

with mean values around 85132 cps. Values near 0 cps were also related to deposits that ranged from brown silt to very fine sand with large amount of plant remains and high porosity. From 800 to 400 mm, the values displayed a great oscillation that went between ca. 11600 and ca. 86400 cps. The uppermost part of the record (from 400 mm to top) the values became more stable displaying a mean of 52860 cps.

K showed similar evolution patterns than Al and Si but, the values oscillated between ca. 2160 and ca. 122870 cps and the mean value was ca. 68610 cps. The cps values from the bottom to 800 mm of the core depth were the highest with a mean of ca. 92900 cps. The values near 0 cps were associated to deposits that range from brown silt to very fine sand with large amount of plant remains and high porosity. The highest oscillation was found from 800 to 400 mm with values between ca. 2160 and 99040 cps.

The Ca cps values oscillated between 2630 and 33490 and showed a mean values profile of 22250 cps that did not change along the profile except for the points related to deposits that range from brown silt to very fine sand with large amount of plant remains and high porosity.

Ti displayed similar pattern than Ca, with its mean value ca. 22800 cps and range between ca. 2200 and ca. 32780 cps.

The Mn values oscillated between 2470 and ca. 14530 cps with a mean value of 10250 cps. From bottom to 850 mm of the sedimentary record there was an increasing trend that went from ca. 12000 to ca. 13500 cps. This increment was followed by a rapid decrease from 850 mm to 780 mm that went from 13500 cps to 2000 cps. From 780 mm to 400 mm was observed that the values were between ca. 2470 and ca. 13080 cps. From 400 to 100 mm, it was observed a decreasing trend from ca. 11000 to ca. 7500 cps. And from 100 mm to the top of the record Mn data displayed an increasing trend that went from ca. 7500 to ca. 10700 cps.

The Fe values went from ca. 36290 to ca. 266340 cps with a mean value of ca. 178900 cps. From bottom to 650 mm of core depth the profile showed an increasing trend that went from ca. 176400 to ca. 235500 cps, except for the values associated to deposits

that range from brown silt to very fine sand with large amount of plant remains and high porosity. From 650 mm to the 40 mm of the record the values decreased from 235500 to 134500 cps whereas from 40 mm to the top of the sequence the Fe profile showed an increasing trend from ca. 134500 to ca. 192500 cps.

The Rb values went from ca. 1960 to ca. 5700 cps with a mean value of ca. 3390 cps. The Rb profile showed the highest values from the bottom of the core to 390 mm of core depth with mean values around ca. 3670 cps. From 390 mm to 50 mm of the sequence, the Rb profile showed the lowest values with a mean situated ca. 2780 cps. From 50 mm to top of the record there was an increasing trend from ca. 2600 to ca. 3600 cps.

The Sr displayed values between ca. 1200 and ca. 7220 cps with a mean value of about 3270 cps. The Sr profile showed an increasing trend from bottom of the core to 600 mm of core depth with values that oscillated between ca. 1800 and ca. 6400 cps. From 600 mm to 450 mm of core depth, the Sr showed the highest values (6500 cps) with a mean of ca. 4170 cps. From 450 to 50 mm of the record, the Sr profile showed the lowest values with a mean of 2920 cps. From 50 mm to the top, strontium values had an increasing trend from ca. 2400 to ca. 3500 cps.

The Zr profile had a mean value of ca. 33250 cps that oscillated between ca. 20680 and ca. 47380 cps. From the bottom of the core to 900 mm of core depth there was an increasing trend from ca. 2900 to ca. 4100 cps. From 900 to 450 mm of core depth there was a decreasing trend that went from ca. 4100 to ca. 2500 cps. There was a decrease associated to deposits that range from brown silt to very fine sand with large amount of plant remains and high porosity from 450 to 400 mm followed by a rapid increase to around 40000 cps. From 400 to 50 mm of core depth, the Zr profile had the highest values that went between ca. 20000 and ca. 40000 cps. From 50 mm to the top of the core there was an increasing trend from ca. 2800 to ca. 3600 cps.

The Nb profile had a mean value of ca. 6860 cps that oscillated between ca. 3940 and ca. 9400 cps. Its evolution was rather similar than the Zr profile.

Core AZ11_14

For the core AZ11_14, eight chemical elements had been identified (Fig. 4.4).

The K profile displayed values between 74 and ca. 5500 cps with a mean of 2930 cps. This profile also showed a long-term upwards decreasing trend with sudden decreases associated to deposits that range from brown silt to very fine sand grain size with large amount of plant remains and high porosity. From 1200 to 1000 mm and from 500 to 250 mm of core depth there were an increase in the K profile, with mean values of 4050 and 3600 cps, respectively.

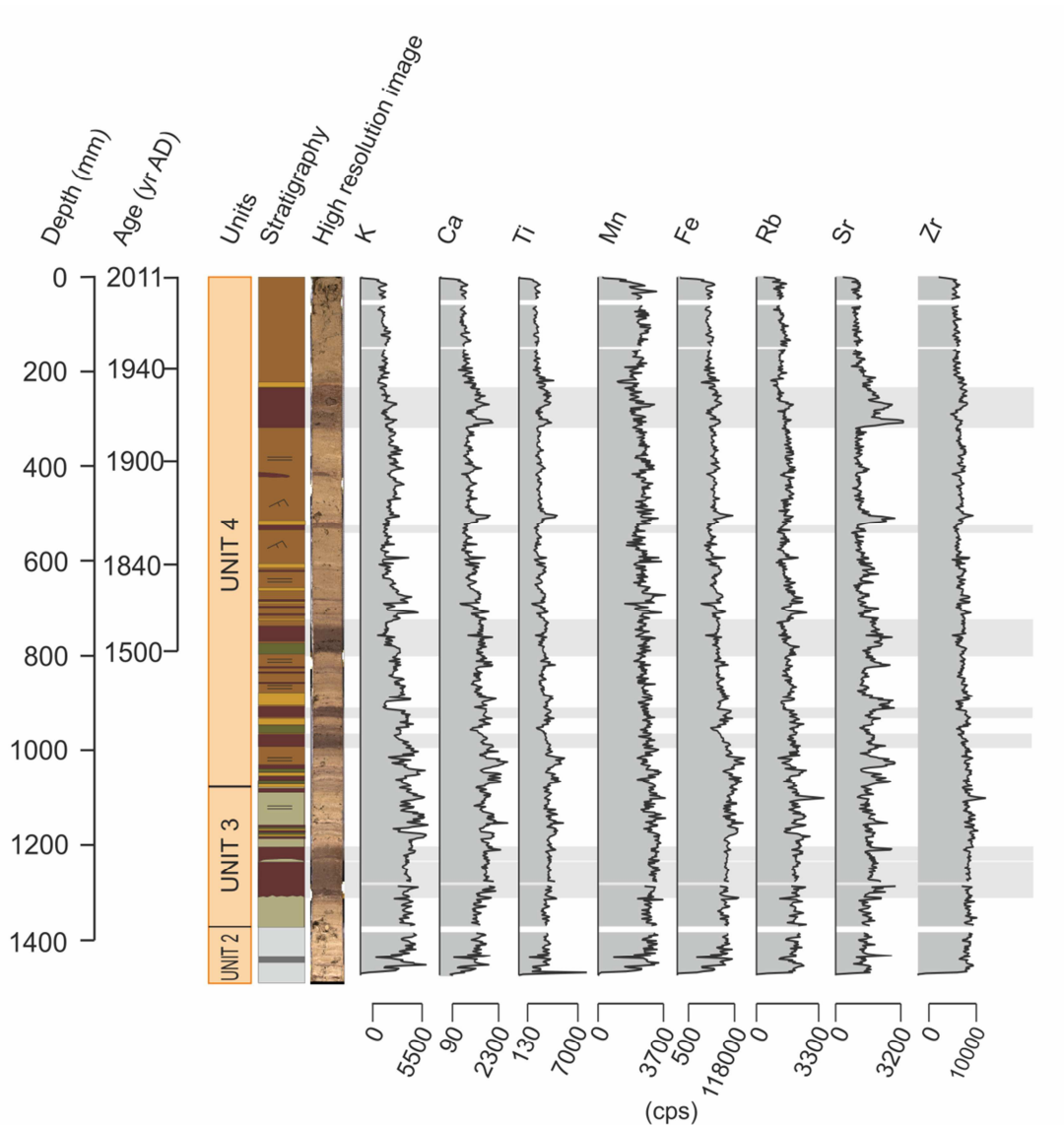


Figure 4.4: XRF geochemical elements analyzed in Azul Lake sequence (core AZ11-14) expressed in counts per second (cps). Sequence of elements shows no clear modification while flood events deposits.

The Ca values oscillated between ca. 80 and ca. 2290 cps with a mean value of ca. 1280 cps. The trends of this chemical element was similar that described for K. The maximum values of Ca were observed from 1200 to 1000 mm and 250 mm with mean values of ca. 1660 and ca. 1200 cps, respectively.

The Ti profile showed values that ranged between ca. 130 and ca. 6890 cps, with a mean value of about 2580 cps.

The Mn values did not have significant changes along the profile. The mean value of this chemical element was ca. 2480 cps and it oscillated between near 0 cps and ca. 3640 cps. The values near 0 cps were found at the top and bottom of the core. This pattern was observed for other elements.

The Fe profile showed a mean value of ca. 72480 cps, with variations between ca. 540 and ca. 118450 cps. The lowest values were observed at the top and base of the core as for the Mn profile. From bottom to 1000 mm of core depth, the profile displayed an increasing trend from ca. 35110 to ca. 85350 cps. From 1000 mm to the top of the sedimentary record there was a decreasing trend from ca. 85350 to ca. 34150 cps.

The Rb profile displayed values between 0 at both extremes of the core and ca. 3280 cps, with mean values around ca. 1570 cps. From bottom of the record to 600 mm of core depth the Rb values were around 1700 cps whereas from 600 mm to the top of the record the mean values of this chemical element were around 1340 cps.

The Sr profile showed values that ranged from 0 at both ends of the core to ca. 3140 cps, with a mean value of 1450 cps. There were not significant trends or oscillations but some peaks were observed at 1000, 900, 750, 500 and 250 mm of core depth with values higher than 3000 cps.

The Zr profile had a mean value of about 7730 cps, not displaying significant trends or variations along the profile.

Total Organic Carbon, Total Nitrogen and their stable isotopes ($\delta^{13}\text{C}$, $\delta^{15}\text{N}$) on bulk organic matter.

Total Organic Carbon (TOC) percentages were greater in core AZ11_14 (from 1 to 6 % wt) than in AZ11_02 (with values from 0.5 and 3.5 % wt). The Total Nitrogen (TN) percentages were also greater in core AZ11_14 (values from 0.1 to 0.6 % wt) than in AZ11_02 (from 0.05 and 0.35 % wt). Both, AZ11_02 and AZ11_14 records displayed a TOC and TN long-term increasing upwards trend.

The $\delta^{13}\text{C}$ values range was between -27 ‰ and -22 ‰ for both cores. The $\delta^{15}\text{N}$ values were lighter in core AZ11_02 (between 0 ‰ and 3 ‰) than in AZ11_14 (between 1.5 and 4 ‰). $\delta^{13}\text{C}$ depleted on dark brown silts to very fine sand deposits with great amount of plant remains and high porosity for both cores. On the contrary, $\delta^{15}\text{N}$ values had different response on those deposits. In AZ11_02, the $\delta^{15}\text{N}$ was depleted for those layers; and, in AZ11_14 showed enrichment.

The TOC/TN ratio varied from 5 to 20 for AZ11_02 whereas it oscillated from 8 to 16 for the core AZ11_14.

Based on Meyers (2003), the $\delta^{13}\text{C}$ was plotted against TOC/TN for the core AZ11_02 (Fig. 4.5) and AZ11_14 (Fig. 4.6). Both figures demonstrated that the organic matter contained on the sediment is mainly from algal origin. AZ11_02 profile showed organic matter from terrestrial (C_3 plants) origin but, AZ11_14 did not show this terrestrial plant signal for the section analyzed.

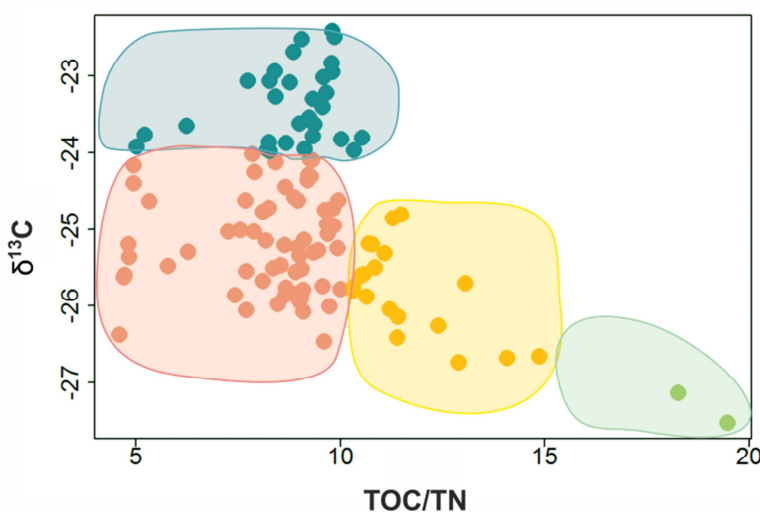
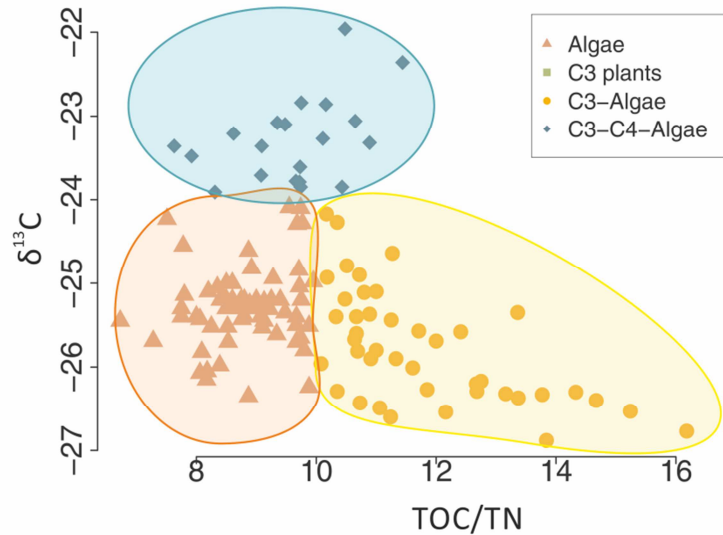


Figure 4.5: Graph of the $\delta^{13}\text{C}$ values against TOC/TN ratio for the AZ11-02 sequence. This figure highlight the metabolic pathways based on Meyers (2003). On turquoise are presented values from a mix between C_4 plants and Algae composition, the light red color showed values of Algae composition, the yellow color corresponds to values of a mix between C_3 plants, and the green color showed a C_3 plants composition. Note that the major part of the sediment is composed of Algae.

Figure 4.6: Graph of the $\delta^{13}C$ values against TOC/TN ratio of samples of the core AZ11_14 sequence analyzed samples from top to 775 mm. This figure highlights the metabolic pathways based on Meyers (2003). Turquoise color represents mix values between C4 plants and Algae composition, the light red color showed values of Algae composition and the yellow color corresponds to values of a mix between C3 plants. Note that the C3 plants composition did not appear on this figure because from top to 775 mm of the core AZ11_14 there is only one flood event that has no porosity or plants remains. Therefore, this flood event seems to be less intense than those events found on AZ11_02.



Core AZ11_02

In the core AZ11_02, TOC profile increased from 0.05 to 3.5 % wt from the bottom to 100 mm of core depth (Fig. 4.7). Then, a final decrease was observed from 100 mm to the top with values that oscillated between 3.5 and 1.5 % wt. TN values, in turn, increased from the bottom of the record to 100 mm of the sedimentary sequence with values from 0.05 to 0.35 % wt and decreased from 100 mm to top with values that went from 0.35 to 0.15 % wt. AZ11_02 TOC/TN ratio values remained constant around 9 despite some peaks at 750 mm and around 400 mm that reached values around 15 and 12, respectively. The lowest TOC/TN ratio value was observed at the bottom of the core and it was around 5.

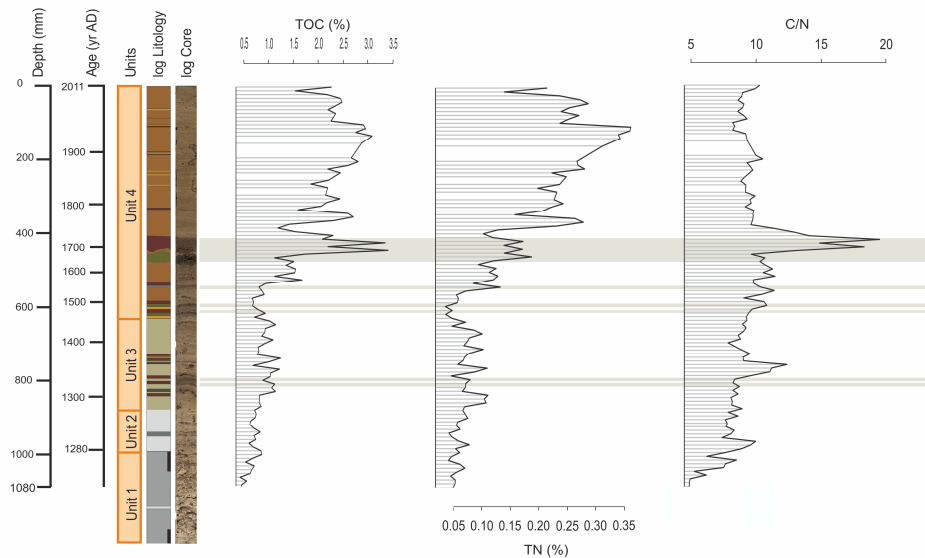


Figure 4.7: Bulk organic composition for the core AZ11_02 sedimentary sequence. The grey horizontal bars refer to flood events deposits (facies D) that range from brown silt to very fine sand with large amount of plant remains. Note that TOC (%) is rich on flood events layers with plants remains

The $\delta^{13}\text{C}$ values in core AZ11_02 showed enrichment from the bottom to 840 mm of core that went from -26.5 to -23.5 ‰ (Fig. 4.8). This enrichment was followed by depletion from 840 to 790 mm that went from -23.5 to -26 ‰. After that, a rapid enrichment was observed from 790 to 700 mm that comprised values between -26 and -23.5 ‰. The profile showed depletion from 700 mm to 400 mm with values between -23 and -27 ‰. This depletion was interrupted by a rapid enrichment that went from -26 to -24.5 ‰ from 600 mm to 550 mm. After a small enrichment from 400 to 350 mm with values from -27 to -22.5 ‰, the profile remained stable from 350 to 100 mm with mean values around -24‰. The upper 100 mm displayed an enrichment trend that went from -23 to -25.5 ‰. The $\delta^{15}\text{N}$ profile overall followed an upward trend of depletion with values from 2.5 to 0.0 ‰. This trend was interrupted by sudden enrichments right after dark brown silt to very fine sand deposits with great amount of plant remains and high porosity with variable mean values.

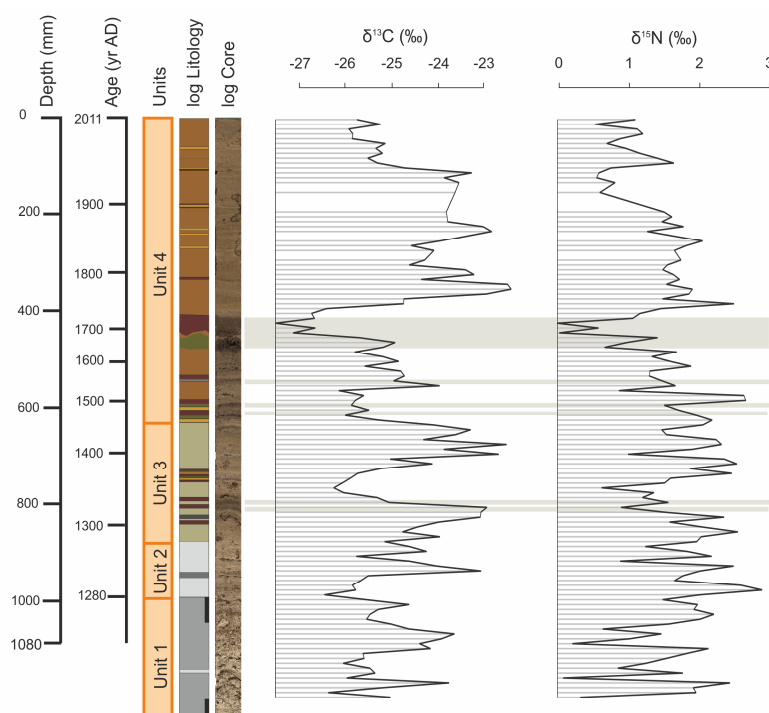


Figure 4.8: Bulk isotopic composition $\delta^{13}\text{C}$ and $\delta^{15}\text{N}$ for the core AZ11_14 sequence. The grey horizontal bars refer to flood event deposits (facies D) that range from brown silt to very fine sand with large amount of plant remains and high porosity. Note that the $\delta^{13}\text{C}$ and $\delta^{15}\text{N}$ decrease on flood events.

Core AZ11_14

For the core AZ11_14, TOC followed a long-term increasing upwards trend from 1 to 5 % wt as well as the TN that also followed an increasing upwards trend from 0.1 to 0.6 % wt (Fig. 4.9). The core AZ11_14 showed important fluctuations in the TOC/TN ratio profile. From bottom to 700 mm of core depth, the TOC/TN decreased from 12 to 8 while from 700 to 600 mm of the sedimentary record, an increasing trend was observed with values between 8 and 10. From the 600 to the 400 mm, the profile displayed a decreasing trend that went from 10 to 8. The highest values of AZ11_14 TOC/TN profile were observed from 400 to almost 200 mm with values that oscillated between 10 and 16. From 200 mm to the top of the record a decreasing trend was

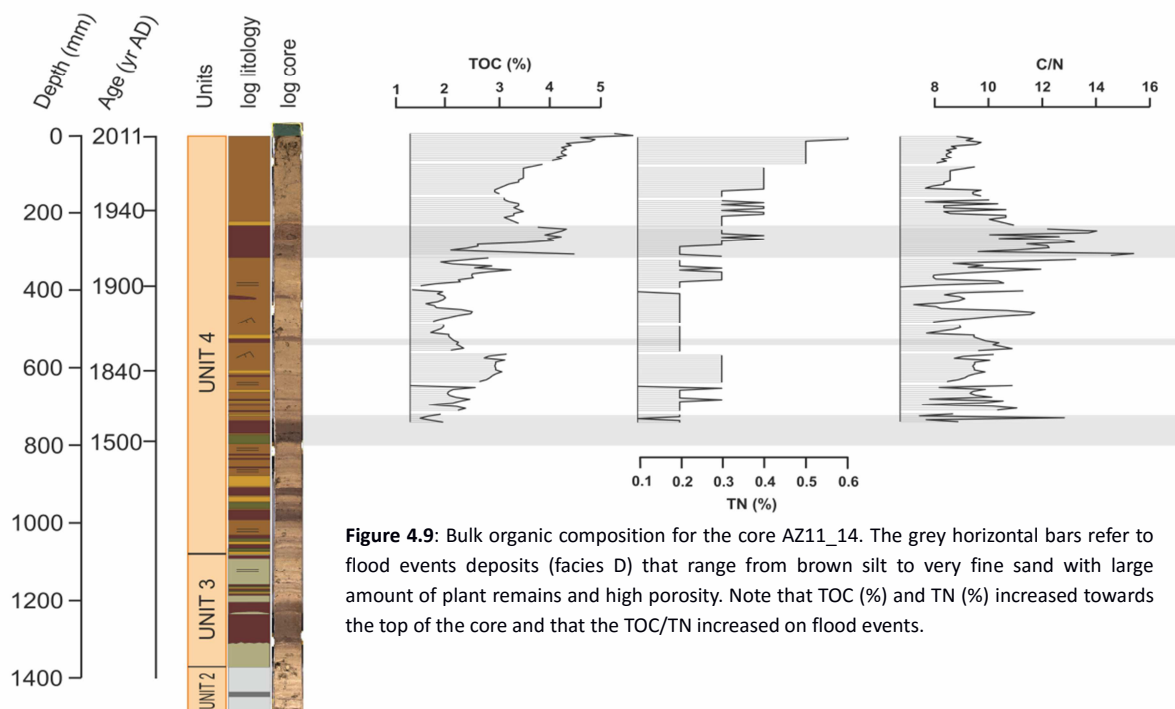
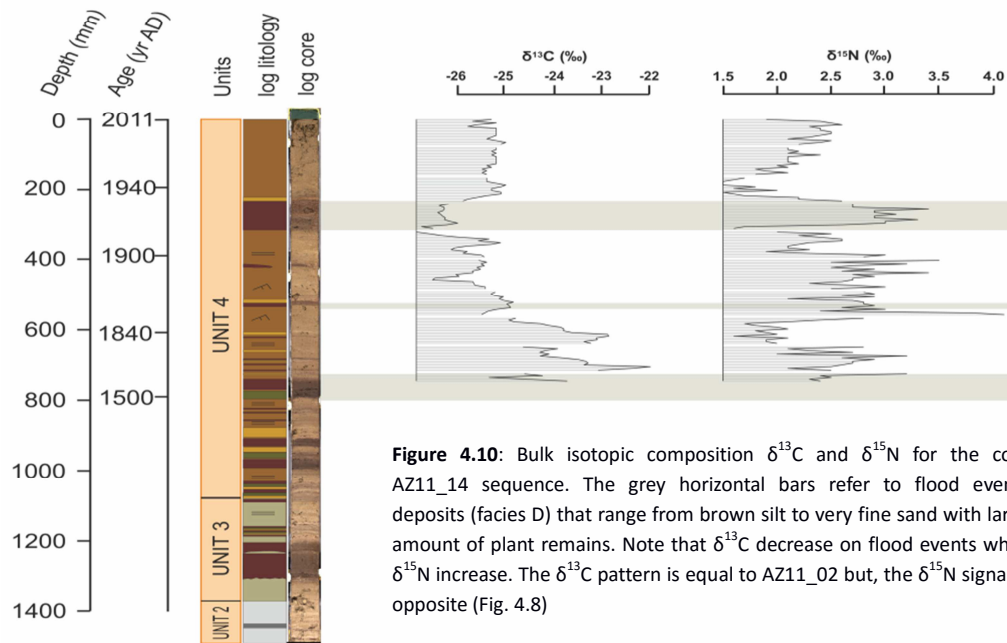


Figure 4.9: Bulk organic composition for the core AZ11_14. The grey horizontal bars refer to flood events deposits (facies D) that range from brown silt to very fine sand with large amount of plant remains and high porosity. Note that TOC (%) and TN (%) increased towards the top of the core and that the TOC/TN increased on flood events.

AZ11_14 $\delta^{13}\text{C}$ profile displayed a trend of depletion from 740 mm to 350 mm that went from -22 to -26.5 ‰ whereas from 350 to 200 mm, there was an enrichment trend from -26.5 to -25.5 ‰ (Fig. 4.10). From 200 mm to the top of the core, the $\delta^{13}\text{C}$ values remained stable at around -25.5 ‰. Between 740 and 600 mm of core depth the $\delta^{15}\text{N}$ profile showed a depletion trend from 3 to 1.5 ‰. Later, a small enrichment between 1.5 and 3.5 ‰ was observed from 600 to 580 mm. The $\delta^{15}\text{N}$ profile remained stable

from 580 to 400 mm with a mean value around 2.6 ‰. From 400 to 180 mm, a long-term depletion trend was observed with values between 2.6 and 1.5 ‰. Finally, the uppermost 180 mm of the sedimentary record showed a general enrichment from 1.5 to 2.5 ‰.



Diatoms

The diatom counts for the core AZ11_02 were performed by David Vazquez Loureiro at the Universidade da Coruña (Fig. 4.11). A total of 29 diatom taxa were observed 2 of these taxa were euplanktonic (*Aulacoseira ambigua*, *Aulacoseira granulate*), 6 facultative (*Disco Stella woltereckii*, *Nitzschia gracilis*, *Pseudostaurosira brevis triata*, *Pseudostaurosira eliptica*, *Staurosira mutabilis* and *Tabellaria flocculosa* morph 1), and 21 benthic taxa (*Achnanthis minutissimum*, *Adieta minuscula* var *muralis*, *Diadsmis contenta*, *Diadsmis perpusilla*, *Diploneis oblongella*, *Diploneis ovalis*, *Encyonopsis* spp. att. *Cesatii*, *Eolimna* sp1, *Eolimna* sp2, *Eunotia implicate*, *Fragilaria cappucina*, *Navicula notha*, *Nitzschia lacuum*, *Nitzschia perminuta*, *Nitzschia pseudofonticola*, *Nitzschia veldestriata*, *Planothidium* sp., *Psammothidium abundans* f. *rosenstockii*, *Rossidium pusillum*, *Stauroforma exiformis* and *Staurosira pseudoconstruens*). According to their living conditions, the diatom distribution in this core can be subdivided in three zones. From the bottom of the core to the 900 mm, almost the 100 % of the diatoms were

from the benthic taxa. From the 900 mm to the 580 mm of the core depth, the 50% of the taxa were benthic and the other 50 % were facultative. From the 580 mm to the top, the percentage of euplanktonic taxa increased from around 0 % to 60 % whereas the facultative taxa changed from the 50 % to the 20 %, and the benthic taxa decreased from the 50 % to around 20 %. Those changes might indicate that the lake has become progressively deeper from its origins to the present day.

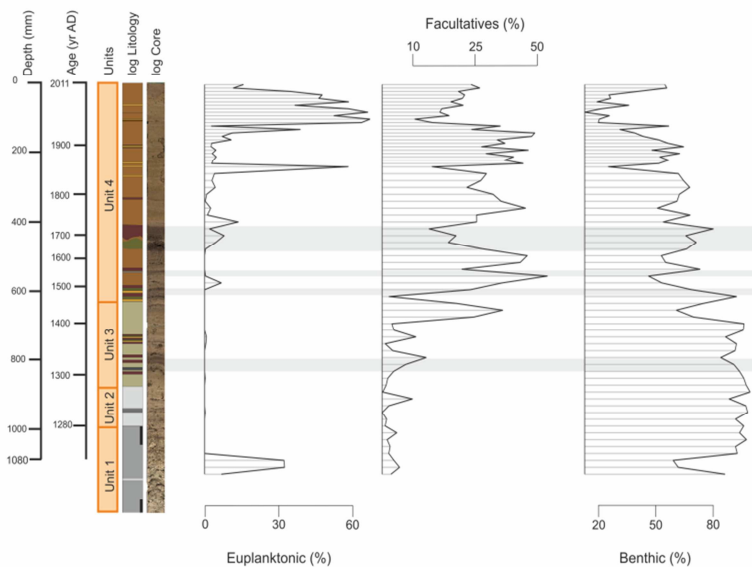


Figure 4.11: Diatom composition of the core AZ11_02. Those data were acquired by David Vazquez Loureiro (PhD, work in progress). The grey horizontal bars refer to flood events deposits (facies D) that range from brown silt to very fine sand with large amount of plant remains. Note that the lake was shallower in the top of Unit 1 than in the top of the sequence.

Chironomids

The chironomids head capsules for the core AZ11_02 were analyzed by Dr. Pedro M.V. Raposeiro from the Universidade dos Açores, Portugal (Fig. 4.12). The variation on head capsule counts went from 0 to 127 heads/cm³. A total of 18 Chironomidae taxa were observed and distributed in 14 genera and 3 subfamilies. The dominant taxa were *Microsetra contracta*-type (84% of occurrence), *Psectrocladius sordidellus* (67 %) and *Micropsectra* type A (64 %) while the subdominant taxa were *Polypdeditum nubifer*-type (51%), *Macropselepi*-type (48%) and *Chironomus plumosus*-type (43%). A significant peak on *Tanytarsine* species occurred around 360 – 350 mm of core depth with values that reached 98 heads/cm³. The total number of head capsules oscillated between 0 and 20 head/cm³ of dry sediment from the bottom to the 1000 mm of the core depth while from 1000 to 360 mm, the chironomids head capsules showed an increasing trend from 20 head/cm³ to 120 head/cm³. This increase on head capsules

culminated with the peak at 360 mm mainly produced by the gender *Tanytarsine*. From 360 mm to the top of the record, the number of head capsules was lower than for the previous sections and oscillated between 10 and 20 head/cm³ of dry sediment. This decrease was produced by the fishes introduction.

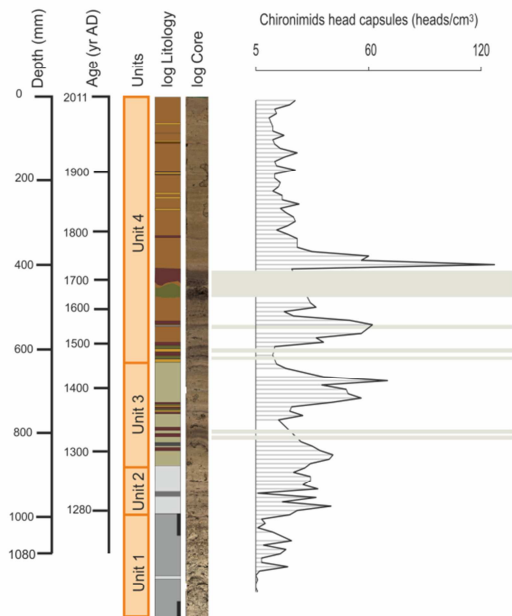
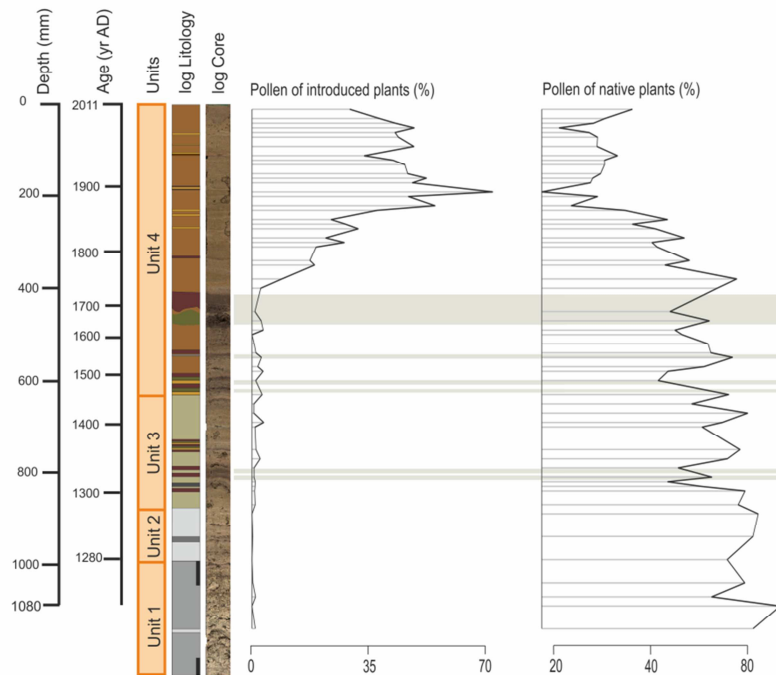


Figure 4.12: Total chironomid head capsules in heads/cm³ of the core AZ11_02. Those data were obtained by the Dr. Pedro Raposeiro (work in progress). The grey horizontal bars refer to flood events deposits (facies D) that range from brown silt to very fine sand with large amount of plant remains. Note the decreasing trend of chironomids in the upper part of Unit 4 (see text for more explanation).

Pollen

The pollen was analyzed by Arantzazu Lara Corbacho, Dr. Valentí Rull del Castillo and Dra. Nuria Cañellas Bolta from the Institut de Ciències de la Terra Jaume Almera (ICTJA-CSIC) (Fig. 4.13). A total of 85 species were determined and divided in native (51 species), introduced (13 species) and endemic (21 species). Trees such as *Cryptomeria japonica*, *Morella faya* and *Pinus pinaster* dominated the pollen composition. Shrubs (*Erica azorica* and *Myrsine africana*), herbs (*Poaceae* and *Plantago lanceolata*), *Pteridophyte spores* (*Psilate monoletes*, *Culcita macrocarpa*, *Pteridium aquilinum*, *Pteris incompleta* and *Selaginella kraussiana*) and fungi spores, mainly from coprophilous taxa (*Sporormiella*, *Cercophora*, *Podospora* and *Sordaria*), were also present in the assemblages.

Figure 4.13: Pollen composition of the core AZ11_02. The pollen of Lake Azul was analyzed by Arantazu Lara, Dr. Valentí Rull and Dra. Nuria Cañellas (work in progress). The grey horizontal bars refer to flood events deposits (facies D) that range from brown silt to very fine sand with large amount of plant remains. Note the decreasing trend on native plants presence while an increase of introduced plants in the upper part of Unit 4 (see text for explanation).



From 1130 mm to 740 mm of core depth, the trees, shrubs and ferns were native species except for the *Secale Cerealis* (introduced). From 740 to 230 mm of the sedimentary record, native species such as *Juniperus brevifolia* and *Picconia azorica* disappeared while *Morella faya* and *Juniperus laurifolia* decreased their presence. From 220 mm to top of the core, a drastic decrease was observed in native species (*Erica azorica* and *Myrsine Africana*) whereas introduced species such as *Coprophilaus fungi*, *Myriophyllum alterniflorum*, *Pteridium aquilinum*, *Psilate monolets*, *Secale cereale* and *Plantago lanceolata* also suffered a decline. In contrast, other introduced species such as *Morella faya*, *Pinus pinaster*, *Cryptomeria japonica*, *Alnus*, *Olea europaea*, *Hydrangea macrophylla* observed an increase.

The charcoal content oscillated between 0 and 1500 particles/g of dry sediment from the bottom of the core to the 400 mm. From the 400 mm to the top the charcoal content increased significantly, with values that ranged between 2000 and 7000 particles/g of dry sediment (Fig.4.14).

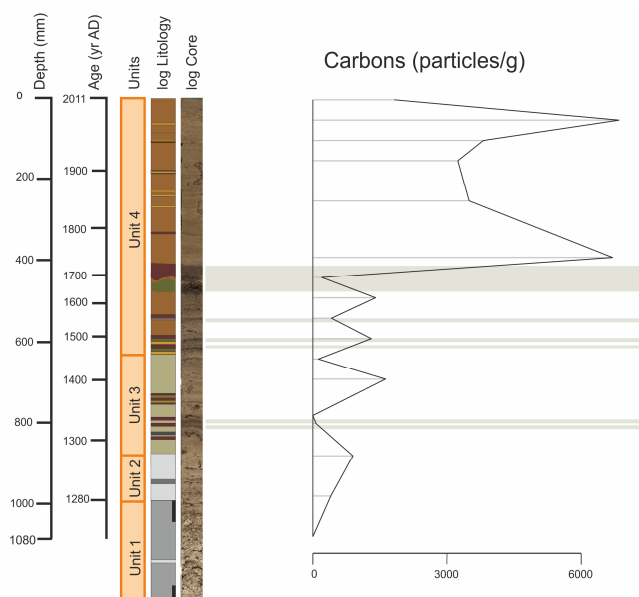


Figure 4.14: Charcoal composition for the core AZ11_02. The charcoal of Lake Azul was analyzed by Arantazu Lara, Dr. Valentí Rull and Dra. Nuria Cañellas (work in progress). The grey horizontal bars refer to flood events deposits (facies D) that range from brown silt to very fine sand with large amount of plant remains. Note the increasing trend in the upper part of Unit 4 (see text for explanation).

The morphology of the littoral line of Azul Lake was conditioned by: (a) the internal vent abrupt slope of the main Sete Cidades Caldera forming the convex NE littoral zone of the lake, (b) the volcanic vents emerged in two sectors of the lake with concave morphology (Caldeira do Alferes to the NW and lake Santiago vent to the SE), (c) the occurrence of one deltaic system in NE (Cerrado das Freiras) forming a delta plain, and (d) the existence of an alluvial plain expanding from SW to NE in Sete Cidades village coast and other, less developed, alluvial plain at the NW sector of the lake (Fig. 4.15).

Echo sounding (Fig. 4.16) and seismic data (Fig. 4.17) showed a number of morphological areas from bottom surface and subsurface geological structures in the lake. The tectonic structure is mainly configured by the NW-SE orientation of the Mosteiros graben faults family system (Moore, 1991). From the SW to the NE four main morphological units could be distinguished: (1) a shallow platform-ramp (from 0 to 12 meters depth) that occupied the southern half part of the lake, which corresponded to a raised block of the graben; (2) a slope-rise zone (from 12 to 25 m depth) dipping to the NE that occupies a little less than a third of the lake surface, and which corresponded to the slope formed by a normal fault plane; (3) a deep plain, from 25 to 27 m of water depth, which belonged to the upper surfaces of a fall block of the graben, and which covered a little more than the third part of the lake surface, and (4) a very dip slope, between 27 and 0 m of water depth, which follows the internal vent slope of the main caldera vent, forming a narrow nearshore belt in the NW shore of the

lake and which was occupied by large blocks from rock avalanches (not cored). Two circular submerged and partial submerged crater structures in the lake could be recognized in NW extreme of the deep plain and in the narrow connection with Verde Lake respectively.

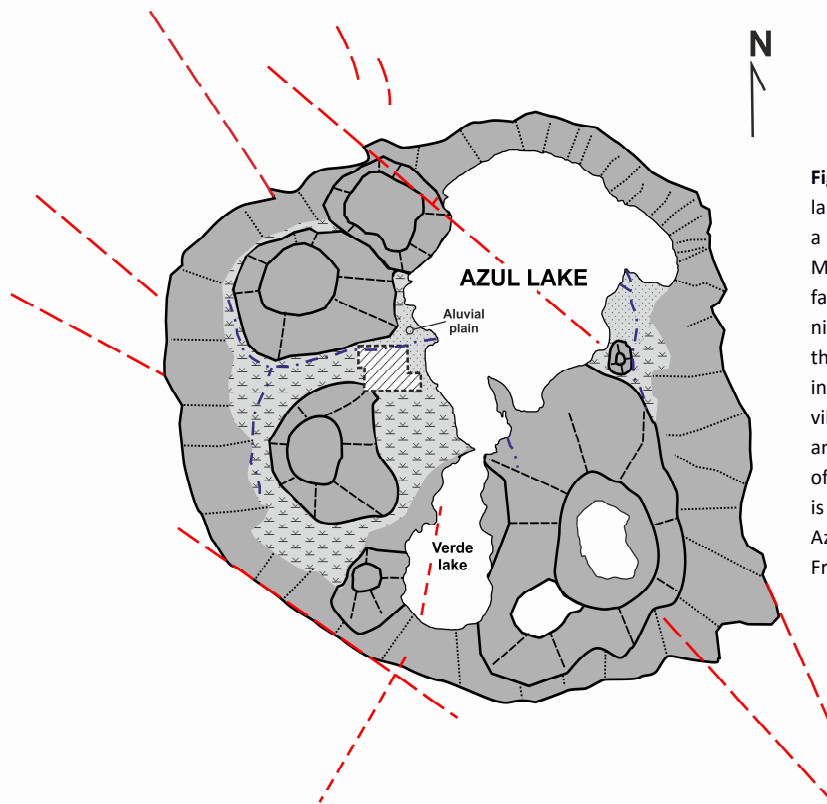
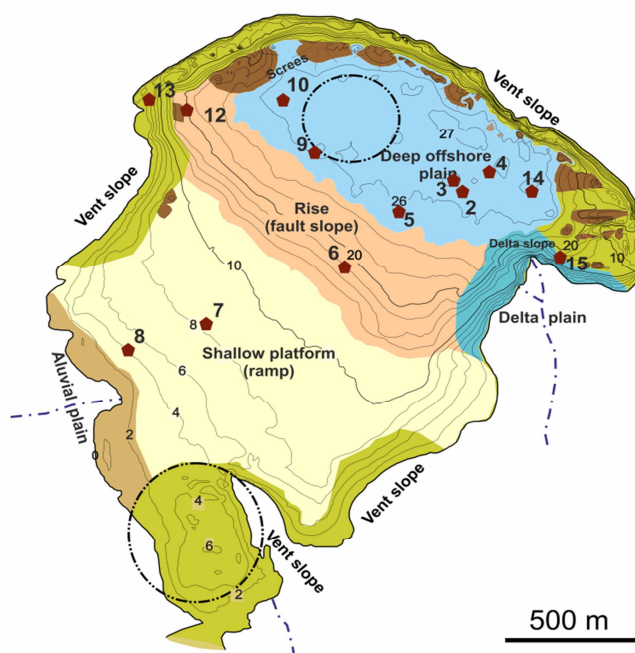


Figure 4.15: Catchment environments for lake Azul. The red line that usually follows a NW-SE orientation corresponds to the Mosteiros Graben and the subsequent faults. The catchment area is composed by nine craters (two of them are not visible in this picture because they are submerged in lake Azul and Verde). Sete cidades village is located between Caldeira Alferes and Caldeira Seca just in the alluvial plain of the west coast of the lake. A delta plain is observed in the eastern side of Lake Azul bringing water from Cerrado das Freiras.

The NE ends of the seismic profile 2 (Fig. 4.17) shows that the strait connection between Lake Azul and Lake Verde is built by a small crater subbasin structure threshold. This crater structure continues to the S with the shallow platform-ramp that changed abruptly to the deep plain by a normal fault that crosses the lake in a NW-SE direction. Seismic profile (Fig. 4.17) also shows as the lacustrine deposits above the volcanic-lacustrine Unit 1 (described below) was thicker in the deep off-shore plain than in the other sedimentary environments. The deep plain located at the north caldera wall foot has been zoomed and it showed that there was a low-degree downlap of lacustrine deposits of units 2 to 4 (described below) on the volcanic-lacustrine deposits of unit 1. This occurred between the position of the cores AZ11_02 and AZ11_03, and the position of the cores AZ11_05 and AZ11_09 (Fig. 4.19).

Figure 4.16: Sete Cidades Caldera and Lagoa Azul bathymetry. Tectonic structures and main sedimentary lake sub-environments are also represented. Circles indicate submerged or partially submerged crater subbasins. Observe that the tectonic graben blocks conditioned the lake topography and the lake sedimentary subenvironments distribution.



The characterization of the sedimentary infill was realized from the fifteen cores retrieved (Fig. 4.19). Most of the cores reached a hard volcanic unit, including those in offshore zones. Four lithological units and nine litofacies have been defined mainly based on grain-size, color, texture, mineralogy, geochemical composition, biological contents and sub-environmental location (Table 4.1). These facies were grouped in five facies associations: deep plain fine deposits (including facies A, B, C, D and E), shallow platform-ramp fine deposits (facies F), deltaic coarse deposits (facies G), alluvial, non-lacustrine coarse deposits on the ramp (facies H), and rock avalanche scree very coarse deposits on the caldera slope lake margin (facies I). Sediments retrieved from the platform-ramp, deltaic deposits, littoral alluvial plain areas and/or avalanche scree deposits contained coarse material with diverse origin (terrestrial and lacustrine) and non-mature textures that could difficult analytical results (i.e. XRF core scanner or ^{14}C AMS dating). In order to avoid these problems, the sedimentary records analyzed in detail in this work belonged to offshore-deep plain environment, which contained fine material adequate for the analytical process. The deep plain facies were further described in the present chapter and the facies located in other sub-environments are represented in figure 4.19.

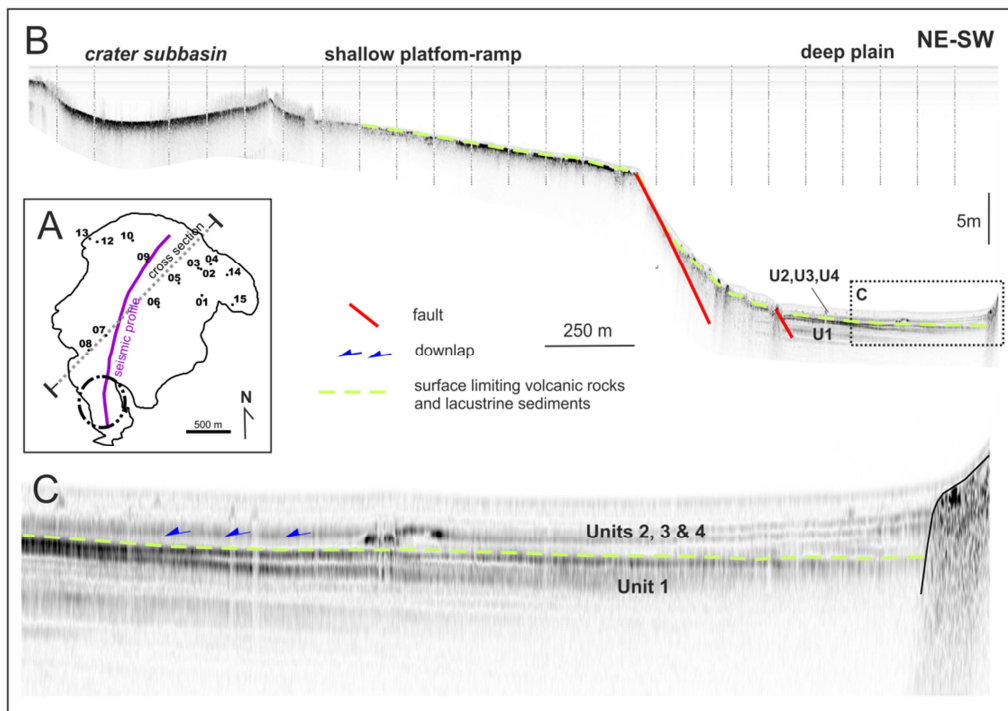


Figure 4.17: (A) Lake Azul map showing position of the 15 cores retrieved and the seismic profile (purple). (B) NE-SW seismic profile. This profile crossed through the crater subbasin, the shallow platform ramp and the deep plain. Lithological units are interpreted from seismic facies. (C) Detailed image of the northeastern sector of the seismic profile. Observe downlap relation (blue arrows) between units 2, 3 and 4 on the lacustrine- and the volcanic unit 1.

Facies description

Facies A_(deep plain silts).- Facies A was composed of brown massive fine sands and silts forming layers from 20 to 50 mm in thickness. TOC values ranged between 0 and 2 % wt while TN fluctuated between 0.1 and 0.36 % wt. The isotopic composition varied from -27 to -22 ‰ for $\delta^{13}\text{C}$ and between -0.02 and 2.6 ‰ for $\delta^{15}\text{N}$. TOC/TN atomic ratio varied from 7 to 10, indicating that the organic matter was rich in algae and aquatic plant remains. Facies A was the most abundant sediment type recorded on offshore zones (cores 2, 3, 4, 5, 14, 12) and it prevailed in the uppermost part of the lake sequence (Unit 3, Fig. 4.19). This facies can be interpreted as deposited by decantation of the fine sediment transported by runoff currents generated during regular precipitations in the catchment as suspended material in relative deep lake areas. The transport of these fine sediments within the lake would be favored by occurrence of nepheloid layers over the thermocline.

FACIES TYPES	FACIES	UNIT	FACIES DESCRIPTION	DIATOM LIVE GROUP	SEDIMENTARY PROCESSES AND PALEOBATHIMETRY
Continuously sedimented lake deposits (Facies Co)	Facies A	4	Brown, massive, sandy fine-medium silt Layers 2 – 10 cm thick	planktonic diatoms (ticoplankton and euplankton)	Deposited by decantation of the suspended fine particles in deep lake conditions
	Facies B	4	Light brown, sandy fine silt Rich in volcanic glass particles (shards) Layers 0.1 - 1 cm thick.	Not enough information	Deposited by decantation of the suspended fine particles incorporating ash fall-out particles during weak or distal eruptions phases
	Facies C	3	Brown greenish laminated fine to coarse silts. Layers 2 – 10 cm	Benthic diatoms	Deposited by decantation of the suspended fine particles in shallower lake conditions
	Facies E	2	Grey laminated silty sand	Scarce benthic diatoms	Deposited in shallow lake conditions from currents transporting volcanic ash deposits accumulated from local eruptions in the catchment
Rapid to instantaneous lake deposits (Facies Ra)	Facies D	3 - 4	Dark brown silts to very fine sand rich in terrestrial plant remains Layers 6.2 - 4 cm thick	Barren or very few diatoms	Deposited in lobe bodies from hypopycnal flashy currents. Any deep.
	Facies V	1	Tephra layers	Scarce or very few diatoms	Deposited by fallout from explosive eruptions that emitted great amounts of lapilli and ash

Table 4.1: Table of the facies observed in the core AZ11_02 and AZ11_14 located in the offshore plain. A total of 6 facies are divided in two types: instantaneous deposits (Facies Ra) and continuously deposited (Facies Co).

Facies B (deep plain silts, rich in volcanic particles).- Facies B was composed of light brown sands and fine silts forming layers from 1 to 10 mm in thickness, showing high XRF values in Ti, Zr, Sr, Al, Fe that indicates large amounts of volcanic terrigenous particles. In fact, SEM observations indicated the presence of volcanic glass in high amounts including well preserved shard particles. This facies have carbon percentages

that ranged between 0 and 2.5 % wt whereas nitrogen percentages are between 0.17 and 0.27 % wt. The isotopic composition is -25 and -22 ‰ for $\delta^{13}\text{C}$ and between 0.08 and 1.74 ‰ for $\delta^{15}\text{N}$. The carbon-nitrogen atomic (TOC/TN) ratio has values that vary between 9 and 13 suggesting that the organic matter comes from algae and aquatic plants. The diatoms presented on this facies are micoplankton and euplankton taxa, mainly composed of *Aulacoseira* sp. colonies. The pollen composition is dominated by introduced plants but also, some natives. Facies B was present in the upper part of the offshore core sequence like for facies A. The grain-size and chemical composition of this facies suggested that it was deposited under similar offshore terrigenous conditions than facies A, but the deposition of facies B occurred during periods of volcanic ash eruptions that added glass particles to the sediments by direct fallout and/or by runoff carrying ash-rich sediments previously deposited in the catchment. The presence of high quantities of charcoal and introduced pollen indicates an intense human activity during the sedimentation of this facies.

Facies C (deep plain, greenish silt).- Facies C were made up of brown greenish laminated from fine to coarse silt layers from 20 to 70 mm thick. TOC values were between 0.4 and 1.13 % wt whereas TN values were around 0.04 and 0.11 % wt, respectively, and TOC/TN atomic ratio values ranged between 7 and 12. These organic proxies suggest that the organic matter was a mix of algae and aquatic plants remains. The isotopic composition was around -26 and -22 ‰ for $\delta^{13}\text{C}$ and 0.69 and 2.84 ‰ for $\delta^{15}\text{N}$. This facies was recorded in the central part of the sequence of the sedimentary infill in offshore cores 2, 3, and 4 (Fig. 4.19). This facies might represent the sedimentation by decantation of fine sediments transported by suspension into the lake, most likely as the transport process that generated facies A. The difference is that this facies originated in the lake areas under low anthropogenic activity influence.

Facies D (sand and debris from flood event).- Facies D corresponded to dark brown silts to very fine sand deposits recorded as layers that ranged from 2 to 40 mm in thickness. This facies was interbedded between the deposits of facies A and C and they were only recorded in cores 2, 4, and 14, all located in the NE part of the deep offshore plain. This facies had barren or contained very few diatoms and chironomids remains, while

showing a high proportion of macro and micro terrestrial plant remains. TN values were around 0.17 and 0.27 % wt whereas TOC values oscillated between 2.25 and 3.5 % wt. The great amount of organic matter and plants remains produced porosity in the sediment matrix. This porosity generated lower than average values of XRF, despite of the slight increase of Rb. Two subfacies could be distinguished into this facies. Subfacies D1 was composed by dark silt and very fine sand layers rich in organic matter. The TOC/TN atomic ratios were higher (between 11.5 and 15) than average (9) for this subunit. This large TOC/TN ratio together with larger amounts of organic matter suggested the dominance of C₃ terrestrial plant remains transported from the catchment. In fact, smear slides showed high micro phytoclasts quantities that were observed as transparent tissues and opaque particles, supporting the previous hypothesis. Subfacies D2 were rather similar to dark D1 facies, but dominated by macro terrestrial plant debris. This subfacies had greenish dark brown tonalities. TOC values were between 2.25 and 3.5 % wt and TOC/TN atomic ratio ranged between 12 and 19. Layers of subfacies D2 were scarcer than subfacies D1. The lateral correlation panel showed that the dark layers of facies D (D1 and D2) corresponded to tens- to hundreds-meters-long lobe bodies deposited in the NE part of the offshore zone (Fig 4.16 and 4.19). The lobes were deposited from to hyperpicnal currents as a consequence of flood events that occurred during major precipitations episodes and/or regular precipitations that eroded previously deposited sediments enriched in terrestrial vegetation. The lobes deposition became more frequent after the enhancement of the human activity in the catchment (i.e. crop down, deforestation, and fires).

Facies E (laminated grey muds).- Facies E was made up of grey laminated silty sand mainly composed by volcanic glass ash particles and phytoclasts. TOC values (0.99 - 1.6 % wt) were lower than the mean value profile while TN values were between 0.10 and 0.14 % wt, and TOC/TN atomic ratio values ranged from 10 to 12. The isotopic composition ranged around -25 and -24 ‰ for $\delta^{13}\text{C}$ and from 1.38 and 2 ‰ for $\delta^{15}\text{N}$. The chemical and isotopic composition of the organic matter suggested that the lake organic matter might be related to the mixture of algae and C₄ plants such as aquatic plants from the nearshore. The composition and stratigraphically position of this facies suggested that they were deposited in shallow lacustrine conditions from suspended,

load of floods generated by regular precipitations and/or pyroclastic direct fall-out from volcanic eruptions. In the first case, the terrigenous load was enriched in volcanoclastics fine material such as ash deposits accumulated in the catchment during the last volcanic eruption phase (P17) of Caldeira Seca (Moore, 1991), that occurred at the end of the 16th century (Fructuoso, 1522-1591).

Facies V (tephra).- This facies was composed of coarse light grey tephra. It belonged to the last eruption in Caldeira Seca labeled as P17 and radiocarbon dated at 660 ± 30 cal. yr. BP (Cole et al., 2008, Moore, 1991, Queiroz et al., 2008). These materials corresponded to explosive eruptions that emitted large amounts of lapilli and ash materials.

The non-volcanic lacustrine facies for the units 2, 3 and 4 in Lake Azul can be grouped in two main facies types according to the origin of the organic matter (see table 4.1 for equivalences with all facies described): (1) shallow to deep lacustrine deposits, rich in diatom remains, accumulated by a more or less continuously sedimentation, from terrigenous regular inputs mainly from Cerrado das Freiras fluvial delta system which includes organic matter mainly produced within the lake (i.e. phytoplankton) (Facies Continuous or Co), and (2) lacustrine deposits forming layers rich in terrestrial plant debris, barren of diatoms, which have been transported by rapid and flashy currents (flood events) from the catchment (Facies Rapid or Ra).

Lake sedimentary architecture

The architecture of the lake sedimentary infill was defined using the stratigraphic distribution of the previously defined lacustrine and alluvial facies. According to that, nine lithological units were established and correlated thorough extent zones of the lake (Fig. 4.19).

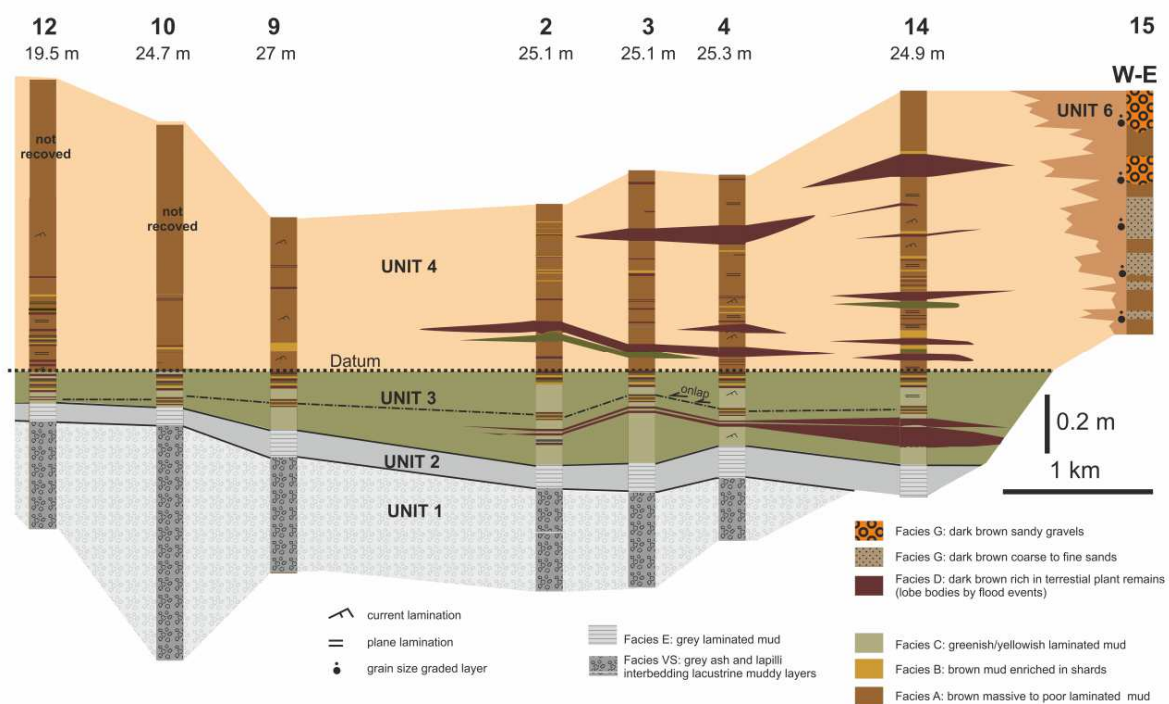


Figure 4.18: W-E stratigraphic cross-section. Stratigraphic correlation is based on stratigraphical and sedimentological criteria, limits between lithological units and key flood event layers. Datum of the panel is top surfaces of Unit 3.

Unit 1 (from 980 mm to 1330 mm in AZ11_02, lapilli and lacustrine silts)

Unit 1 was composed by coarse volcaniclastic tephra deposits (facies V) interbedded with thin beds of grey lacustrine silts (facies E, described below). The volcanic nature of this unit did not allow the geochemical characterization of these deposits. Therefore, only diatoms, pollen and chironomids were analyzed in the uppermost 60 mm of this deposit. Diatom assemblages were mainly composed by benthic species. The pollen content was made up of native and endemic species and the charcoal particles were almost inexistent. The chironomids head capsule number was low (20 head/cm³ of dry sediment in total for 60 mm) for this unit. The total thickness of the unit was unknown because it was too hard to be cored. This unit was observed in the entire lake basin.

Unit 2 (900 mm to 980 mm, grey deep plain laminated silts)

Unit 2 overlaid volcanic rocks from the basal unit and it was exclusively composed of laminated facies E. This second unit has a thickness that oscillates between 100 - 1000 mm and it occupies the deep plain and the slope zones. The XRF signal was relatively low but, the presence of the P17 volcanic eruption between the base of the unit and 800 mm provoked an enhancement mainly for Al. The XRD results showed low sanidine values and large number of samples containing smectite. The diatoms present in this

unit were mainly benthic and the chironomidae composition was made of oligotrophic-mesotrophic and detritivore species. Both proxies suggest that this unit developed in a shallow and oligotrophic lake conditions. The vegetation that surrounded the lake was mainly composed by native and endemic plant species. However, some human presence in the surroundings was observed owing to the presence of *Secale cerealis*. The charcoal amount was low with values between 500 and 1000 particles/g of dry sediment, suggesting that fires had low impact.

Unit 3 (from 900 to 580 mm in AZ11_02, deep plain green laminated silts with flood events lobe deposits).

Unit 3 was composed of laminated brown silts (facies C) interbedding brown dark layers (facies D). This unit occupies the deep plain and the slope areas. The mineralogical composition of this facies was mainly composed by sanidine but, an increase of plagioclases and smectite was observed. XRF values of terrigenous elements (Ti, Sr, Rb, Zr, Nd, Al, Si, K, Mn, Fe, Ca) were variable indicating shifting towards terrigenous presence. Pollen content of unit 3 was marked by the decrease of native and endemic species such as *Juniperus laurifolia* and the disappearance of *Juniperus brevifolia* and *Picconia azorica*. The charcoal increased having a mean value around 1000 particles/g of dry sediment. The last two proxies suggest that the human presence and impact on the island increased. Diatoms were mostly facultative with a decrease on the benthic diatoms compared to the previous units and the euplanktonic taxa were almost inexistent. This diatom assemblage suggests that the lake level rose during the deposition of this unit.

Unit 4 (0 mm to 580 mm in the core AZ11_02, deep plain massive brown muds)

Unit 4 was contained three facies (facies A, B and D). This unit occupied the deep plain and the slope areas, increasing its thickness from 300 to 900 mm. The mineralogical composition of this unit was made of sanidine with subordinate quantities of chlorite, plagioclases and amphiboles grains from felsic volcanic rocks. The organic matter was present as scattered amorphous with very low composition of phytoclasts. Diatoms were abundant and dominated by micoplanktonic genera such as *Tabellaria ssp.* and

Fragilaria *sl* and, with euplanktonic genera such as *Aulacoseira* *sp* colonies. The major part of the pollen found at this unit corresponds to introduced plants including *Cryptomeria Japonica*, *Pinus* and *Plantago Lanceolata* but also, some natives species appeared such as *Myrica Faya* and *Pteridium aquilinum*. Charcoal particles were high showing values between 1000 and 7500 particles/g of dry sediment. The presence of high quantities of charcoal and introduced pollen suggested an intense human activity during the sedimentation of these recent deposits. The number of chironomid head capsules suffered a rapid increase around 360 mm mainly produced by the increase of the gender *Tanytarsini*. This rapid increase was followed by a decrease on the head capsules and the appearance of new species such as *Parachironomus varus-type* and *Cricotpus sylvestris-type*.

Apart from the offshore units detailed above, other five lithological units were recognized from the core study. Unit 5, located at NE margin of the lake, was composed of deltaic coarse deposits (facies G). These deposits had a thickness of around 830 mm and are laterally equivalent to deposits of basin plain (units 2 to 4). Unit 6 was accumulated in the platform-ramp over volcanic deposits, had an average thickness of 5 mm and it was made up of non-lacustrine alluvial gravelly deposits (facies H). Unit 7 reached a thickness of 100 mm, and it was recorded in the platform-ramp, underlying Unit 6. None of these nearshore facies were studied in detail.

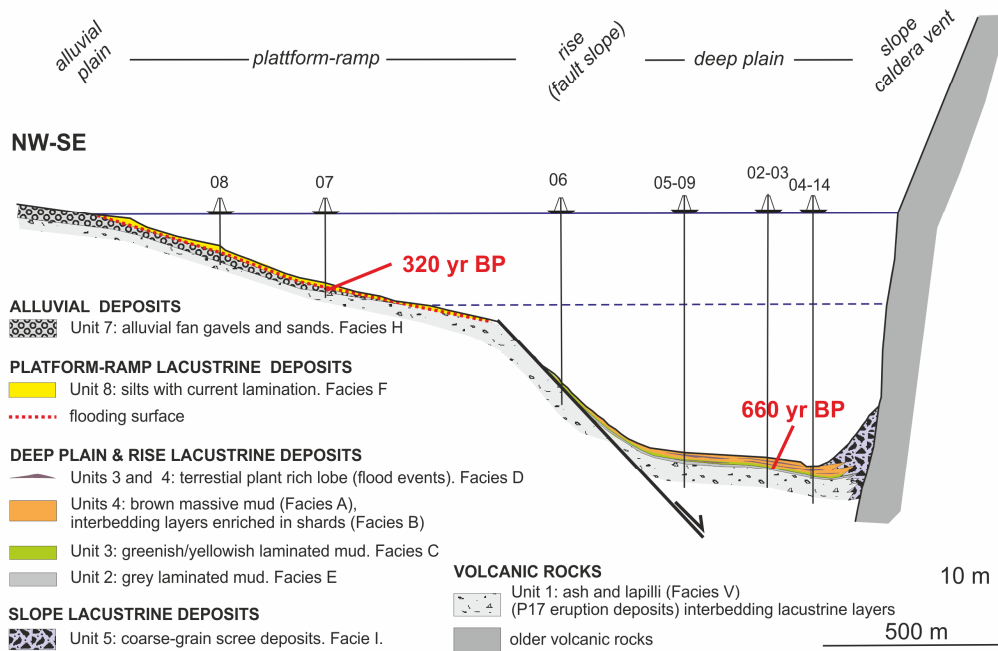


Figure 4.19: N-S geological cross section. Data are from core sequences and seismic profile of Fig. 16A . Ages displayed in red corresponds to the eruption of Caldeira Seca called P17 (Unit 1, 660 yr BP; Queiroz et al., 2008) and base of the platform-ramp deposits flooding (Unit 8, core AZ_11-7) indicating age of flooding of platform-ramp (320 yr BP).

4.3 INSTRUMENTAL DATA ANALYSES.

Temperature

According to the temporal evolution of the instrumental Mean Air Temperature (MAT) in Ponta Delgada, this climate record can be subdivided in three main periods: (1) from 1872 to 1900 AD, it had large oscillations that went from 16.5 to 19 °C; (2) the period between 1900 and 1970 AD was characterized by decadal oscillations with temperature amplitude between 16.7 and 17.8 °C, and (3) from 1970 AD to 2012 AD the temperature profile showed an increasing trend that went from 17 to 18.5 °C (Fig. 4.20). The application of the monthly time series decomposition in their respective trend, seasonality and random components using the additive moving average method showed that from 1970 AD to the present the trend has changed into an overall increasing trend (Fig. 4.21). Moreover, the random component showed a decadal oscillation. The random factor showed a decadal oscillation that decreased in amplitude from 1900 to 1960 AD where this oscillation became messy but, it was still observed.

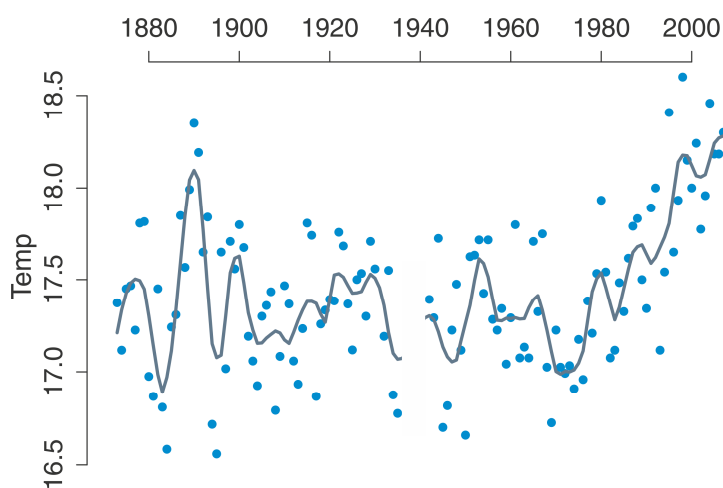


Figure 4.20: Temperature data in Ponta Delgada village for the period comprised between 1873 and 2012 AD. Data from 1873 to 1946 AD were extracted from the “Annaes do Observatório Infante D. Luiz” whereas from 1947 to 2012 AD were supplied by the Instituto Portugues do Mar e da Atmosfera (IPMA). The light blue points are the annual mean temperature values and the dark blue-grey line is the smooth applied to the temperature data with a span of 0.1. Note the increasing trend from the 1970 AD to the Present corresponding Global Warming period.

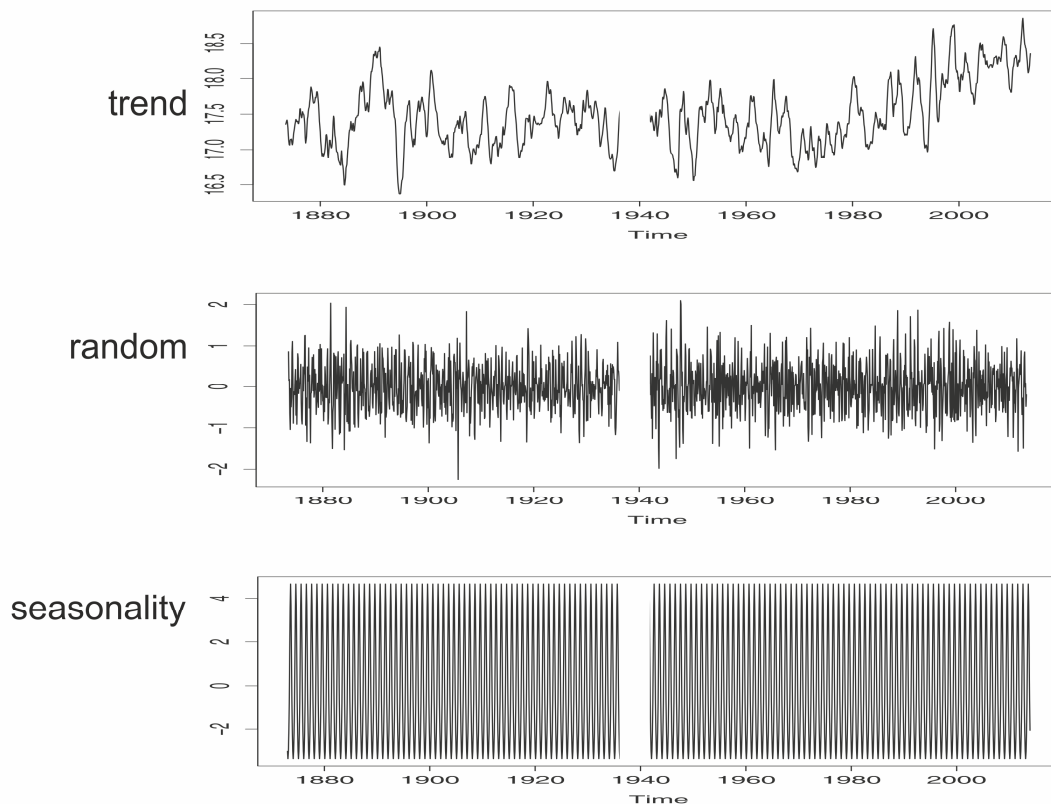


Figure 4.21: Trend, random and seasonality components of the monthly mean temperature data for the period comprised between 1873 and 2012 AD. Those data were obtained from the temperature data from Ponta Delgada (Fig 4.19). Observe the increasing trend from 1970 AD to the present and that the random data observed a decadal oscillation.

The MAT Ponta Delgada has been plotted together with the mean minimum and mean maximum temperature profiles (Fig. 4.22). The mean maximum temperature oscillated between 18.5 and 22 °C while the mean minimum temperature fluctuated between 13 and 16 °C. Both profiles displayed equal oscillations and trends along the studied period, except for the period comprised between 1935 and 1965 AD. This last period was characterized by an increase of the mean maximum temperature and a decrease of the mean minimum temperature.

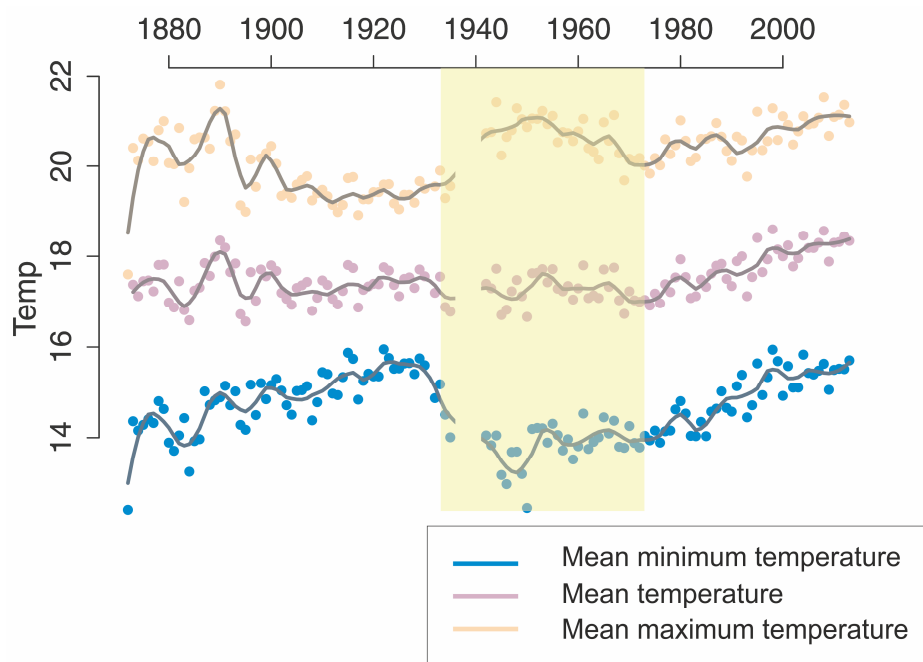


Figure 4.22: Temperatures curves obtained from Annaes do Observatório Infante D.Luiz and IPMA. The annual minimum temperature (brown), the mean annual temperature (pink) and the mean annual maximum temperature (blue) for the period comprised between 1873 and 2012 AD. The smooth (lines) was applied to each dataset with a span of 0.1. The yellow colored area refers to the period were the amplitude between the minimum and maximum temperature is larger.

The MAT Ponta Delgada values from 1873 to 1885 AD were lower than the mean (Fig. 4.23). An increase on mean air temperature was observed from 1885 to 1895 AD of about 0.6 °C. The largest period with low temperatures was observed between 1895 and 1985 AD. This period comprised temperatures that were lower than the mean temperature value for the entire period of about 0.5 °C. From 1985 to 2012 AD, the temperature suffered a rapid increase that went from 0.7 °C below the mean value to more than 1 °C above mean. The warmest year was 1998 AD, with a mean annual temperature of 18.6 °C, and the coolest was 1895 AD, with a mean annual temperature of 16.5 °C.

Precipitation

The MWL graph demonstrated that the 94.6 % (139 samples) of the 147 samples that composed the dataset were inside the boundaries of the linear regression of the MWL plus uncertainties and only eight samples (5.4 %) were unselected from the dataset (Fig. 4.24). The weeks with more than one origin were not useful for isotopic purposes because of the possible different fractionation depending on origin. Therefore, the next

step was to discard weeks with more than one different air mass origin. The origin in the present work was the location of the air mass that produces rain in Ponta Delgada 72 hours before reach the island.

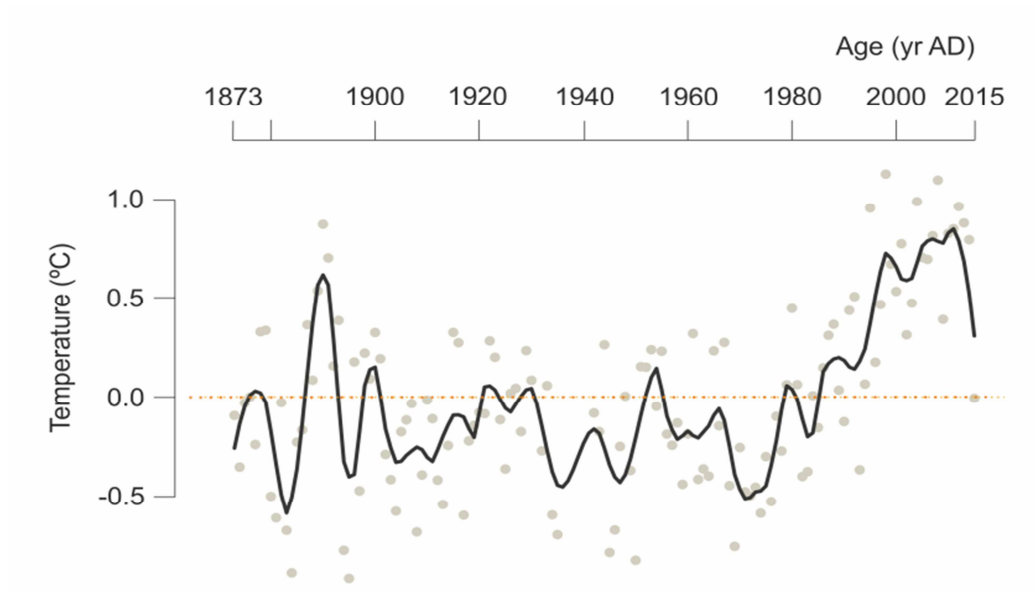


Figure 4.23: The temperature anomalies for the period between 1873 and 2015 AD. Those data were obtained from Annaes do Observatório Infante D.Luiz and IPMA.

From the 139 weeks left after remove samples sensitive of evaporation, 25 weeks (17%) had more than one origin and 114 weeks (77.5 %) had only one origin. Those 25 weeks with more than one origin were removed.

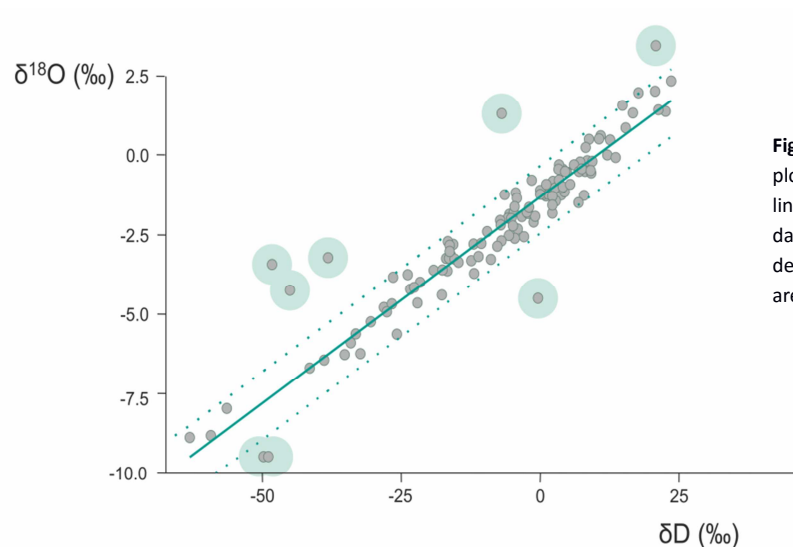


Figura 4.24: Meteoric Water Line (MWL) plotted $\delta^{18}\text{O}$ against δD . The turquoise line is the MWL and the turquoise dashed lines are the 2σ standard deviations. The values outside the MWL are circled with a light turquoise circle.

4.4 GLYCEROL DYALKYL GLYCEROL TETRAETHER (GDGT) COMPOSITION OF THE SEDIMENTS.

The GDGTs contained on AZ11_02 (GDGT-0, GDGT from gender Thaumarchaeota and Branched GDGTs) have been plotted in a ternary diagram (Fig. 4.25). This figure showed that Lake Azul sediments were mainly composed by GDGTs from bacterial origin (brGDGT). This great amount of bacterial GDGTs produced high Branched-Isoprenoid Tetraether Index (BIT), which in the present work oscillated between 0.9 and 1. Those values did not show statistical differences between facies Co and facies Ra (Fig. 4.26). The BIT values oscillated between 0.92 and 1. There was a decrease around 700 mm a mean value ca. 0.95. The MBT index showed values from 0.3 to 0.45. From bottom to the 400 mm, it could be observed a small increasing trend with values between 0.7 and 0.42. At 400 mm there was a rapid decrease with values around 0.3 followed by a rapid increase to top. The CBT index showed values from 0.4 to 0.9 but, the mean value was 0.55. The lowest values were observed from 400 to 200 mm with a mean ca. 0.4. Figure 4.25 suggested that the major part of the samples were not affected by methanogenesis. Further calculations revealed that only the 20% of the samples were prone to be affected by methanogenesis and that the major part of these samples were located between 440 mm and the top of the core.

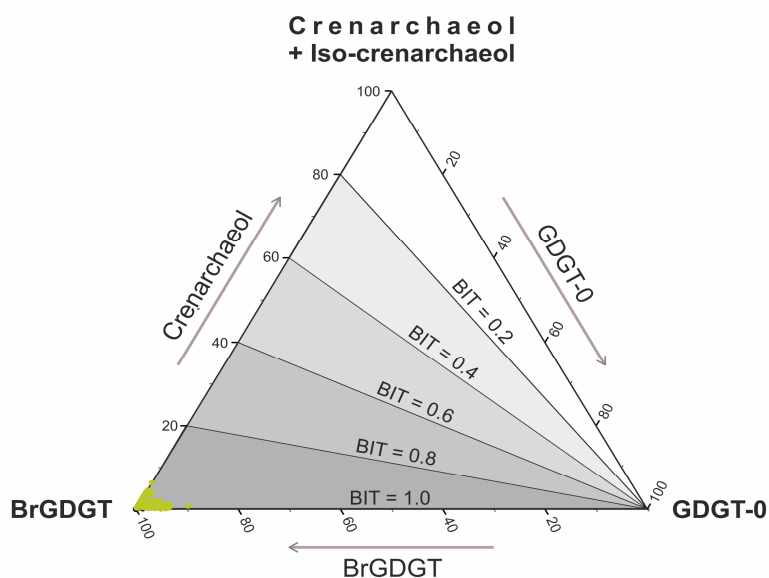


Figure 4.25: Ternary diagram showing the relative proportions of crenarchaeol, iso-GDGT-0 and total br-GDGTs in Lake Azul sediments. The BIT index is colored with different grey tonalities. Note that the BrGDGT (GDGTs from bacterial composition) dominated the sediment composition. This great amount of BrGDGT displayed BIT values between 0.9 and 1.

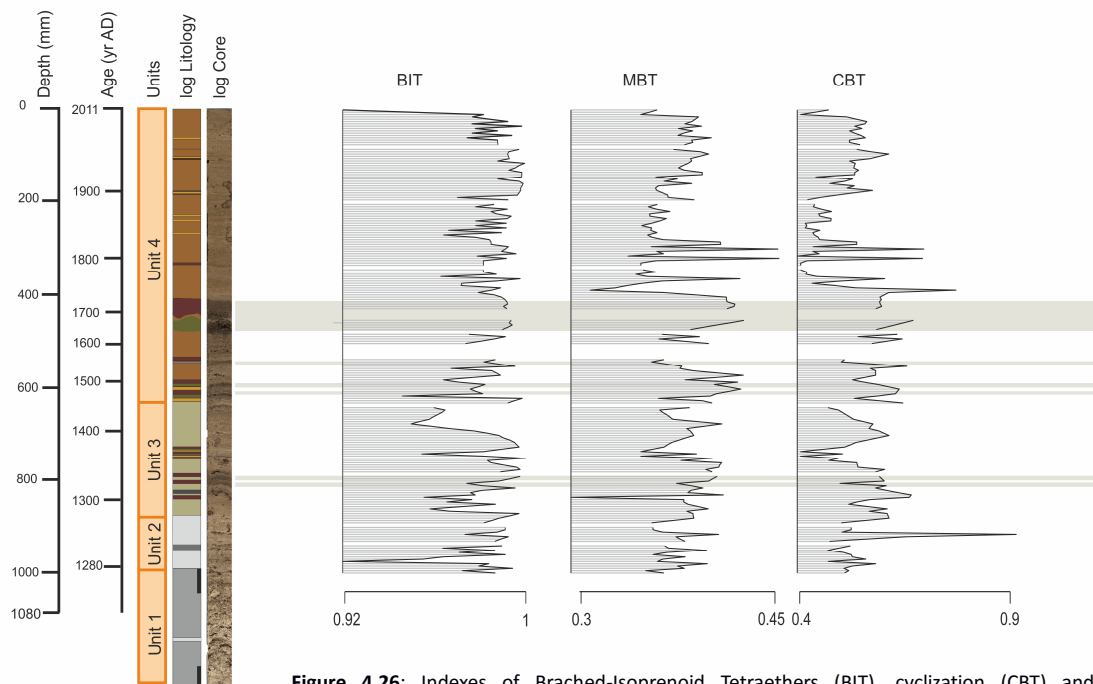


Figure 4.26: Indexes of Brached-Isoprenoid Tetraethers (BIT), cyclization (CBT) and methylation (MBT). The grey horizontal bars refer to flood events deposits (facies D) that range from brown silt to very fine sand with large amount of plant remains. Note that BIT, CBT and MBT did not show variations on composition on the flood event deposits.

The GDGTs relative values exhibited greater amount of Bacterial GDGTs than Archaeal GDGTs (Fig. 4.27). Inside the Archaeal production, the Crenarchaeol and GDGT-0 were the GDGTs with major percentage with mean values around 2.5 % for the Crenarchaeol and 1 % for the GDGT-0. For the bacterial production, the major percentages appeared in GDGT- III (1050), GDGT-II (1036) and GDGT-I (1022); with values around 25 %, 34 % and 15 %, respectively. The triplet with highest contribution was GDGT-II, GDGT-IIb and GDGT-IIc that accounts with almost the 45% of the GDGT production.

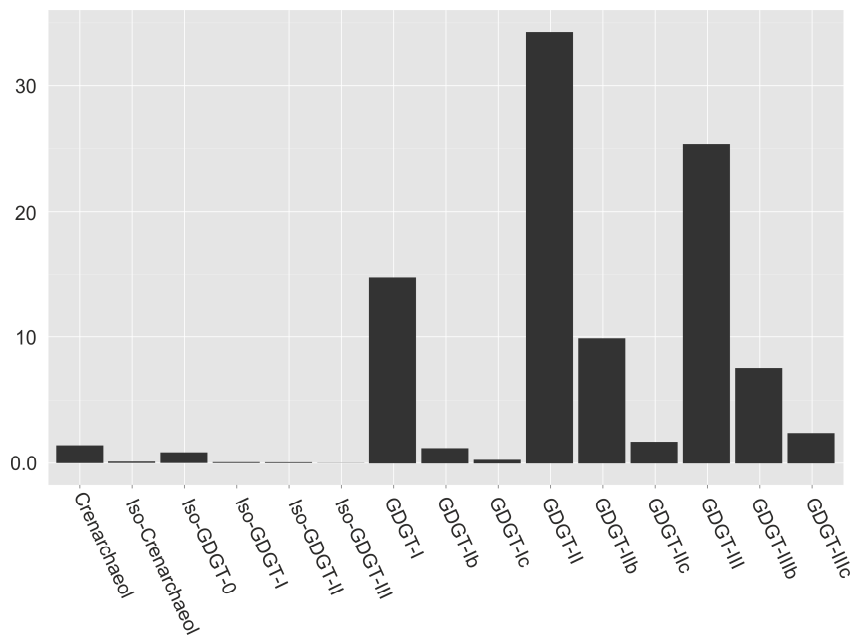


Figure 4.27: Bar diagram with the percentage of GDGTs on Lake Azul lacustrine sediments. Note that the most abundant bacterial components are GDGT-I, GDGT-II and GDGT-III, the brGDGTs without cyclopentane rings. The most abundant Archaeal GDGT is the Crenarchaeol.

In order to observe differences between depositional environments a linear discriminant prediction function was applied between the four units. The application of this function demonstrated that there were no significant differences between stratigraphical units.

4.5 δD LEAF WAX DISTRIBUTION IN LAKE AZUL. CHARACTERIZATION PERFORMED FROM THE CORES AZ11_02 AND AZ11_14 COMPOSITE.

General characteristic of δD n-alkanoic profiles.

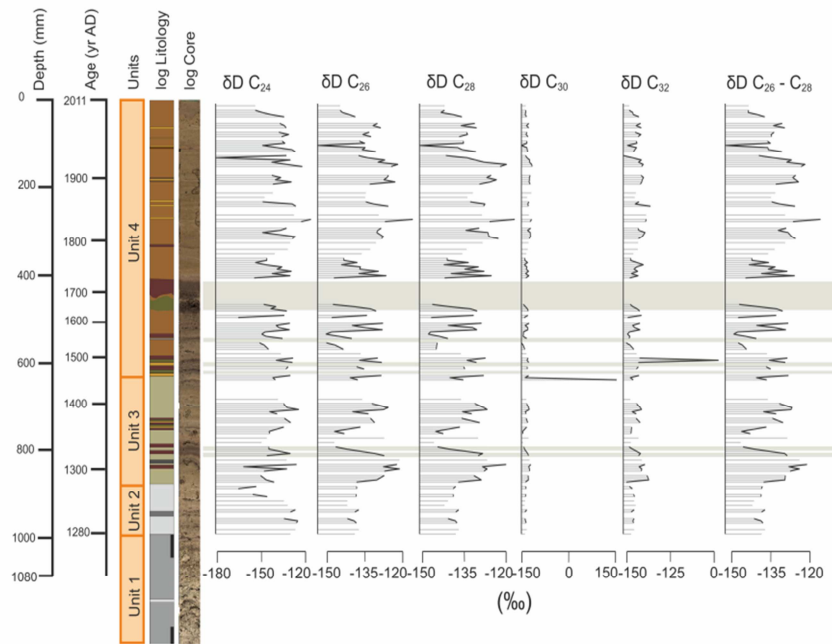
δD values were analyzed for n-alkanoic acids chains that went from 24 to 32 carbon units for the cores AZ11_02 and AZ11_14. Those n-fatty acids, mainly produced by leaf epicuticular waxes, present a strong even over odd carbon number preference.

Core AZ11_02

For the core AZ11_02, the data from the different compounds demonstrated similar mean values that went from -139.31 ‰ in n-C₂₄ to -132.32 ‰ in n-C₃₂. The n-alkanoic quantity for n-C₃₀ and n-C₃₂ was very small and their profiles look a bit different (Fig.4.28). Otherwise, the most abundant compounds were n-C₂₆ and n-C₂₈. The standard deviation was of 2.7 ‰ for all the species. The widest δD data range was found in n-C₃₀ and n-C₃₂ that went from positive values (around 150 ‰) to negative values (around -150 ‰). The narrowest δD data range was found in n-C₂₆ and n-C₂₈, which went from -120 ‰ to -160‰. The trends were similar for n-C₂₄, n-C₂₆ and n-C₂₈ but different for n-C₃₀ and n-C₃₂. The highest correlation between species δD data was found between n-C₂₆ and n-C₂₈ ($r=0.96$, $p<0.01$); but, n-C₂₄ and n-C₂₆ still had a strong correlation ($r=0.78$, $p<0.01$).

The n-C₂₆ and n-C₂₈ δD profiles for AZ11_02 showed similar mean values (-135.2 ± 2.7 and -134.8 ± 2.7 ‰ respectively), equal standard deviation ($sd = 2.7$ ‰), equal range (between -120‰ and -160‰) and high correlation ($r=0.96$, $p<0.01$). Then, in order to interpret the δD record the mean between n-C₂₆ and n-C₂₈ was applied for this core. From now onwards, the mean applied between n-C₂₆ and n-C₂₈ is going to be named δD_{wax02} .

Figure 4.28: Isotopic values (δD) for the different leaf wax chain lengths with an odd preference for the core AZ11_02. The grey horizontal bars refer to deposits that range from brown silts to very fine sands with large amount of plant remains and high porosity (Facies D). Note that δD C30 and δD C32 have different values than



Core AZ11_14

For the core AZ11_14, the mean values oscillated between -138.2 ‰ in n-C₂₄ to -126.4 ‰ in n-C₃₂ (Fig 4.29). The n-alkanoic quantity for n-C₃₀ and n-C₃₂ was also small and the most abundant compounds were n-C₂₆ and n-C₂₈. The standard deviation was around 2.7 ‰ for all the species. The widest δD data range was found in n-C₃₀ and n-C₃₂ and went from 0 ‰ to -200 ‰. The narrowest δD data range was found in n-C₂₆ and n-C₂₈, which went from -120 ‰ to -160‰. The trends were similar for n-C₂₄, n-C₂₆ and n-C₂₈ but different for n-C₃₀ and n-C₃₂. The highest correlation between species δD data was found between n-C₂₆ and n-C₂₈ ($r=0.92$, $p<0.01$); but, n-C₂₄ and n-C₂₆ still had a strong correlation ($r=0.69$, $p<0.01$).

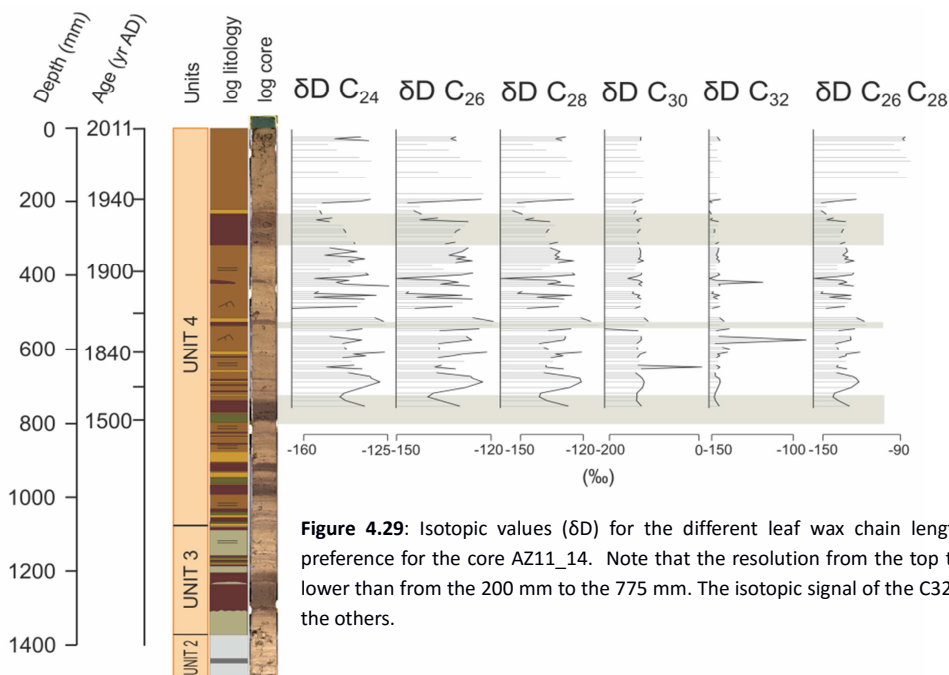


Figure 4.29: Isotopic values (δD) for the different leaf wax chain lengths with an odd preference for the core AZ11_14. Note that the resolution from the top to the 200 mm is lower than from the 200 mm to the 775 mm. The isotopic signal of the C32 is different from the others.

The n-C₂₆ and n-C₂₈ δ D profiles for AZ11_14 showed similar mean values (-134.2 ± 2.7 and -134.5 ± 2.7 ‰ respectively), equal standard deviation ($sd = 2.7$ ‰), equal range (between -120 ‰ and -160 ‰) and high correlation ($r=0.99$, $p<0.01$). Then, in order to interpret the δ D record the mean between n-C₂₆ and n-C₂₈ was applied for this core. The mean for these 2 species has been named δ Dwax14.

Cores composites.

The δ Dwax14 and δ Dwax02 had similar characteristics such as the mean value -135.0 and -134.3 ‰, respectively. Those two profiles have equal standard deviation, equal range and high correlation.

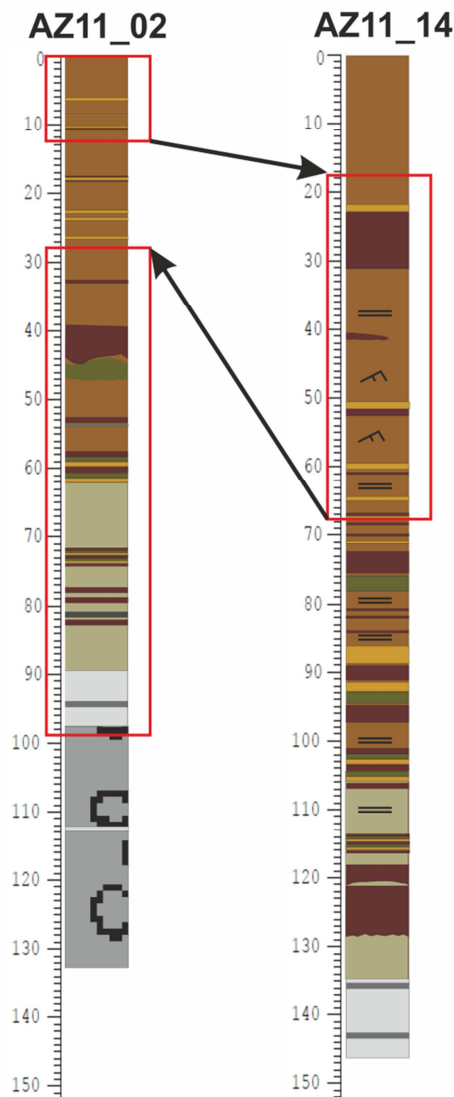


Figure 4.30: Composite of the core AZ11_02 and AZ11_14 sequences. The selected intervals for each core are red-squared.

The δD_{wax02} was the core with more data available but the resolution was poorer than δD_{wax14} profile for the section comprised between 150 and 300 mm. Then, based on the stratigraphic correlation a composite between the two cores has been performed (Fig. 4.30). This composite contains data of the δD_{wax02} profile from the bottom to the 275 mm and from 125 mm to the top whereas δD_{wax14} data was added from the 675 mm to the 175 mm. From this point onwards the results of this composite is named δD_{wax} (Fig. 4.31). Those data were presented regular in time at one year resolution.

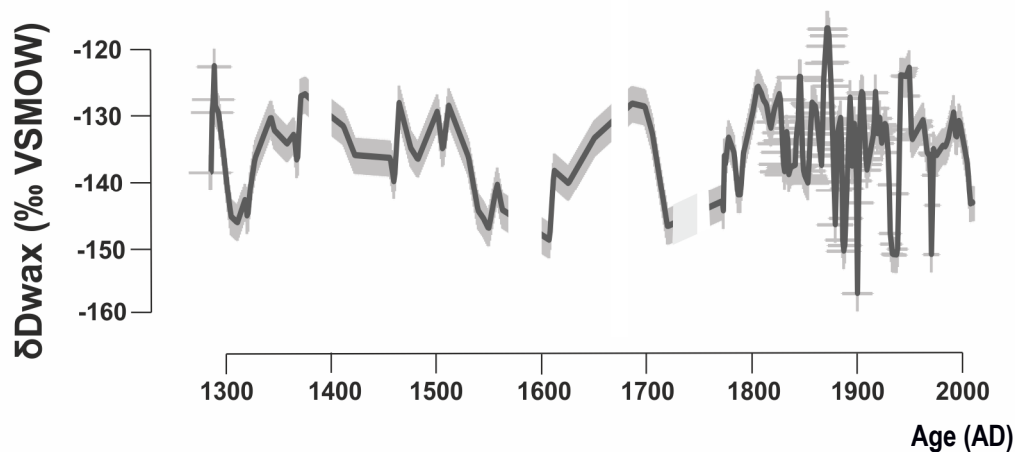


Figure 4.31: The AZ11_02 and AZ11_14 δD composite for the period between 1280 and 2011 AD. The light grey color showed the error bars and the dark grey color the δD_{wax} data at one year resolution.

General characteristic and trends of δD_{wax} profile.

δD_{wax} showed a mean value of -135.32 ‰ with an standard deviation of 2.7 ‰ . The profile range went from -120 ‰ to -160 ‰ . From 1285 to 1300 AD, the δD depleted from -120 ‰ to -145 ‰ . A rapid enrichment was found from 1300 to 1370 AD that went from -145 ‰ to almost -128 ‰ . Then, a decreasing trend was found from 1370 to 1610 AD that ranged between -128 ‰ to -148 ‰ . Around this point, it can be observed the most depleted profile valley. After that, a rapid increase was observed till 1700 AD. At this point the δD values were around -128 ‰ . Another profile valley was observed between 1700 and 1800 AD, which deepest value oscillated around -148 ‰ . Finally from 1800 to 1875 AD there was an increase of the δD signal that went from -148 to -120 ‰ . This increase was followed by a rapid decrease until 1900 AD that went from $-$

120 to -160 ‰. From 1900 AD to the present, there was a general decreasing trend with 3 main moments of depletion at 1940 AD (with a value of -150 ‰), 1960 AD (-150 ‰) and 2011 AD (-145 ‰).

*If you ignore your past,
you jeopardize your future
(Clone Wars Morals)*

5. DISCUSSION

5.1 NOVEL DYNAMIC AGE MODEL (DAM) APPROACH FOR HISTORICAL ENVIRONMENTAL AND CLIMATE RECONSTRUCTIONS: THE LAKE AZUL (AZORES ARCHIPELAGO, PORTUGAL) STUDY CASE.

The present section exposes the new methodology to construct age-depth models for historical sedimentary sequences where long- and short-term changes in the sedimentation rate are taken into account. The most significant feature of this new Dynamic Age Model (DAM) is that, unlike the other age-depth model construction approaches, the SR at one specific time window is not determined by its previous history, thus allowing abrupt and significant changes in the SR. This new methodology has been applied to two sedimentary cores located in the deep offshore plain from Lake Azul (AZ11_02 and AZ11_14) which are largely dominated by siliciclastic sediments. The obtained DAM has been compared with those derived from the application of other age-depth models (i.e. mixed-effect model and Bacon) in order to display the strengths and weaknesses of this new methodology uniquely for the core AZ11_02.

Previous considerations before the DAM construction

The construction of any age-depth model requires a prior detailed facies analysis to elucidate the main processes involved on the sediments accumulation. Different sedimentary processes might imply a diverse nature of components (i.e. organic versus mineral), origins (i.e. in-lake vs external) and mechanisms (i.e. instantaneous vs continuous). The characterization of these sedimentary processes is especially important when trying to clarify timing differences in the SR of terrigenous material deposited into the lake basin (i.e. turbidite-like events versus tractive-suspended loads from regular fluvial currents). This implies that before the depth-age model can be built, the employment of a number of proxies such as visual characterization of the sediments, smear slides and bulk organic geochemical analyses is of capital importance when constructing a chronological model that tries to capture the abrupt SR changes. Different sedimentary processes or velocities might imply a diversification of the

nature and features of the biological/geological particles that in turn produce a different response in the geochemical analyses. Commonly, the allochthonous input of sedimentary particles in a lake is dominated by one process. The proposed DAM takes advantage of that since this allochthonous material usually has the same chemical composition during the studied period. As stated in the Introduction, XRF data might help to improve the construction of age-depth models since it can be used to accurately track these allochthonous material changes. Therefore, the DAM uses only one chemical element from the XRF core scanner dataset to calculate the both long- and short-term SR changes associated to the input of this allochthonous material (see the construction of DAM below for further information). The selected chemical element should be the most representative of the chemical composition of the siliciclastic particles present in the sediments.

When the facies analysis reveals that a different and secondary sedimentary process is related to the input of terrigenous particles (i.e. punctual inputs of material due to flood flashy transport process of particles), and prior the construction of the age-depth model, the XRF data of the selected chemical element must be removed from the zones where this secondary process dominates. Otherwise, the dynamical age model will incorrectly attribute the correspondent time to these secondary areas (i.e. the flashy flood must be considered as instantaneous processes by definition). This previous XRF data “removal” is discussed in more detail in the DAM calculation in Lake Azul presented below.

Another key consideration that must be assessed prior the construction of the DAM is the reliability and calibration of the ages. The already available software, such as Clam, Bpeat, Chron, and Bacon, perform both the calibration of the supplied dates and the assessment of the reliability of the obtained calibrated age within the framework of the dataset of the dated core (Blaauw, 2010; Blaauw and Christen, 2005; Blaauw and Christen, 2011). The result of both tasks is the construction of a chronological model accepting or rejecting to a certain degree of freedom the supplied dates. In other words, the software performs a more or less automatic assessment (with a variable intervention of the user) of the validity of the ages and constructs the chronological model accordingly. These two tasks are not carried out by the proposed DAM and they

must be accomplished by the user. The calibration can be easily performed using the radiocarbon calibration software already available (either online or offline) such as Calib (<http://intcal.qub.ac.uk/>) and Oxcal (<https://c14.arch.ox.ac.uk/oxcal/>). Furthermore, all radiometric dates should follow a stratigraphic order because of the construction of the model do not discriminate between normal and reverse ages. Therefore, the assessment of the reliability of the obtained dates should consist in rejecting the reversals since the model only assumes that rapid and abrupt SR changes occur and must be taken into account. These sudden changes in the SR must be in accordance with other lithological proxies, such as those proposed above.

When the studied core ranges ages older than the last 100 years and depending on the nature of the sediment (organic, carbonated, volcanic, siliciclastic), radiocarbon dates, Uranium-series disintegration ($^{234}\text{U}/^{230}\text{Th}$), Optical Stimulated Luminescence (OSL), and Thermoluminescence (TL) dating methods can be employed. The DAM also allows the incorporation of other absolute time markers (i.e. tie points) such as tephra layers and historical events. Tephra layers are rather frequent in Late Quaternary lacustrine deposits located in active volcanic settings. Their chemical composition (major and minor elements and REE) can be precisely determined, and in some cases, an age can be assigned if can be attributed to an historical volcanic eruption. On the other hand, historical events are commonly recorded in recent deposits (introduction of exotic plants, large catchment modifications, wars, etc.) which can be easily identified providing an additional tie point to the DAM. Nevertheless, these tie points must be dated using independent and absolute radiometric methods in order to ensure their correct temporal attribution.

Construction of the DAM

In this section a detailed explanation about the implementation of the DAM is provided. The reader is referred to the Appendix where a theoretical R session, with all the mathematical details, is given (Appendix 1). The schematic workflow of the DAM construction is represented in Figure 5.1.

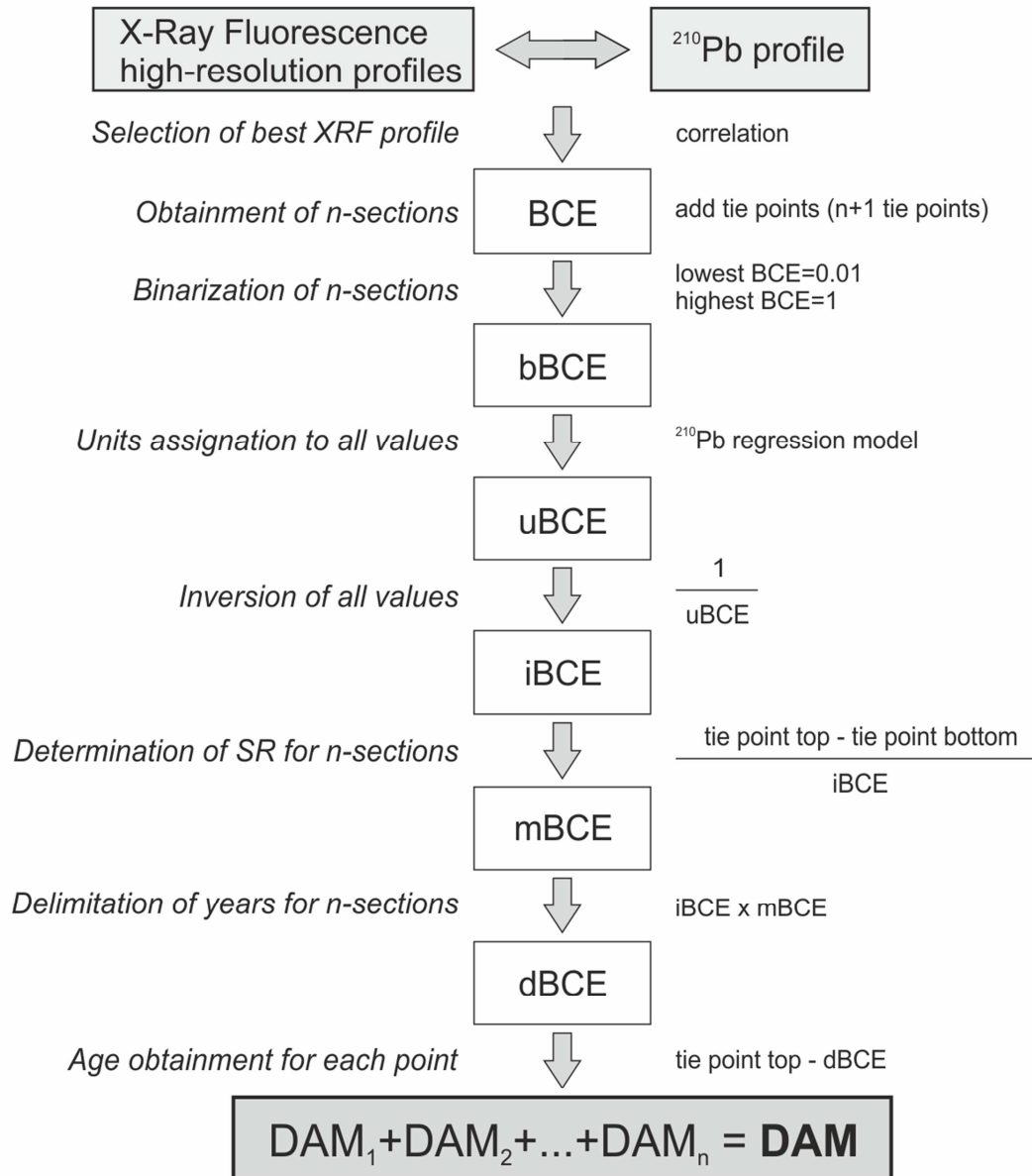


Figure 5.1: Flow diagram representing steps required to fulfill the Dynamic Age Model (DAM). See text for a detailed explanation.

Best Correlated Element (BCE)

Since the XRF data reflects large variety of physical and chemical processes, the first task is to determine which XRF chemical element better tracks and assess the terrigenous inputs. Changes in the volume of terrigenous inputs will led to fluctuations in the SR. At present, the best method to accurately determine short-term fluctuations in the rate of accumulation of sediments is the ^{210}Pb dating, since the content of this radioisotope can be measured with a high degree of accuracy for a sediment interval (e.g. the uppermost 100 mm of the lacustrine infill). The Constant Atmospheric Rate of Supply (CRS) model is one of the most widely used models in the ^{210}Pb dating. The CRS model implies that the atmospheric supply of ^{210}Pb is constant through time, and therefore, changes in the ^{210}Pb accumulation profile must be led by fluctuations in the sedimentation rate (Appleby and Oldfield, 1978). Therefore, the comparison of the XRF dataset with the sedimentation rates derived from the ^{210}Pb profile will identify the best chemical element to track SR changes.

In order to compare the XRF data with the ^{210}Pb sedimentation rates profile both datasets must be at the same spatial resolution, which implies to downscale the first dataset, usually measured at higher resolution (i.e. <10mm). According to our results, the best option to downscale the XRF data is by making the median of all XRF values comprised between two ^{210}Pb ages since it permits to overcome the problems derived from the presence of anomalous XRF values (i.e. outliers and/or small gaps). To disentangle which is the most representative XRF element of the siliciclastic input, a Pearson product-moment correlation coefficient can be used. The Best Correlated Element (BCE) is expected to be the element with the highest r value and the lowest p-value.

Tie points constraining

The core depths where the absolute radiocarbon dates as well as the other absolute ages are found, in fact, they correspond to tie points from which both the age-depth model and the age of the intermediate samples will be calculated. Once the BCE is

selected, the tie points from which the chronological model will be constructed must be attached to the BCE profile. These tie points imply two components, i.e. their respective depth and absolute age. Therefore, the depth of the tie points constitutes the limits of the n-sections in which the BCE will be split in order to calculate the DAM. Obviously, the reliability and accuracy of the DAM increase with the number of tie points. The larger number of tie points, the more precise will be the DAM since less distance will be between them. For a given sedimentary sequence thickness, the DAM model will be more robust if five tie points are employed rather than two of them. There are several classes of tie points that can be introduced in the construction of the chronological model, such as the year of the core retrieval, ^{210}Pb , ^{137}Cs , ^{241}Am and ^{244}Pu profiles, AMS ^{14}C dates and key markers (e.g. tephra layers, historical events). It is worthy to note that the year of the core retrieval can be added to the DAM construction when the water-sediment interphase is well preserved. Nevertheless, the complete obtainment of this interphase must be verified by independent and objective methodologies, such as the use of radioisotopes (i.e. ^{210}Pb). Thus, the loss of the most recent sediments due to coring problems or to erosion episodes might introduce errors to the construction of the DAM. The BCE selection implied the use of the ^{210}Pb profile but only the SR has been used, not the absolute ages derived from this profile. Therefore, the most recent, oldest and/or intermediate ages can be used as a tie points in the DAM construction.

Once the tie points are established, the BCE must be split in the n-sections defined between these tie points (Fig. 5.1). The construction of the age-depth model by splitting the profile in n-sections is observed in other available software such as Clam and Bpeat and, therefore, it is not an intrinsic feature of the DAM. This segmentation permits to calculate the intermediate ages of the samples located between the tie points. The main difference between the proposed DAM and the already available software relies in the method employed to calculate these intermediate ages. The available software calculates these intermediate ages using several mathematical methods that range from linear interpolation to sophisticated techniques such as the Bayesian approach (Blaauwn, 2010; Ramsey, 2009). In spite of the mathematical calculation method, all these software assume that changes in the SR only occur at

long-term (at multi-decadal and/or centennial time scale) and not at short-term (annual and decadal time scale). In other words, these softwares assume that the sedimentary system has a certain degree of “memory” since the SR calculated for the previous sample partially determines the SR of the next sample. The degree of determination, in other words the degree of “memory” of the sedimentary environment is established by the mathematical method used to calculate the intermediate ages. Linear interpolation assumes a high degree of memory whereas the Bayesian approach implies a low degree of memory. The DAM approach assumes that the sedimentary environment has no “memory” (i.e., the SR of the previous sample is completely independent of the next one) and changes in both long- and short-term sedimentation rates can occur. The use of BCE permits to track changes on SR at all possible temporal scales since the relative changes of this chemical element are roughly proportional to the concentration of the allochthonous material present in the sediments.

Binarization of BCE values

The XRF dataset can only trace the relative abundance of the identified chemical elements due to some limitations, such as the variable quality of the measurement surface of the core, changes in the physical properties of the sediment matrix and fluctuations in the total amount of water and/or organic matter (Richter et al., 2006). Therefore, the matrix effect (as the previous limitations are commonly known) might attenuate or enhance the XRF element intensity (Potts, 1987), hampering, in this case, the correct qualitative determination of the terrigenous inputs for the complete sequence. In other words, the variable presence of organic matter in two distinct sections of the same core but with similar proportion of terrigenous material might result in the apparent perception that, owing to the matrix effect, the content of terrigenous material in both sections is different. One way to overcome this limitation is maximizing the variance of the BCE. For this purpose, the BCE is binarized for every section, attributing the highest BCE value to 1 and the lowest one to 0.01. The intermediate values are calculated using a linear regression model between these two binary end members. The lowest BCE values are assigned to 0.01 and not to 0 since the later value generates infinite values in posterior calculations. The obtained values for

every section correspond to the binarized BCE (bBCE) series and now they represent the maximum variance of the terrigenous inputs of the studied sequence (Fig 5.1). Binary values close to 1 correspond to the periods of largest input of terrigenous particles and whereas binary values close to 0.01 represent the periods where the siliciclastic inputs were the lowest.

Units assignation

The bBCE profile is dimensionless and it only represents relative and maximized variations of the terrigenous input. To assign units of SR (i.e., mm/yr) to this profile, these relative variations must be compared with an independent method that provides a profile with quantitative sediment rate values. The technique that can provide quantitative SR changes is ^{210}Pb . Therefore, a regression model can be established between the common depths of the bBCE and ^{210}Pb , i.e. the uppermost part of the studied sequence. Since, the BCE (and thus the bBCE) represent the main sedimentary process that rules the input of allochthonous particles in the entire sequence, this regression model between the bBCE and the ^{210}Pb can be extended to the complete sequence. The easiest procedure to apply this regression model is to employ the n-sections previously defined by the tie points. The result of the application of this regression model is the acquisition of a two dimension (uBCE) profile (Fig. 5.1).

Values inversion

Once the BCE profile has dimensions (uBCE), next step is to calculate the absolute age of the intermediate samples. For that, every section must be treated separately. The main purpose of the DAM is to calculate the age of the samples for every point present in the BCE, therefore it is necessary to calculate the inverse of the uBCE (iBCE; Fig. 5.1). By this inversion, the model switches from calculating the number of depth units (e.g. mm) deposited per unit of time (e.g. yr) to the number of units of time present per unit of depth.

Determination of SR and age

The age difference between the two tie points located at the top and bottom of every section divided by the summation of the iBCE of every section enables to determine

the mean number of units of depth accumulated per unit of time for each section (mBCE; Fig. 5.1). The mBCE is a scalar number with dimensions of depth units (i.e. mm) and it should be calculated as much mBCE as sections exist. mBCE adds the depth information (and indirectly the age information) of the two tie points that limit every section and it can be considered as a mean SR. The multiplication of mBCE per iBCE determines for every point of every section the difference of units of time (i.e. yr) that exists between two consecutive points (dBCE; Fig. 5.1). Finally, the age for every point of every section can be obtained by consecutively subtracting dBCE to the age of the tie point located at the top of every section. Finally, the DAM is constructed by compiling all the sections into one following their respective stratigraphic depth (Fig. 5.1). The compilation of the n-sections creates a decreasing monotonic age profile in which the age on the top would be the sampling year (if the water/sediment interphase is preserved) and the year on the bottom corresponds to the lowest tie point. The units of the DAM are units of time (i.e. yr) whereas the stratigraphic position of the samples corresponds to the sample depths of the BCE (i.e. mm).

Origin of the uncertainties associated to the Dynamic Age Model

The main sources of uncertainties associated to the DAM might have two origins: one derived from the reproducibility of the XRF measurements and the second one related to the uncertainties of the ages obtained by radiometric methods. Both uncertainties directly affect the calculation of the age of every sample and they must be assessed before (XRF data) and after (radiometric dating) the DAM construction.

During the acquisition of the XRF data the sediments might lose some water in spite of the presence of a thin foil that prevents water loss, among other facts. This slight and progressive sediment dehydration might provoke changes in the response of the XRF signal. Nowadays, the XRF core scanners are prepared to repeat several times one measure every certain number of measurements. These extra measurements allow the user to accurately evaluate the uncertainties associated to the acquisition of the XRF data and, therefore, they are highly recommended to be performed. Nevertheless, the XRF uncertainties associated to the data acquisition (and therefore in the age

calculation of the sequence) are negligible when compared to the uncertainties associated to the radiometric dating ages.

All radiometric dates have associated an age range that includes the analytical errors and the measurement uncertainties. These age ranges follow a Gaussian probability distribution except those derived of the calibration of radiocarbon dates that became more complex (Bennet 1994, Telford et al., 2004). The DAM does not model the age range for every point at the same time that it calculates the central age for every sample. It must be conducted in a second step. The procedure employed by DAM to calculate the age ranges is the same that have been used to construct the age model, but the tie points correspond to the extremes of the age ranges of the dates. Therefore, the DAM must be calculated twice, first with the ages plus one standard deviation (otherwise the oldest ages) of the tie points, and afterwards with the ages minus one standard deviation (i.e., the youngest possible ages). When calculating the DAM for the age extremes, there is no need to restart the process from the beginning because the selection of the BCE remains the same as for the age calculation. Therefore, the calculation of the uncertainties of the DAM should start with the determination of the mBCEs. The final DAM construction results from the plot of the three DAM models. The first one permits to assess the mean age of the samples whereas the two later ones permit to determine the age uncertainties of the samples.

Application to Lake Azul.

The panels of lithological correlation indicated that core AZ11_02 sequence was the most representative of the sedimentary infill of this lake and core AZ11_14 sequences contain higher resolution from the 125 to the 270 mm of core AZ11_02 that corresponds to the section from 185 to 660 mm of the core AZ11_14 (Unit 4).

The chronological model was based on: 1) ^{210}Pb profile (see chapter Material and methods tables 3.1 and 3.2), 2) radiocarbon AMS dates (see chapter Material and methods table 3.3) and, 3) XRF data. The ^{14}C datings were converted to calendar years using the latest online version of the software Calib 7.1 (Stuiver, 1993). According to the ^{210}Pb profile and the five AMS radiocarbon dates AZ11_02 core recovered the lacustrine sedimentary infill (1330 mm thick) from Lake Azul that included the last 660

cal. yr. BP from the top to the 860 mm. For core AZ11_14, the age model has been applied from the top of the core to the deepest tie point at 810 mm. This section recorded the last 520 cal. yr. BP. As mentioned in previous sections, the different facies of the sedimentary infill could produce different responses on the XRF signal. For DAM application purposes, non-volcanic, lacustrine facies of units 2, 3 and 4 could be grouped in two main facies types according to the origin of the organic matter, which are Facies Co deposited by more or less continuously sedimentation (Facies A, B, C and E) and Facies Ra transported by rapid and flashy currents (Facies D and V) (see table 4.1 for equivalences with all facies described in chapter Results). These flood events form discrete dark layers with low XRF signal were easily recognizable because of its instantaneous sedimentation particular nature. Therefore, these layers of Facies Ra were manually removed from the XRF dataset prior to the application of the DAM.

The XRF core scanning was continuously performed from the top of the core to the 1086 mm in core AZ11_02. The coarse surface of the tephra at the top of Unit 1 made impossible the acquisition of the signal for the lowest 330 mm. The core AZ11_14 was

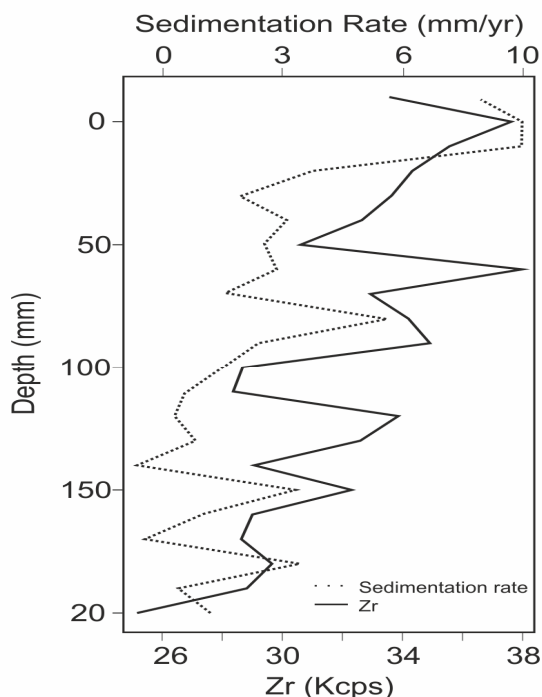


Figure 5.2: Comparison of the Sedimentation rate values in mm/yr obtained from the application of the Constant Rate of Sedimentation (CRS) model to the ^{210}Pb data and the Zircon (the Best Correlated Element in the case study) in counts per second. Note the good agreement between both curves.

analyzed from the top to the 1480 mm but, the age modelling was performed from the top to the deepest tie point at 860 mm. A statistical median of 5 XRF measurements was applied to the uppermost 210 mm in core AZ11_02 and for the upper 810 mm in the core AZ11_14 in order to obtain the median value for every centimeter. These median XRF values were compared with the ^{210}Pb data to calculate the Pearson product-moment correlation coefficients. The BCE selected for AZ11_02 was the

zirconium (Zr) because the r value was the highest ($r=0.65$) and the p -value was 0.001 (Fig 5.2). The subenvironmental location for the core AZ11_14 changed a bit. Therefore, the BCE selected was the Strontium (Sr) for the same reasons mentioned above ($r=0.54$, $p<0.05$).

The procedure performed for core AZ11_02 and AZ11_14 was identical. Then, to avoid redundancy, only the core AZ11_02 is going to be explained in detail. In order to follow the DAM procedure steps see figure 5.1 scheme.

The tie points used to construct the DAM were five: the core retrieval year (2011 AD), the $^{210}\text{Pb}_{\text{ex}}$ onset at 210 mm of core depth and the three selected AMS ^{14}C dates (Fig. 5.3). The ^{210}Pb profile did not reveal any sediment loss and the first tie point were assigned to the uppermost centimeter of the core corresponding to 2011 AD, when the field coring survey was conducted. The associated error to the first tie point was, therefore, negligible. The five tie points divided the core in four sections (Fig. 5.3). From top to bottom, the second tie point was at 210 mm corresponding to the $^{210}\text{Pb}_{\text{ex}}$ onset (1868 AD). The following tie points were located at 460, 610 and 860 mm corresponding to 1770, 1475 and 1290 AD, respectively (Fig 5.3). In spite of the tephra deposit from the last eruption in Sete Cidades Caldera (Booth et al., 1978, Cole et al., 2008) was recorded, mixed with some lacustrine fine facies, in the lower part of the core and its age was well-constrained, the lithological point where this tephra dominated unit ends was not well recorded in the retrieved sediments. Therefore, from the 860 mm to the bottom of the core, the DAM has not been applied.

The highest (10.46 mm/yr) and lowest (0.32 mm/yr) SRs calculated from the ^{210}Pb profile were assigned to 1 and 0.01 values, respectively, and the entire BCE was binarized accordingly. As stated above, the binarization was carried out per sections in order to maximize the variance of the Zr. The unit assignment to the entire bBCE was carried out by linear regression between the ^{210}Pb ages and the entire bBCE. The obtained profile (uBCE) had now the units of mm/yr (Fig. 5.1). The inversion of uBCE (iBCE) switched the units of this profile from mm/yr to yr/mm. The addition of the five available tie points to the iBCE obliged us to divide again this profile in 4 sections (Fig 5.1). From this point on, the calculations were carried 4 times, one per section. For

every section, the top and bottom tie point age difference was divided by the summation of the iBCE of the correspondent section. Finally, four mBCE were obtained (0.55, 0.28, 1.37 and 0.05, respectively). Then, the iBCE of the first section was multiplied by 0.55, the iBCE of the second one per 0.28, the third one per 1.37, and finally the iBCE of the fourth one was multiplied per 0.05. These multiplications resulted in the obtainment of four profiles (dBCE) that consisted in the age difference between samples. The absolute ages of the samples for every section were obtained by subtracting to the age difference profile (dBCE) the age of the top tie point. Finally, the DAM for Lake Azul was achieved merging in stratigraphic order the results obtained in the previous step (Fig. 5.1).

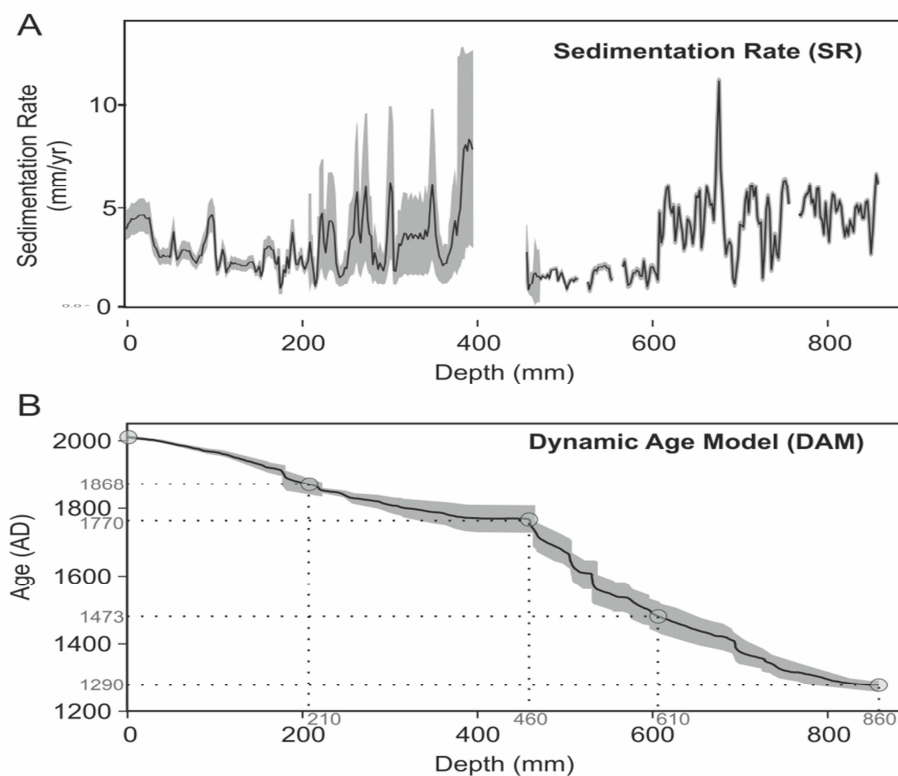


Figure 5.3: A. Sedimentation rate profile obtained by the application of the DAM from the top of the core AZ11_02 (0 cm) to the lowest tie point (860 mm). In grey color, the error of the SR profile that is also obtained from the application of the DAM model but based on \pm one standard deviation of the ^{14}C and ^{210}Pb dating errors. Gaps in the curve correspond to rapid (instantaneous-like) flood events (Facies Ra). Note that the greatest error is found between 200 and 400 mm depth, above (left) the major flood event. B. The age model profile obtained from the application of the DAM. The age on the top (0 mm) is 2011 AD (year of the core retrieval) and the age on the bottom (860 mm) is 1290 AD (year of the lowest tie point). The ages and depths values of the tie points are grey colored and graphically represented by circles. The error is related with ^{14}C and ^{210}Pb dating errors and calculated by means of the DAM but based on \pm one standard deviation of the ^{14}C and ^{210}Pb dating errors (see text for further details). The grey circles make reference to the tie points used in the DAM construction.

The age model and the sedimentation rate obtained were shown in Figure 5.3. The sedimentation rate profile comprised values between 0.046 mm/yr and 10.46 mm/yr

with the exception of the flood events that accumulated the sediment instantaneously. The thickest flood event was from 390 to 460 mm depth but, usually these events varied from 2 to 40 mm thick. From top to 180 mm, the sedimentation rate profile has a roughly decreasing trend despite four moments of increasing sedimentation at 6, 20, 96 and 190 mm. From 180 to 390 mm, the intensification on the sediment accretion reaches its maximum at 380 mm. From 460 to 600 mm, the sedimentation profile was quite homogenous despite some peaking points. From 600 to 860 mm an increasing trend was observed with a peak around 674 mm. The maximum sedimentation rate for this section was found at 674 mm. The age model was characterized by moments of regular sedimentation rate, and moments of abrupt changes. These moments of abrupt changes usually appeared at the flood event sites. These events appeared more often on the units 3 but, they were thicker in the lower part of the unit 4. The uncertainty introduced by the reproducibility of the XRF measurements was negligible compared to the ^{14}C uncertainty. Therefore, it was not accounted. The uncertainties associated to the radiocarbon calibration were used to calculate the uncertainties of the age model. For that, the age-depth model was calculated using the central calendar year minus the uncertainty and the central calendar year plus the uncertainty.

The age-depth model for the core AZ11_14 was calculated in the same way than for the core AZ11_02 (Fig. 5.4). The sedimentation rate profile of the former core display values between 0.5 mm/yr and 6 mm/yr. From 0 mm to 150 mm, the sedimentation rate oscillated between 1 mm/yr and 3 mm/yr without any noticeable trend. The following downwards 100 mm were characterized by an increasing trend that culminates at the upper flood event. From the flood event onset (≈ 250 mm) to the 500 mm, the sedimentation rate oscillated around 2 mm/yr except for the two peaking points around 300 and 400 mm. At 510 mm of core depth, the sedimentation rate increased drastically reaching values of 6 mm/yr. From 520 mm to 700 mm, the sedimentation rate tended to decrease reaching the lowest value of the entire profile. From this point to almost the 800 mm, the sedimentation increased dropping at the end of the profile (lowest 100 mm).

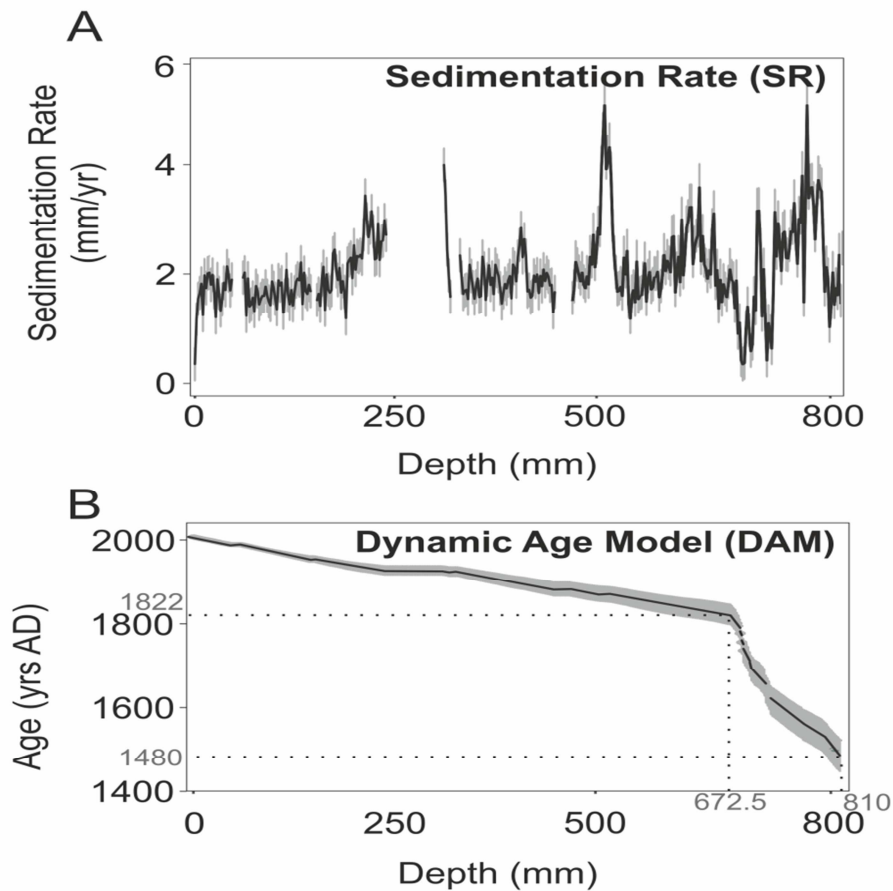


Figure 5.4: A. Sedimentation rate profile obtained by the application of the DAM from the top of the core AZ11_14 (0 cm) to the lowest tie point (810 mm). In grey color, the error of the SR profile that is also obtained from the application of the DAM model but based on \pm one standard deviation of the ^{14}C and ^{210}Pb dating errors. Gaps in the curve correspond to rapid (instantaneous-like) flood events (Facies Ra). Note that the error does not have significant changes along the profile. B. The age model profile obtained from the application of the DAM. The age on the top (0 mm) is 2011 AD (year of the core retrieval) and the age on the bottom (810 mm) is 1480 AD (year of the lowest tie point). The ages and depths values of the tie points are grey colored and graphically represented by circles. The error is related with ^{14}C and ^{210}Pb dating errors and calculated by means of the DAM but based on \pm one standard deviation of the ^{14}C and ^{210}Pb dating errors (see text for further details). The grey circles make reference to the tie points used in the DAM construction.

The age of the samples comprised between 860 mm and 1330 mm, where the first pollen remains appear, was obtained by applying a linear regression model assuming that the lithology of the bottom of the core represents the latest phase of the last volcanic eruption (P17) that affected the lake. This eruption was dated at 6700 \pm 30 cal. yrs BP (Shotton and Williams, 1971). These lowermost 470 mm correspond to the lacustrine-volcaniclastic units 1 and 2 and it was not possible to obtain reliable XRF measurements due to the high roughness of the core surface. According to the

obtained results, the recovered lacustrine sedimentary infill (Units 1, 2, 3 and 4; 1330 mm thick) from Lake Azul records the last 660 +/- 20 cal. yrs BP.

Comparison between the DAM and other age-depth models

The SR in siliciclastic lakes, as Lake Azul, is mainly determined by terrigenous inputs triggered by precipitation which enhances the soil erosion and transport capacity of streams and rivers (Peng, 2005). Therefore, variations in the SR of the Lake Azul record would be mainly related to fluctuations in the precipitation.

This hypothesis can be a useful tool to test and compare the accuracy of the DAM with previous age model approaches to reconstruct the variable SRs of records highly influenced by siliciclastic inputs. For this purpose, we compared the reconstructed SR using three age-depth models from different statistical approaches with the meteorological precipitation record (1936 – 2011 AD) from Sete Cidades. The employed age-depth models were the widely used mixed-effect regression by Heegaard et al. (2005) and Bayesian (Bacon) software by Blaauw and Christen (2011), as well as the new DAM presented in this thesis (Fig. 5.5).

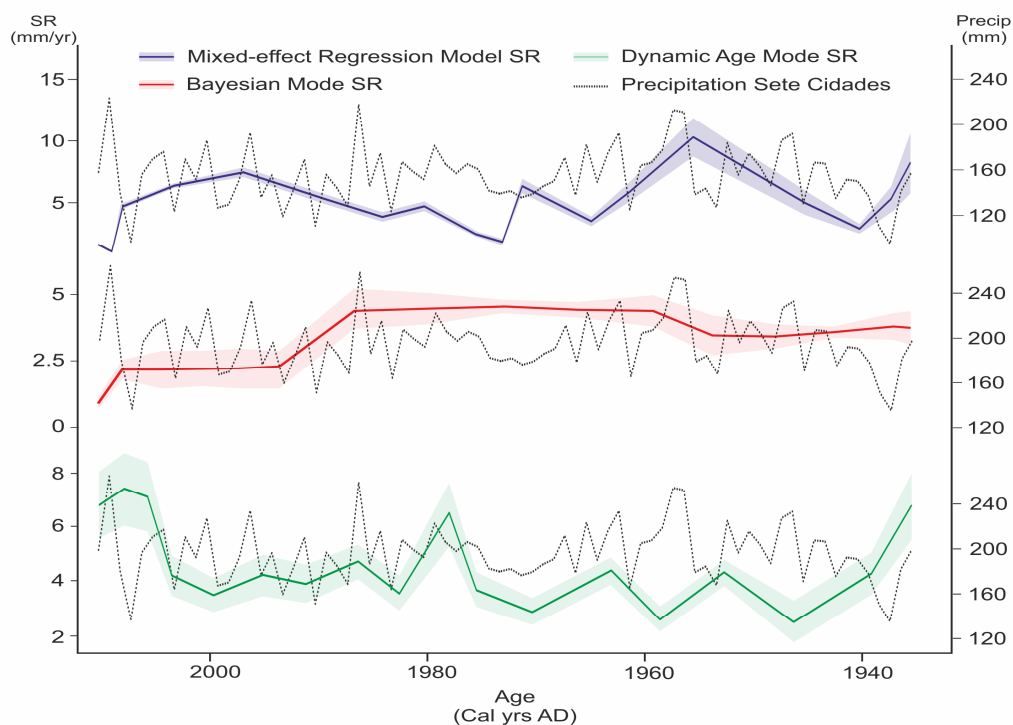


Figure 5.5: Sedimentation rate obtained from Dynamic Age Model (DAM, green color), Bayesian (Bacon, red color) and Mixed-effect Regression (Heegaard, blue color) models applied to the upper part of core AZ11_02. Models uncertainties are represented by shadow bands. The models have been plotted against the mean annual precipitation data from Sete Cidades meteorological station (dashed black lines). See text for a detailed discussion.

Figure 5.5 shows that the unique age-depth model capturing both long- (decadal) and a short-term (multiannual) fluctuation in the SR is the DAM. The main precipitation changes fit better with fluctuations in the calculated SR of the DAM than the others. Nevertheless, the adjust between both curves is not perfect most possibly because of both the chronological uncertainties of the radiometric dates and that non-varved lakes commonly act as a low-pass filters smoothing out the annual signal (Giralt et al., 2011, Hernández et al., 2015). The SR modeled using the mixed-effect regression follow the long-term precipitation fluctuations but fail to record the short-term oscillations (Fig. 5.5). The obtained SR using the age-depth model obtained with the Bacon software does not encompasses neither the long- and short-term fluctuations displayed by the precipitation. The most probably reason for this disagreement is that both models assume more or less explicitly that the sedimentary systems have “memory”, namely the SR of the previous sample determines the following one. Whereas the mixed-regression model do not allow to the user to modify this assumption, the Bacon software permits the user to modify this “memory” to a certain degree of freedom by adding to the model the prior knowledge that the user possesses of the studied core (Blaauw and Christen, 2011). Even with this possibility of “memory” modification, the Bacon software does not capture correctly these abrupt sedimentation changes. By contrast, the new DAM assumes the opposite perspective: that the sedimentary system has no “memory”, namely the SR of the previous sample is unrelated to the SR of the following one.

5.2 PRESENT DAY ATMOSPHERE AND OCEAN DYNAMICS AND THEIR IMPACT ON SÃO MIGUEL'S TEMPERATURE AND PRECIPITATION.

The air temperature in Ponta Delgada shows an increasing trend for the last century of about 1.4 °C displaying multidecadal variability. Similar results were observed for the North Atlantic Ocean (Desser et al., 2010) despite of the zonally variable temperature of the ocean (van Hengstum et al., 2015).

Some authors have suggested that the temperature oscillations in the North Atlantic are triggered by different forcings such as the Total Solar Irradiation (TSI, Mayewski et al., 2004; Moffa-Sanchez et al., 2014), the volcanic activity (Wannamaker et al., 2012) and changes in the SSTs and the oceanic currents (Moffa-Sanchez et al., 2014, Borkman et al., 2009).

The TSI and the volcanic activity are two important and complex forcings that might partially rule the climate variability of the Azores archipelago but their complex interaction with the climate variables deserves a special attention that it is not the main purpose of this PhD Thesis. The present work has focused on the SSTs and oceanic currents. In any case, the SSTs and the oceanic currents are partially influenced by the TSI.

The Lake Azul sedimentary record can be considered a marine record in spite of being a lacustrine one owing to it is located in the middle of the Atlantic Ocean. In fact, one of the main climate features of the Azores archipelago is that it can be classified as oceanic temperate due to the significant role that plays the oceanic currents and the SSTs in modulating the climate of these tiny islands.

Temperature changes in the North Atlantic Ocean are mainly governed by fluctuations in the ocean currents and SSTs (Moffa-Sanchez et al., 2014, Borkman et al., 2009) which in turn are mainly driven by two forcings: the solar radiation and the rotation of the Earth (“Sciencedaily”, 2016).

The solar radiation affects the ocean in two ways; (1) heating the atmosphere creating winds which move the sea surface through friction dragging the water surface as the wind blows over it, and (2) altering the density of the ocean surface water directly by

changing its SSTs and/or its salinity (“Sciencedaily”, 2016). If the ocean's water is cooled or becomes saltier through evaporation, it becomes denser, and vice versa. This can result in the water column instability, setting up density-dependent currents, also known as the thermohaline circulation (“Currents”, 2015).

The rotation of the Earth affects the ocean currents through the Coriolis force by moving the water to the right in the Northern Hemisphere and to the left in the Southern one. The Coriolis exists because only at the seafloor the moving ocean water is affected by friction with the seafloor and because the eastward linear velocity of the Earth decreases towards the poles. However, the rotational velocity of the water does not change.

Moreover, there are other forcings affecting the SSTs and the oceanic currents relationship. Previous works have mentioned the role of the NAO in the North Atlantic oceanic currents (Moffa-Sanchez et al., 2014; Wannamaker et al., 2012; Bartolomé et al., 2015; Lund et al., 2006). The NAO affects the modulation of the Eddy Kinetic Energy (EKE), which in turn, marks the position of the Gulf Stream North Wall (GSNW) affecting the Gulf Stream (GS) direction. A NAO+ phase increases the EKE (Borkman and Smayda, 2009), which in turn displaces towards northern latitudes the GSNW and this displacement affects the Gulf Stream (GS) direction driving it towards northern latitudes (Taylor and Stephens, 1998; Hamned and Piontkovski, 2004; Curry and McCartney, 2001). Those changes on GS direction (Taylor et al., 1997) and velocity (Olsen et al., 2012; Trouet et al., 2009) affects temperature in the north Atlantic, deep water production dynamics (Olsen et al., 2012), and even, ocean productivity (Borkman and Smayda, 2009).

These ocean current changes modify the latent heat flux balance for a given location. Since it has been largely demonstrated that air temperature and SSTs are closely related, changes in the SSTs should, at least, partially rule the air temperature changes of the islands (Curry and McCartney, 2001).

The best way to determine the relationship between the mean annual air temperature (MAT) of Ponta Delgada and the Atlantic ocean currents around the island was to calculate the correlation between the SST and MAT for the area enclosed between the

coordinates 80° to 20° W and from 23° to 45° N and to compare the obtained SST annual temperature with that from the meteorological instrumental series. Pearson's correlation between both temporal series was significant ($p < 0.05$) but, it was relatively low ($r = 0.4$). Therefore, air temperatures and SSTs are partially related, suggesting that a common forcing is ruling them.

The correlation between SSTs and the magnitude of the vector defined by the oceanic currents for the aforementioned area will inform about the pathways of the oceanic currents. A negative or null correlation would imply that despite the ocean velocity might be high; the SSTs will be low suggesting that the warm currents pathway did not choose that specific pathway. Otherwise, a positive correlation between the resultant velocity vector and the SSTs will imply that an increase on temperature in this area is related to an increase on currents velocity. Increased water current velocities might imply that larger volumes of warmer water might arrive farther. But, the ocean currents pathway also implies a given direction of this warmer water. An increase on the zonal velocity of the GS reduces the distance between the São Miguel Island and this current, also shortening the distance with the AzC. The variable distance between São Miguel island and the oceanic GS and AzC currents might have significant consequences on the air temperature of the island, modulating it. Since the NAO climate mode partly rules the EKE, and hence the velocity of the ocean surface currents, the relationship between the SSTs and the magnitude of the ocean currents vector have been investigated separately for the years with a positive phase and for the negative phase of NAO. The results of the Pearson's product moment correlation for the positive (superior) and negative (inferior) NAO phases can be observed in Figure 5.6.

It is worth noting the significant differences of surface water circulation and SSTs during the positive and the negative NAO modes. During NAO+, warmer and faster water masses of the GS are driven towards northern latitudes, warming the eastern coast of US (Fig. 5.6). This northwards trajectory of the GS produces an area of low correlation values in the middle of the north Atlantic that englobes the Azores surroundings ($r = -0.4$, $p < 0.05$). This negative correlation implies that during the NAO+, the surface waters around São Miguel Island, and therefore its mean air temperatures, would be colder

than the mean values. On the other hand, during NAO- a zonal movement of the GS, from Caribbean towards Iberian Peninsula is produced, increasing the possibilities of warmer surficial waters to reach the Azores archipelago. The correlation values for the surrounding area of Azores archipelago are positive and significant ($r= 0.51, p<0.05$), suggesting that during the NAO- phase, the surficial waters around Sao Miguel Island, and therefore its mean air temperatures, would be warmer than the mean values. Similar results were already observed by Björk et al., (2006).

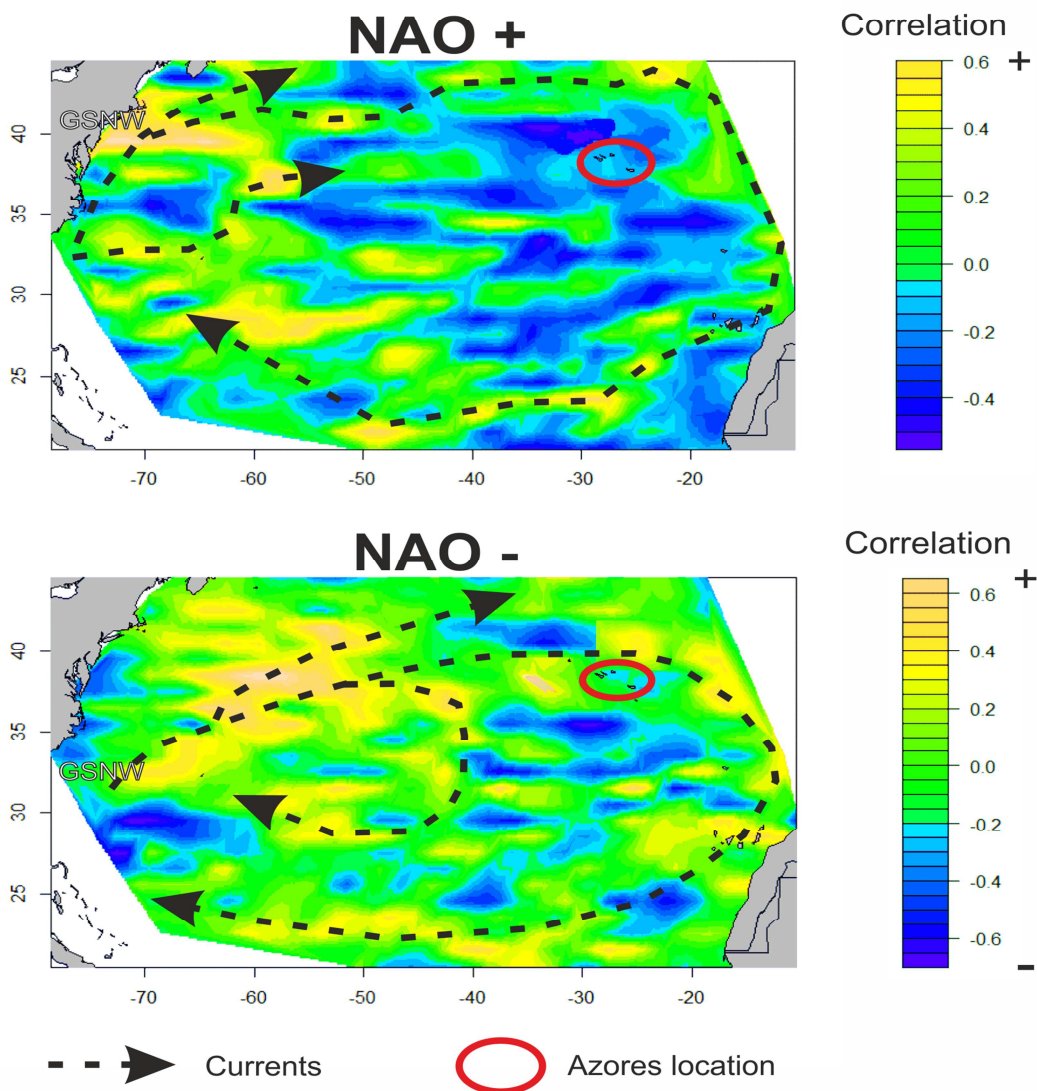


Figure 5.6: Maps of North Atlantic showing the variations of Pearson product-moment correlation between the resultant oceanic current vector and the SST each degree for the area comprised between 80° to 20° W and from 23° to 45° N. The data were obtained for the period between 1992 and 2015 from the OSCAR-NOAA. The dataset was divided for years of NAO negative (upper map) and years of NAO positive phase (lower map). The mean annual NAO data were extracted from NOAA. Yellow-orange colors mean a positive correlation, dark-blue colors mean a negative correlation and green colors mean no-correlation or low correlation. The black arrows are interpreted as likely oceanic currents pathways. The red circle establishes the position of Azores archipelago. The GSNW means the position in the North Atlantic coast of the Gulf Stream North Wall. Note that different NAO phase produces different oceanic currents pathways selection.

It is noticeable the lack of correlation between the SSTs and the vector of the ocean currents both during the positive and negative phases of the NAO just in the vicinity of the Azores archipelago. This might be explained by two possible factors: 1) the island or seamount effect (Bashmachnikov et al, 2004) and, 2) the upwelling phenomenon that occurs around the islands (Morato et al., 2013). The seamounts usually modify the water circulation, creating a typical structure called Taylor's column that cause the upwelling of intermediate waters that decrease the surficial sea temperature, increase the nutrients, and consequently, the biological productivity (Aristegui et al., 2009). Despite of that, the temperature variations of Ponta Delgada seems to be governed by a wider geographical area.

The different path followed by the ocean water currents in both climate scenarios implies that the bifurcation of the AzC occurs in a different geographical location. The NAO+ phase favors the AzC bifurcation from the GS in a more northwestern position regarding to the Azores location, what makes more difficult to the AzC to reach the archipelago. During the NAO- phase, the AzC path is located in northern positions with respect to the Azores archipelago, facilitating its reach to these Portuguese islands. Volvok and Fu (2011) also suggested the relationship between the increases (decreases) of eddy vorticity of the AzC, and hence its stronger (weaker) eastwards flow during the NAO+ (NAO-) phase using altimetry data and climate reanalysis data.

Trouet et al. (2009) described similar oceanic mechanisms but with different result. These authors found that under the NAO+ phase enhanced North Atlantic Current (NAC; GS continuity) velocity increased the temperature at northern latitudes. This enhancement of velocity currents towards northern latitudes has been observed in this PhD Thesis, but the AA suffered a decrease in temperature. This fact could be explained by the rapid transport of the GS that produces a minimum heat lost that rapidly reach north latitudes incrementing temperatures. Therefore, it is expected that temperatures at the coldest sites of the North Atlantic will increase during the NAO+ phase.

Another factor playing an important role on the North Atlantic temperature is the Atlantic Meridional Oscillation (AMO) (Schlesinger et al., 1994). The AMO describe, in

terms of surface temperature, variations on the Thermohaline Circulation (THC) that, in turn, affects the oceanic currents such as the GS or the NAC (Schlesinger et al., 1994). These fluctuations on the ocean currents are reflected in the SSTs of the North Atlantic, which might be described in two phases of AMO: one warm phase and other cold one (Kushnir, 1994). The warm AMO is characterized by a temperature increase in the north Atlantic, an intensification of the ocean currents, certain regimes of precipitation in America and Sahel area, and an increase in the intensity and frequency of the hurricanes (Goldenberg et al., 2001). The cold phase of the AMO would rule the inverse climate conditions. These climate changes are mainly produced during summer season (Goldenberg et al., 2001). The available instrumental data shows that the AMO warm phases have been observed from 1860 to 1880 AD and from 1940 to 1960 AD, whereas the cold ones have been observed from 1905 to 1925 AD and from 1970 to 1990 AD (Endfield et al., 2001). Since the air temperature in Ponta Delgada is related to the ocean temperature, a positive AMO phase should imply an increase on temperature in Ponta Delgada and vice versa. Therefore, the AMO index has been compared with the MAT showing no significant results despite of the first years of the record showed similar variability (Fig. 5.7). Nevertheless, when comparing the long-term fluctuations of maximum MAT and AMO, both signals showed the similar trends suggesting that the AMO exerted its influence on the maximum MAT at decadal scale (Fig 5.8). The period from 1940 to 1960 AD, corresponds to a warm phase of AMO (Endfield et al., 2001), this period observed in Ponta Delgada temperatures the highest amplitude between minimum and maximum MAT suggesting an increase on seasonality during this period. We suggest that the temperature amplitude between maximum and minimum MAT is created by two reason: 1) the AMO is dominant during the summer (Marini and Frankignoul, 2014) when the NAO has less influence; 2) the increase on currents velocity during AMO positive, increases the northwards trajectory of the GS that could be enhanced by a persistent NAO positive phase decreasing temperature in Azores. Hernández et al., (2016) already observed for precipitation that the influence of NAO increase when the influence of NAO decrease.

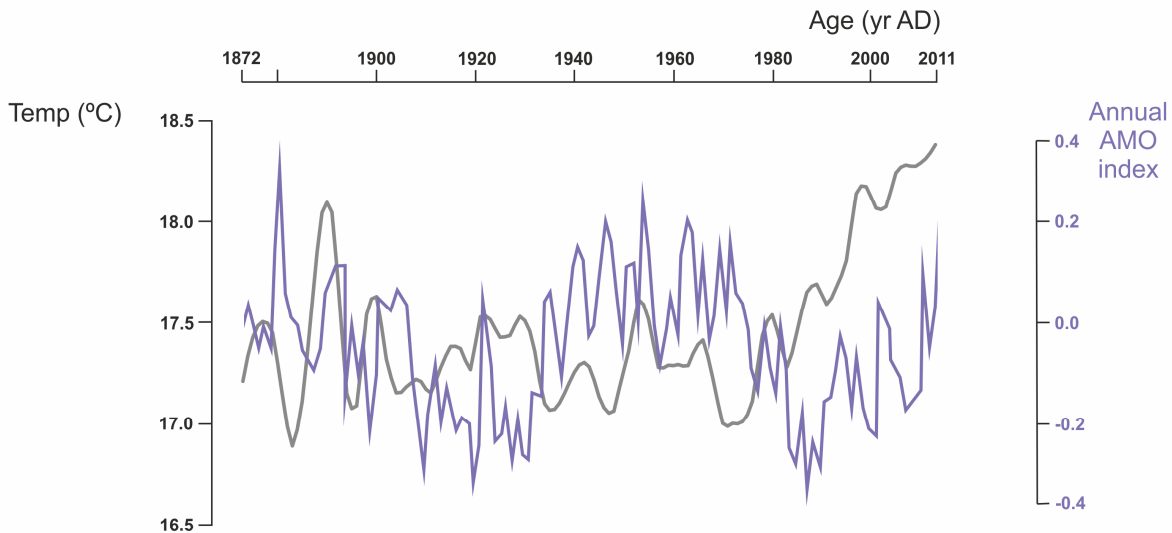


Figure 5.7: Graphical comparison between the mean annual temperature in Ponta Delgada (grey line) in degree Celsius and AMO index (purple line). The mean annual temperature was obtained by the application of the mean to the daily data acquired for the period between 1873 and 1946 AD from the 'Annaes do Observatório Infante D. Luiz' and for the period between 1947 and 2012 AD were supplied by (IPMA). The AMO index data were acquired from the NOAA-ESRL. Note that long-term fluctuations in the AMO are not observed in the mean annual temperature in Ponta Delgada.

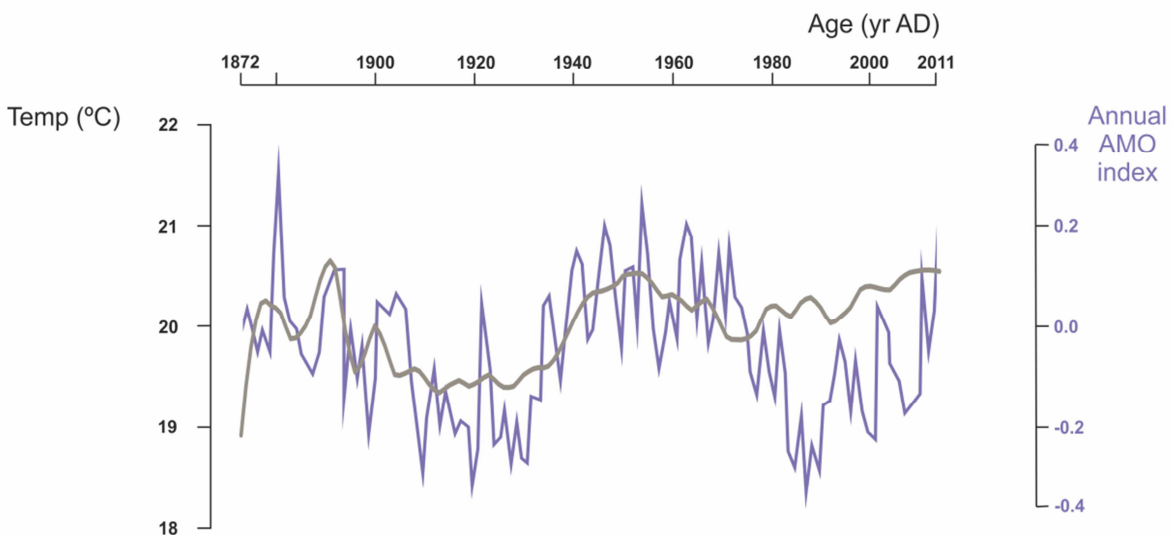


Figure 5.8: Graphical comparison between the mean maximum annual temperature in Ponta Delgada (grey line) in degree Celsius and AMO index (purple line). The mean maximum annual temperature was obtained by the application of the mean to the daily data acquired for the period between 1873 and 1946 AD from the 'Annaes do Observatório Infante D. Luiz' and for the period between 1947 and 2012 AD were supplied by (IPMA). The AMO index data were acquired from the NOAA-ESRL. Note that long-term AMO fluctuations are observed in the mean maximum temperature.

Origin and changes of the precipitation in S. Miquel Island

The path of the storms tracks that crosses the North Atlantic and produce rainfall in most of the Atlantic European facade can be easily tracked using the isotopic composition (δD) of the rain water (Araguas-Araguas, 2000).

The backtracking of the vapor masses reaching São Miguel Island has been obtained using the Hysplit software. For the studied 114 weeks of Ponta Delgada rainfall, five origin places have been determined: a) North America (NA, 62 weeks), b) moving around Atlantic (AT, 38 weeks), c) Gulf of Mexico (GM, 11 weeks), d) Europe (EU, 2 weeks) and, Sahara (SAH, 1 week). The available data from the most predominant three vapor mass origins (NA, AT and GM) were plotted in a boxplot against δD (Fig 5.9). This figure highlights that δD signature for all waters from NA, AT and GM did not account with significant differences. The reason for this is that probably the air masses reaching Azores are recharged in the Atlantic Ocean. In fact, the isotopic values of the water surface from the North Atlantic Ocean (mean δD -3 ‰, Araguas-Araguas et al., 2000) are quite similar to the mean isotopic precipitation value (δD mean -4.7 ‰ standard deviation 3.6 ‰) recorded in Ponta Delgada.

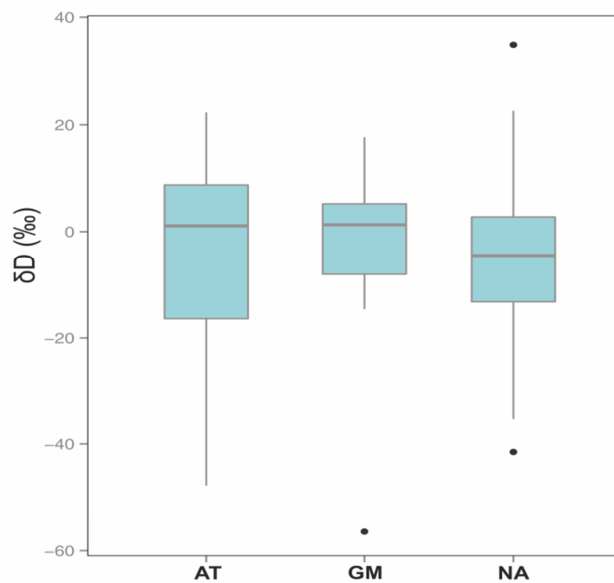


Figure 5.9: Boxplot representing the three most recurrent air mass track producing precipitation in Azores compared to the δD signal. The δD signal has been acquired weekly from real precipitation data collected from the upper terrace of the University of Azores and analyzed at the CCTiUB. The air mass tracks were obtained by the use of the Hybrid Single Particle Lagrangian Integrated Trajectory Model (HYSPLIT) software (see section 3.6 for initial acquisition modelling parameters). AT air mass is used for air masses that move through the north Atlantic before produce rainfalls in Ponta Delgada, GM means Gulf of Mexico origin and NA is used for United States and Canada origin. Note that the three air mass track do not show significant differences on δD signal.

The rain water isotope composition depends on the origin of precipitation, the air temperature, elevation and/or the total amount of precipitation. The three forcings might produce different isotope fractionations (Dansgard, 1964; Araguas-Araguas, 2000).

Temperature fractionation usually occurs because an increase on air temperature produces an enhancement of the evaporation, removing the lighter hydrogen from the surface ocean waters (Araguas-Araguas, 2000). The comparison between the δD and

the MAT series for the period 1873 – 2012 AD produced no significant correlation ($r=0.14$; $p>0.05$), thus, suggesting that evaporation does not play a significant role in determining the hydrogen isotopic composition (δD) of the precipitation water.

The fractionation due to the altitude is not observed in the Ponta Delgada rain water because this place is located at sea level. Moreover, São Miguel Island does not have enough high peaks to observe this phenomenon. This type of fractionation has been observed at high elevation places such as Andes mountain range (Anderson et al., 2015). The effects derived from the continentalism are not accounted for this site because Ponta Delgada is located in the coast and Lake Azul close to it.

The hydrogen fractionation can be also related to the amount of precipitation because at the beginning of a rainfall, the falling drops are heavier than the last falling drops of the precipitation event (Araguas-Araguas, 2000). Therefore, the water from short or light rainfall events accounted with heavier composition than long or more intense events. This is known as the amount effect (Dansgaard, 1964). Since isotopic rainfall data had a weekly resolution, the weekly weighted average was calculated giving the highest weight to the most intense rainfall episodes for the weeks with a unique air mass origin. The origin means the location of the air mass 72 hours before reach Azores (see Material and Methods for further information). The isotope values were plotted against the weekly precipitation weighted average (Fig 5.10). Isotopic composition correlation with amount of precipitation showed a linear significant correlation ($r=-0.84$, $p<0.01$) suggesting that the δD can be used as a proxy to reconstruct precipitation amount fluctuations in the Azores islands.

The Spearman correlation coefficient, after removal of NAO neutral, between precipitation and NAO showed a value of $r=-0.74$ for the winter and $r=-0.51$ for the summer (Hernández et al., 2015). These authors observed that NAO- phase is associated with more continuous rainfall events but, not related to the intensity of these events. Andrade et al., (2008) suggested that intense rainfalls are more common during the NAO- phase. Based on that, the weighting average of the weekly precipitation might proportionate variations on NAO effects in São Miguel. For that reason, differences between the NAO phase and the δD of the precipitation collected

must be detected. In order to find this out, the mean has been applied to the rain water δD samples retrieved in a month to obtain the mean month δD value. The monthly δD data were separated in NAO+ months and NAO- months. Finally, the mean and standard deviation was applied to the months with NAO+ and the months with NAO-. The months with NAO+ showed a mean value of 4.15 ‰ with a standard deviation of 6 ‰. In the other hand, the NAO- months had a mean value of -5.18 ‰ with a standard deviation of 5 ‰. Those data showed significant differences despite of the small dataset size.

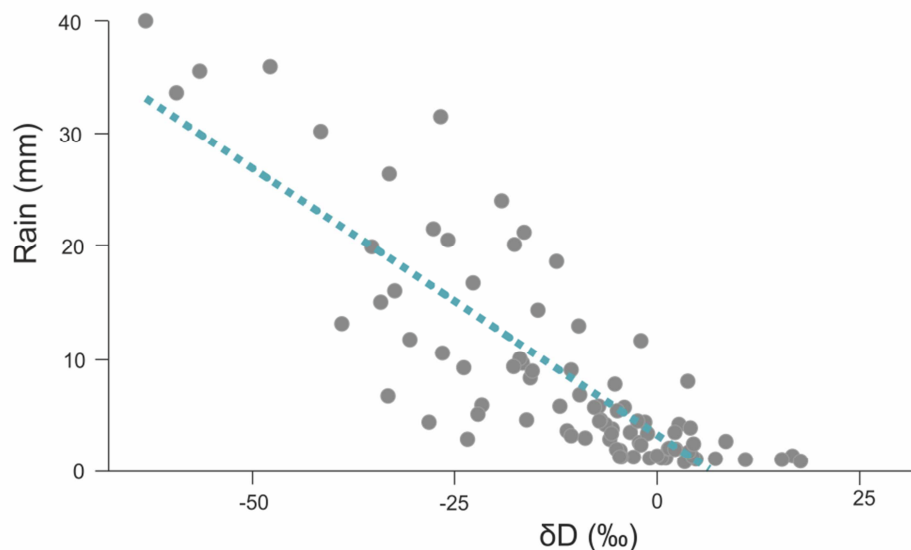


Figure 5.10: Linear regression between δD data obtained from real precipitation data collected from the upper terrace of the University of Azores and analyzed at the CCTiUB and precipitation supplied by IPMA. The light-blue dashed line shows the linear regression and the grey circles the scatter data. Note that there is a good linear fitting between these two variables (see text for further information and linear regression values).

In summary, the δD rain data are recording the amount of precipitation registered weekly. Therefore, this rainfall amount in the Azores archipelago is mainly modified by the NAO phase.

The rain water falls to the ground giving to the soil and soil-water similar isotopic composition (Lawrence and Taylor, 1971). The isotopic composition of the water present in the soil can suffer enrichment due to evaporation. This kind of fractionation is marked on arid climates (Sachse et al., 2012 and references therein). São Miguel Island with a mean annual precipitation of 958 mm does not suffer extreme aridity even on summer. This water is taken by plants to maintain their living conditions and

for biosynthetic purposes. Among other biosynthetic purposes, the photosynthetic pathway is an important via of fractionation (Sachse et al., 2012). A different photosynthetic pathway implies differences in the fractionation. These differences have been previously reported in some works (Polissar and Freeman 2010; Collins et al., 2013). The palinological study of Lake Azul sediments (Dr Valentí Rull work in progress) has shown that the vegetation in the catchment area was formed by plants using the same metabolic pathway (C_3). In fact, variations on δD triggered by humidity and/or photosynthetic pathways have been found to be almost negligible compared to the water source in eastern Africa (Collins et al., 2013). Therefore, no correction was applied to the δD on sediments.

The plants also suffered evapotranspiration fractionation (enrichment in the δD plant) that is more intense on arid climates (Sachse et al., 2012 and references therein). The living plants also produce lipids that cover leaves to protect cells by different mechanisms producing fractionation (see introduction for further details). This lipid cover is called the leaf wax. Those leaves covered with wax fall into the lake directly or fall into the ground and are dragged to the lake by wind or precipitation water. This dragging towards the lake occurs in a very short-scale (days or months). Once inside the lake, those leaves sink until the lake floor where they get sedimented after degradation (Sachse et al., 2012). The degradation of the major part of the leaf organelles occur in a short-timing but, the lipids get preserved at least until late Pleistocene (Cranwell, 1988; Sachse et al., 2012). Previous works have reconstructed changes on precipitation by using δD in ice cores (Thompson et al., 1985 and 2003) in the lacustrine sediments (von Grafensten et al., 1999; Tierney et al., 2008; Fornace et al., 2014) and in the water ocean (Scheffuß et al., 2005; Collins et al., 2013).

Whereas the precipitation δD samples omitted the evaporation because the collector was prepared to avoid that, the Lake Azul water is effectively affected by evaporation and precipitation. Therefore, Lake Azul δD record should display variations on Evaporation/Precipitation ratios. São Miguel Island has a humid climate except for the summer, which is not totally dry; therefore, variations on precipitation are going to influence more than evaporation on δD . The evaporation factor should not be omitted.

5.3 TEMPERATURE RECONSTRUCTION BY GDGTS AND PRECIPITATION BY δD LEAF WAXES USING LACUSTRINE SEDIMENTS: THE LAKE AZUL CASE.

Temperature calibration from GDGTs.

In order to qualitatively reconstruct the air temperature, two main approaches can be followed: 1) to build an specific temperature transfer function for the studied site or 2) employ one of the already available calibrations (Weijers et al., 2007; Tierney et al., 2009; Pearson et al., 2010; Sun et al., 2010; Loomis et al., 2012).

Local transfer function construction. The construction of an adhoc transfer function requires that the temporal resolution for the overlapping period between the meteorological instrumental data and the GDGTs data must be the same. The last 138 years that cover the instrumental meteorological series from the Ponta Delgada Meteorological Station are also recorded in the sediments between the top of the core and the 205 mm of core depth (upper part of Unit 4). This part of the core was subsampled at constant interval thickness of 5 mm but, according to the age-depth model, this spatial resolution is not constant in time. The time interval contained at each sample responds to a Gaussian function in which the central year is the expected value and the edges of the time interval are the tails of the variance. Therefore, the instrumental temperature has been sampled accordingly to the age of the sediment and following this Gaussian function. In order to apply the Gaussian function, the temperature has been calculated by a weighting average, in which, the temperature from the expected year has been bestowed with more weight than the tails. This Gaussian distribution procedure has been applied to the MAT, for winter (wTemp), spring (spTemp), summer (suTemp) and the autumn (auTemp). These temperatures have been compared with the branched GDGT (brGDGT) data because they were 10 times more abundant than the isoprenoidal GDGT (isoGDGT).

Pearson's product moment correlation coefficients between GDGTs and wTemp, auTemp or spTemp were not significant for any GDGT specie whereas the correlation between GDGTs and suTemp and MAT were significant for more than one GDGT species (Table 5.5). The GDGT species are presented in the Introduction chapter and represented in the figure 1.4. The mean suTemp was highly correlated with GDGT-IIIb

($r=0.62$, $p<0.05$) and GDGT-IIIc ($r=0.60$, $p<0.05$). Besides, MAT found its strongest correlation with GDGT-IIIb ($r=0.64$, $p<0.05$) and GDGT-IIIc ($r=0.62$, $p<0.05$). MAT was also significantly correlated with GDGT-I ($r=-0.5$, $p<0.05$), GDGT-Ic ($r=0.47$, $p<0.05$) and GDGT-IIc ($r=0.42$, $p<0.05$). Other authors have found that GDGT-IIIb is not correlated with the MAT, but strongly related to pH and that GDGT-IIIc is directly related to water depth (Tierney et al., 2010) and, indirectly, to O_2 concentration (Loomis et al., 2012). Furthermore, GDGT-I, which is negatively correlated in Lake Azul sedimentary sequence, has been correlated with MAT by other authors but, the correlation showed a positive sign (Tierney et al., 2010; Loomis et al., 2012). GDGT-Ic and GDGT-IIc have been associated to water depth (Tierney et al., 2010; Loomis et al., 2012). Weijers et al., (2007) also found the same relation between GDGT-Ic and MAT. For Lake Azul, a transfer function was established between GDGTs and the air temperature giving the results observed in figure 5.11. But, the large uncertainties about the Lake Azul paleolimnological dynamics due to the lack of large temporal datasets, has hampered the critical review of the relationships between the Lake Azul GDGTs and the MAT. Therefore, owing to the contradictory results between the GDGTs and the MAT in Lake Azul with respect to those results in the already existing literature, as well as the lack of long limnological datasets forced the abandonment of the adhoc transfer function. Therefore, the qualitatively reconstruction of the air temperature in Ponta Delgada was performed by following the already existing calibrations.

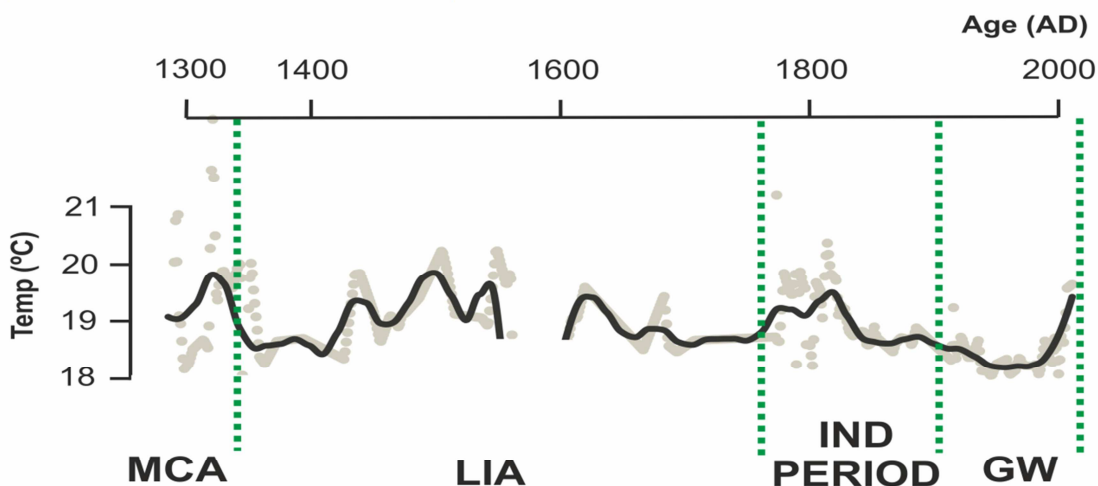


Figure 5.11: Temperature reconstruction obtained from an adhoc transfer function construction. The data used were the GDGTs analyzed on sediments from Lake Azul at the University of Texas at Austin and the temperature data obtained from 'Annaes do Observatório Infante D. Luiz' and IPMA. The black line was obtained by the application of a smooth of span 0.1 with the R function loess. The grey points are the results without applying the smooth. Based on the temperature results, four climatic periods have been defined: the end of the Medieval Climate Anomaly, the Little Ice Age, the Industrial Period and the Global Warming. Note that the LIA does not have especially cold temperatures.

Autumn data

GDGTs	Tmin	Tmax	Tmean
mz1050	0.27	-0.2	0.03
mz1048	0.45	0.11	0.4
mz1046	0.42	0.21	0.45
mz1036	-0.13	-0.01	-0.09
mz1034	0.31	-0.21	0.06
mz1032	0.31	-0.17	0.09
mz1022	-0.38	0.23	-0.08
mz1020	-0.31	0.29	0.01
mz1018	0.36	-0.14	0.14

Winter data

GDGTs	Tmin	Tmax	Tmean
mz1050	0.21	-0.21	0.04
mz1048	0.25	0.06	0.24
mz1046	0.19	0.09	0.21
mz1036	0.07	-0.02	-0.07
mz1034	0.29	-0.15	0.13
mz1032	0.26	-0.14	0.12
mz1022	0.32	0.21	-0.12
mz1020	0.37	0.24	-0.14
mz1018	0.39	0	0.32

Total year data

GDGTs	Tmin	Tmax	Tmean
mz1050	0.31	-0.2	0.2
mz1048	0.6	0.11	0.64
mz1046	0.5	0.21	0.62
mz1036	-0.2	-0.01	-0.26
mz1034	0.43	-0.2	0.3
mz1032	0.51	-0.17	0.42
mz1022	-0.5	0.23	-0.33
mz1020	-0.3	0.29	-0.02
mz1018	0.47	-0.13	0.38

Spring data

GDGTs	Tmin	Tmax	Tmean
mz1050	0.24	-0.14	0.09
mz1048	0.43	0.13	0.43
mz1046	0.38	0.18	0.42
mz1036	-0.12	-0.07	-0.14
mz1034	0.29	-0.17	0.11
mz1032	0.31	-0.11	0.16
mz1022	-0.35	0.2	-0.13
mz1020	-0.31	0.3	-0.03
mz1018	0.39	-0.03	0.29

Summer data

GDGTs	Tmin	Tmax	Tmean
mz1050	0.23	0	0.19
mz1048	0.54	0.3	0.62
mz1046	0.49	0.32	0.6
mz1036	-0.14	-0.21	-0.24
mz1034	0.29	-0.02	0.23
mz1032	0.35	0.09	0.35
mz1022	-0.36	0.06	-0.26
mz1020	-0.25	0.32	-0.02
mz1018	0.31	-0.01	0.26

Significant correlation

Table 5.1: Pearson product moment correlation between the GDGTs relative production and the minimum, mean, maximum annual and seasonal temperature. The purple color means the significant correlations.

Temperature calibration selection. There are 8 calibrations proposed by other authors (Table 5.2). The appropriate selection of the calibration for Azul site requires a discussion on three basic points: 1) if the temperature reconstruction permits to obtain reasonable temperatures values for the Azorean climate conditions; 2) if the temperature range oscillation is acceptable; and 3) the necessary existing similarities between the reconstructed temperature and the instrumental data from Ponta Delgada.

Author	Formula name	GDGTs used	Formula
Weijers et al., 2007	Weijers MBT/CBT for soils	all brGDGT	$MAAT = -6.1 + 50 \cdot MBT - 9.35 \cdot CBT$
Tierney et al., 2010	Tierney MBT/CBT for lakes	all brGDGT	$MAAT = 11.84 + 32.54 \cdot MBT - 9.32 \cdot CBT$
Tierney et al., 2010	Tierney MbrGDGT for lakes	I, II, III	$MAAT = 50.47 - 74.18 \cdot I - 31.6 \cdot II - 34.69 \cdot III$
Pearson et al., 2011	Pearson MbrGDGT for lakes	I, II, III	$MAAT = 47.4 - 53.5 \cdot I - 37.1 \cdot II - 20.9 \cdot III$
Pearson et al., 2011	Pearson (BSR)	I, II, IIIb	$MAAT = 20.9 - 20.5 \cdot I - 12 \cdot II - 98.1 \cdot IIIb$
Sun et al., 2011	Sun MBT/CBT	all brGDGT	$MAAT = 6.8 + 37.09 \cdot MBT - 7.06 \cdot CBT$
Loomis et al., 2012	Loomis (SFS)	I, II, IIc, IIIb	$MAAT = 22.77 - 33.58 \cdot I - 12.88 \cdot II - 418.53 \cdot IIc + 86.43 \cdot IIIb$
Loomis et al., 2012	Loomis MbrGDGTs for lakes	I, II, III	$MAAT = 36.9 - 50.14 \cdot I - 35.52 \cdot II - 0.96 \cdot III$
Loomis et al., 2012	Loomis MBT/CBT	all brGDGT	$MAAT = 2.54 + 45.28 \cdot MBT - 5.02 \cdot CBT$

Table 5.2: Calibration proposed by other authors. The first column display the name of the authors, the second the type of formula, the third column refers the GDGTs used in the formula and the fourth column shows the formula.

As mentioned in the Results chapter, the BIT index in the core AZ11_02 oscillated between 0.9 and 1. These high values indicate that GDGTs found on the sediments of this core were from bacterial production. Commonly, brGDGTs have been attributed to be produced on soils (Weijers et al., 2007), but Tierney and Russell (2009) observed an underestimation of the temperature when they used the soil temperature calibration of GDGTs even with high BIT index. Moreover, they also found an intact core brGDGT in the water column that proved the production of these compounds in this media (Tierney and Russell, 2009). Any previous work has been able to identify the possible

organism responsible for the brGDGTs production and still it remains as unanswered question.

Weijers et al. (2007) calibration was used in order to discard or accept the soil origin of the Azul Lake GDGTs. This calibration transfer function was used to reconstruct the MAT. Figure 5.12 shows that the obtained temperature reconstruction using Weijers' calibration underestimate, by more than 10 degrees, the instrumental temperature of the air that is similar to the soil temperature (≈ 2.5 °C; Watts, 1975). Therefore, the GDGTs contained in the sediment retrieved in Lake Azul were not produced in the surrounding lake soils but in the lake water column. The facies have been divided in rapid (Ra) and continuously (Co) according to their sedimentation nature. The Ra facies include the D and V facies whereas the Co facies is made up of A, B, C and E facies (see Chapter 4 for a detailed lithological description). The Ra facies deposited in the lake material from the catchment and, most probably, these facies are prone to be incorporating GDGTs from the catchment soils. Otherwise, the BIT, CBT and MBT results do not show differences on these indexes for these facies suggesting that all GDGTs are originated within the water column of the lake. For this reason, other available transfer functions were tested.

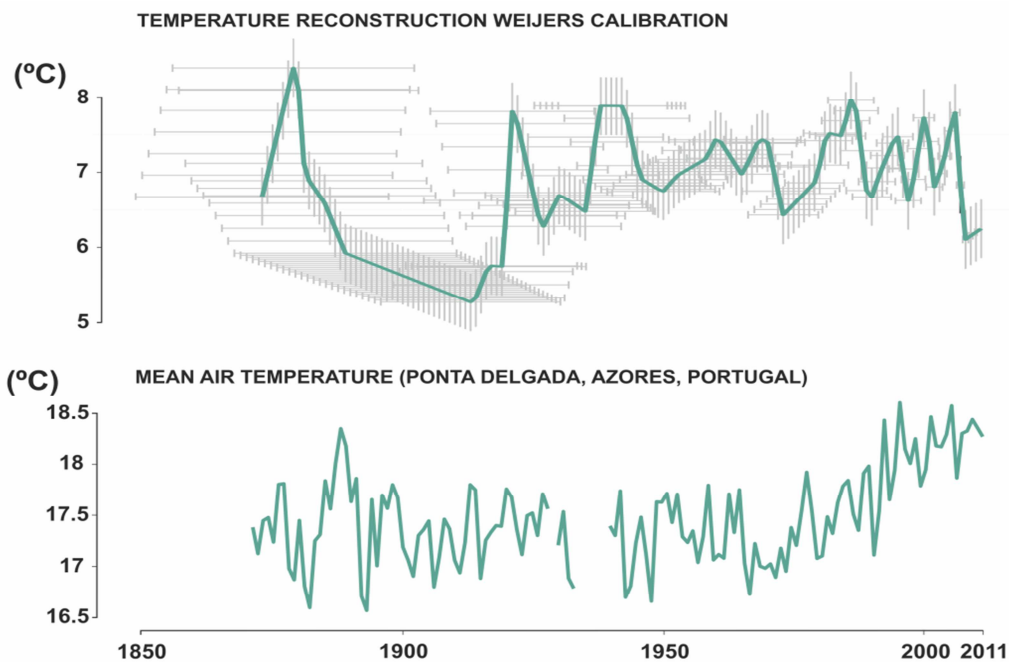


Figure 5.12: Comparison of the temperature reconstruction by GDGTs from Lake Azul using Weijers et al., (2007) calibration function and the temperature in Ponta Delgada for the period comprised between 1873 AD and 2011 AD. The annual temperature data from Ponta Delgada were obtained from the daily data acquired for the period between 1873 and 1946 AD from the 'Annaes do Observatório Infante D. Luiz' and for the period between 1947 and 2012 AD from IPMA. Note that the temperature reconstruction using Weijer's calibration underestimates the real temperature by more than 10 °C.

The other available GDGTs calibration transfer functions are based on 1) the ratio between the methylation of branched tetraether (number of methyl groups) and the cyclization of branched tetraether (number of cyclopentane moieties) (MBT/CBT-based paleo-thermometer; Tierney et al., 2010; Loomis et al., 2012; Sun et al., 2011); 2) on the GDGTs methyl branches amount (MbrGDGTs) (Tierney et al.; 2010, Pearson et al., 2011; Loomis et al., 2012); 3) on the stepwise forward selection (SFS; Loomis et al., 2012) and 4) on the best subset regression (BSR; Pearson et al., 2011).

The MBT/CBT-based paleo-thermometers have not been used in the present work because these calibrations use GDGTs with cyclopentane moieties have been proved to be affected by other environmental factors, such as pH and water depth (Tierney et al., 2010, Loomis et al., 2012; Weijers et al., 2007). Moreover, those paleo-thermometers seemed to be less accurate than other alkenone-based paleo-thermometers such as TEX₈₆ (Tierney et al., 2010).

Therefore the MbrGDGTs (Tierney et al.; 2010, Pearson et al., 2011; Loomis et al., 2012), the SFS (Pearson et al., 2011) and the BSR (Loomis et al., 2012) have been used. From these five functions, only three have been tested worldwide. And these calibrations are: (1) MbrGDGTs transfer functions (Tierney et al.; 2010, Pearson et al., 2011), (2) the Best Subset Regression (BSR, Pearson et al., 2011) and (3) the Stepwise Forward Selection (SFS, Loomis et al., 2012).

The application of the BSR transfer function to the Lake Azul GDGTs sequence underestimates the MAT by more than 10 °C and, therefore, it was discarded (Fig 5.13). The application of the SFS transfer function gave values of reconstructed temperatures under 0 °C, which are not possible for the island's latitude and were not consistent with instrumental records (Fig. 5.14). The MbrGDGT calibrations proposed by Tierney et al. (2010) and Pearson et al. (2011) reproduced better the temperature fluctuations and these reconstructed temperature values laid within the temperature range for the instrumental period (Fig 5.15). Pearson et al. (2010) calibration displayed values in the same range and trends than the summer instrumental meteorological temperature of the Ponta Delgada record. Tierney et al. (2010) calibration showed the same range and trends than the instrumental meteorological autumn temperature. Pearson and

Tierney calibration fluctuations are almost identical, showing a high correlation degree between them ($r=0.9$, $p<0.01$) and display a thermal amplitude of 3 and 3.5 degrees Celsius, respectively. This thermal amplitude is also observed in the instrumental meteorological record.

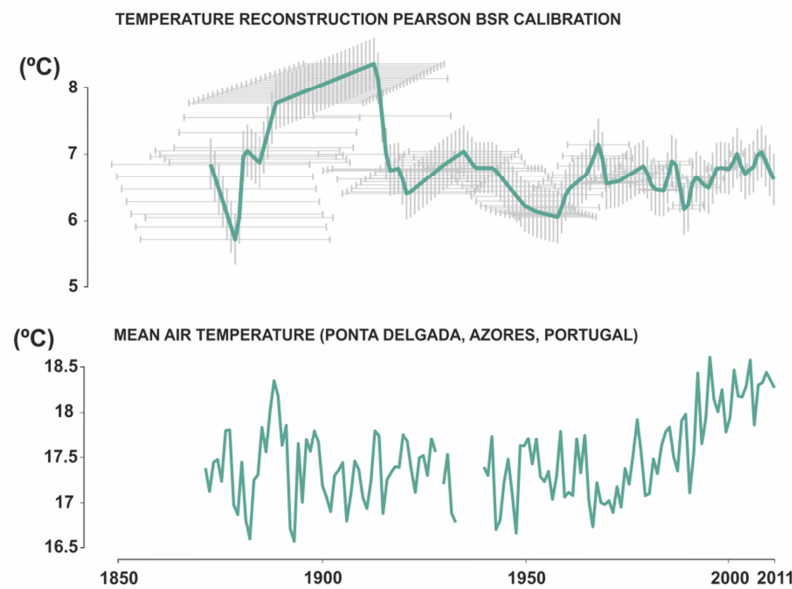
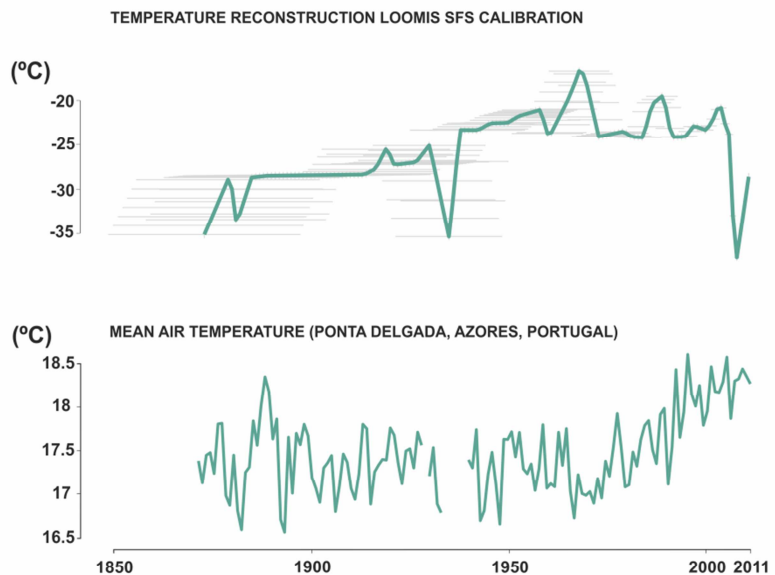


Figure 5.13: Comparison of the temperature reconstruction by GDGTs from Lake Azul using BSR Pearson et al., (2011) calibration function (upper graphic) and the temperature in Ponta Delgada for the period comprised between 1873 AD and 2011 AD (lower graphic). The annual temperature data from Ponta Delgada were obtained from the daily data acquired for the period between 1873 and 1946 AD from the 'Annaes do Observatório Infante D. Luiz' and for the period between 1947 and 2012 AD from IPMA. Note that the temperature reconstruction using Pearson BSR's calibration underestimates the real temperature by more than 10 °C.

Figure 5.14: Comparison of the temperature reconstruction by GDGTs from Lake Azul using BSR Loomis et al., (2012) calibration function (upper graph) and the temperature in Ponta Delgada for the period comprised between 1873 AD and 2011 AD (lower graph). The annual temperature data from Ponta Delgada were obtained from the daily data acquired for the period between 1873 and 1946 AD from the 'Annaes do Observatório Infante D. Luiz' and for the period between 1947 and 2012 AD from IPMA. Note that the temperature reconstruction using Loomis BSR's calibration produce negative temperatures no coherent with instrumental data and for Azores latitudes.



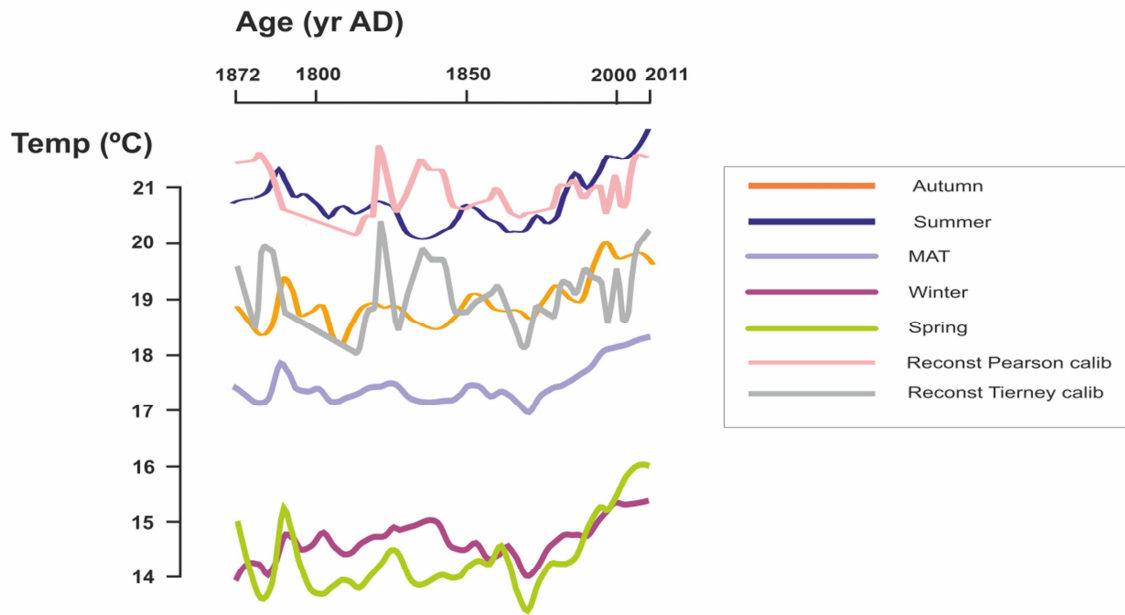


Figure 5.15: Comparison of the temperature reconstruction using the calibration proposed by Tierney et al., (2010) (light-pink) and by Pearson et al., (2011) (light-grey). Also are represented the annual mean temperature (MAT, light-purple), the summer mean temperature (dark-blue), the autumn mean temperature (orange), the winter mean temperature (dark-pink), and the spring mean temperature (green). The mean temperature data were obtained from the 'Annaes do Observatório Infante D.Luiz' for the period between 1873 AD and 1946 AD and from IPMA for the period between 1946 AD to 2011 AD. Note that Tierney's calibration reflects the autumn temperature and Pearson's calibration reflects the summer temperature.

Lake productivity at low latitude lakes is observed through the year (Tierney et al., 2010) but, as latitude is increased the lake productivity is mainly restricted to the summer season (Shanahan et al., 2012). Lake Azul develops a thermocline during summer season, which is the period of highest productivity. The thermocline breaks at the end of this high productivity period. Therefore, according to the lake dynamics, the use of the Pearson et al. (2011) calibration transfer function makes more sense for this site than that of Tierney et al (2010) since the first was built for a worldwide dataset including mid-latitude lakes like Lake Azul whereas the second transfer function was constructed for a tropical lake. Moreover, temperature amplitude was closer to other authors reconstruction for the Late Holocene.

Temperature reconstruction validation. Finally, the temperature reconstruction for Lake Azul obtained by the application of the transfer function developed by Pearson et al. (2011) has been compared with the seasonal and annual mean air temperatures for the period between 1872 and 2011 AD in order to validate the reconstruction (Fig

5.15). The comparison of the reconstructed temperature with the instrumental data displays an identical oscillation pattern but, at some points, a slightly uncoupling of more or less 5 years is observed between both curves. This uncoupling might be related to the age-depth model uncertainties of the reconstructed series. In both cases, from 1872 to 2011 AD, the reconstructed and instrumental temperature series oscillate between 20 and 22.5 °C. The main trends observed in both series were also similar. The temperature from both records decrease from 1880 to 1910 AD by 1.5 °C (a bit more in the reconstructed temperature). From 1910 to 1970 AD both temperature series fluctuated between 20.5 and 22 °C without any noticeable trend. Finally, from 1970 AD to the present, both temperature series showed an increasing trend. This comparison permits to determine that the reconstructed temperature oscillations using the SFS method of Pearson et al. (2011) is valid.

Calibration of the precipitation by δD

The instrumental data showed that the δD values are recording changes on precipitation amount. The precipitation amount is the quantity of rain that fall in a certain place per unit of time. These changes on precipitation are mainly based on fluctuations on the NAO phase (section 5.2). Based on that, the weighting average of the δD leaf wax preserved in the sediments for year of NAO+ should be different than that for years of NAO-. Since the instrumental record of NAO covers from 1821 to 2011 AD, the δD leaf wax sediment data were selected for the same time period and separated for NAO+ and NAO-. The weighting average and the standard deviation were calculated for the years of NAO+ and the years of NAO-. The time interval contained at each sample responds to a Gaussian function in which the central year is the expected value and the edges of the time interval are the tails of the variance. Therefore, the NAO phase observed from the instrumental data has been sampled accordingly to the age of the sediment and following this Gaussian function. In order to apply the Gaussian function, the yearly NAO index has been calculated by a weighting average, in which, the NAO index from the expected year has been bestowed with more weight than the tails. The years with NAO+ showed a mean value of -133‰ with a standard deviation of 3 ‰. The years with NAO- showed a mean value of -141‰ with a

standard deviation of 4%. Those data showed significant differences despite of the small dataset size.

5.4 HIGH-RESOLUTION TEMPERATURE AND PRECIPITATION EVOLUTION OF THE NORTH ATLANTIC FOR THE LAST 730 YEARS: THE LAKE AZUL (AZORES ARCHIPELAGO) CASE.

The temperature and precipitation reconstruction obtained from Lake Azul sediments according to the previously calculated age-model allowed us to identify four main climatic periods for the Sao Miguel Island (Fig 5.16):

- (1) the last stages of the Medieval Climate Anomaly (MCA) and its transition to the Little Ice Age (LIA) from 1285 to 1370 AD,
- (2) the LIA that showed a complex internal thermal and hydrological structure between the 1370 and the 1820 AD,
- (3) the Industrial Period located from 1820 to 1920 AD, and,
- (4) the Global Warming (GW) period between the 1920 and 2011 AD.

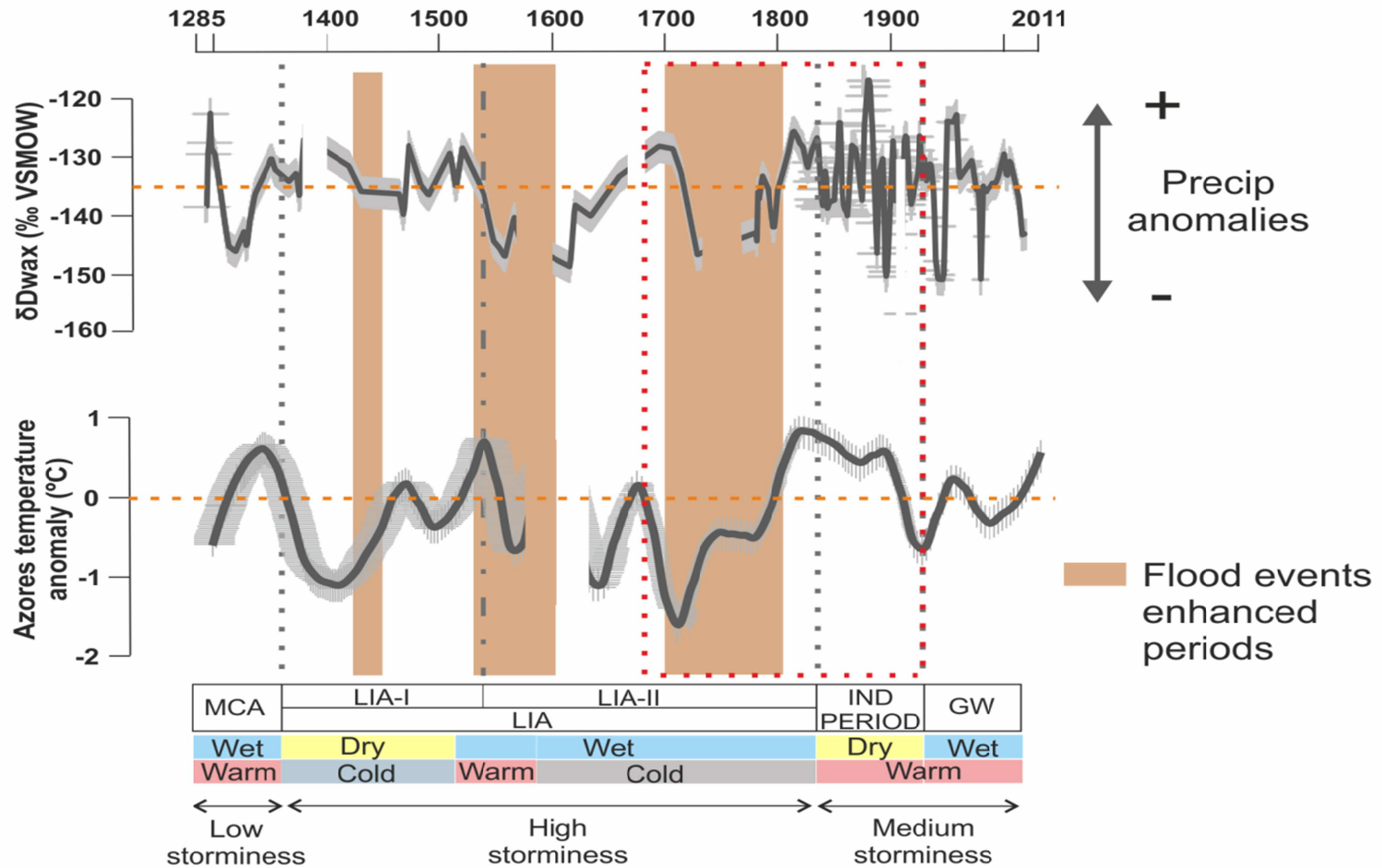


Figure 5.16: The upper graph shows the precipitation anomalies registered on Lake Azul record for the period comprised between 1285 and 2011 AD using δD leaf waxes (‰). The lower graph shows the temperature reconstruction anomalies in Lake Azul based on GDGTs using Pearson et al., (2011) MbrGDGT calibration. The data have been made at one year resolution. The error bars have been constructed for the precipitation analyzing by duplicate the samples with great amount of n-alkanoics. And for the temperature, the error bars were constructed by analyzing the samples 2 or 3 times depending on the amount of GDGTs. The periods of flood events were shadowed in brown. The climatic periods defined (see text for more information) are added in a bar at the bottom of the figures. Relative wet and dry interpreted periods are indicated and also general trends on temperature and periods of intensities of storminess. The dotted squared section represents the 1680-1920 period. Note that an increase on precipitation is usually followed by an increase on temperature.

MCA-LIA transition period (1285 - 1350 AD)

The MCA in Lake Azul was characterized by an increasing trend on temperature of about 1.5 °C from 1285 AD that culminates around 1350 AD (figure 5.16). This highest temperature peak was followed by a decrease on temperature of about 1.5 °C. Similar patterns have been observed in the NW of the Iberian Peninsula (Martínez-Cortizas et al., 1999) (Fig 5.17). On the other hand, temperature reconstructions performed in North America (Wahl et al., 2012; Cronin et al., 2003), south of Greenland (Miettinen et al., 2011) and north of Europe showed opposite patterns. The highest temperature peak on Lake Azul corresponds to the lowest temperature for those sites. Temperature in central Europe (Glaser et al., 2009; Larocque-Toblar et al., 2012), on Tagus estuary (Abrantes et al., 2005) and SW Mediterranean (Nieto-Moreno et al., 2011) also suffered a small decrease of about 0.5 °C during this period.

In hydrological terms, the transition between the MCA and LIA in Lake Azul was divided in two phases, one dry from 1285 to 1300 AD and the next one humid from 1300 to 1370 AD (Fig 5.18). Similar dry conditions have been also recognized in Lake Caveiro (Azores; Björk et al., 2006), Eastern USA (Stahle and Cleaveland, 1994), north of Morocco (Esper et al., 2007), Iberian Peninsula (Corella et al, 2013; Sánchez-López et al., submitted) and south-west Mediterranean basin (Nieto-Moreno et al., 2014). Conversely, an increase on storminess was observed on the Gulf of Lion (Sabatier et al., 2012). Whereas the humid phase was in agreement with the results observed in Lake Caveiro of Pico Island (Björk et al., 2006) and Eastern USA (Stahle and Cleveland, 1994); data from south of Europe (Corella et al., 2013; Nieto-Moreno et al., 2014; Sánchez-López et al., submitted) and North Africa (Esper et al., 2006) lead to these authors to propose a continuation of the dry period.

LIA period

The Little Ice Age (LIA) was a climatic period characterized by cold temperatures in the North Atlantic. LIA onset depends on the considered author and it went from 1300 AD (Mayewski et al., 2004; Nieto-Moreno et al., 2014) to 1420 AD (Trouet et al., 2009). The LIA onset transition happened earlier (\approx 1300 AD) in Arctic, Europe and Asia than at southern hemisphere latitudes (Ahmad et al., 2013). The lake Azul temperature

reconstruction by GDGTs led us to establish the onset of the LIA around 1350 AD (Fig. 5.16).

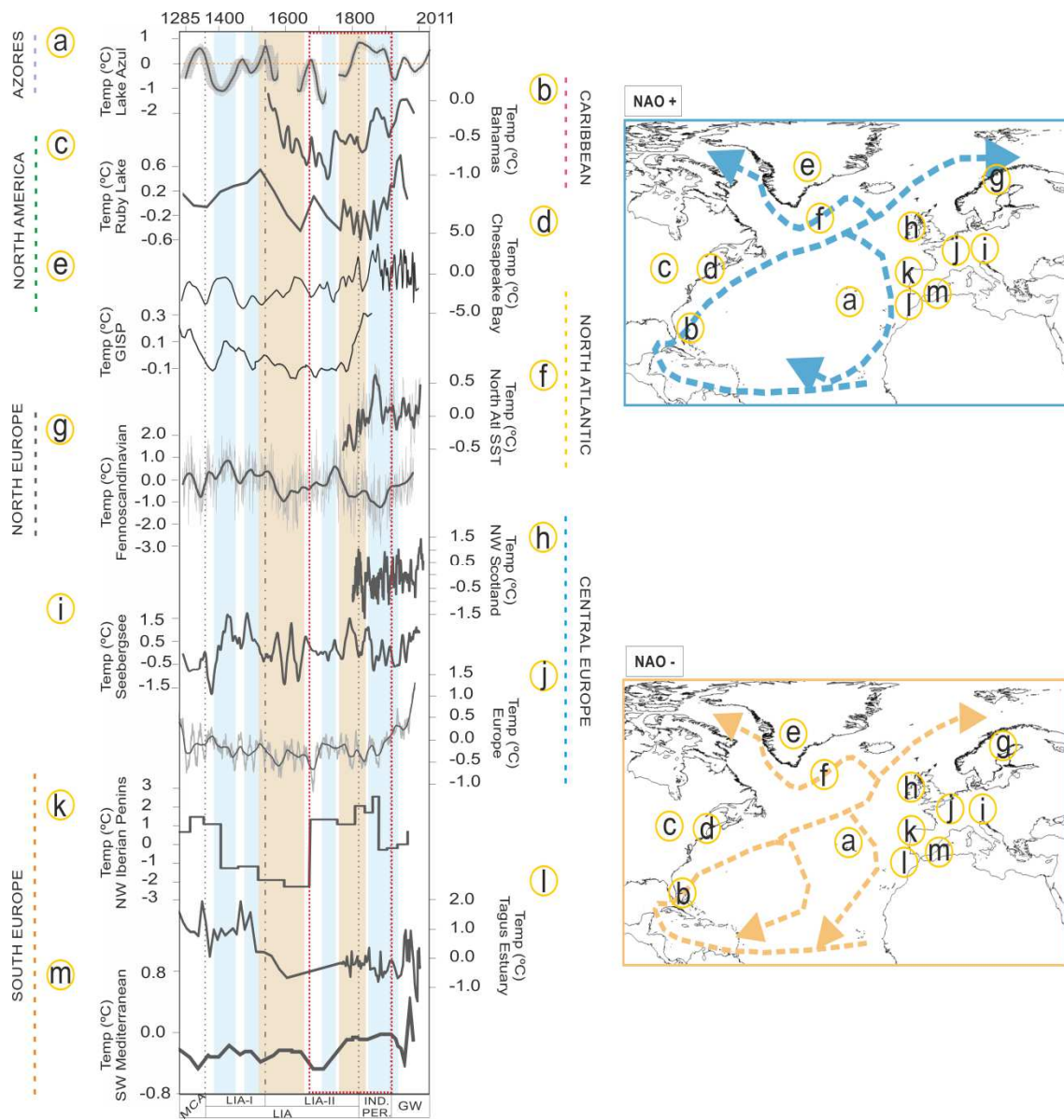


Figure 5.17: Temperature reconstruction for Lake Azul record for the period comprised between 1285 and 2011 AD based on GDGT using Pearson et al., (2011) calibration comparison with other temperature reconstructions around the North Atlantic. From top to bottom: (a) Lake Azul reconstruction (this work), (b) reconstruction from corals in Bahamas (Saenger et al., 2009), (c) reconstruction in Ruby Lake (Wahl et al., 2012), (d) reconstruction in Chesapeake Bay (Cronin et al., 2003), (e) reconstruction from the GISP core in Greenland (Alley et al., 1997), (f) reconstruction from a marine core in South of Greenland (Miettinen et al., 2011), (g) reconstruction from tree ring in Fennoscandinavia (Grudd et al., 2008), (h) reconstruction of Hebridean spring sea surface temperatures NW Scotland (Reynolds et al., 2013), (i) reconstruction from the lake Seeburgsee (Larocque-Toblar et al., 2012), (j) temperature reconstruction composite from Europe (Glaser et al., 2009), (k) reconstruction from peat bog in NW Spain (Martínez-Cortizas et al., 1999), (l) reconstruction from the Tagus estuary (Abrantes et al., 2005) and (m) reconstruction from a marine core in the SW Mediterranean (Nieto-Moreno et al., 2011). Blue bars represent periods (based on Lake Azul reconstruction) that show NAO+ characteristics. Light-orange bars represent periods (based on Lake Azul reconstruction) that show NAO- characteristics. The dotted squared section represents the 1680-1920 period. This period is highlighted because anomalies on the general north Atlantic atmospheric and oceanic circulation have been observed. The climatic periods are shown in a lower bar. Maps on the right represent the oceanic currents pathway for NAO+ (upper map) and NAO – phase (lower map) suggested from the comparison of the temperature reconstructions. Note that an increase on temperature in Azores is also observed in the Caribbean area and Spain.

This onset was marked by a sudden decrease on temperature of about 1.5 °C. The end of LIA was established around 1730 AD for some works (Saenger et al., 2009; Mann et al., 2009) and at 1950 AD for other studies (Cronin et al., 2003; van Hegstum et al., 2015). The Lake Azul reconstruction temperature variations were witness of the transition from LIA to Industrial Period (IND period) around 1820 AD. The LIA has been defined by many works as a cold period (Büntgen et al., 2011; Nieto-Moreno et al., 2014; Moffa-Sánchez et al., 2014; Sánchez-López et al., submitted). However, the LIA in the central North Atlantic displayed two marked phases: LIA I (from 1370 to 1520 AD) and LIA-II (from 1520 to 1820 AD). Those two LIA phases have been observed in previous works in North Iberia (Morellón et al., 2012) but, the exact moment of change differs between records. The LIA-I is characterized by low temperatures with a final increase and the LIA-II is characterized by the period of lowest temperatures of the record. The temperature amplitude variations during LIA also changed between places around North Atlantic. Variations on Lake Ruby (Wahl et al., 2012) or Fennoscandinavia (Grudd et al., 2008) were within 1 °C; whereas, LIA variations in Lake Azul, Bahamas (Saenger et al., 2009), Pigmy Basin (Richey et al., 2009) or NW Iberian Peninsula (Martinez-Cortizas et al., 1999) were within 3°C.

The precipitation in Lake Azul during the LIA was highly variable from interannual to interdecadal time scales (Fig 5.18). Despite of its variability, LIA in São Miguel Island could be generally considered as a period of increased precipitation. Moreover, the sedimentation rate at this period is the lowest in Lake Azul record with mean values of 0.24 mm/yr in comparison with 0.31 mm/yr for the other periods. As exposed in the section 5.1 of the present chapter, the sedimentation rate increased with precipitation. The reason of these “a priori” contradictory findings is that the LIA in Lake Azul site has an increment of the presence of Facies D, reaching values of 8 Facies D layers/100 years of record. Facies D, as explained in the results chapter, were considered flood events deposited in a short-term period (see section 4.3). Therefore, we suggest that one of the factors governing this increase on flood events frequency was an increment of intense rainfall events from an increase in the storminess. In this sense, Gomes et al., (2005) observed in historical data from 1500 AD to the present that extraordinary precipitation events, amongst other factors, produce an increase on flood events

occurrence; even more, in the north-western flank of the Lake Azul crater. These wet LIA conditions have also been described by other authors in the south of Europe (Corella et al., 2013; Nieto-Moreno et al., 2014; Sánchez-López et al., submitted), north of Morocco (Esper et al., 2007) and Pico island (Björk et al., 2006) (Fig 5.18). Meanwhile, a decrease of storminess was observed in the Gulf of Lion during this period (Sabatier et al., 2012). Precipitation in the Caribbean area (Lozano-Garcia et al., 2007; Stansell and Cleveland, 1994) and British Isles (Proctor et al., 2000; Swindles et al., 2012) decreased but, the British Isles suffered huge variations on water regime.

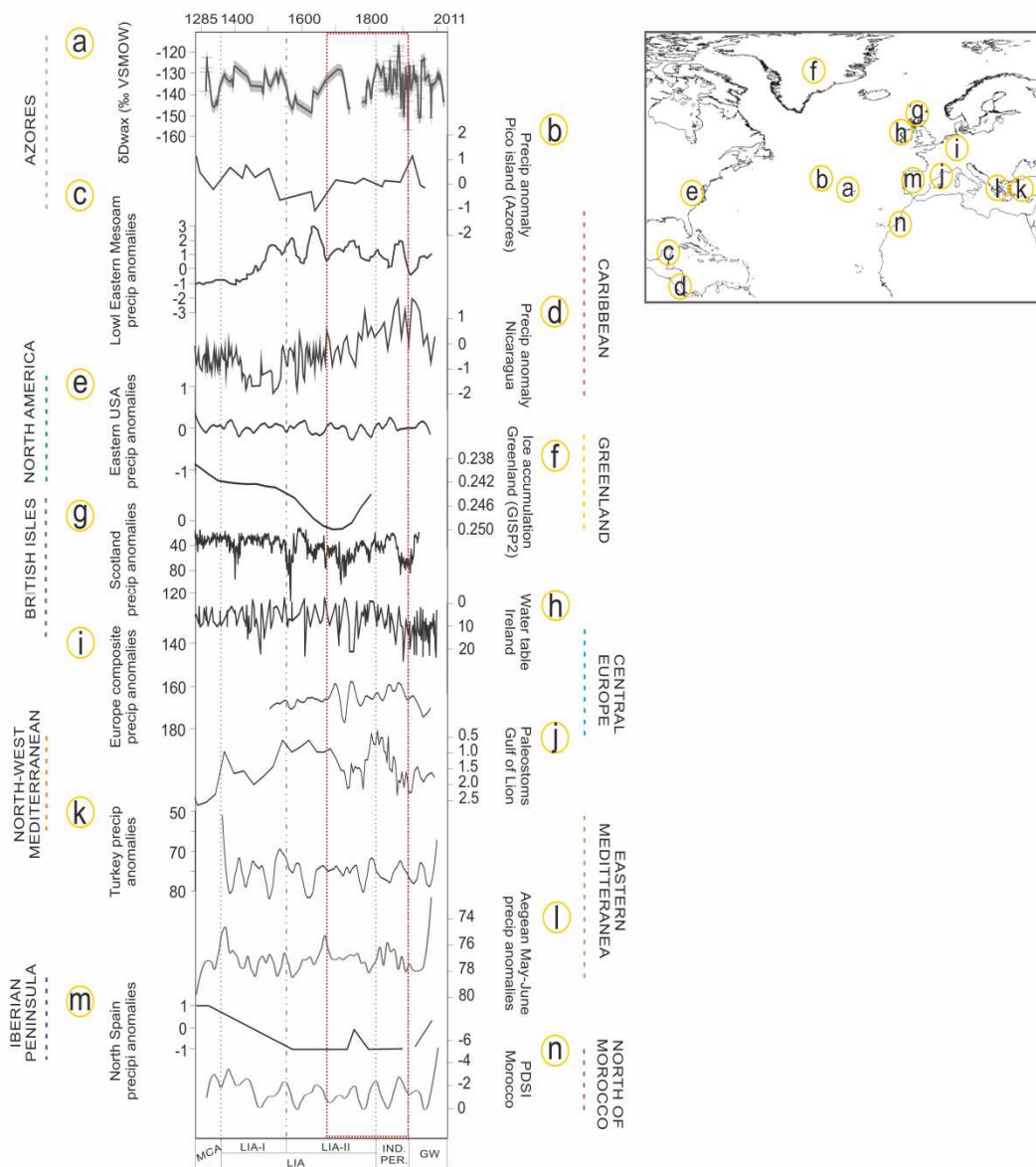


Figure 5.18: Precipitation reconstruction for Lake Azul record for the period comprised between 1285 and 2011 AD based on δD leaf wax comparison with other temperature reconstructions around the north Atlantic. From top to bottom reconstructions corresponds to : (a) Lake Azul reconstruction (this work), (b) lake Caveiro in Pico island Azores (Björk et al., 2006), (c) lowland Mesoamerican lakes (Lozano-Garcia et al., 2007), (d) Nicaraguan lakes (Stansell et al., 2012), (e) precipitation anomalies in US based on a tree ring reconstruction (Stahle and Cleveland, 1994), (f) GISP core in Greenland (Alley et al., 1997), (g) speleothem in Scotland (Proctor et al., 2000), (h) lake water table reconstruction in Ireland (Swindles et al., 2012), (i) Europe composite reconstruction (Pauling et al., 2006), (j) paleostorms reconstruction in the Gulf of Lion (Sabatier et al., 2012), (k) Turkey spring precipitation (Touchan et al., 2003), (l) Aegean sea precipitation reconstruction (Griggs et al., 2007), (m) Lake Arreo (Corella et al., 2013) and (n) Palmer Drought Severity Index reconstruction from tree rings in North of Morocco (Esper et al., 2007). The climatic periods are shown in a lower bar. In map on the right are represented the position of the above mentioned reconstructions. Note that an increase on precipitation in Azores is also observed in the Pico Island and Spain except for the 1680-1920 period (dotted squared). This period is highlighted because anomalies on the general north Atlantic atmospheric and oceanic circulation have been observed.

Owing to changes on temperature, the LIA period in São Miguel has been divided in two parts (defined previously). And, paleo-precipitation changes during LIA period can also be divided in two periods, one of relatively dry conditions from 1370 to 1520 AD and other of wet conditions from 1520 to 1820 AD.

The first LIA phase (1370 – 1520 AD) in Lake Azul was characterized by a temperature decrease of about 1.5 °C. This decrease is also observed in the Tagus estuary but with a lower temperature range (1°C; Abrantes et al., 2005). Conversely, the eastern coast of North America (Cronin et al., 2003), in Fennoscandinavia (Grudd et al., 2008) and in SW Mediterranean the temperature rose 0.5, 1, and 0.3 °C, respectively (Fig. 5.18). Greenland (GISP2; Alley et al., 2000) and Sebergsee (Larocque-Toblar et al., 2012) observed an increase of 0.2 and 3 °C, respectively, that is followed by a sudden temperature decrease of similar magnitude. This temperature decrease occurred 50 years before than that of Lake Azul. At the NW of the Iberian Peninsula a temperature decrease of 2.5 °C was also observed but delayed around 20 years with respect to Lake Azul. However, this last time lag should be taken with caution since it is within the age model uncertainties. The end of this LIA-I period was characterized by a sudden increase on temperature. These warm temperatures were also observed in Bahamas (Saenger et al., 2009), Bermuda (van Hegstrum et al., 2015), Bermuda rise (Oppo et al., 2003), Ruby Lake (Wahl et al., 2012), and some European temperature composites (Büntgen et al., 2011; Moffa-Sánchez et al., 2014). Lake Azul and Bahamas (Saenger et al., 2009) reconstructions suggested temperatures as warm as today for this LIA phase. These warm temperatures were mainly observed around the Caribbean area probably owing to a short-lived Florida Current temperature increase episode (Oppo et al., 2003; van Hegstrum et al., 2015), which probably increase the GS temperature and their branches CC and AzC. This could be the factor of the Lake Azul temperature increase. An increasing trend on temperatures was also observed in Chesapeake Bay but, the highest temperature peak is delayed more than 100 years. Temperatures in Greenland (Alley et al., 2000), Fennoscandinavia (Grudd et al., 2008), Europe (Glaser et al., 2009), NW Iberian peninsula (Martinez-Cortizas et al., 1999) and Tagus estuary (Abrantes et al., 2005) observed a decreasing trend between 0.1 and 1 °C that was strongly marked at the Tagus estuary (3°C).

In terms of precipitation, this first LIA period was characterized by mostly permanent dry conditions in Lake Azul with a small increase on precipitation around 1490 AD. Dry conditions were also observed in Pico Island (Björk et al., 2006), North of Morocco (Esper et al., 2007), North of Spain (Corella et al., 2013) and Greenland (Alley et al., 2000). The dry conditions observed from 1460 to 1550 AD were also observed by Mesoamerica Lowlands (Lozano-Garcia et al., 2007), Greenland (Alley et al., 2000), Turkey (Touchan et al., 2003) and a decrease of storminess in the Gulf of Lion (Sabatier et al., 2012). On the contrary, wet conditions were observed in the Caribbean area (Lozano-Garcia et al., 2007; Stansell et al., 2012) and Aegean Sea (Griggs et al., 2007).

The second LIA phase (1520 – 1820 AD) contained the lowest temperatures of the Lake Azul record with values 2°C lower than the mean values of the entire record. This low temperatures were also observed on Bahamas (Saenger et al., 2009), Ruby Lake (Wahl et al., 2012), SW Mediterranean (Nieto-Moreno et al., 2011) and some European temperature composites (Büntgen et al., 2011) (Fig. 5.17). This period was also characterized by the coolest winters of the Late Holocene in Europe (Lutherbacher et al., 2002). Chesapeake bay (Cronin et al., 2003), Seebergsee (Larocque-Toblar et al., 2012) reconstructions also observed a small decrease of ≈ 0.5 °C but, not as marked as for Lake Azul record. Glaser et al., (2009) in a Europe temperature composite found a decrease of about 0.4 °C on temperature that occurred around 50 years before Lake Azul lowest temperature peak. However, an increase of 1 °C in temperature was observed in Fennoscandinavia (Grudd et al., 2008) and an increase of around 4 °C on the NW Iberian Peninsula (Martinez-Cortizas et al., 1999). The last 50 years of this period were characterized by a rapid increase of temperature (+1.5 °C) in Lake Azul. Similar conditions were observed in the Caribbean area (Saenger et al., 2009), Chesapeake Bay (Cronin et al., 2003), Greenland (Alley et al., 2000), North Atlantic SST (Miettinen et al., 2011), SW Mediterranean (Nieto-Moreno et al., 2011) and some places in Europe (Büntgen et al., 2011). Glaser et al. (2009) reconstruction showed an increasing trend of 1.5 °C, 100 years later than Lake Azul. This warm up was evidenced by a rapid sea level rise about 1750 – 1850 AD (Varekamp and Thomas, 1998) owing to the ice-cap melt. Despite of that, Fennoscandinavia record (Grudd et al., 2008) showed a decrease on temperature of about 2 °C.

In terms of hydrology, the second LIA phase was the most humid period of Lake Azul record despite of the relatively dry period from 1650 to 1710 AD. The first humid phase of this second LIA period from 1550 to 1650 AD can be considered the most humid period of Lake Azul record (Fig. 5.16). Those results are consistent with findings in Morocco (Glueck and Stockton, 2001; Esper et al., 2006), Pico island (Björk et al., 2006), Iberian Peninsula (Rodrigo et al., 2001; Corella et al., 2013; Sánchez-López et al., submitted), Greenland (Alley et al., 2000), Turkey (Touchan et al., 2003) and Aegean sea (Griggs et al., 2007) (Fig. 5.19). Documentary data from the south of Spain also describe this period as one of the most humid period registered (Rodrigo et al., 2001). The short period from 1650 to 1710 AD recorded dry conditions also observed in the south of Spain (Rodrigo et al., 2001) and Caribbean (Lozano-Garcia et al., 2007; Stansell et al., 2012). Surprisingly, Pico Island (Björk et al., 2006) and studies from the north of Spain (Corella et al., 2013) revealed a continuation of the previous humid period at that time. The last 110 years of the LIA-II (from 1710 to 1820 AD) were characterized by wet conditions in Lake Azul. These wet conditions are in agreement with precipitation reconstructions in Eastern USA (Stahle and Cleaveland, 1994), Morocco (Glueck and Stockton, 2001; Esper et al., 2007), Turkey (Touchan et al., 2003) and south of Spain (Rodrigo et al., 2001). But, those results are again in contrast with findings in Pico Island (Björk et al., 2006) and NW of Spain (Corella et al., 2013). The last 20 years of the LIA observed a trend towards more arid conditions. This trend was also observed in Morocco (Glueck and Stockton, 2001; Esper et al., 2007) and south of Spain (Rodrigo et al., 2001); but, those results were contradictory with the Pico island reconstruction (Björk et al., 2006) and north of Spain (Corella et al., 2013).

Industrial Period (1820 - 1920 AD)

This climatic period was the warmest period of the Lake Azul record with temperature anomalies higher than 1 °C above the mean value of the entire record (Fig 5.16). These warm temperatures were also observed in Bahamas (Saenger et al., 2009), Chesapeake Bay (Cronin et al., 2003), North Atlantic SST (Miettinen et al., 2011), NW Iberian Peninsula (Martinez-Cortizas et al., 1999) and SW Mediterranean (Nieto-Moreno et al., 2011) (Fig 5.17). Temperatures in North (Grudd et al., 2008) and central (Reynolds et al., 2013; Larocque-Toblar et al., 2012; Glaser et al., 2009) Europe suffered an small

decrease that oscillated between 1 °C (Grudd et al., 2008) and less than 0.5 °C (Glaser et al., 2009).

Those warm temperatures were followed by a sudden decrease of about 1 °C of Lake Azul temperature. This decrease on temperature could be explained as a consequence of the ice-cap melting producing high fresh and cold water entrance to the ocean. This decrease was also observed in Bahamas (Saenger et al., 2009), south of Greenland (Miettinen et al., 2011), NW Iberian Peninsula (Martinez-Cortizas et al., 1999) and central Europe (Büntgen et al., 2011). Fennoscandinavian record (Grudd et al., 2008) suffered a small increase ($\approx 0.5^{\circ}\text{C}$) on temperature. And, these cold temperatures were delayed around 50 years for the SW Mediterranean.

The IND period was mostly characterized by arid conditions in Lake Azul but, the last 20 years of this period observed punctual precipitation period of few years (Fig 5.18). Similar patterns were observed in Pico island (Björk et al., 2006), Caribbean (Lozano-Garcia et al., 2007; Stansell et al., 2012), British Isles (Proctor et al., 2000; Swindles et al., 2012); central Europe (Pauling et al., 2006) and Spain (Corella et al., 2013) (Fig 5.16). Opposite conditions were observed in Morocco where the degree of drought was less prominent (Esper et al., 2007) and the storminess of the Gulf of Lion observed an increasing trend (Sabatier et al., 2012).

Global Warming (1920 - 2011 AD)

The most recent period has been widely known as the Global Warming (GW) that went from 1920 AD onwards (Fig 5.16). During this period, the temperature in Lake Azul suffered an increasing trend smaller than 0.5 °C. This tendency has been observed almost globally except for the Chesapeake Bay (Cronin et al., 2003) and for the Tagus estuary (Abrantes et al., 2005) (Fig 5.17). Surprisingly, the warming up in Azores archipelago does not seem to be as extraordinary ($< 0.5^{\circ}\text{C}$) as for other sites ($> 2.5^{\circ}\text{C}$) such as NW Scotland (Reynolds et al., 2013) and central Europe (Larocque-Toblar et al., 2012; Glaser et al., 2009).

The precipitation in Lake Azul for this recent period was highly variable but, it can be considered mostly dry with punctual rainfall episodes produced by the highly variable

precipitation patterns observed at that period (Fig 5.18). Dry conditions were also observed in Pico island (Björk et al., 2006), Nicaragua (Stansell et al., 2012), eastern USA (Stahle and Cleaveand, 1994) and North of Spain (Corella et al., 2013). Andrade et al., (2008) suggested that this period was characterized by an increase on storminess and this could be the reason of the highly variable precipitation observed.

Summary

In terms of temperature we could conclude saying that fluctuations on temperature in Lake Azul are closer to temperature changes in the Caribbean area and usually opposite to temperature variability in the northern and central Europe. Variations on North America east coast were usually in opposite phase to variations in Azores but, sometimes, those changes are in phase. Moreover, it could be observed that the north and south of the Iberian Peninsula were usually in opposite phase and that temperature fluctuations in Azores are closer to temperature fluctuations of the NW of Iberian Peninsula than to the South. Probably temperature in the south is affected by the Mediterranean Water Outflow (MOW; Ambar and Howe, 1979)

Lake Azul past precipitation patterns were similar to these defined for Spain (Corella et al., 2013; Nieto-Moreno et al., 2014), Morocco (Esper et al., 2006), Pico Island (Björk et al., 2006) and mostly coherent with the Greenland Ice accumulation rate (Alley et al., 2000). Contradictory results were observed at the end of LIA and the IND period. The British Isles are usually in opposite phase. Storminess in the Gulf of Lion was more intense while dry periods in Azores. But the possible increase on storminess while GW in Azores, was coherent with an increase of storminess in the Gulf of Lion (Sabatier et al., 2012). Precipitation reconstructions in Turkey (Touchan et al., 2003) and Aegean Sea (Griggs et al., 2007) and those in America (Lozano-Garcia et al., 2007; Stansell et al., 2012; Stahle and Cleaveland, 1994) did not show any clear similarity with the reconstruction carried out in Lake Azul. It is important to point out that, except for the GW period, the precipitation in the Caribbean area and North America acts in an opposite phase with respect to each other.

5.5 CLIMATE-FORCINGS DEFINING CLIMATIC PATTERNS OVER THE NORTH ATLANTIC.

The NAO dynamics

Temperature instrumental data and previous works based on instrumental precipitation (Hernandez et al., 2016) demonstrated that changes on the phase of NAO directly affects precipitation patterns and indirectly temperature variations.

In the present study, we suggest that a positive NAO phase produces dry conditions in São Miguel Island and we confirm, in agreement with other authors, that a negative phase of NAO produces greater accumulation of water by rain episodes (Hernández et al., 2016) and more intense precipitation events (Andrade et al., 2008).

The temperature, in turn, is directly affected by the position of the Gulf Stream but, this position is linked to the phase of NAO. A positive NAO phase enhance the currents velocity, increasing the EKE, moving towards north latitudes the GSNW that directs towards northern latitudes the GS. This makes difficult to reach the Azores. On the other hand, the NAO negative phase cease the EKE activity transporting the GS towards southern latitudes. Moreover, the reduction of EKE activity blocks the GS heat near Bahamas making that the GS has a zonal movement and, this position facilitates to reach Azores. Therefore, short-term temperature variations in Lake Azul are triggered by the ocean dynamics.

Based on that, we expect to find that during positive (negative) phase of NAO the precipitation in Lake Azul decreases (increases) as the temperature decreases (increases). Figure 5.16 showed that this pattern is observed for the entire profile except for the end of LIA and for the IND period where an increase on precipitation has a decrease on temperature and vice versa. From this point onwards the period comprised between 1680 and 1920 AD will be called 1680-1920 AD period.

By observing the general configuration of the North Atlantic ocean and atmosphere, a clear temperature and precipitation pattern has been observed.

In terms of precipitation, the general pattern showed that a decrease (increase) on precipitation in Lake Azul due to a positive (negative) phase of NAO was linked with a decrease (increase) on precipitation in the NW Iberian Peninsula (Corella et al., 2013),

Pico (Björk et al., 2006) and, sometimes, Morocco (Esper et al., 2006) and SW Iberian Peninsula (Nieto-Moreno et al., 2014) were added to the other sites. Otherwise, the 1680-1920 AD period showed that a decrease (increase) on precipitation in Lake Azul had a decrease (increase) on precipitation in Morocco (Esper et al., 2006) and south of the Iberian Peninsula (Nieto-Moreno et al., 2014); while this decrease (increase) was not observed in Pico Island (Björk et al., 2006) and the North of Spain (Corella et al., 2013). These findings suggested that for 1680-1920 AD period the southern NAO dipole suffered a south-eastern migration.

Moore et al. (2013) proposed that the Eastern Atlantic (EA) modulates the multi-decadal variability of the location of the southern NAO dipole. Based on that, a positive and in-phase EA-NAO could produce and intensification of the southern dipole triggering its southwards shift. EA phase has been observed to modify precipitation patterns in Europe generating spatial N-S gradients and intensifying or decreasing the effects on the NAO while those patterns are in-phase or opposite phase, respectively (Hernández et al., 2014; Comas-Bru et al., 2015). The effects of EA have not been observed in Ponta Delgada for the last 138 years that ranges the instrumental series (Hernández et al., 2016) but, the end of LIA and the IND period were moments of high climate variability.

In terms of temperature, an increase (decrease) in Lake Azul was also observed in Pico Island, south of Europe and the Caribbean area; while a decrease (an increase) was observed in the North of Europe and Eastern American Coast. During the 1680-1920 AD period, the temperatures in the north Atlantic displayed similar patterns except of the variation on temperature in the American coast. The North American Coast that usually showed a decrease on temperature while Azores temperature increase, sometimes covariate for this period. For example, the IND period showed an increase of temperature on both Azores and North American East coast. This could be because the enhancement of the southern NAO dipole moved towards north the GSNW but, the south position of the southern NAO dipole allows a zonal movement that reach Azores.

In order to observe how those movements of the NAO centers of action affect to the reproducibility of the NAO in other reconstructions, Lake Azul hydrological reconstruction realized in this work has been compared with two of the most used NAO reconstructions (Fig. 5.19). The NAO reconstruction based on a yearly resolved NAO reconstruction compilation (Ortega et al., 2015) and the NAO reconstruction based in a tree ring composite from Morocco (Esper et al., 2006) and Scotland (Trouet et al., 2009). In general, Lake Azul reconstruction showed more similitudes with the first than with the second but, all the reconstructions showed similar trends within the age model uncertainties. The 1680-1920 AD period displays decadal positive-negative-positive-negative NAO phase alternation in Lake Azul that is observed by the Trouet's NAO reconstruction taking into account the age model uncertainties. Ortega's NAO reconstruction showed different variations that sometimes are opposite in phase.

The AMO influence

The AMO has been related to variations on temperature (section 5.2) and to precipitation (Hernández et al., 2016). Variations on precipitation for a large scale might be produced by AMO when the NAO loose intensity. Moreover, we observed on the present section that the position of the southern NAO dipole might be playing an important role for the end of LIA and the IND period.

On the other hand, decadal temperature variations in Lake Azul are affected by the AMO and that these changes are observed for the maximum MAT data and by the amplitude between maximum and minimum MAT. This amplitude was the response of a major seasonality that means harsh winters and hot summers. Since the GDGTs temperature reconstruction has a summer to fall bias, we should be recording the periods of warm AMO phase.

Therefore, the AMO reconstruction proposed by Gray et al., (2004) was compared by the temperature reconstruction for Azul lake (Fig. 5.20). The periods of AMO positive (warm) phase observed an increase on temperature for the Lake Azul. But, periods of AMO negative (cold) phase do not observe a temperature decrease in Lake Azul record.

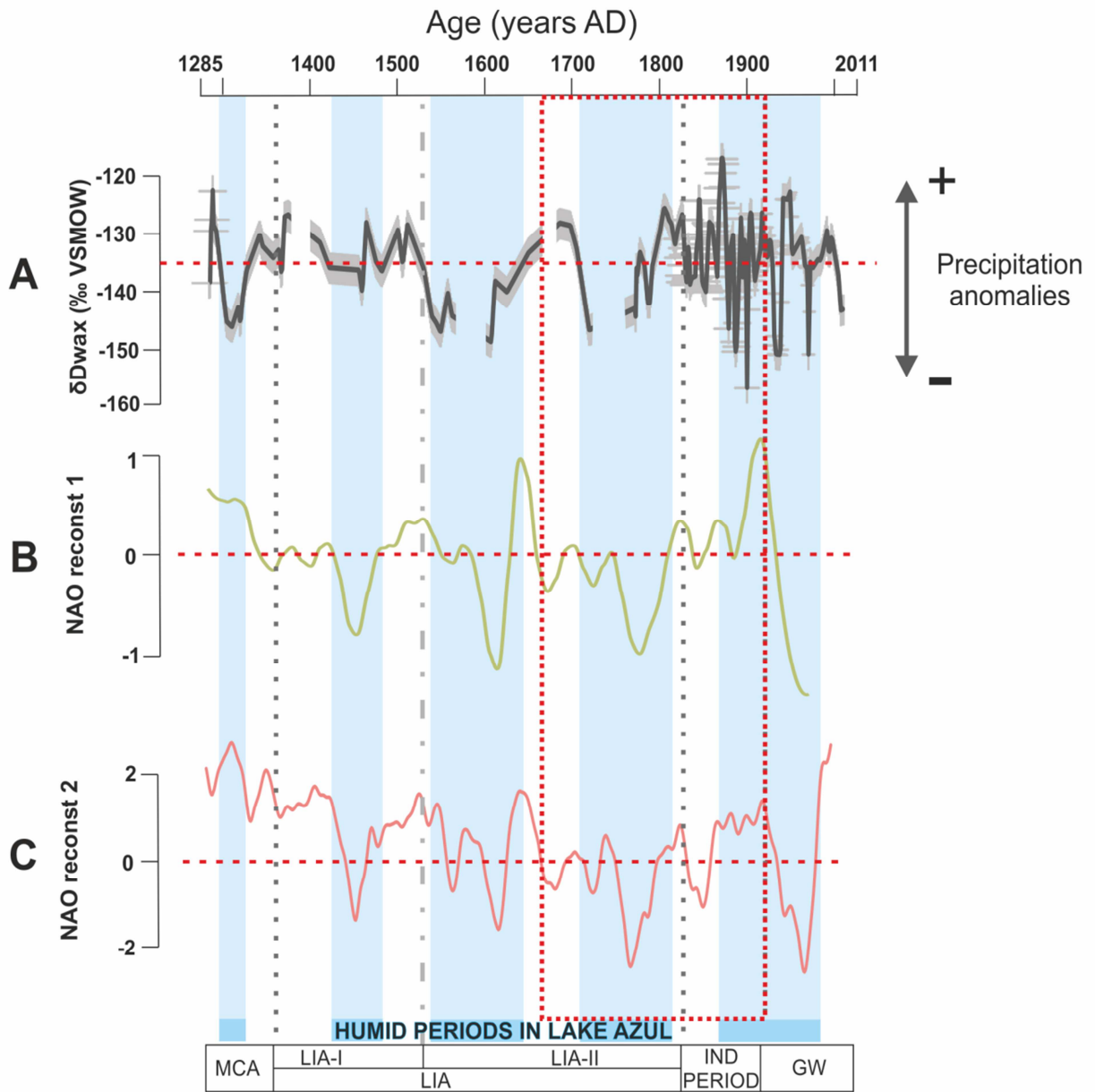


Figure 5.19: Precipitation reconstruction for Lake Azul record for the period comprised between 1285 and 2011 AD based on δD leaf wax comparison with two NAO reconstructions. From top to bottom (A) Lake Azul reconstruction, (B) Ortega et al., (2015) reconstruction and (C) Trouet et al., (2009) reconstruction. The blue bars represent humid periods based on Lake Azul reconstruction. The dotted squared section represents the 1680-1920 period. This period is highlighted because anomalies on the general north Atlantic atmospheric and oceanic circulation have been observed. The climatic periods are shown in a lower bar. Note that the humid periods in Azores reconstruction are consistent with the other reconstructions.

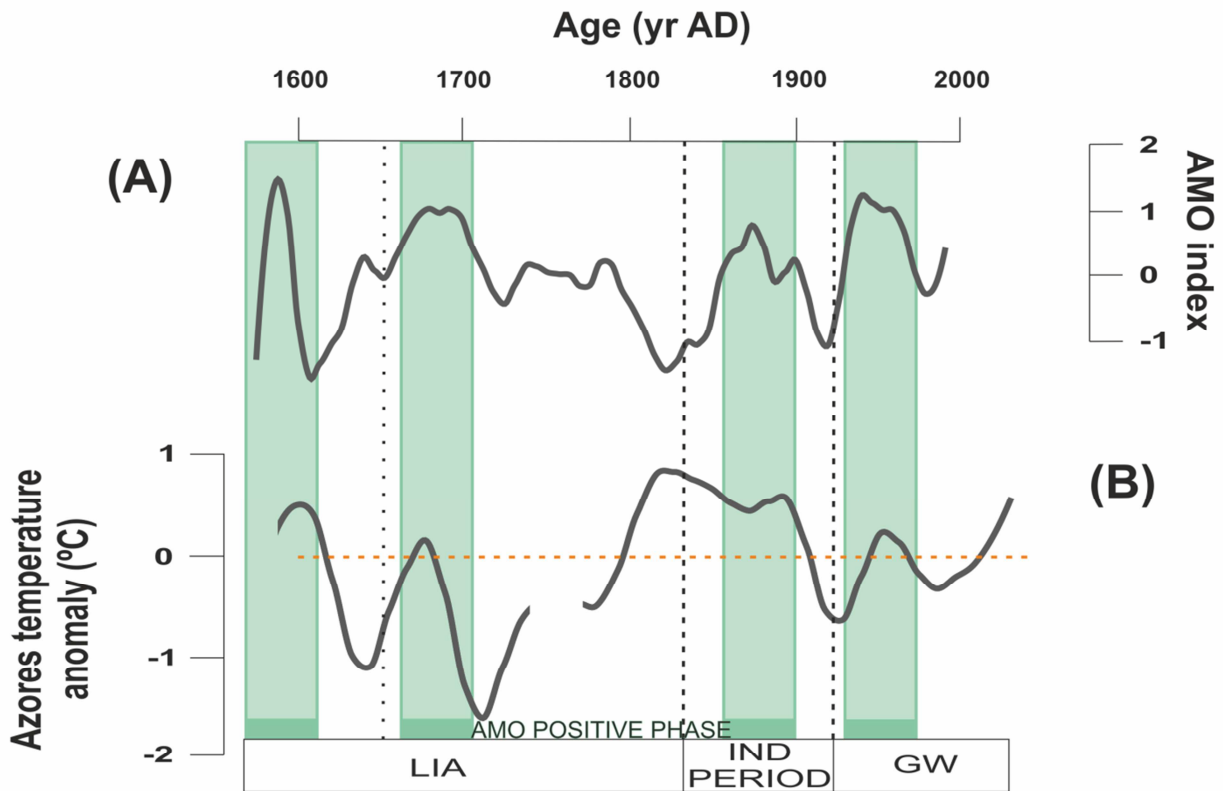


Figure 5.20: Comparison between (A) Grey et al., (2004) tree ring composite for the entire Atlantic ocean that reconstruct the Atlantic Meridional Oscillation (AMO) and (B) temperature reconstruction from lake Azul for the period comprised between 1567 and 2011 AD (this The blue bars represent periods of positive AMO based on Gray et al., (2004) reconstruction. The climatic periods are shown in a lower bar. Note that AMO positive phases are related to an increase on temperature in Lake Azul.

Summary

The NAO phase modulates temperature and precipitation patterns over the North Atlantic. A positive phase of NAO enhances the precipitation in northern Europe while it decreases in the south of Europe and Azores. A negative phase of NAO, in turn, produces a precipitation enhancement in the south of Europe while a decrease in the north.

In terms of temperature, a positive phase of NAO enhances temperature in the eastern coast of USA and the north of Europe while a decrease is observed from Caribbean to the Iberian Peninsula and North of Morocco. On the contrary, a negative phase of NAO produces an enhancement of the temperature from the Caribbean towards the Iberian Peninsula.

The 1680-1920 AD period displayed a different pattern. It observed that a decrease on precipitation in Lake Azul (indicating NAO positives conditions) was not recognized in

Pico Island or North of Spain as it was expected. Moreover, the temperature increase in Azores that expected a decrease on the USA east coast was not observed. Those conditions suggested a shift southwards of the southern NAO dipole promoted by EA-NAO in-phase conditions.

*No Hay nada más poderoso,
Que una idea a la que le ha llegado su hora.*

Victor Hugo

6. SUMMARY and CONCLUSIONS

The morphology of Lake Azul basin has been characterized, distinguishing 3 main sedimentation areas: a) the shallow ramp-platform, b) a nearshore delta system, and c) the deep plain. A recovered sequence of offshore deposits covers last the last 730 yrs., and is dominated by a fine lacustrine sedimentary sequence interbedding volcanoclastic deposits (at the base) and flood events rich in terrestrial plant remains (in mid-upper part of the record).

A Dynamic Age Model (DAM) is proposed to assess short- and long-term SR changes in the sedimentation. The chronological model is based on (1) core-scanner XRF data that can continuously reproduce changes in siliciclastic inputs; and (2) ^{14}C and ^{210}Pb datations as a tie points. The singular characteristic of the DAM is the assumption that that SR in one point is not related at all with SR of previous point. The robustness of the DAM has been checked with the Lake Azul sediments and compared with other chronological models (Bacon and mixed-effect regression). The comparison of the SR obtained with the DAM and the precipitation changes for the 1936 – 2011 AD period shows that this method enables the capture of the short- and long-term SR fluctuations better than the other approaches. The DAM has also been tested with some historical events such as the *Cryptomeria sp.* introduction and fish introduction that can be observed at the correspondent age within the age model uncertainties. The DAM opens an opportunity to obtain robust and reliable chronological models in recent sedimentary sequences in which the age models are of paramount importance to correlate with meteorological instrumental and historical datasets.

A temperature reconstruction was performed by Glycerol Dyalkyl Glycerol Tetraether (GDGT) on the Azul sedimentary sequence. This reconstruction reveals warm conditions during the Medieval Climate Anomaly (MCA) but, not stable for the entire period. The LIA contains the periods of lowest temperatures of Lake Azul record from 1370 to 1470 and from 1680 to 1820 AD. But, from 1470 to 1680 AD was a period characterized by warmth temperatures that look like actual conditions. The end of LIA and the IND PERIOD were characterized by relatively warm temperature followed by

an abrupt decrease right before the onset of the Global Warming (GW). This recent is characterized by an increasing trend on temperatures.

The study on the δD leaf wax shows that precipitation in Azores is divided in two characteristic main periods: a) from 1285 to 1820 AD were the precipitation described a recurrent multidecadal oscillation, and b) from 1820 to 2011 AD were the precipitation describes a random pattern. There are not characteristic droughts or wet circumstances that describe any climatic period but in rough lines it can be observed that the LIA was the wettest period of our record and that the storminess are more recurrent for the IND PERIOD and the GW.

The main atmospheric pattern triggering climate conditions in Lake Azul is the North Atlantic Oscillation (NAO) affecting both, precipitation and temperature. A positive (negative) phase of NAO produces a decrease (enhancement) on precipitation in Lake Azul. Dry (Wet) conditions can be extrapolated to the entire AA, south of Europe and north of Africa except for the end of LIA where a small shift of the NAO southern center of action is suggested. In addition, a positive (negative) phase of NAO increases (decreases) the Eddy Kinetic Energy (EKE) helping the Gulf Stream North Wall to be produced at higher (lower) latitudes. This situation together with an increase (decrease) of westerlies moves to a north-east (north-west) position the bifurcation of the Azores Current (AzC) making more difficult (facilitating) to reach Azores. Therefore, a positive NAO phase decrease the temperature nearby São Miguel and increase temperature in the east coast of USA and north of Europe. On the contrary, the temperature around the island while a negative phase of NAO has more chances to increase. But, temperatures in the north of Europe are going to the decrease because the GS heat transport is slower and lose more energy while travelling.

The MCA is divided in two periods one dry and cold suggesting a positive NAO phase from 1285 to 1310 yr AD; and, the other wet and warm suggesting a negative NAO phase from 1310 to 1370 yr AD.

The LIA can be divided in four periods based on the NAO conditions. Dry and cold conditions suggesting a positive phase of NAO occurred at the LIA onset (between 1370 and 1530 yr AD) and between 1650 and 1730. NAO negatives conditions were observed for the periods from 1530 to 1650 and from 1730 to 1800 yr AD. The first of those periods was characterized by variable temperature and wet conditions. And the second was wet and cold. The IND PERIOD and the GW denoted an increase of storminess and, majorly, an increase on temperature mainly suggesting a negative NAO phase conditions.

APPENDIX

To apply the DAM model, the R script DAM.R has to be used. This model has been created using the software R (<http://www.r-project.org/>) with the R studio interface (<http://www.rstudio.com/>).

In order to use this script:

1. Download R and Rstudio
2. Open Rstudio
3. Open DAM file: (File -> Open file -> DAM.R)
4. Follow the instructions present in the DAM.R script.

DAM.R is a relatively easy to understand script that runs in a open software. This model permits the user to adapt the script to the needed requirements because; it has an open code nature. Therefore it is not a “black box”.

```

## DYNAMIC AGE MODEL SCRIPT FOR R IN WINDOWS VERSION.

##Set working directory

setwd("~/Directory")

## File extension should be .cvs

## Upload CRS210Pb profile

## Upload XRF data without flood events.

## The .cvs file should be saved with ";" as separator between columns

## The .cvs file for the XRF should have the elements in columns and the first column
should be "Depth".

## The .cvs file for the 210Pb should have 3 columns "Depth", "Age", "Sed_rate"

PB210 <- read.csv("clipboard", sep=";", header=T)

XRF <- read.csv("clipboard", sep=";", header=T)

#####

##Step1

##BEST CORRELATED ELEMENT IDENTIFICATION

#####

## Make both parameters (XRF, 210Pb) at the same resolution.

## It can be done manually.

## Here the example for one centimeter.

Depth_r <- floor(XRF$Depth)##Erase the decimals and keep the number round at floor.

XRF2 <- as.data.frame(cbind(Depth_r, XRF))## Link the Depth rounded and the XRF
data

XRF_cm <- aggregate(XRF2[,3:ncol(XRF2)], list(Depth2 = XRF2$Depth_r),
median)##Calculate the median every centimeter

## This part can only be done after have both parameters (XRF, 210Pb) at the same
resolution

```

```
Length_210 <- length(PB210[,1]) ## Length of the Pb 210

XRF_equal <- XRF_cm[1:Length_210,] ## Equalize the XRF length to the Pb210 length.

matrix_cor <- as.matrix(cbind(PB210[,3], XRF_equal[,2:ncol(XRF_equal)]))## Join the
XRF element with the Sed rate from the 210Pb

require(Hmisc)## Upload the package Hmisc

rcorr(matrix_cor)

### Select by hand the element with maximum r and lower than 0.05 p.

BCE <- XRF["Introduce column number"] #### Introduce the column number of the
best correlated element from the XRF dataset you have introduced to the model

Depth <- XRF[,1] ## Depth of the model

#####

##Step2

##TIE POINTS ESTABLISHMENT

#####

n_tie_points <- "Introduce number of tie points" #### Determine the number of tie
points

n <- n_tie_points-1 ##### Determine the number of sections of your model

## The number of section will determine the times that you have to repeat the
process.

## Copy and paste the following script section by section depending on the repetitions

## Each copy increase one number (for example Depth.base1, Depth.base2)

##We have to copy and paste and increase the number until the n tie points we have

Depth.base.n <- "INTRODUCE_tie_depth_point n"; Depth.top.n <- Depth.base.n-1

Age.base.n <- "INTRODUCE_tie_age_point n"; Age.top.n <- Age.base.n-1
```

```
#####

##Step3

##BCE BINARIZATION PROCESS

#####

XRF.measu.cm <- "INTRODUCE NUMBER OF XRF MEASUREMENTS PER CM" ##number
of XRF measurements per centimeter

## For example for a 0.2cm resolution XRF.measu.cm is 5

### The number of Corresp.BCE.measu are equal to the n (number of sections)

## Section 1

Corresp.BCE.measu1 <- 1 ## Corresponding BCE measurement for the upper tie point

Corresp.BCE.measu2 <- ((Depth.base1*XRF.measu.cm)+1) ## Corresponding BCE
measurement for the lower tie point

BCE.measu1 <- (Corresp.BCE.measu1:Corresp.BCE.measu2) ## Sequence of
correspondent measurements.

Sect_range1 <-range(BCE[BCE.measu1], na.rm = TRUE) ##Calculate the range of the
BCE for this section

Sect_bin1 <- c(min(Sect_range1), max(Sect_range1), 0.01, 1) ## Set up the parameters
for the binarization matrix

dim(Sect_bin1) <- c(2,2)##Create the binarization matrix

Lin_reg1 <- lm(Sect_bin1[,2] ~ Sect_bin1[,1]) ## Linear regression calculation

Lin_reg1 ##View of the linear regression

bBCE1 <- Lin_reg1$coefficients[1] + Lin_reg1$coefficients[2]*BCE[BCE.measu1] ##
Application of the linar regression to

##the first section.

## Section 2

Corresp.BCE.measu1 <- ((Depth.base1*XRF.measu.cm)+1) + 1 ## Corresponding BCE
measurement for the upper tie point

Corresp.BCE.measu2 <- ((Depth.base2*XRF.measu.cm)+1) ## Corresponding BCE
measurement for the lower tie point
```

```
BCE.measu2 <- (Corresp.BCE.measu1:Corresp.BCE.measu2) ## Sequence of
correspondent measurements.

Sect_range2 <-range(BCE[BCE.measu2], na.rm = TRUE) ##Calculate the range of the
BCE for this section

Sect_bin2 <- c(min(Sect_range2), max(Sect_range2), 0.01, 1) ## Set up the parameters
for the binarization matrix

dim(Sect_bin2) <- c(2,2)##Create the binarization matrix

Lin_reg2 <- lm(Sect_bin2[,2] ~ Sect_bin2[,1]) ## Linear regression calculation

Lin_reg2 ##View of the linear regression

bBCE2 <- Lin_reg2$coefficients[1] + Lin_reg2$coefficients[2]*BCE[BCE.measu2] ##
Application of the linear regression to

##the second section.

### Repeat it as many times you need depending on the number of sections

##We have to copy and paste and increase the number until the of sections we have

## Change z for the section number

## Section z

Corresp.BCE.measu1 <- ((Depth.basez-1*XRF.measu.cm)+1) + 1 ## Corresponding BCE
measurement for the upper tie point

Corresp.BCE.measu2 <- ((Depth.basez*XRF.measu.cm)+1) ## Corresponding BCE
measurement for the lower tie point

BCE.measuz <- (Corresp.BCE.measu1:Corresp.BCE.measu2) ## Sequence of
correspondent measurements.

Sect_rangez <-range(BCE[BCE.measuz], na.rm = TRUE) ##Calculate the range of the
BCE for this section

Sect_binz <- c(min(Sect_rangez), max(Sect_rangez, 0.01, 1) ## Set up the parameters
for the binarization matrix

dim(Sect_binz) <- c(2,2)##Create the binarization matrix

Lin_regz <- lm(Sect_binz[,2] ~ Sect_binz[,1]) ## Linear regression calculation

Lin_regm ##View of the linear regression
```



```
bBCEz <- Lin_regz$coefficients[1] + Lin_regz$coefficients[2]*BCE[BCE.measuz] ##
Application of the linear regression to

##the z section.

bBCE <- c(bBCE1, bBCE2, bBCEz) ##bBCE vector created

## Optional

plot(bBCE, type="l") ##Observe how it looks.

#####

##Step4

## UNITS ADDITION (ubBCE)

#####

## All sections together.

range <- range(bBCE, na.rm = TRUE) ##Calculate the range of the bBCE for this section

units_matrix <- c(min(range), max(range), min(PB210[,3]), max(PB210[,3])) ## Set up
the parameters for the binarization matrix

dim(units_matrix) <- c(2,2) ##Create the transposition matrix

formula_units <- lm(units_matrix[,2] ~ units_matrix[,1]) ## Linear regression
calculation

## Optional

formula_units ##View of the linear regression

uBCE <- formula_units$coefficients[1] + formula_units$coefficients[2]*bBCE ##
Application of the linear regression

## Optional

plot(uBCE, type="l") ##Observe how it looks.
```

```
#####

##Step5

## INVERSE uBCE (iBCE)

#####

## Section 1

iBCE1 <- 1/uBCE[BCE.measu1] ## Inverse of the uBCE

iBCE1[is.na(iBCE1)] <- 0 ## Change to 0 all the NA's

## Section 2

iBCE2 <- 1/uBCE[BCE.measu2]## Inverse of the uBCE

iBCE2[is.na(iBCE2)] <- 0 ## Change to 0 all the NA's

### Repeat it as many times you need depending on the number of sections

##We have to copy and paste and increase the number until the z of sections we have

## Change z for the section number

## Section z

iBCEz <- 1/uBCE[BCE.measuz]## Inverse of the uBCE

iBCEz[is.na(iBCEz)] <- 0 ## Change to 0 all the NA's

#####

##Step6

## MEAN NUMBER OF UNITS (mBCE)

#####

## Section 1

mBCE1 <- (Age.top1-Age.base1)/sum(iBCE1) ## Apply the formula

## Section 2

mBCE2 <- (Age.top2-Age.base2)/sum(iBCE2) ## Apply the formula
```

```

#### Repeat it as many times you need depending on the number of sections

##We have to copy and paste and increase the number until the m of sections we have

## Change z for the section number

## Section z

mBCEz <- (Age.topz-Age.basez)/sum(iBCEz) ## Apply the formula

#####

##Step7

## DIFFERENCE OF TIME UNITS (dBCE)

#####

## Section 1

dBCE1 <- iBCE1*mBCE1 ## Obtain the Age difference between points.

## Section 2

dBCE2 <- iBCE2*mBCE2 ## Obtain the Age difference between points.

#### Repeat it as many times you need depending on the number of sections

##We have to copy and paste and increase the number until the m of sections we have

## Change z for the section number

## Section z

dBCEz <- iBCEz*mBCEz ## Obtain the Age difference between points.

#####

##Step8

## AGE MODEL CONSTRUCTION (DAM)

#####

## Section 1

DAM1 <- Age.top1 - cumsum(dBCE1) ## Obtain the ages for the section 1

## Section 2

```

```
DAM2 <- Age.top2 - cumsum(dBCE2) ## Obtain the ages for the section 2
### Repeat it as many times you need depending on the number of sections
##We have to copy and paste and increase the number until the m of sections we have
## Change z for the section number
## Section z
DAMz <- Age.topz - cumsum(dBCEz) ## Obtain the ages for the section z
##Compilation of the different sections.
DAM <- c(DAM1, DAM2, DAMz) ##Age vector created
## Optional
plot(DAM, type="l") ##Observe how it looks.
#####
##Step7
## SEDIMENTATION RATE CALCULATION
#####
Depth_top <- Depth[1:(Corresp.BCE.measu2-1)] ## Select the points from 1 to length
BCE -1
Depth_bottom <- Depth[2:Corresp.BCE.measu2] ## Select the points from 2 to length
BCE
Dif_depth <- Depth_bottom - Depth_top ##
Age_top <- Age[1:(Corresp.BCE.measu2-1)]
Age_bottom <- Age[2:Corresp.BCE.measu2]
Dif_age <- Age_top - Age_bottom
Sedimentation_rate <- c((Dif_depth/Dif_age), NA)
## Optional
plot(Sedimentation_rate, type="l") ##Observe how it looks.
```

#####

Last Step

CREATE AN EXCEL TO WORK WITH

#####

```
Depth <- Depth[1:Corresp.BCE.measu2]
```

```
DAM <- as.data.frame(cbind(Depth, DAM, Sedimentation_rate))
```

```
write.table(DAM, file = "DAM.csv", sep = ",", col.names = NA)
```

REFERENCES

- ABRANTES, F., LEBREIRO, S., RODRIGUES, T., GIL, I., BARTELS-JÓNSDÓTTIR, H., OLIVEIRA, P., & GRIMALT, J. O., 2005. *Shallow-marine sediment cores record climate variability and earthquake activity off Lisbon (Portugal) for the last 2000 years*. *Quaternary Science Reviews*, 24(23), 2477-2494.
- AHMED ET AL., 2013. Continental-scale temperature variability during the last two millennia. *Nature Geoscience* 6, 339 – 346.
- ALLEN, J., ARCHER, S. D., BLACKFORD, J. C., GILBERT, F. J., & TAYLOR, A. H., 2006. Changes in DMS production and flux in relation to decadal shifts in ocean circulation. *Tellus B*, 58(3), 242-254.
- ALLEY R.B., SHUMAN C.A., MEESE D.A., GOW A.J., TAYLOR K.C., CUFFEY K.M., FITZPATRICK J.J., GROOTES P.M., ZIELINSKI G.A., RAM M., SPINELLI G., ELDER B., 1997. *Visual-stratigraphic dating of the GISP2 ice core: Basis, reproducibility, and application*. *Journal of Geophysical Research, Oceans*, 102(C12), 26367-26381. doi: 10.1029/96JC03837.
- AMBAR, I., & HOWE, M. R., 1979. *Observations of the Mediterranean outflow—I mixing in the Mediterranean outflow*. *Deep Sea Research Part A. Oceanographic Research Papers*, 26(5), 535-554.
- ANDERSON, V. J., SAYLOR, J. E., SHANAHAN, T. M., & HORTON, B. K., 2015. Paleoelevation records from lipid biomarkers: Application to the tropical Andes. *Geological Society of America Bulletin*, 127(11-12), 1604-1616.
- ANDRADE C., TRIGO R.M., FREITAS M.C., GALLEGO M.C., BORGES P., RAMOS A.M.; 2008. *Comparing historic records of storm frequency and the North Atlantic Oscillation (NAO) chronology for the Azores region*. *The Holocene* vol 18: 745-754.
- ANDRADE C., BORGES P., FREITAS M.C., 2006. *Historical tsunami in the Azores archipelago (Portugal)*. *Journal of Volcanology and Geothermal Research* 156: 172-185.
- ANTUNES, P., & RODRIGUES, F. C., 2011. *Azores Volcanic Lakes: factors affecting water quality*. *Water Quality: Currents Trends and Expected Climate Change Impacts*, 106-114.
- APPENZELLER, C., STOCKER, T. F., & ANKLIN, M., 1998. *North Atlantic Oscillation dynamics recorded in Greenland ice cores*. *Science*, 282(5388), 446-449.
- APPLEBY P. G., 2001. *Chronostratigraphic techniques in recent sediments, in Tracking Environmental Change Using Lake Sediments Volume 1: Basin Analysis, Coring, and Chronological Techniques*, (eds W M Last & J P Smol), Kluwer Academic, 2001, pp171-203
- APPLEBY P.G., OLDFIELD F., 1978. *The calculation of lead-210 dates assuming a constant rate of supply of unsupported 210Pb to the sediment*. *Catena*. Vol. 5. 1 -8. Braunschweig 1978.
- ARAGUÁS-ARAGUÁS, L., FROELICH, K., & ROZANSKI, K., 2000. *Deuterium and oxygen-18 isotope composition of precipitation and atmospheric moisture*. *Hydrological Processes*, 14(8), 1341-1355.
- ARGUS, D.F., GORDON, R.G., DEMETS, C. AND STEIN, S., 1989. *Closure of the Africa-Eurasia-North America plate motion circuit and tectonics of the Gloria fault*. *Journal of Geophysical Research* 94: doi: 10.1029/88JB03988. issn: 0148-0227.
- ARÍSTEGUI, J., MENDONÇA, A., VILAS, J. C., ESPINO, M., POLO, I., MONTERO, M. F., & MARTINS, A., 2009. *Plankton metabolic balance at two North Atlantic seamounts*. *Deep Sea Research Part II: Topical Studies in Oceanography*, 56(25), 2646-2655.
- BAKER, A., HELLSTROM, J. C., KELLY, B. F., MARIETHOZ, G., & TROUET, V., 2015. *A composite annual-resolution stalagmite record of North Atlantic climate over the last three millennia*. *Scientific reports*, 5.
- BAKUN, A., 1990. *Global climate change and intensification of coastal ocean upwelling*. *Science*, 247(4939), 198-201.
- BASTOS, A., JANSSENS, I. A., GOUVEIA, C. M., TRIGO, R. M., CIAIS, P., CHEVALLIER, F., ... & RUNNING, S. W., 2016. *European land CO2 sink influenced by NAO and East-Atlantic Pattern coupling*. *Nature communications*, 7.
- BARD E, ROSTEK F, AND SONZOGNI C. 1997. *Interhemispheric synchrony of the last deglaciation inferred from alkenone palaeothermometry*. *Nature* 385: 707-710.
- BARNES, E. A., & GARFINKEL, C. I., 2012. *Barotropic impacts of surface friction on eddy kinetic energy and momentum fluxes: An alternative to the barotropic governor*. *Journal of the Atmospheric Sciences*, 69(10), 3028-3039.
- BARTOLOMÉ M., MORENO A., SANCHO C., STOLL H.M., CACHO I., SPÖTL C., BELMONTE A., LAWRENCE E., CHENG H., HELLSTROM C., 2015. *Hydrological change in Southern Europe responding to increasing North Atlantic overturning during Greenland Stadial 1*. *PNAS*. Doi: 10.1073/pnas.153990112.
- BECK C., 2009. *"Late Quaternary lacustrine paleo-seismic archives in north-western Alps: Examples of earthquake origin assessment of sedimentary disturbance."* *Earth Science Reviews* 96 327-344.
- BEHL, R., AND J. P. KENNETT, 1996. Brief interstadial events in the Santa Barbara basin, NE Pacific, during the past 60 kyr, *Nature*, 379, 243 – 246.

- BEIER C., HAASE K.M., HANSTEEN T.H., 2006. *Magma evolution of Sete Cidades Volcano, São Miguel, Azores*. Journal of petrology, vol 47, num 7, pag 1375-1411.
- BENNETT, K.D., 1994. *Confidence intervals for age estimates and deposition times in late-Quaternary sediment sequence*. The Holocene 4, 337-348.
- BERTH-WURTZEL J., BLACK D.E., THUNELL R.C., PETERSON L.C., TAPPA E., PAHMAN S. 2013. *Mechanisms of southern Caribbean SST variability over the last two millennia*. Geophysical research letters, vol.40, 1-5.
- BINDOFF, N. L., WILLEBRAND, J., ARTALE, V., CAZENAVE, A., GREGORY, J. M., GULEV, S., ... & SHUM, C. K., 2007. *Observations: oceanic climate change and sea level*.
- BIRKS, H.J.B., HEIRI, O., SEPPÄ H., BJUNE A.E., 2010. *Strengths and weaknesses of Quantitative climate reconstructions based on Late-Quaternary biological proxies*. The open journal, 3, 68-110.
- BJÖRCK, S., RITTENOUR, T., ROSÉN, P., FRANÇA, Z., MÖLLER, P., SNOWBALL, I., ... & KROMER, B., 2006. *A Holocene lacustrine record in the central North Atlantic: proxies for volcanic activity, short-term NAO mode variability, and long-term precipitation changes*. Quaternary Science Reviews, 25(1), 9-32.
- BJÖRCK S. AND WOHLFARTH B., 2001. *¹⁴C Chronostratigraphic techniques*. In: Ivanovich & R.S. Harmon (eds.), Uranium-series Disequilibrium: Applications to Earth, Marine & Environmental Sciences, Oxford University Press, 731-778.
- BLAGA, C. I., G.-J. REICHART, O. HEIRI, AND J. S. SIN-NINGHE DAMSTÉ. 2009. *Tetraether membrane lipid distributions in water-column particulate matter and sediments: a study of 47 European lakes along a north-south transect*. Journal of Paleolimnology. 41 (3), 523-540.
- BLAGA, C., G. REICHART, S. SCHOUTEN, A. LOTTER, J. WERNE, S. KOSTEN, N. MAZZEO, N., G. LACEROT, AND J. S. SINNINGHE DAMSTÉ. 2010. *Branched glycerol dialkyl glycerol tetraethers in lake sedi-ments: Can they be used as temperature and pH proxies?* Organic Geochemistry, 41:1225-1234.
- BLAAUW, M., 2010. *Methods and code for 'classical' age-modelling of radiocarbon sequences*. Quaternary Geochronology 5, 512-518.
- BLAAUW, M. & CHRISTEN, J. A., 2005. Radiocarbon peat chronologies and environmental change. Applied Statistics 54, 805-816.
- BLAAUW M., CHRISTEN A., 2011. *Flexible paleoclimate Age-Depth models using an autoregressive Gamma process*. Bayesian Analysis. Vol. 6, Number 3, pp. 457-474.
- BOOTH B., CROASDALE R., WALKER G.P, 1978. *A quantitative study of the five thousand years of volcanism on São Miguel, Azores*. Philosophical Transactions of the Royal Society of London 288, 271-319.
- BORGES, P.A.V. & BROWN, V.K., 1999. *Effect of island geological age on the arthropod species richness of Azorean pastures*. Biological Journal of the Linnean Society, 66, 373-410.
- BORKMAN D.G., SMAYDA T., 2009. *Gulf Stream position and winter NAO as drivers of long-term variations in the bloom phenology of the diatom Skeletonema costatum "species-complex" in Narragansett Bay, RI, USA*. Journal of plankton research, vol31, num 11-1407.
- BRADLEY, R. S., 2015. *Chapter 9 - Lake Sediments*. Paleoclimatology (Third Edition). R. S. Bradley. San Diego, Academic Press: 319-343.
- BRASELL SC, DUMITRESCU M, AND PARTY OLSS. 2004. *Recognition of alkenones in a lower Aptian porcellanite from the west-central Pacific*. Organic Geochemistry 35: 181-188.
- BRASSEL S. C., EGLINTON G., MARLOWE I. T., PFLAUMANN U. AND SARNTHEIN M. 1986. *Molecular stratigraphy: a new tool for climatic assessment*. Nature 320, 129-133.
- BRASELL, S., A. WARDROPER, I. THOMSON, J. MAX-WELL, AND G. EGLINTON. 1981. *Specific acyclic isoprenoids as biological markers of methanogenic bacteria in marine sediments*. Nature, 290:693.
- BRENNER, M., WHITMORE, T.J., CURTIS, J.H., HODELL, D.A., SCHELSKE, C.L., 1999. *Stable isotope (d13C and d15N) signatures of sedimented organic matter as indicators of historic lake trophic state*. Journal of Paleolimnology 22, 205-221.
- BRIFFA K.R., JONES P.D., SCHWEINGRUBER F.H., OSBORN T.J., 1998. Influence of volcanic eruptions on Northern Hemisphere summer temperature over the past 600 years. Nature 393, 450-455.
- BRIFFA K. R., OSBORN T. J. AND SCHWEINGRUBER F. H. 2004. *Largescale temperature inferences from tree rings: a review*. Global Planet. Change 40, 11-26.
- BROCHIER-ARMANET, C., B. BOUSSAU, S. GRIBALDO, AND P. FORTERRE. 2008. *Mesophilic Crenar-chaeta: proposal for a third archaeal phylum, the Thaumarchaeota*. Nature Reviews Microbiology, 6:245-252.

REFERENCES

- BROECKER W.S. 2000. *Was a change in thermohaline circulation responsible for the little Ice Age?* Perspective PNAS. Vol 97, no4, 1339-1342.
- BUCK C.E., KENWORTHY J.B., LITTON C.D., SMITH A.F.M., 1991. *Combining archaeological and radiocarbon information: a Bayesian approach to calibration*. *Antiquity*, 65, 808-821.
- BUCHACA, T., SKOV, T., AMSINCK, S. L., GONÇALVES, V., AZEVEDO, J. M. N., ANDERSEN, T. J., & JEPPESEN, E., 2011. *Rapid ecological shift following piscivorous fish introduction to increasingly eutrophic and warmer Lake Furnas (Azores Archipelago, Portugal): a paleoecological approach*. *Ecosystems*, 14(3), 458-477.
- BUEH, C., & NAKAMURA, H., 2007. *Scandinavian pattern and its climatic impact*. *Quarterly Journal of the Royal Meteorological Society*, 133(629), 2117-2131.
- BUKER GEORGE E., 1992. *The search for the seven cities and early American Exploration*. *The Florida Historical Quarterly*. Vol.71, No2, Oct, 1992.
- BÜNTGEN U., TEGEL W., NICOLUSSI K., MCCORNICK M., FRANK D., TROUET V., KAPLAN J.O., HERZIG F., HEUSSNER K.U., WANNER H., LUTHERBACHER J., ESPER J., 2011. *2500 years of European Climate Variability and human susceptibility*. *Science*, 331.
- BURJACHS F., LÓPEZ-SÁNCHEZ J.A., IRIARTE M.J., 2003. *Metodología arqueopalinológica*. In: Buxó, R., Piqué R. (Eds.). *La recogida de las muestras de arqueobotánica: objetivos y propuestas metodológicas*. Museu d'Arqueologia de Catalunya. Barceloa, pp. 11-18 (in Spanish).
- CAMPAN, A., 1995. *Analyse cinématique de l'Atlantique équatorial: Implications sur l'évolution de l'Atlantique sud et sur la frontière des plaques Amérique du nord/Amérique du sud*, these de doctorat, 352 pp., Univ. Pierre et Marie Curie (Paris VI), Paris, 1995
- CANNAT, M., BRIAIS, A., DEPLUS, C., ESCARTÍN, J., GEORGEN, J., LIN, J., ... & RABAIN, A., 1999. *Mid-Atlantic Ridge-Azores hotspot interactions: along-axis migration of a hotspot-derived event of enhanced magmatism 10 to 4 Ma ago*. *Earth and Planetary Science Letters*, 173(3), 257-269.
- CALIB 7.0 <http://calib.qub.ac.uk/calib/calib.html>
- CALIBOMB <http://calib.qub.ac.uk/CALIBomb/>
- CARLSON, R.E. AND J. SIMPSON., 1996. *A Coordinator's Guide to Volunteer Lake Monitoring Methods*. North American Lake Management Society. 96 pp.
- CASTAÑEDA, I., E. SCHEFUß, J. PÄTZOLD, J. S. SIN-NINGHE DAMSTÉ, S. WELDEAB, AND S. SCHOUTEN. 2010. *Millennial-scale sea surface temperature changes in the eastern Mediterranean (Nile River Delta region) over the last 27,000 years*. *Paleoceanography*, 25:PA1208.
- CATALAN, J., PLA-RABÉS, S., WOLFE, A. P., SMOL, J. P., RÜHLAND, K. M., ANDERSON, N. J., ... & CAMARERO, L., 2013. *Global change revealed by palaeolimnological records from remote lakes: a review*. *Journal of Paleolimnology*, 49(3), 513-535.
- CHAPPE, B., W. MICHAELIS, AND P. ALBRECHT. 1980. *Molecular fossils of archaeobacteria as selective degradation products of kerogen*. *Physics and Chemistry of the Earth*, 12:265-274.
- CHRISTEN, J. A. 1994. *Summarising a set of radiocarbon determinations: a robust approach*. *Applied Statistics*, 43(3): 489.
- CHUNG F.H., 1974. *Quantitative interpretation of X-Ray diffraction patterns of mixture*. *J.Appl. Cryst.*7, 519-531.
- COHEN AS., 2003. *Paleolimnology: the history and evolution of lake systems*. Oxford University Press, New York
- COLE P.D., PACHECO J.M, GUNASEKERA R., QUEIROZ G., GONÇALVES P., GASPAR J.L., 2008. *Contrasting styles of explosive eruption at Sete Cidades, Sao Miguel, Azores, in the last 5000 years: Hazard implications from modelling*. *Journal of volcanology and geothermal research* 178 574-591, doi:10.1016/j.jvolgeores.2008.01.008.
- COLLINS, J. A., SCHEFUß, E., MULITZA, S., PRANGE, M., WERNER, M., THARAMMAL, T., ... & WEFER, G., 2013. *Estimating the hydrogen isotopic composition of past precipitation using leaf-waxes from western Africa*. *Quaternary Science Reviews*, 65, 88-101.
- COMAS-BRU L, MCDERMOTT F, 2014. *Impacts of the EA and SCA patterns on the European twentieth century NAO winter climate relationship*. *Q J R Meteorol Soc* 140(679):354-363.
- COMAS-BRU, L., MCDERMOTT, F., & WERNER, M. (2016). *The effect of the East Atlantic pattern on the precipitation $\delta^{18}O$ -NAO relationship in Europe*. *Climate Dynamics*, 1-11.
- CONNOR, S. E., VAN LEEUWEN, J. F., RITTENOUR, T. M., VAN DER KNAAP, W. O., AMMANN, B., & BJÖRCK, S., 2012. *The ecological impact of oceanic island colonization—a palaeoecological perspective from the Azores*. *Journal of Biogeography*, 39(6), 1007-1023.
- CONSTÂNCIA JP, BRAGA TJ, NUNES JC, MACHADO E, SILVA L. 2000. *Lagoas e lagoerios da ilha de São Miguel. Amigos de las Azores-Asociación ecológica*. Editorial: Nova Gráfica, Lda. p: 7-131.

- CONTE MH, EGLINTON G, AND MADUREIRA LAS. 1992. *Long-chain alkenones and alkyl alkenoates as paleotemperature indicators: Their production, flux and early sedimentary diagenesis in the eastern North Atlantic*. *Organic Geochemistry* 19(1-3): 287-298.
- CONTE MH, THOMPSON A, LESLEY D, AND HARRIS RP. 1998. *Genetic and physiological influences on the alkenone/alkenoate versus growth temperature relationship in *Emiliania huxleyi* and *Gephyrocapsa oceanica**. *Geochimica et Cosmochimica* 62(1): 51-64.
- CONTE MH, WEBER JC, KING LL, AND WAKEHAM SG. 2001. *The alkenone temperature signal in western North Atlantic surface waters*. *Geochimica et Cosmochimica Acta* 65(23): 4275-4287.
- COOK, E. R., 2003. Multi-Proxy Reconstructions of the North Atlantic Oscillation (NAO) Index: A Critical Review and a New Well-Verified Winter NAO Index Reconstruction Back to AD 1400. *The North Atlantic Oscillation: climatic significance and environmental impact*, 63-79.
- CORELLA, J.P., STEFANOVA, V., EL ANJOURI, A., RICO, E., GIRALT, S., MORENO, A., PLATA-MONTERO, A., VALERO-GARCÉS, B.L., 2013. *A 2500-year multi-proxy reconstruction of climate change and human activities in northern Spain: the lake Arreo record*. *Palaeogeogr., Palaeoclimatol., Palaeoecol.* 386, 555-568.
- CRAIG, H., 1961. *Isotopic variations in meteoric waters*. *Science*, 133(3465), 1702-1703.
- CRANWELL, P. A., 1988. Lipid geochemistry of late Pleistocene lacustrine sediments from Burland, Cheshire, UK. *Chemical geology*, 68(3), 181-197.
- CRONIN, T. M., G. S. DWYER, T. KAMIYA, S. SCHWEDE, AND D. A. WILLARD. 2003. *Medieval Warm Period, Little Ice Age and 20th century temperature variability from Chesapeake Bay*, *Global Planet. Change*, 36, 17 - 29, 2003.
- CROPPER TE, HANNA E. 2014. *An analysis of the climate of Macaronesia, 1865-2012*. *Int. J. Climatol.* 34: 604-622, doi: 10.1002/joc.3710.
- CROWLEY, T. J. 2000. *Causes of Climate Change Over the Past 1000 Years*, *Science*, 289, 270 - 277.
- CRUZ, J.V., PACHECO, D.M, MENDES, S.C., MEDEIROS, M.C., 2007. *Atlas da Água nos Açores*. Ed. Secretaria Regional do Ambiente e do Mar, Direção Regional do Ordenamento do Território e dos Recursos Hídricos, 159p.
- CRUZ, J. V., ANTUNES, P., AMARAL, C., FRANÇA, Z., & NUNES, J. C., 2006. Volcanic lakes of the Azores archipelago (Portugal): Geological setting and geochemical characterization. *Journal of Volcanology and Geothermal Research*, 156(1), 135-157.
- CULLEN, H. M., D'ARRIGO, R. D., COOK, E. R., & MANN, M. E., 2001. *Multiproxy reconstructions of the North Atlantic oscillation*. *Paleoceanography*, 16(1), 27-39.
- CURRENTS, 2015. http://oceanservice.noaa.gov/education/tutorial_currents/05conveyor1.html checked on 18/06/2016.
- CURRY, R. G., & MCCARTNEY, M. S., 2001. *Ocean gyre circulation changes associated with the North Atlantic Oscillation*. *Journal of Physical Oceanography*, 31(12), 3374-3400.
- CRUZ J.V., ANTUNES P., AMARAL C., FRANÇA Z., NUNES J.C., 2006. *Volcanic lakes of the Azores arcipelago (Portugal): Geological setting and geochemical characterization*. *Journal of Volcanology and Geothermal Research* 156 (2006) 135-157.
- D'ANJOU, R. M., BRADLEY, R. S., BALASCIO, N. L., & FINKELSTEIN, D. B., 2012. *Climate impacts on human settlement and agricultural activities in northern Norway revealed through sediment biogeochemistry*. *Proceedings of the National Academy of Sciences*, 109(50), 20332-20337.
- DANSGAARD, W., 1964. *Stable isotopes in precipitation*. *Tellus*, 16(4), 436-468.
- DAWSON, A. G., ELLIOTT, L., MAYEWSKI, P., LOCKETT, P., NOONE, S., HICKEY, K., ... & FOSTER, I., 2003. *Late-Holocene North Atlantic climate 'seesaws', storminess changes and Greenland ice sheet (GISP2) palaeoclimates*. *The Holocene*, 13(3), 381-392.
- DAWSON, A. G., HICKEY, K., MAYEWSKI, P. A., & NESJE, A., 2007. Greenland (GISP2) ice core and historical indicators of complex North Atlantic climate changes during the fourteenth century. *The Holocene*, 17(4), 427-434.
- DEAN, W. E., & GORHAM, E., 1998. *Magnitude and significance of carbon burial in lakes, reservoirs, and peatlands*. *Geology*, 26(6), 535-538.
- DELWORTH, T. L., & DIXON, K. W., 2000. *Implications of the recent trend in the Arctic/North Atlantic Oscillation for the North Atlantic thermohaline circulation*. *Journal of Climate*, 13(21), 3721-3727.
- DELWORTH, T. L., & GREATBATCH, R. J., 2000. *Multidecadal thermohaline circulation variability driven by atmospheric surface flux forcing*. *Journal of Climate*, 13(9), 1481-1495.
- DELWORTH, T.L., MANN, M.E., 2000. *Observed and simulated multidecadal variability in the Northern Hemisphere*. *Climate Dynamics* 16, 661e676.

REFERENCES

- DESER, C., ALEXANDER, M. A., XIE, S. P., & PHILLIPS, A. S., 2010. *Sea surface temperature variability: Patterns and mechanisms*. Annual Review of Marine Science, 2, 115-143.
- DESER, C., AND M. L. BLACKMON, 1995. *On the relationship between tropical and North Pacific sea surface temperature variations*. J. Clim., 8, 1677 – 1680.
- DONDERS T. H., WEIJERS J. W. H., MUNSTERMAN D. K., KLOOSTERBOER-VAN HOEVE M. L., BUCKLES L. K., PANCOST R. D., SCHOUTEN S., SINNINGHE DAMSTE J. S. AND BRINKHUIS H. 2009. *Strong climate coupling of terrestrial and marine environments in the Miocene of northwest Europe*. Earth Planet. Sci. Lett. 281, 215–225.
- DRAY, S. AND DUFOUR, A.B., 2007. *The ade4 package: implementing the duality diagram for ecologists*. Journal of Statistical Software. 22(4): 1-20.
- DROTRH-INAG, 2001. *Plano regional da água*. Relatório técnico. Versão para consulta pública. Rep. DROTRH-INAG, Ponta Delgada.
- DROUET H., 1861. *Elements de la Faune Acoreene*. Mem. Soc. Acad de l'Aude 26.
- ENCYCLOPEDIA OF SCIENCE, 2002. <http://www.encyclopedia.com/topic/lake.aspx> checked on 04/12/2016.
- ENFIELD, D. B., MESTAS-NUÑEZ, A. M., & TRIMBLE, P. J., 2001. *The Atlantic multidecadal oscillation and its relation to rainfall and river flows in the continental US*. Geophysical Research Letters, 28(10), 2077-2080.
- EINSELE, G. 2000. *Sedimentary Basins. Evolution, Facies, and Sediment Budget*, 2nd ed. 792 pp. Berlin, Heidelberg, New York, London, Paris, Tokyo, Hong Kong: Springer-Verlag.
- ENGLER, A. 1879: *Versuch einer Entwicklungsgeschichte, insbesondere der Florengebiete seit der Tertiärperiode. I. Die extratropischen Gebiete der nördlichen Hemisphäre*. — W. Engelmann, Leipzig.
- ENGLBRECHT AC AND SACHS JP. 2005. *Determination of sediment provenance at drift sites using hydrogen isotopes and unsaturation ratios in alkenones*. Geochimica et Cosmochimica Acta 69(17): 4253-4265
- ELSNER, J. B., 2003. *Tracking hurricanes*. Bulletin of the American Meteorological Society, 84(3), 353-356.
- ESPER, J., FRANK, D., BÜNTGEN, U., VERSTEGE, A., LUTERBACHER, J., & XOPLAKI, E., 2007. *Long-term drought severity variations in Morocco*. Geophysical Research Letters, 34(17).
- FEDOSEEV, A., 1970. *Geostrophic circulation of surface waters on the shelf of north-west Africa*. Rapp. P.-V. Reun. Cons. Int. Explor. Mer., 159, 32-37.
- FERNÁNDEZ-PALACIOS, J.M., DE NASCIMENTO L., OTTO R., DELGADO J.D., GARCIA-DEL-RAY E., ARÉVALO J.R., WHITTAKER R.J., 2011. *A reconstruction of Paleo-Macaronesia with particular reference to the long-term biogeography of the Atlantic island laurel forests*. Journal of Biogeography, vol 38: 226-246.
- FISCHER E.M., LUTERBACHER J., ZORITA E., TETT S.F.B, CASTY C., AND WANNER H., 2007. *European climate response to tropical volcanic eruptions over the last half millennium*. Geophysical research letters, 34, L05707, doi:10.1029/2006GL027992
- FOGEL, M. L., & CIFUENTES, L. A., 1993. *Isotope fractionation during primary production*. In Organic geochemistry (pp. 73-98). Springer US.
- FORNACE, K. L., HUGHEN, K. A., SHANAHAN, T. M., FRITZ, S. C., BAKER, P. A., & SYLVA, S. P., 2014. *A 60,000-year record of hydrologic variability in the Central Andes from the hydrogen isotopic composition of leaf waxes in Lake Titicaca sediments*. Earth and Planetary Science Letters, 408, 263-271.
- FLOR DE LIMA, H.M. Q. 1993. *Contribuição para o estudo ictiológico das lagoas das Furnas e Sete Cidades*. In: Estudos, experimentação e divulgação. Eds, p.99, Secretaria Regional da Agricultura e Pescas, Ponta Delgada.
- FRUCTUOSO G., 1522-1591 "Saudades da Terra". In: Frutuoso G, (ed). Saudades da terra. – Instituto cultural da Ponta Delgada, Ponta Delgada.
- GILLET, N., F. ZWIERS, A. WEAVER, AND P. STOTT, 2003. *Detection of human influence on sea-level pressure*, Nature, 422(6929), 292–294, doi:10.1038/nature0148
- GIRALT, S., RICO-HERRERO, M.T., VEGA, J.C., VALERO-GARCÉS, B.L., 2011. *Quantitative climate reconstruction linking meteorological, limnological and XRF core scanner datasets: the Lake Sanabria case study, NW Spain*. J Paleolimnol., 46, 487-502.
- GLASER, R., 1999. *Seasonal temperature and precipitation fluctuations in selected parts of Europe during the sixteenth century*. Clim. Change, 43, 169–200.
- GLASER, R., & RIEMANN, D., 2009. *A thousand-year record of temperature variations for Germany and Central Europe based on documentary data*. Journal of Quaternary Science, 24(5), 437-449.

- GLIOZZI, A., G. PAOLI, M. DE ROSA, AND A. GAMBA-CORTA. 1983. *Effect of isoprenoid cyclization on the transition temperature of lipids in thermophilic archaeobacteria*. *Biochimica et Biophysica Acta (BBA)—Biomembranes*, 735:234–242.
- GOEURY CL., DE BEAULIEU J.L., 1979. *À propos de la concentration du pollen à l'aide de la liqueur de Thoulet dans les sédiments minéraux*. *Pollen et spores* 21, 239-251.
- GOLDENBERG, S.B., LANDSEA, C.W., MESTAS-NUNEZ, A.M., GRAY, W.M., 2001. *The recent increase in Atlantic hurricane activity: causes and implications*. *Science* 293,474e479.
- GOMES A., GASPAS, C., GOULART, C., QUEIROZ G., 2005. *Evaluation of landslide susceptibility of Sete Cidades Volcano (S. Miguel island, Azores)*. *Natural Hazard and Earth system science* 5:251-257. Doi: 1684-9981/nhess/2005-5-251.
- GOMEZ-NAVARRO, J. J. AND ZORITA, E., 2013. *Atmospheric annular modes in simulations over the past millennium: no long-term response to external forcing*. *Geophys. Res. Lett.*40, 3232–3236
- GONÇALVES, V., 2008. *Contribuição do estudo das microalgas para a avaliação da qualidade ecológica das Lagoas dos Açores: fitoplancton e diatomáceas bentónicas*. Doutoramento em Biologia, especialidade de Biologia Vegetal, Universidade dos Açores, Ponta Delgada.
- GONFIANTINI R., 1985. *On the isotopic composition of precipitation in tropical stations*. *Acta Amazonica* 04
- GONG C AND HOLLANDER DJ. 1999. *Evidence for differential degradation of alkenones under contrasting bottom water oxygen conditions: Implication for paleotemperature reconstruction*. *Geochimica et Cosmochimica Acta* 63(3/4): 405–411.
- GRAY, S. T., GRAUMLICH, L. J., BETANCOURT, J. L., & PEDERSON, G. T., 2004. *A tree-ring based reconstruction of the Atlantic Multidecadal Oscillation since 1567 AD*. *Geophysical Research Letters*, 31(12).
- GREEN J., 1992. *Island biogeography, diversity and dominance of zooplankton in crater lakes on the Azores*. *Biol J Linn Soc* 46:189–205.
- GRIGGS, C., DEGAETANO, A., KUNIHOLM, P., & NEWTON, M., 2007. *A regional high-frequency reconstruction of May–June precipitation in the north Aegean from oak tree rings, AD 1089–1989*. *International Journal of Climatology*, 27(8), 1075-1089.
- GRIMM, E. C., 1991. *Tilia 1.12, Tilia Graph 1.18*. Springfield, Illinois State Museum, Research and Collection Center.
- GROSSMANN, I., & KLOTZBACH, P. J., 2009. *A review of North Atlantic modes of natural variability and their driving mechanisms*. *Journal of Geophysical Research: Atmospheres*, 114(D24).
- GRUDD, H., 2008. *Tornetråsk tree-ring width and density AD 500–2004: a test of climatic sensitivity and a new 1500-year reconstruction of north Fennoscandian summers*. *Climate Dynamics*, 31(7-8), 843-857.
- HAMANAKA J, SAWADA K, AND TANOU E. 2000. *Production rates of C37 alkenones determined by 13C-labeling technique in the euphotic zone of Sagami Bay, Japan*. *Organic Geochemistry* 31: 1095–1102.
- HAMEED, S., AND S. PIONTKOVSKI, 2004. *The dominant influence of the Icelandic Low on the position of the Gulf Stream northwall*, *Geophys. Res. Lett.*, 31, L09303, doi:10.1029/2004GL019561
- HASSELMANN, K., 1976. *Stochastic climate models. Part 1. Theory*. *Tellus*, 28, 473-485 (3.1, 3.3)
- HASSLET J., PARNELL A., 2008. *A simple monotone process with application to radiocarbon-dated depth chronologies*. *Appl. Statist.* 57, Part 4, pp. 399-418.
- HAUG, G. H., HUGHEN, K. A., SIGMAN, D. M., PETERSON, L. C., & RÖHL, U., 2001. *Southward migration of the intertropical convergence zone through the Holocene*. *Science*, 293(5533), 1304-1308.
- HEEGAARD E., BIRKS H.J.B., TELFORD R.J., 2005. *Relationships between calibrated ages and depth in stratigraphical sequences: an estimation procedure by mixed-effect regression*. *The Holocene* 2005; 15; 612. Doi:10.1191/0959683605hl836rr.
- HAUG GH, GUNTHER D, PETERSON LC, SIGMAN DM, HUGHEN KA AND AESCHLIMANN B., 2003. *Climate and the collapse of Maya civilization*. *Science* 299(5613): 1731–1735.
- HELGE W. ARZ, J. P., GEROLF WEFER, 1998. *Correlated Millennial-Scale Changes in surface Hydrography and Terrigenous Sediment Yield Inferred from Last-Glacial Marine Deposits off Northeastern Brazil*. *Quaternary Research* 50: 157 - 166.
- HENGSTUM, P. J., DONNELLY, J. P., KINGSTON, A. W., WILLIAMS, B. E., SCOTT, D. B., REINHARDT, E. G., ... & PATTERSON, W. P., 2015. *Low-frequency storminess signal at Bermuda linked to cooling events in the North Atlantic region*. *Paleoceanography*, 30(2), 52-76.

REFERENCES

- HENNEKAM, R., DE LANGE, G., 2012. *X-ray fluorescence core scanning of wet marine sediments: methods to improve quality and reproducibility of high-resolution paleoenvironmental records*. *Limnology and Oceanography: Methods*, 10, 991-1003. doi: 10.4319/lom.2012.10.991
- HERBERT, T. D., 2003. *Alkenone paleotemperature de-terminations*. *Treatise on Geochemistry*, 6:391-432.
- HERNÁNDEZ A., KUTIEL H., TRIGO R.M., VALENTE M.A., SIGRÓ J., CROPPER T. AND ESPÍRITO SANTO F., 2016. *New Azores archipelago daily precipitation dataset and its links with large-scale modes of climate variability*. *International Journal of Climatology*
- HERNÁNDEZ, A., TRIGO, R.M., PLA-RABES, S., VALERO-GARCÉS, B.L., JEREZ, S., RICO-HERRERO, M., VEGA, J.C., JAMBRINA-ENRÍQUEZ, M., GIRALT, S., 2015. *Sensitivity of two Iberian lakes to the North Atlantic atmospheric circulation modes*. *Clim Dyn*, 45, 3403-3417. doi 10.1007/s00382-015-2547-8
- HODELL, D.A., SCHELSKE, C.L., 1998. *Production, sedimentation, and isotopic composition of organic matter in Lake Ontario*. *Limnology and Oceanography* 43, 200-214.
- HOGG, N.G. AND W.E. JOHNS, 1995: *Western boundary currents*. U.S. National Report to International Union of Geodesy and Geophysics 1991-1994, Supplement to Reviews of Geophysics, 33, 1311-1334.
- HOLLANDER, D.J., MACKENZIE, J.A., 1991. *CO₂ control on carbon-isotope fractionation during aqueous photosynthesis: a paleo-pCO₂ barometer*. *Geology* 19, 929-932.
- Hollander, D.J., Mackenzie, J.A., ten Haven, H.L., 1992. A 200 year sedimentary record of progressive eutrophication in Lake Greifen (Switzerland): implications for the origin of organic-carbon rich sediments. *Geology* 20, 825-828.
- HOPMANS, E. C., J. W. H. WEIJERS, E. SCHEFUß, L. HERFORT, J. S. SINNINGHE DAMSTÉ, AND S. SCHOUTEN. 2004. *A novel proxy for terrestrial organic matter in sediments based on branched and isoprenoid tetraether lipids*. *Earth and Planetary Sciences Letters*, 224:107-116.
- HUBENY, J.B., KING, J.W., SANTOS, A., 2006. *Subdecadal to multidecadal cycles of late Holocene North Atlantic climate variability preserved by estuarine fossil pigments*. *Geology* 34, 569e572.
- HUGUET, C., G. J. DE LANGE, O. GUSTAFSSON, J. J. MIDDELBURG, J. S. SINNINGHE DAMSTÉ, AND S. SCHOUTEN. 2008. *Selective preservation of soil organic matter in oxidized marine sediments (Madeira Abyssal Plain)*. *Geochimica et Cosmochimica Acta*, 72: 6061-6068.
- HUGUET A., FOSSE C., LAGGOUN-DÉFARGE F., TOUSSAINT M. L. AND DERENNE S. 2010. *Occurrence and distribution of glycerol dialkyl glycerol tetraethers in a French peat bog*. *Org. Geochem.* 41, 559-572.
- HUGUET C., HOPMANS E. C., FEBO-AYALA W., THOMPSON D. H., SINNINGHE DAMSTÉ J. S. AND SCHOUTEN S. 2006. *An improved method to determine the absolute abundance of glycerol dibiphytanyl glycerol tetraether lipids*. *Org. Geochem.* 37, 1036-1041.
- HURRELL, J.W., LOON, H.V., 1997. Decadal variations in climate associated with the North Atlantic Oscillation. *Climatic Change* 36, 301e326.
- HURRELL, J. W., KUSHNIR, Y., OTTERSEN, G., & VISBECK, M., 2003. *An overview of the North Atlantic oscillation* (pp. 1-35). American Geophysical Union.
- HURRELL J.W., KUSHNIR Y., VISBECK M., 2001. *The North Atlantic Oscillation*. *Science* 26, Vol 291 no. 5504pp. 603-605. Doi: 10.1126/science.1058761.
- JANSEN J.H.F., KOSTER S. J. V. D. G., B., VAARS A.J., 1998. *CORTEX, a shipboard XRF-scanner for element analyses in split sediment cores*. *Marine Geology* 151: 10.
- JIMÉNEZ-MUNT, I., BIRD, M., & FERNANDEZ, M., 2001. *Thin-shell modeling of neotectonics in the Azores-Gibraltar Region*. *Geophysical Research Letters*, 28.
- JONES, P. D., T. J. OSBORN, AND K. B. BRIFFA. 2001. *The Evolution of Climate Over the Last Millennium*, *Science*, 292, 662 - 667.
- JOHNS, W. E., SHAY, T. J., BANE, J. M., & WATTS, D. R., 1995. *Gulf Stream structure, transport, and recirculation near 68 W*. *Journal of Geophysical Research: Oceans*, 100(C1), 817-838.
- JOYCE, T. M., C. DESER, AND M. A. SPALL, 2000. *On the relation between decadal variability of subtropical mode water and the North Atlantic Oscillation*. *J. Climate*, 13, 2550-2569
- JUGGINS, S. 2012 *Rioja: Analysis of Quaternary Science Data*, R package version (0.8-5). (<http://cran.r-project.org/package=rioja>).
- KENWARD, R., 2006. *The Goshawk*. London, UK: T & A D Poyser. p. 274. ISBN 978-0-7136-6565-9.

- KHOKHLOV, V. N., GLUSHKOV, A. V., & TSENENKO, I. A., 2004. *Atmospheric teleconnection patterns and eddy kinetic energy content: wavelet analysis*. Nonlinear Processes in Geophysics, 11(3), 295-301.
- KILBOURNE K.H., QUINN T.M., WEBB R., GUILDERSON T., NYBERG J., WINTER A. 2010. Coral windows onto seasonal climate variability in the northern Caribbean since 1479. *Geochemistry, geophysics, geosystems*, 10. Doi:10.1029/2010GC003171.
- KIM, J.-H., S. SCHOUTEN, E. C. HOPMANS, B. DONNER, AND J. S. SINNINGHE DAMSTÉ. 2008. *Global sediment core-top calibration of the TEX₈₆ paleothermometer in the ocean*. *Geochimica et Cosmochimica Acta* 72 (4), 1154–1173.
- KIM, J., J. VAN DER MEER, S. SCHOUTEN, P. HELMKE, V. WILLMOTT, F. SANGIORGI, N. KOC, E. HOPMANS, J. S. SINNINGHE DAMSTÉ. 2010. *New indices and calibrations derived from the distribution of crenarchaeal isoprenoid tetraether lipids: Implications for past sea surface temperature reconstructions*. *Geochimica et Cosmochimica Acta*, 74:4639–4654.
- KIRTMAN, B., VECCHI, G.A., 2004. *Why climate modelers should worry about atmospheric and oceanic weather*. In: Chang, C.P. (Eds). *The global monsoon system: research and forecast*. World Scientific Publishing Co. 511-523.
- KITA, M., S. AIBARA, M. KATO, M. ISHINAGA, AND T. HATA. 1973. *Effect of changes in fatty acid composition of phospholipid species on the b-galactoside transport system of Escherichia coli K-12*. *Biochimica et Biophysica Acta (BBA)-Biomembranes* 298:69–74.
- KNIGHT, J.R., ALLAN, R.J., FOLLAND, C.K., VELLINGA, M., MANN, M.E., 2005. *A signature of persistent natural thermohaline circulation cycles in observed climate*. *Geophysical Research Letters* 32, L20708. <http://dx.doi.org/10.1029/2005GL024233>.
- KNIGHT J, FOLLAND C, SCAIFE A, 2006. *Climate impacts of the Atlantic Multidecadal Oscillation*. *Geophys Res Lett* 33:L17706
- KNUDSEN, M.F., SEIDENKRANTZ, M.-S., JACOBSEN, B.H., KUIJPERS, A., 2011. *Tracking the Atlantic Multidecadal Oscillation through the last 8,000 years*. *Nature Communications* 2, 178.
- KÖNNEKE, M., A. E. BERNHARD, J. R. DE LA TORRE, C. B. WALKER, J. B. WATERBURY, AND D. A. STAHL. 2005. *Isolation of an autotrophic ammonia-oxidizing marine archaeon*. *Nature*, 437:543–546.
- KOSSIN J.P., CAMARGO S.J., SITKOWSKI M., 2010. *Climate modulation of North Atlantic Hurricane Track*. *Journal of Climate*. Vol 23, doi:10.1175/2010JCLI3497.1
- KRAUSS, W., 1986. *The North Atlantic Current*. *Journal of Geophysical Research*, 91, 5061-5074.
- KUSHNIR Y, 1994. Interdecadal variations in North Atlantic sea surface temperature and associated atmospheric conditions. *J Clim* 7:141–157
- KUTIEL H, TRIGO RM. 2014. *The rainfall regime in Lisbon in the last 150 years*. *Theor. Appl. Climatol.* 118: 387–403, doi: 10.1007/s00704-013-1066-y.
- KYLANDER, M.E., AMPEL, L., WOHLFARTH, B., VERES, D., 2011. *High-resolution X-ray fluorescence core scanning analysis of Les Echets (France) sedimentary sequence: new insights from chemical proxies*. *J. Quat. Sci.* 26 (1), 109-117
- LAKENET. (2004). Recuperado el 14 de junio de 2016, de <http://www.worldlakes.org/lakeprofiles.asp?anchor=area>
- LAMB, H.H., 1979. *Climatic variation and changes in the wind and ocean circulation: The Little Ice Age in the Northeast Atlantic*. *Quatern. Res.* 11, 1–20.
- LAMB, H.H., FRYDENDAHL, K., 1991. *Historic Storms of the North Sea, British Isles and Northwest Europe*. Cambridge University Press, Cambridge. 203 pp.
- LARA A., 2014. *Lagoa Azul São Miguel (Açores): Estudi paleoecològic preliminar dels Segles XIII al XXI*. Tesis Master Universitat de Barcelona, Facultat de Biologia.
- LAROCQUE-TOBLER, I., STEWART, M. M., QUINLAN, R., TRACHSEL, M., KAMENIK, C., & GROSJEAN, M., 2012. A last millennium temperature reconstruction using chironomids preserved in sediments of anoxic Seebergsee (Switzerland): consensus at local, regional and Central European scales. *Quaternary Science Reviews*, 41, 49-56.
- LARSON, G. AND SCHAETZL, R., 2001. *Origin and evolution of the Great Lakes*. *Journal of Great Lakes Research* 27: 518-546.
- LATIF, M., 2006. *On North Pacific multidecadal climate variability*, *J. Clim.*, 19, 2906 – 2915.
- LAU, N.-C., AND M. J. NATH, 1994. *A modeling study of the relative roles of tropical and extratropical SST anomalies in the variability of the global atmosphere-ocean system*, *J. Clim.*, 7, 1184 – 1207
- LAWRENCE, J.R., TAYLOR, H.P., Jr., 1971. *Deuterium and oxygen-18 correlation' clay minerals and hydroxides in Quaternary soils compared to meteoric waters*, *Geochim. Cosmochim. Acta* 35, 993.
- LENG, M. J. (Ed.), 2006. *Isotopes in palaeoenvironmental research (Vol. 10)*. New York: Springer.

REFERENCES

- LÉZINE, A. M., HÉLY, C., GRENIER, C., BRACONNOT, P., & KRINNER, G., 2011. *Sahara and Sahel vulnerability to climate changes, lessons from Holocene hydrological data*. Quaternary Science Reviews, 30(21), 3001-3012.
- LI, L., LI, W., & KUSHNIR, Y., 2012. *Variation of the North Atlantic subtropical high western ridge and its implication to Southeastern US summer precipitation*. Climate Dynamics, 39(6), 1401-1412.
- LIPIDS. (2016). Recuperado el 14 de junio de 2016, de <http://biology.tutorvista.com/biomolecules/lipids.html>
- LIVINGSTON D.M., LOTTER A.F., WALKER I.R. 1999. The decrease in Summer surface water temperature with altitude in Swiss alpine lakes: A comparison with air temperature lapse rates. Arctic, Antarctic and Alpine research, 31, 341-352.
- LOOMIS, S.E., RUSSELL, J.M., HEUREUX, A.M., SINNINGHE-DAMSTÉ, J.S., 2014. *Seasonal variability of branched GDGTs in a temperate lake system*. Geochimica et Cosmochimica Acta 144,173-187.
- LOOMIS S. E., RUSSELL J. M., LADD B., STREET-PERROTT F. A. AND SINNINGHE DAMSTÉ J. S. 2012. *Calibration and application of the branched GDGT temperature proxy on East African lake sediments*. Earth Planet. Sci. Lett. 357-358, 277-288.
- LOWE, J. J. AND WALKER, M. J. C. 1997. *Reconstructing Quaternary Environments*. (2nd edition) Prentice Hall
- LOZANO-GARCÍA, M.S., CABALLERO, M., ORTEGA, B., RODRÍGUEZ, A., & SOSA, S., 2007). *Tracing the effects of the Little Ice Age in the tropical lowlands of eastern Mesoamerica*. Proceedings of the National Academy of Sciences, 104(41), 16200-16203.
- LUND, D. C., & CURRY, W. B., 2004. *Late Holocene variability in Florida Current surface density: Patterns and possible causes*. Paleoceanography, 19(4).
- LUND D.C., LYNCH-STIEGLITZ J., CURRY W.B., 2006. *Gulf stream density structure and transport during the past millennium*. Nature letters, vol444.-601
- LUTERBACHER, J., XOPLAKI, E., DIETRICH, D., JONES, P.D., DAVIES, T.D., PORTIS, D., GONZALES-ROUCO, J.F., VON STORCH, H., GYALISTRAS, D., CASTY, C., WANNER, H., 2001. *Extending North Atlantic oscillation reconstructions back to 1500*. Atmospheric Science Letters 2, 114e124.
- LUTERBACHER, J., XOPLAKI, E., DIETRICH, D., RICKLI, R., JACOBETT, J., BECK, C., ... & WANNER, H., 2002. *Reconstruction of sea level pressure fields over the Eastern North Atlantic and Europe back to 1500*. Climate Dynamics, 18(7), 545-561.
- MACHADO, F., PARSONS, W. H., RICHARDS, A. F., & MULFORD, J. W., 1962. *Capelinhos eruption of Fayal volcano, Azores, 1957-1958*. Journal of Geophysical Research, 67(9), 3519-3529.
- MCCARTHY, G. D., HAIGH, I. D., HIRSCHI, J. J. M., GRIST, J. P., & SMEED, D. A., 2015. *Ocean impact on decadal Atlantic climate variability revealed by sea-level observations*. Nature, 521(7553), 508-510.
- MALHEIRO A., 2006. *Geological hazards in the Azores archipelago: Volcanic terrain instability and human vulnerability*. Journal of Volcanology and geothermal research 156: 158-171.
- MANN, C.R., 1967: *The termination of the Gulf Stream and the beginning of the North Atlantic Current*. Deep-Sea Research, 14, 337-359.
- MANN, C.R., 1972: *A review of the branching of the Gulf Stream System*, Proc. R. Soc. Edinb., B72, 341-349.
- MANN, M. E., ZHANG, Z., RUTHERFORD, S., BRADLEY, R. S., HUGHES, M. K., SHINDELL, D., ... & NI, F., 2009. *Global signatures and dynamical origins of the Little Ice Age and Medieval Climate Anomaly*. Science, 326(5957), 1256-1260.
- MANTUA, N. J., S. R. HARE, Y. ZHANG, J. M. WALLACE, AND R. C. FRANCIS, 1997. *A Pacific interdecadal climate oscillation with impacts on salmon production*, Bull. Am. Meteorol. Soc., 78, 1069 - 1079.
- MARGALEF, R. 1983. *Limnología*. Ediciones Omega, S.A., Barcelona. 1010 p.
- MARINI, C., & FRANKIGNOUL, C., 2014. *An attempt to deconstruct the Atlantic multidecadal oscillation*. Climate dynamics, 43(3-4), 607-625.
- MARLOWE, I., J. GREEN, A. NEAL, S. BRASSELL, G. EG-LINTON, AND P. COURSE. 1984. *Long chain (n-C37-C39) alkenones in the Prymnesiophyceae. Distribution of alkenones and other lipids and their taxonomic significance*. British Phycological Journal, 19:203-216.
- MARSHALL J, KUSHNER Y, BATTISTI D, CHANG P, CZAJA A, DICKSON R, HURRELL J, MCCARTNEY M, SARAVANAN R AND VISBECK M. 2001. *North Atlantic climate variability: Phenomena, impacts and mechanisms*. International Journal of Climatology, 21, 1863-1898
- MARTÍN-CLOSAS C., PERMANYER A., VILA M-J., 2005. *Palynofacies distribution in a lacustrine basin*. Geobios 38 197-210. Doi: 10.1016/j.geobios.2003.09.007.
- MARTÍNEZ-CORTIZAS, A., PONTEVEDRA-POMBAL, X., GARCÍA-RODEJA, E., NOVOA-MUNOZ, J.C., SHOTYK, W., 1999. *Mercury in a Spanish Peat Bog: archive of climate change and atmospheric metal*

deposition. *Science* 284, 939–942. doi:10.1126/ science.284.5416.939

MARTINS G, RIBEIRO D.C., PACHECO D., CRUZ J.V., CUNHA R., GONÇALVES V., NOGUEIRA R., BRITO A.G., 2008. *Prospective scenarios for water quality and ecological status in Lake Sete Cidades (Portugal): The integration of mathematical modelling in decision processes*. *Applied Geochemistry* 23 2171-2181. Doi:10.1016/j.apgeochem.2008.03.001

MAYEWSKI P.A., ROHLING E.E., STAGE J.C., KARLÉN W., MAASCH K.A., MEEKER L.D., MEYERSON E.A., GASSE F., VAN KREVALD S., HOLGREN K. LEE-THORP J., ROSQVIST G., ROCK E., STAUBWASSER M., SCHENEIDER R.R., STEIG E.J., 2004. Holocene Climate variability. *Quaternary Research* 62, 243-255.

MEEKER, L. D., & MAYEWSKI, P. A., 2002. *A 1400-year high-resolution record of atmospheric circulation over the North Atlantic and Asia*. *The Holocene*, 12(3), 257-266.

MESTAS-NUFIEZ, A.M., AND D. B. ENFIELD, 1999. *Rotated global modes of non-ENSO sea surface temperature variability*, *J. Climate*, 12, 2734-2746.

MEYERS, P. A., 2003. *Applications of organic geochemistry to paleolimnological reconstructions: a summary of examples from the Laurentian Great Lakes*. *Organic geochemistry*, 34(2), 261-289.

MEYERS, P. A., & ISHIWATARI, R., 1993. *Lacustrine organic geochemistry—an overview of indicators of organic matter sources and diagenesis in lake sediments*. *Organic geochemistry*, 20(7), 867-900.

MEYERS, PA, TERANES JL., 2001. *Sediment Organic Matter. Tracking environmental change using lake sediments*. Volume 2, Physical and geochemical methods. 2(Last WM, Smol JP, Eds.):239-270., Dordrecht; Boston: Kluwer Academic Publishers.

MIETTINEN, A., KOÇ, N., HALL, I. R., GODTLIEBSEN, F., & DIVINE, D., 2011. *North Atlantic sea surface temperatures and their relation to the North Atlantic Oscillation during the last 230 years*. *Climate dynamics*, 36(3-4), 533-543.

MILLER, A. J., AND N. SCHNEIDER, 2000. *Interdecadal climate regime dynamics in the North Pacific Ocean: Theories, observations, and ecosystem impacts*, *Progr. Oceanogr.*, 47, 355 – 379.

MOFFA-SÁNCHEZ P., BORN A., HALL I.R., THORNALLEY D.J.R., BARKER, 2014. Solar forcing of North Atlantic surface temperature and salinity over the past millennium. *Nature geoscience* vol 14.

MOORE, G. W. K., RENFREW, I. A., PICKART R.S., 2013. *Multidecadal mobility of the north Atlantic Oscillation*. *J. Clim*, 26, 2453-2466.

MORATO, T., KVILE, K. Ø., TARANTO, G. H., TEMPERA, F., NARAYANASWAMY, B. E., HEBBELN, D., & PITCHER, T. J., 2012. *Seamount physiography and biology in North-East Atlantic and Mediterranean Sea*. *Biogeosciences Discussions*, 9(12), 18951-18992.

MORELLÓN, M., PÉREZ-SANZ, A., CORELLA, J. P., BÜNTGEN, U., CATALÁN, J., GONZÁLEZ-SAMPÉRIZ, P., ... & SAZ-SÁNCHEZ, M. A., 2012. *A multi-proxy perspective on millennium-long climate variability in the Southern Pyrenees*. *Climate of the Past*, 8(2), 683-700.

MORENO, A., VALERO-GARCÉS, B.L., GONZÁLEZ-SAMPÉRIZ, P., RICO, M., 2008. *Flood response to rainfall variability during the last 2000 years inferred from the Taravilla Lake record (Central Iberian Range, Spain)*. *J. Paleolimnol.* 40, 943–961. <http://dx.doi.org/10.1007/s10933-008-9209-3>.

MORENO, A. ET AL., 2012. The Medieval Climate Anomaly in the Iberian Peninsula reconstructed from marine and lake records. *Quat. Sci. Rev.* 43, 16–32.

MOORE R.B., 1991. *Geology of the three Late Quaternary Stratovolcanoes on São Miguel , Azores*. US geological survey bulletin 1900.

MOORE, D., HISARD, P., MCCREARY, J., MERLE, J., O'BRIEN, J., PICAUT, J., ... & WUNSCH, C., 1978. *Equatorial adjustment in the eastern Atlantic*. *Geophysical Research Letters*, 5(8), 637-640.

MOORE, R.B., RUBIN, M., 1991. *Radiocarbon dates for lava flows and pyroclastic deposits on São Miguel, Azores*. *Radiocarbon* 33,151–164

MORATO T., KVILE K. Ø., TARANTO G. H., TEMPERA F., NARAYANASWAMY B. E., HEBBELN D., MENEZES G. M., WIENBERG C., SANTOS R. S., AND PITCHER T. J., 2013. *Seamount physiography and biology in the north-east Atlantic and Mediterranean Sea*. *Biogeosciences*, 10, 3039–3054.

MOREIRA J.M., 1987. ALGUNS ASPECTOS DE INTERVENÇÃO HUMANA NA EVOLUÇÃO DA PAISAGEM DA ILHA DE S.MIGUEL (AÇORES). *Colecção Natureza e Paisagem* nº1.

MULLER, R. A. 1977 Radioisotope dating with a cyclotron. *Science* 196: 489-494. 1979 Radioisotope dating with accelerators. *Physics Today* 32: 23-30.

MÜLLER PA AND FISCHER G. 2001. *A 4-year sediment trap record of alkenones from the filamentous upwelling region off Cape Blanc, NW Africa and a comparison with distributions in underlying sediments*. *Deep Sea Research Part I: Oceanographic Research Papers* 48: 1877–1903.

REFERENCES

- MÜLLER PJ, KIRST G, RUHLAND G, VON STORCH I, AND ROSELL-MELE A. 1998. *Calibration of the alkenone paleotemperature index Uk37 based on core-tops from the eastern South Atlantic and the global ocean (60N–60S)*. *Geochimica et Cosmochimica Acta* 62(10): 1757–1772.
- NAEHER S., SMITTENBERG R.H, GILLI A., KIRILOVA E.P., LOTTER A.F., SCHUBERT C.J. 2012. Impact of recent lake eutrophication on microbial community changes as revealed by high lipid biomarkers in Rotsee (Switzerland). *Organic geochemistry* 49, 86-95.
- NAGLE JF, MOROWITZ HJ. 1978. [Molecular mechanisms for proton transport in membranes](#). *Proceedings of the National Academy of Sciences* 75 (1), 298-302
- NIETO-MORENO V., MARTINEZ-RUIZ F., GALLEGO-TORRES D., GIRALT S., GARCIA-ORELLANA J., MASQUÉ P., SINNINGHE-DAMSTÉ J.S., ORTEGA-HUERTAS M., 2014. Paleoclimate and paleoceanographic conditions in the westernmost Mediterranean over the last millenium: an integrated organic and inorganic approach. *Holocene Climate Change*, 172, 264-271.
- NIETO-MORENO, V., MARTÍNEZ-RUIZ, F., GIRALT, S., JIMÉNEZ-ESPEJO, F., GALLEGO-TORRES, D., RODRIGO-GÁMIZ, M., ... & DE LANGE, G. J., 2011. *Tracking climate variability in the western Mediterranean during the Late Holocene: a multiproxy approach*. *Climate of the Past*, 7(4), 1395-1414.
- NOAA Aoml.noaa.gov., 2016. Physical Oceanography Division -. [online] Available at: http://www.aoml.noaa.gov/phod/amo_faq.php [Accessed 8 Jun. 2016].
- NOLLER, J.S., 2000. *Lead-210 Geochronology*. In: *Quaternary Geochronology Methods and Applications* (J. S. Noller et al, eds), AGU Reference Shelf 4, pp. 115–120. American Geophysical Union, Washington.
- NOZAWA, Y., H. IIDA, H. FUKUSHIMA, K. OHKI, AND S. OHNISHI. 1974. *Studies on Tetrahymena membranes: Temperature-induced alterations in fatty acid composition of various membrane fractions in Tetrahymena pyriformis and its effect on membrane fluidity as inferred by spin-label study*. *Bio-chimica et Biophysica Acta (BBA)-Biomembranes*, 367:134–147.
- NUNES, J.C.C., 1999. *A actividade vulcanica na ilha do Pico do Plistoceno Superior ao Holoceno: mecanismo eruptivo e hazard vulcanico*. PhD Thesis, Universidade dos Acores, Ponta Delgada, Acores.
- OHKOUCHI N, KAWAMURA K, KAWAHATA H, AND OKADA H. 1999 *Depth ranges of alkenone production in the central Pacific Ocean*. *Global Biogeochemical Cycles* 13(2): 695–704.
- OKSANEN J., GUILLAUME BLANCHET F., KINDT R., LEGENDRE P., MINCHIN P.R., O'HARA R.B., SIMPSON G.L., SOLYMOS P., STEVENS H.H. AND WAGNER H., 2013. *Vegan: Community Ecology Package*. R package version 2.0-10. <http://CRAN.R-project.org/package=vegan>
- ÓLAFSDÓTTIR, K. B., GEIRSDÓTTIR, Á., MILLER, G. H., & LARSEN, D. J., 2013. *Evolution of NAO and AMO strength and cyclicity derived from a 3-ka varve-thickness record from Iceland*. *Quaternary Science Reviews*, 69, 142-154.
- OLSEN J., ANDERSON N.J., KNUDSEN M.F., 2012. Variability of the North Atlantic Oscillation over the past 5200 years. *Nature geoscience*, 5. Doi:10.1038/NNGEO1589.
- OPPO, D. W., MCMANUS, J. F., & CULLEN, J. L., 2003. *Palaeo-oceanography: Deepwater variability in the Holocene epoch*. *Nature*, 422(6929), 277-277.
- ORTEGA P., LEHNER F., SWINGEDOUW D., MASSON-DELMOTTE V., RAIBLE C.C., CASADO M., YIOU P., 2015. *A model-tested North Atlantic Oscillation reconstruction for the past millennium*. *Nature* vol 523, 71.
- PARNELL, A.C., BUCK, C.E., DOAN, T.K., 2011. *A review of statistical chronology models for high-resolution, proxy-based Holocene paleoenvironmental reconstruction*. *Quaternary Science Reviews*, 30, 2948-2960. doi:10.1016/j.quascirev.2011.07.024
- PAULING, A., LUTERBACHER, J., CASTY, C., & WANNER, H., 2006. *Five hundred years of gridded high-resolution precipitation reconstructions over Europe and the connection to large-scale circulation*. *Climate Dynamics*, 26(4), 387-405.
- PEARSON, E., S. JUGGINS, H. TALBOT, J. WECKSTÖRM, P. ROSÉN, D. RYVES, S. ROBERTS, AND R. SCHMIDT. 2011. *A lacustrine GDGT-temperature calibration from the Scandinavian Arctic to Ant-arctic: Renewed potential for the application of GDGT-paleothermometry in lakes*. *Geochimica et Cosmochimica Acta*, 75:6225–6238.
- PEINGS, Y., SIMPKINS, G., & MAGNUSDOTTIR, G., 2016. *Multidecadal fluctuations of the North Atlantic Ocean and feedback on the winter climate in CMIP5 control simulations*. *Journal of Geophysical Research: Atmospheres*, 121(6), 2571-2592.
- PENG Y., XIAO J., NAKANURE T., LIN B., INOUCHE Y., 2005. *Holocene East Asian monsoonal precipitation patterns revealed by grain size distribution of core sediments of Daihai Lake in Inner Mongolia of north-central China*. *Earth and Planetary Science Letters*. Vol. 233, p 467-479.
- PETERSE, F., E. HOPMANS, S. SCHOUTEN, A. METS, W. RIJSTRA, AND J. SINNINGHE DAMSTÉ. 2011. *Identification and distribution of intact polar branched tetraether lipids in peat and soil*. *Organic Geo-chemistry*, 42:1007–1015.

- PIERCE, D. W., T. P. BARNETT, N. SCHNEIDER, R. SARAVANAN, D. DOMMENGET, AND M. LATIF, 2001. *The role of ocean dynamics in producing decadal climate variability in the North Pacific*, *Clim. Dyn.*, 18, 51 – 70.
- PINTO, J. G., & RAIBLE, C. C., 2012. *Past and recent changes in the North Atlantic oscillation*. *Wiley Interdisciplinary Reviews: Climate Change*, 3(1), 79-90.
- PITCHER, A., N. RYCHLIK, E. HOPMANS, E. SPIECK, W. RIJSTRA, J. OSSEBAAR, S. SCHOUTEN, M. WAGNER, AND J. SINNINGHE DAMSTÉ. 2010. *Crenar-chael dominates the membrane lipids of Candida-tus Nitrososphaera gargensis, a thermophilic Group I. 1b Archaeon*. *The ISME Journal*, 4:542–552.
- PRATIGYA J. POLISSAR P.J., FREEMAN K.H. 2010. Effects of aridity and vegetation on plant-wax dD in modern lake sediments. *Geochimica and Cosmochimica Acta*, 74; 5785-5797.
- POLISSAR, P. J., & FREEMAN, K. H., 2010. *Effects of aridity and vegetation on plant-wax δD in modern lake sediments*. *Geochimica et Cosmochimica Acta*, 74(20), 5785-5797.
- PORTEIRO, J.M., 2000. *Lagoas dos Açores : elementos de suporte ao planeamento integrado*. Ph.D. Thesis, Azores Univ., Portugal. (in Portuguese, with English abstr.).
- POTTS, P. J., 1987. *A handbook of silicate rock analysis*. 2nd ed. Blackie.
- POWERS, L. A., T. C. JOHNSON, J. P. WERNE, I. S. CAS-TAÑEDA, E. C. HOPMANS, J. S. SINNINGHE DAM-STÉ, AND S. SCHOUTEN. 2005. *Large temperature variability in the southern African tropics since the Last Glacial Maximum*. *Geophysical Research Letters* 32: L08706. doi:10.1029/2004GL022014.
- POWERS, L. A., J. P. WERNE, T. C. JOHNSON, E. C. HOPMANS, J. S. SINNINGHE DAMSTÉ, AND SCHOUTEN, S. 2004. *Crenarchaeotal membrane lipids in lake sediments: A new paleotemperature proxy for continental paleoclimate reconstruction?* *Geology*, 32:613–616.
- POWERS, L. A., J. P. WERNE, A. J. VANDERWOUDE, J. S. SINNINGHE DAMSTÉ, E. C. HOPMANS, AND S. SCHOUTEN. 2010. *Applicability and calibration of the TEX₈₆ paleothermometer in lakes*. *Organic Geochemistry*, 41:404–413.
- PRAHL FG, COLLIER RB, DYMOND J, LYLE M, AND SPARROW MA. 1993. *A biomarker perspective on prymnesiophyte productivity in the northeast Pacific Ocean*. *Deep-Sea Research* 1 40: 2061–2076.
- PRAHL FG, DE LANGE GJ, LYLE M, AND SPARROW MA. 1989. *Post-depositional stability of long-chain alkenones under contrasting redox conditions*. *Nature* 341: 434–437.
- PRAHL FG, MUEHLHAUSEN LA, AND ZAHNLE DL. 1988. *Further evaluation of long-chain alkenones as indicators of paleoceanographic conditions*. *Geochimica et Cosmochimica Acta* 52: 2303–2310.
- PRAHL FG, POPP BN, KARL DM, AND SPARROW MA. 2005. *Ecology and biogeochemistry of alkenone production at Station Aloha*. *Deep Sea Research Part I: Oceanographic Research Papers* 52(5): 699–719.
- PRAHL FG, RONTANI JF, ZABETI N, WALINSKY SE, AND SPARROW MA. 2010. *Systematic pattern in – Temperature residuals for surface sediments from high latitude and other oceanographic settings*. *Geochimica et Cosmochimica Acta* 74(1): 131–143.
- PRAHL FG AND WAKEHAM SG. 1987. *Calibration of unsaturation patterns in long-chain ketone compositions for paleotemperature assessment*. *Nature* 330: 367–369.
- PRAHL FG, WOLFE GV, AND SPARROW MA. 2003. *Physiological impacts on alkenone paleothermometry*. *Paleoceanography* 18(2): 1025. <http://dx.doi.org/10.1029/2002PA000803>.
- PROCTOR, C. J., BAKER, A., BARNES, W. L., & GILMOUR, M. A., 2000. *A thousand year speleothem proxy record of North Atlantic climate from Scotland*. *Climate Dynamics*, 16(10-11), 815-820.
- PURCELL A., 1941. *Lakes*. Basic Biology.
- QUARTAU, R., TRENHAILE, A. S., MITCHELL, N. C., & TEMPERA, F., 2010. *Development of volcanic insular shelves: Insights from observations and modelling of Faial Island in the Azores Archipelago*. *Marine Geology*, 275(1), 66-83.
- QUEIROZ, G., 1997. *Vulcão das Sete Cidades (S.Miguel, Açores) História Eruptiva e Avaliação do Hazard*. PhD Thesis. Azores University, 226 pp.
- QUEIROZ, G., PACHECO, J.M., GASPAS, J.L., ASPINALL, W.P., GUEST, J.E., FERRERIRA, T. 2008. *The last 5000 years of activity at Sete Cidades volcano (São Miguel Island, Azores): Implications for hazard assessment*. *Journal of volcanology and geothermal research*, 178, 562-573.
- RAHMSTORF, S., FEULNER, G., MANN, M. E., ROBINSON, A., RUTHERFORD, S., & SCHAFFERNICHT, E. J. (2015). *Exceptional twentieth-century slowdown in Atlantic Ocean overturning circulation*. *Nature climate change*.

REFERENCES

- RAMSEY, B.C., 2008. *Deposition models for chronological records*. Quaternary Science Reviews, 27(1-2), 42-60.
- RAMSEY, C. B., 2009. *Bayesian analysis of radiocarbon dates*. Radiocarbon 51:24.
- RASMUSSEN E.A., TURNER J, 2003. *Polar Lows*. Cambridge University Press. p. 68.
- RAPOSEIRO P.M., RUBIO-INGLÉS M.J., HERNANDEZ A., SÁNCHEZ-LÓPEZ G., COSTA A., GONÇALVES V., SAEZ A., GIRALT S. 2016. *Impacts on top predators' introduction on the chironomid community in a natural lake*. *Fresh water biology* (in press)
- RAY, P., D. WHITE, AND T. BROCK. 1971. *Effect of temperature on the fatty acid composition of Thermus aquaticus*. Journal of Bacteriology 106:25.
- RAYNER, N. A., ET AL., 2003. *Global analyses of sea surface temperature, sea ice, and night marine air temperature since the late nineteenth century*, J. Geophys. Res., 108(D14), 4407, doi:10.1029/2002JD002670.
- REIMER, P.J., BARD, E., BAYLISS, A., BECK, J.W., BLACKWELL, P.G., RAMSEY, C.B., BUCK, C.E., CHENG, H., EDWARDS, R.L., FRIEDRICH, M., GROOTES, P.M., GUILDERSON, HAFLIDASON, H., HAJDAS, I., HATTÉ, C., HEATON, T.J., HOFFMANN, D.L., HOGG, A.G., HUGHEN, K.A., KAISER, K.F., KROMER, B., MANNING, S.W., NIU, M., REIMER, R.W., RICHARDS, D.A., SCOTT, E.M., SOUTHON, J.R., STAFF, R.A., TURNEY, C.S.M., VAN DER PLICHT, J., 2013. *IntCal13 and Marine13 Radiocarbon Age Calibration Curves 0–50,000 Years cal BP*. Radiocarbon, 55, 4, 1869-1887. doi: 10.2458/azu_js_rc.55.16947
- REYNOLDS, D. J., BUTLER, P. G., WILLIAMS, S. M., SCOURSE, J. D., RICHARDSON, C. A., WANAMAKER, A. D., ... & SAYER, M. D. J., 2013. *A multiproxy reconstruction of Hebridean (NW Scotland) spring sea surface temperatures between AD 1805 and 2010*. Palaeogeography, Palaeoclimatology, Palaeoecology, 386, 275-285.
- RICHEY J.N, POORE B.P., FLOWER B.P., QUINN T.M. 2007. *1400yr multiproxy record of climate variability from the northern Gulf of Mexico*. Geology;35,432-426.
- RICHEY J.N, POORE B.P., FLOWER B.P., QUINN T.M., HOLLANDER D.J., 2009. Regionally coherent Little Ice Age in the Atlantic Warm Pool. Geophysical Research Letters, 36.
- RICHTER, T.O., VAN DER GAAST, S.J., KOSTER, B., VAARS, A., GIELES, R., DE STIGTER, H.C., DE HAAS, H., VAN WEERING, T.C.E., 2006. *The Avaatech XRF Core Scanner: technical description and applications to NE Atlantic sediment*. In: Rothwell, R.G. (Ed.) (2006). *New techniques in sediment core analysis*. Geological Society Special Publication, 267: pp. 39-50.
- RODRIGO, F. S., POZO-VÁZQUEZ, D., ESTEBAN-PARRA, M. J., & CASTRO-DÍEZ, Y. (2001). *A reconstruction of the winter North Atlantic Oscillation index back to AD 1501 using documentary data in southern Spain*. Journal of Geophysical Research: Atmospheres, 106(D14), 14805-14818.
- RODRÍGUEZ-PUEBLA, C., & NIETO, S., 2010. Trends of precipitation over the Iberian Peninsula and the North Atlantic Oscillation under climate change conditions. International Journal of Climatology, 30(12), 1807-1815.
- RONTANI J-F, BONIN P, JAMESON I, AND VOLKMAN JK. 2005. *Degradation of alkenones and related compounds during oxic and anoxic incubation of the marine haptophyte Emiliana huxleyi with bacterial consortia isolated from microbial mats from the Camargue, France*. Organic Geochemistry 36: 603–618.
- ROSSI, A., MASSEI, N., LAIGNEL, B., 2011. A synthesis of the time-scale variability of commonly used climate indices using continuous wavelet transform. Global and Planetary Change 78, 1e13.
- ROTHWELL, R. G., HOOGAKKER, B., THOMSON J., CROUDACE I. W., FRENZ M., 2006. *Turbidite emplacement on the southern Balearic Abyssal Plain (western Mediterranean Sea) during Marine Isotope Stages 1–3: an application of ITRAX XRF scanning of sediment cores to lithostratigraphic analysis*. In Rothwell G. G. [ed.], *New techniques in sediment core analysis*. Geological Society Special Publication.
- ROZANSKI, K., ARAGUÁS-ARAGUÁS, L., & GONFIANTINI, R., 1993. *Isotopic patterns in modern global precipitation*. Climate change in continental isotopic records, 1-36.
- ROZANSKI, K., C. SONNTAG, AND K. O. MUNNICH, 1982. *Factors controlling stable isotope composition of European precipitation*, Tellus, 34, 142–150
- RULL V., LARA A., RUBIO-INGLÉS M.J., GIRALT S., GONÇALVES V., RAPOSEIRO P, HERNÁNDEZ A., SÁNCHEZ-LÓPEZ G., SÁEZ A., 2016. *Vegetation changes, human pressure and moisture trends in São Miguel Island (Azores) during the last 700 years: the Lake Azul record*. *Vegetation History and Archaeobotany* (in press).
- RULL, V., STANSELL, N.D., MONTOYA, E., BEZADA, M., ABBOTT, M.B., 2010. *Palynological signal of the Younger Dryas in tropical Venezuelan Andes*. Quaternary Science Reviews 29, 3045–3056.
- RUSTICUCCI, M. y PENALBA, O., 2000. *Interdecadal changes in the precipitation seasonal cycle over Southern South America and their relationship with surface temperature*. Climate Research, nº 16, pp. 1-15.
- SABATIER, P., DEZILEAU, L., COLIN, C., BRIQUEU, L., BOUCHETTE, F., MARTINEZ, P., ... & VON GRAFENSTEIN, U., 2012. *7000years of paleostorm activity in the NW Mediterranean Sea in response to Holocene climate events*. Quaternary Research, 77(1), 1-11.

- SACHS JP AND LEHMAN SJ. 1999. *Subtropical North Atlantic temperatures 60,000 to 30,000 years ago*. Science 286: 756–759.
- SACHS J.P., PAHNKE K., SMITTENBERG R. AND ZHANG Z. 2013. *Biomarker Indicators of Past Climate*. In: Elias S.A. (ed.) *The Encyclopedia of Quaternary Science*, vol. 2, pp. 775-782. Amsterdam: Elsevier.
- SAENGER C., CAME R.E., OPPO D.W., KEIGWIN L.D., COHEN A.L. 2011. Regional climate variability in the western subtropical North Atlantic during the past two millennia. *Paleoceanography*, 26. Doi: 10.1029/2010PA002038.
- SAENGER, C., CHANG, P., JI, L., OPPO, D. W., & COHEN, A. L., 2009. Tropical Atlantic climate response to low-latitude and extratropical sea-surface temperature: A Little Ice Age perspective. *Geophysical Research Letters*, 36(11).
- SAENGER, C., COHEN, A. L., OPPO, D. W., HALLEY, R. B., & CARILLI, J. E., 2009. *Surface-temperature trends and variability in the low-latitude North Atlantic since 1552*. *Nature Geoscience*, 2(7), 492-495.
- SANCETA C., 1979. *Use of semiquantitative microfossil data for paleoceanography*. *Geology*, v.7, p. 88-92. February.
- SÁNCHEZ-CABEZA, J.A., MASQUÉ, P., ANI-RAGOLTA, I., 1998. *Lead-210 and Po-210 Analysis in sediments and soils by Microwave acid digestion*. *Journal of Radioanalytical and Nuclear chemistry*, 227, 1-2, 19-22.
- SÁNCHEZ-LÓPEZ, G., HERNÁNDEZ, A., PLA-RABES, S., TORO, M., GRANADOS, I., SIGRÓ, J., ... & GIRALT, S., 2015. *The effects of the NAO on the ice phenology of Spanish alpine lakes*. *Climatic Change*, 130(2), 101-113.
- SÁNCHEZ-LÓPEZ G., HERNÁNDEZ A., PLA-RABES S., TRIGO R.M., TORO M., GRANADOS I., SÁEZ A., MASQUÉ P., PUEYO J.J., RUBIO-INGLÉS M.J., GIRALT S., 2016. East Atlantic (EA) and North Atlantic Oscillation (NAO) interplay over the Iberian Peninsula for the last two millennia. *Quaternary Science Review* (submitted).
- SAETRE, R. 2007. *The Norwegian Coastal Current—Oceanography and Climate*. Tapir Academic Press; Trondheim. ISBN 82-519-2184-8
- SANTOS, F. D., VALENTE, M. A., MIRANDA, P. M. A., AGUIAR, A., AZEVEDO, E. B., TOMÉ, A. R., & COELHO, F., 2004. *Climate change scenarios in the Azores and Madeira islands*. *World Resource Review*, 16(4), 473-491.
- SCHEFUß, E., SCHOUTEN, S., & SCHNEIDER, R. R., 2005. *Climatic controls on central African hydrology during the past 20,000 years*. *Nature*, 437(7061), 1003-1006.
- SCHLESINGER, M.E. AND NAVIN RAMANKUTTY, 1994. *An oscillation in the global climate system of period 65-70 years*. *Nature*, 367, Issue 6465, pp. 723-726, DOI: 10.1038/367723a0
- SCHMITZ, W. J., & MCCARTNEY, M. S., 1993. *On the north Atlantic circulation*. *Reviews of Geophysics*, 31(1), 29-49.
- SCHOUTEN, S., E. HOPMANS, M. BAAS, H. BOUMANN, S. STANDFEST, M. KÖNNEKE, D. STAHL, AND J. SINNINGHE DAMSTÉ. 2008. *Intact membrane lipids of "Candidatus Nitrosopumilus maritimus," a cultivated representative of the cosmopolitan mesophilic group I crenarchaeota*. *Applied Environmental Microbiology*, 74: 2433.
- SCHOUTEN, S., E. C. HOPMANS, E. SCHEFUß, E., AND J. S. SINNINGHE DAMSTÉ. 2002. *Distributional variations in marine crenarchaeotal membrane lipids: a new tool for reconstructing ancient sea water temperatures?* *Earth and Planetary Sciences Letters*. 204:265–274.
- SCHOUTEN, S., E. C. HOPMANS, A. FORSTER, Y. VAN BREUGEL, M. M. M. KUYPERS, AND J. S. SINNINGHE DAMSTÉ. 2003. *Extremely high sea-surface temperatures at low latitudes during the middle Cretaceous as revealed by archaeal membrane lipids*. *Geology*, 31: 1069–1072.
- SCHOUTEN, S., WOLTERING, M., RIJSTRA, W.I.C., SLUIJS, A., BRINKHUIS, H. & SINNINGHE DAMSTÉ, J.S., 2007. *The Paleocene-Eocene carbon isotope excursion in higher plant organic matter: Differential fractionation of angiosperms and conifers in the Arctic*. *Earth and Planetary Science Letters*, 258, (pp. 581-592) (12 p.).
- SCHOUTEN, S., VAN DER MEER, M. T., HOPMANS, E. C., RIJSTRA, W. I. C., REYSENBACH, A. L., WARD, D. M., & DAMSTÉ, J. S. S., 2007. *Archaeal and bacterial glycerol dialkyl glycerol tetraether lipids in hot springs of Yellowstone National Park*. *Applied and Environmental Microbiology*, 73(19), 6181-6191.
- SCHÖNE, B. R., OSCHMANN, W., RÖSSLER, J., CASTRO, A. D. F., HOUK, S. D., KRÖNCKE, I., ... & DUNCA, E., 2003. *North Atlantic Oscillation dynamics recorded in shells of a long-lived bivalve mollusk*. *Geology*, 31(12), 1037-1040.
- SCHUTTER ME AND DICK RP, 2000. *Comparison of fatty acid methyl ester (FAME) methods for characterizing microbial communities*. *Soil Science Society of America Journal* 64,1659-1668.
- SCIENCEDAILY, 2016. https://www.sciencedaily.com/terms/ocean_current.htm checked on 18/06/2016.
- SEBAG D., GIOVANNI C., OGIER S., MESNAGE V., LAGGOUN-DÉFARGE F., DURAND A., 2006. *Inventory of sedimentary organic matter in modern wetland (Marais Vernier, Normandy, France) as source-indicative tools to study Holocene alluvial deposits (Lower Seine Valley, France)*. *International Journal of Coal Ecology*, 67 1-16.doi: 10.1016/j.coal.2005.08.002.

REFERENCES

- SEITZINGER, S. P., 1988. *Denitrification in freshwater and coastal marine ecosystems: ecological and geochemical significance*. *Limnology and Oceanography*, 33(4part2), 702-724.
- SESSIONS A. L., BURGOYNE T. W., AND HAYES J. M., 2001. *Correction of H₃⁺ contributions in hydrogen isotope ratio monitoring mass spectrometry*. *Analytical Chemistry* 73, 192-199.
- SHABBAR, A., HUANG, J., & HIGUCHI, K., 2001. The relationship between the wintertime North Atlantic Oscillation and blocking episodes in the North Atlantic. *International Journal of Climatology*, 21(3), 355-369.
- SHAKUN J. D., CLARK P. U., HE F., MARCOTT S. A., MIX A. C., LIU Z.Y., OTTO-BLIESNER B., SCHMITTNER A. AND BARD E. 2012. *Global warming preceded by increasing carbon dioxide concentrations during the last deglaciation*. *Nature* 484, 49-54.
- SHANAHAN, T.M., J.W. BECK, J.T. OVERPECK, N. MCKAY, J.E. PIGATI, J.A. PECK, C. SCHOLZ, J. KING. 2012. *Late Quaternary sedimentological and climate changes at Lake Bosumtwi Ghana: new constraints from laminae analysis and radiocarbon age modeling*. *Palaeogeography, Palaeoclimatology, Palaeoecology*, v. 361, pp. 49-60.
- SHANAHAN, T.M., HUGHEN, K.A., VAN MOOY, B.A.S. 2013, *Temperature sensitivity of branched and isoprenoid GDGTs in Arctic lakes*. *Organic Geochemistry*, v. 64, pp. 119-128.
- SHINDELL, D. T., MILLER, R. L., SCHMIDT, G. A., & PANDOLFO, L., 1999. *Simulation of recent northern winter climate trends by greenhouse-gas forcing*. *Nature*, 399(6735), 452-455.
- SHINDELL, D. T., SCHMIDT, G. A., MANN, M. E., RIND, D., AND WAPLE, A. 2001 *Solar Forcing of Regional Climate Change During the Maunder Minimum*, *Science*, 294, 2149-2152
- SIEGENTHALER, U., & SARMIENTO, J. L., 1993. *Atmospheric carbon dioxide and the ocean*. *Nature*, 365(6442), 119-125.
- SINNINGHE DAMSTE J. S., HOPMANS E. C., PANCOST R. D., SCHOUTEN S. AND GEENEVASEN J. A. J. 2000. *Newly discovered non-isoprenoid glycerol dialkyl glycerol tetraether lipids in sediments*. *Chem. Commun.* 17, 1683-1684.
- SIKES EL, O'LEARY T, NODDER SD, AND VOLKMAN JK. 2005. *Alkenone temperature records and biomarker flux at the subtropical front on the Chatham Rise, SW Pacific Ocean*. *Deep Sea Research Part I: Oceanographic Research Papers* 52(5): 721-748.
- SIKES EL AND VOLKMAN JK. 1993. *Calibration of alkenone unsaturation ratios (U_{37k0}) for paleotemperature estimation in cold polar waters*. *Geochimica et Cosmochimica Acta* 57(8): 1883-1889.
- SINNINGHE DAMSTÉ, J. S., E. C. HOPMANS, S. SCHOUTEN, A. C. T. VAN DUIN, AND J. A. J. GEENEVASEN. 2002. *Crenarchaeol: the characteristic core glycerol dibiphytanyl glycerol tetraether membrane lipid of cosmopolitan pelagic crenarchaeota*. *Journal of Lipid Research*, 43:1641-1651
- SINNINGHE DAMSTÉ, J. S., J. OSSEBAAR, B. ABBAS, S. SCHOUTEN, AND D. VERSCHUREN. 2009. *Fluxes and distribution of tetraether lipids in an equatorial African lake: Constraints on the application of the TEX₈₆ palaeothermometer and BIT index in lacustrine settings*. *Geochimica et Cosmochimica Acta*, 73:4232-4249.
- SINNINGHE DAMSTÉ, J., W. RIJPSTRA, E. HOPMANS, J. WEIJERS, B. FOESEL, J. OVERMANN, AND S. DE-DYSH. 2011. *13, 16-Dimethyl octacosanedioic acid (iso-diabolic acid), a common membrane-spanning lipid of Acidobacteria subdivisions 1 and 3*. *Applied Environmental Microbiology*, 77:4147-4154.
- SMITH, M.E., CARROLL, A.R., AND SCOTT, J.J., 2015, *Stratigraphic Expression of Climate, Tectonism, and Geomorphic Forcing in an Underfilled Lake Basin: Wilkins Peak Member of the Green River Formation*, in Smith, M.E., and Carroll, A.R., 2015. *Stratigraphy and Paleolimnology of the Eocene Green River Formation, Western U.S.*: Springer, in press.
- SNYDER, D. C., WIDOM, E., PIETRUSZKA, A. J., CARLSON, R. W., & SCHMINCKE, H. U., 2007. *Time scales of formation of zoned magma chambers: U-series disequilibria in the Fogo A and 1563 AD trachyte deposits, São Miguel, Azores*. *Chemical geology*, 239(1), 138-155.
- SPANGEL, T., CUBASCH, U., RAIBLE, C. C., SCHIMANKE, S., KORPER, J., AND HOFER, D., 2010. *Transient climate simulations from the Maunder Minimum to present day: role of the stratosphere*, *J. Geophys. Res.*, 115, D00110
- Stuiver, M., Reimer, P. J., and Reimer, R. W. 2005. CALIB 7.1. [<http://calib.qub.ac.uk/calib/>] last Access: March 2016.
- SOLANKI, S. K., USOSKIN, I. G., KROMER, B., SCHÜSSLER, M., & BEER, J. (2004). *Unusual activity of the Sun during recent decades compared to the previous 11,000 years*. *Nature*, 431(7012), 1084-1087.
- SONDERGAARD M., HANSEN B. AND MARKAGER S., 1995. *Dynamics of dissolved organic carbon lability in a eutrophic lake*. *Limnol. Oceanogr.* 40, 46±54
- SPANG, A., R. HATZENPICHLER, C. BROCHIER-ARMANET, T. RATTEI, P. TISCHLER, E. SPIECK, W. STREIT, D. STAHL, M. WAGNER, AND C. SCHLEPER. 2010. *Distinct gene set in two different lineages of ammonia-oxidizing archaea supports the phylum Thaumarchaeota*. *Trends In Microbiology*, 18:331-340.
- STAHL D.W., CLEAVELAND M.K., 1994. *Tree-ring reconstructed rainfall over the southern USA during the Medieval Warm Period and the Little Ice Age*. *Climatic Change*, 26,2.

- STANSELL, N. D., STEINMAN, B. A., ABBOTT, M. B., RUBINOV, M., & ROMAN-LACAYO, M., 2013. *Lacustrine stable isotope record of precipitation changes in Nicaragua during the Little Ice Age and Medieval Climate Anomaly*. *Geology*, 41(2), 151-154.
- STICKLER A, BRÖNNIMANN S, VALENTE MA, BETHKE J, STERIN A, JOURDAIN S, ROUCAUTE E, VASQUEZ MV, REYES DA, ALLAN R, DEE D., 2014. *ERA-CLIM: historical surface and upper-air data for future reanalyses*. *Am. Meteorol. Soc.*95: 1419-1430
- STUIVER, M., REIMER P.J., AND REIMER R.W., 2005. *CALIB 5.0* <http://calib.qub.ac.uk/calib>.
- STURT, H. F., R. E. SUMMONS, K. SMITH, M. ELVERT, AND K.-U. HINRICHS. 2004. *Intact polar membrane lipids in prokaryotes and sediments deciphered by high-performance liquid chromatography/electrospray ionization multistage mass spectrometry—new biomarkers for biogeochemistry and microbial ecology*. *Rapid Communications in Mass Spectrometry*, 18:617–628.
- SUN, Q., G. CHU, M. LIU, M. XIE, S. LI, Y. LING, X. WANG, L. SHI, G. JIA, AND H. LÜ. 2011. *Distributions and temperature dependence of branched glycerol dialkyl glycerol tetraethers in recent lacustrine sediments from China and Nepal*. *Journal of Geophysical Research–Biogeoscience*, 116:G01008.
- SUTTON, R.T., HODSON, D.L.R., 2005. *Atlantic Ocean forcing of North American and European summer climate*. *Science* 309, 115e118.
- SWINDLES, G. T., MORRIS, P. J., BAIRD, A. J., BLAAUW, M., & PLUNKETT, G., 2012. *Ecohydrological feedbacks confound peat-based climate reconstructions*. *Geophysical Research Letters*, 39(11).
- TALBOT, M. R., & JOHANNESSEN, T., 1992. *A high resolution palaeoclimatic record for the last 27,500 years in tropical West Africa from the carbon and nitrogen isotopic composition of lacustrine organic matter*. *Earth and Planetary Science Letters*, 110(1), 23-37.
- TAYLOR A.H., STEPHENS J.A. 1998. The North Atlantic Oscillation and the latitude of the Gulf Stream. *Tellus*, 50A. 134-142.
- TELFORD, R. J., HEEGARD E., BIRKS H.J.B., 2004. *All age–depth models are wrong: but how badly?* *Quaternary Science Reviews* 23(1–2), 1-5.
- TERNOIS Y, SICRE M-A, BOIREAU A, BEAUFORT L, MIQUEL J-C, AND JEANDEL C. 1998. *Hydrocarbons, sterols and alkenones in sinking particles in the Indian Ocean sector of the Southern Ocean*. *Organic Geochemistry* 28(7–8): 489–501.
- TIMMERMANN, A., LATIF, M., VOSS, R., & GRÖTZNER, A., 1998. *Northern hemispheric interdecadal variability: a coupled air-sea mode*. *Journal of Climate*, 11(8), 1906-1931.
- TRENBERTH, K. E., & CARON, J. M. (2001). *Estimates of meridional atmosphere and ocean heat transports*. *Journal of Climate*, 14(16), 3433-3443.
- TRENBERTH, K. E., & SHEA, D. J., 2006. Atlantic hurricanes and natural variability in 2005. *Geophysical Research Letters*, 33(12).
- TRIGO, R. M., POZO-VÁZQUEZ, D., OSBORN, T. J., CASTRO-DÍEZ, Y., GÁMIZ-FORTIS, S., & ESTEBAN-PARRA, M. J., 2004. *North Atlantic Oscillation influence on precipitation, river flow and water resources in the Iberian Peninsula*. *International Journal of Climatology*, 24(8), 925-944.
- THIERSTEIN, H., K. GEITZENAUER, AND B. MOLFINO. SHACKLETON, N., 1977. *Global synchronicity of late Quaternary coccolith datum levels: Validation by oxygen isotopes*. *Geology*, 5:400.
- THOMPSON LG, MOSLEY-THOMPSON E, BOLZAN JF, KOCI BR., 1985. *A 1500-year record of tropical precipitation in ice cores from the Quelccaya Ice Cap, Peru*. *Science* 229:971–73.
- THOMPSON LG, MOSLEY-THOMPSON E, DAVIS ME, LIN PN, HENDERSON K, MASHIOTTA TA., 2003. *Tropical glacier and ice core evidence of climate change on annual to millennial time scales*. *Clim. Change* 59:137–55
- TIERNEY, J. E., S. C. LEWIS, B. I. COOK, A. N. LEGRANDE AND G. A. SCHMIDT. 2011. *Model, proxy and isotopic perspectives on the East African Humid Period*. *Earth and Planetary Science Letters* 307,103–112
- TIERNEY, J., M. MAYES, N. MEYER, C. JOHNSON, P. SWARZENSKI, A. COHEN, AND J. RUSSELL. 2010. *Late-twentieth-century warming in Lake Tanganyika unprecedented since AD 500*. *Nature Geoscience*, 3:422–425.
- TIERNEY, J. E., AND J. M. RUSSELL. 2009. *Distributions of branched GDGTs in a tropical lake system: Implications for lacustrine application of the MBT/CBT paleoproxy*. *Organic Geochemistry*, 40:1032–1036.
- TIERNEY, J. E., J. M. RUSSELL, Y. HUANG, J. S. SIN-NINGHE DAMSTÉ, E. C. HOPMANS, AND A. S. COHEN. 2008. *Northern Hemisphere controls on tropical southeast African climate during the past 60,000 years*. *Science*, 322:252–255.

REFERENCES

- TIERNEY, J. E., J. M. RUSSELL, H. EGGERMONT, E. C. HOPMANS, D. VERSCHUREN, AND J. S. SINNINGHE DAMSTÉ. 2010. *Environmental controls on branched tetraether lipid distributions in tropical East African lake sediments*. *Geochimica et Cosmochimica Acta*, 74:4902–4918.
- TIERNEY, J. E., J. E. SMERDON, K. J. ANCHUKAITIS, AND R. SEAGER. 2013. *Multidecadal variability in East African hydroclimate controlled by the Indian Ocean*. *Nature* 493, 389–392.
- TIERNEY, J., S. SCHOUTEN, A. PITCHER, E. HOPMANS, AND J. SINNINGHE DAMSTÉ. 2012. *Core and intact polar glycerol dialkyl glycerol tetraethers (GDGTs) in Sand Pond, Warwick, Rhode Island (USA): Insights into the origin of lacustrine GDGTs*. *Geochimica et Cosmochimica Acta*, 77:561–581.
- TOUCHAN, R.; GARFIN, G.; MEKO, D.M.; FUNKHOUSER, G.; ERKAN, N.; HUGHES, M.K.; WALLIN, B.S., 2013. Southwestern Turkey Spring Precipitation Reconstructions. *International Journal of Climatology*, 23, 157 – 171. <https://www.ncdc.noaa.gov/paleo/study/6301>
- TROMMER, G., M. SICCHA, M. VAN DER MEER, S. SCHOUTEN, J. S. SINNINGHE DAMSTÉ, H. SCHULZ, C. HEMLEBEN, C. AND M. KUCERA. 2009. *Distribution of Crenarchaeota tetraether membrane lipids in surface sediments from the Red Sea*. *Organic Geochemistry*, 40:724–731.
- TROUET V., ESPER J., GRAHAM N.E., BAKER A., SCOURSE J.D., FRANK D.C. 2009. Persistent positive North Atlantic Oscillation Mode Dominated the Medieval Climate Anomaly. *Science*, 324, 78-80.
- TROUET, V., SCOURSE, J. D., & RAIBLE, C. C., 2012. North Atlantic storminess and Atlantic Meridional Overturning Circulation during the last Millennium: Reconciling contradictory proxy records of NAO variability. *Global and Planetary Change*, 84, 48-55.
- TYLER, J., A. NEDERBRAGT, V. JONES, AND J. THUROW. 2010. *Assessing past temperature and soil pH estimates from bacterial tetraether membrane lipids: Evidence from the recent lake sediments of Lochnagar, Scotland*. *Journal of Geophysical Research Biogeoscience*, 115:G01015.
- VALENTE M.A., TRIGO RM, BARROS M, NUNES LF, ALVES EI, PINHA EI, ESPÍRITO-SANTO F, MENDES M, MIRANDA M., 2008. *Early stages of therecovery of Portuguese historical meteorological data. In MEDARE- Proceedings of the International Workshop on Rescue and Digitization of Climate Records in the Mediterranean Basin*, Brunet M, Franz GK (eds), WCDMP no. 67, WMO-TD No. 1432, June 2008. World Meteorological Organisation: Geneva 2, Switzerland, 95–102
- VALERO-GARCÉS, B., MORELLÓN, M., MORENO, A., CORELLA, J. P., MARTIN-PUERTAS, C., BARREIRO, F., PÉREZ, A., GIRALT, S., MATA-CAMPO, M. P., 2014. *Lacustrine carbonates of Iberian Karst Lakes: Sources, processes and depositional environments*. *Sedimentary Geology*, 299, 1-29
- VALOIS E SILVA, F. 1886. *Descricao das aguas minerais das Furnas na ilha de Sao Miguel*. In: *Arquivo dos Açores*. pp. 437-446. Typografia do arquivo dos Acores, Ponta Delgada.
- VAN DE VOSSENBERG J.L.C, ARNOLD J.M DRIESSEN, MILTON S DA COSTA, WIL N KONINGS. 1999. *Homeostasis of the membrane proton permeability in Bacillus subtilis grown at different temperatures*. *Biochimica et Biophysica Acta (BBA) - Biomembranes*, Volume 1419, Issue 1, [http://dx.doi.org/10.1016/S0005-2736\(99\)00063-2](http://dx.doi.org/10.1016/S0005-2736(99)00063-2).
- VAREKAMP, J.C., AND THOMAS, E. 1998. *Sea level rise and climate change over the last 1000 years*. *EOS* 79:69-75.
- VAQUERO J.M., TRIGO R.M. 2012. *Anote on Solar Cycle Length during Medieval Climate Anomaly*. *Solar Phys*, 279:289-294.
- VICENTE A., 1956. *Introdução de peixes da agua doce nas lagoas de S.Miguel*. *Açoreana* 5.
- VOLKMAN, J., G. EGLINTON, E. CORNER, AND T. FORS-BERG. 1980. *Long-chain alkenes and alkenones in the marine coccolithophorid Emiliana huxleyi*. *Phytochemistry*, 19:2619–2622.
- VOLKOV D.L., FU L-L. 2010. *On the reasons for the formation and variability of the Azores Current*. *Journal of physical oceanography*. Vol 40. Doi: 10.1175/2010JPO4326.1
- VOLKOV D.L., FU L-L. 2011. *Interannual variability of the Azores Current strength and eddy energy in relation to atmospheric forcing*. *Journal of geophysical research* 116. Doi:10.1029/2011JC007271.
- VON GRAFENSTEIN U, ERLLENKEUSER H, BRAUER A, JOUZEL J, JOHNSEN SJ., 1999. A mid-European decadal isotope climate record from 15,500 to 5000 years B.P. *Science* 284:1654–57
- WAHL, E. R., DIAZ, H. F., & OHLWEIN, C., 2012. *A pollen-based reconstruction of summer temperature in central North America and implications for circulation patterns during medieval times*. *Global and Planetary Change*, 84, 66-74.
- WANAMAKER A.D., BUTLER P.G., SCOURSE J.D., HEINEMEIER J., EIRÍKSSON J., KNUDSEN K.L., RICHARSON C.A., 2012. *Surface changes in the North Atlantic Meridional Overturning circulation during the last millennium*. *Nature communications*. Vol 3, 899. Doi:10.1038/ncomms1901.

- WANG, C., LEE, S. K., & ENFIELD, D. B., 2007. *Impact of the Atlantic warm pool on the summer climate of the Western Hemisphere*. Journal of Climate, 20(20), 5021-5040.
- WANNAMAKER P.E., CALDWELL T.G., JIRACEK G.R., MARIS V., HILL G.J., OGAWA Y., BIBBY H.M., BENNIE S.L., HEISE W. 2009. Fluid and deformation regime of an advancing subduction system at Marlbotough, New Zealand.
- WANNER, H., BRÖNNIMANN, S., CASTY, C., GYALISTRAS, D., LUTERBACHER, J., SCHMUTZ, C., ... & XOPLAKI, E., 2001. *North Atlantic Oscillation—concepts and studies*. Surveys in geophysics, 22(4), 321-381.
- WATTS, W.R., 1975. Air and soil temperature differences in controlled environments, as a consequence of high radiance flux densities and of day/night temperature changes. Plant and Soil, 42, 299-303.
- WEERING T.C.E., 2006. *The Avaatech XRF Core Scanner: technical description and applications to the NE Atlantic Sediments*. IN Rothwell R.G., 2006. New techniques in Sediment Core Analysis. Geological Society, London, Special Publication, 267, 39 – 50. The Geological Society of London 2006.
- WEIJERS, J. W. H., E. SCHEFUß, S. SCHOUTEN, AND J. S. SINNINGHE DAMSTÉ. 2007. *Coupled thermal and hydrological evolution of tropical Africa over the last deglaciation*. Science, 315:1701–1704.
- WEIJERS, J.W.H., SCHOUTEN, S., SLUIJS, A., BRINKHUIS, H. & SINNINGHE DAMSTÉ, J.S., 2007. *Warm Arctic continents during the Palaeocene - Eocene thermal maximum*. Earth and Planetary Science Letters, 261 (1-2), (pp. 230-238).
- WEIJERS, J. W. H., S. SCHOUTEN, O. C. SPAARGAREN, AND J. S. SINNINGHE DAMSTÉ. 2006. *Occurrence and distribution of tetraether membrane lipids in soils: Implications for the use of the TEX₈₆ proxy and the BIT index*. Organic Geochemistry, 37:1680–1693.
- WETZEL, R. G., & LIMNOLOGY, A., 2001. *Lake and river ecosystems*. Limnology, Academic Press, London, 1006.
- WHEELER, D., GARCIA-HERRERA, R., WILKINSON, C.W., WARD, C., 2010. *Atmospheric circulation and storminess derived from Royal Navy logbooks: 1685 to 1750* (vol 101, pg 257, 2010). Climatic Change 103 (3–4). doi:10.1007/s10584.009.9755.3.
- WU P., RODWELL M.J. 2003. *Gulf Stream forcing of the winter North Atlantic Oscillation*. Atmospheric Science Letter, 5, 57-64.
- WUNSCH, C., 1999. *The interpretation of short climate records, with comments on the North Atlantic and Southern Oscillation*. Bulletin of the American Meteorological Society 80, 245e255.
- WURTZEL J.B., BLACK D.E., THUNELL R.C., PETERSON L.C., TAPPE E.J., RAHMAN S., 2013. Mechanisms of the southern Caribbean SST variability over the last two millennia. Geophysical Research Letters, 40.
- YURTSEVER AND GAT, 1981. Atmospheric waters in Stable Isotope Hydrology: Deuterium and Oxygen in the Water Cycle. Technical Report Series, 109. International Atomic Energy Agency, Vienna.
- ZIEGLER, M., JILBERT, T., LANGE, G.J., LOURENS, L.J., REICHART, G.J., 2008. *Bromine counts from XRF scanning as an estimate of the marine organic carbon content of sediment cores*. Geochemistry, Geophysics and Geosystems, 9, 5, 1525-2027.
- ZINK, K., M. VANDERGOES, K. MANGELSDORF, A. DIEFFENBACHER-KRALL, AND L. SCHWARK, L. 2010. *Application of bacterial glycerol dialkyl glycerol tetraethers (GDGTs) to develop modern and past temperature estimates from New Zealand lakes*. Organic Geochemistry 41:1060–1066.